Nuclear Modification Factors for Hadrons At Forward and Backward Rapidities in Deuteron Gold Collisions at $\sqrt{s_{NN}} = 200$ GeV

Chun Zhang

Submitted in partial fulfillment of
the requirements for the degree
of Doctor of Philosophy in the
Graduate School of Arts and Sciences

Columbia University
2005

© 2005

Chun Zhang

All Rights Reserved

ABSTRACT

Nuclear Modification Factors for Hadrons At Forward and Backward Rapidities in Deuteron Gold Collisions at $\sqrt{s_{NN}} = 200$ GeV

Chun Zhang

We report on the charged hadron production in the deuteron-gold reactions at $\sqrt{s_{NN}} = 200$ GeV. Our measurements in the deuteron-direction cover $1.4 < \eta < 2.2$, referred to as forward rapidity, and in the gold-direction $-2.0 < \eta < -1.4$, referred to as backward rapidity, and a transverse momentum range from $0.5-4.0$ GeV/c. We compare the relative yields for different deuteron-gold collision centrality classes. We observe a suppression relative to binary collision scaling at forward rapidity, sensitive to low momentum fraction (x) partons in the gold nucleus, and an enhancement at backward rapidity, sensitive to high x partons in the gold nucleus.

Contents

1 Introduction **1**

1.1 Structure of hadrons 1

1.1.1 Constituents of the matters. 1

1.1.2 Strong interaction and gluons 3

1.1.3 Static quark model for hadrons 4

1.2 Parton distribution functions in nucleons 6

1.2.1 DIS and Quark structure functions 7

1.2.2 QCD Evolution equations 10

1.2.3 Results from HERA experiments and Gluon PDF 13

1.2.4 PDF at small x 17

1.3 Nuclear modification on PDF 20

1.3.1 Quark Structure functions in nuclei 21

1.3.2 Nuclear modification in p/dA collisions 28

1.4 dA collisions at RHIC 31

1.4.1 The suppression of high p_T particle in gold gold collisions . . . 31

1.4.2 dAu collisions at RHIC and gluon density at small x 36

1.4.3 Studies in this thesis 38

2 Experiment setup **40**

2.1 RHIC and PHENIX detector 40

2.1.1 RHIC [40] 40

2.1.2 PHENIX [41] 42

2.2 PHENIX muon arms 47
2.2.1 Muon Tracker 47
2.2.2 Muon Identifier 50
2.3 Data Acquisition system and offline reconstruction 53
2.3.1 Data Acquisition [47] 53
2.3.2 Data reduction 56
2.3.3 Muon arm event reconstruction 56

3 Nuclear modification in dAu collisions 59
3.1 Selection of Hadrons from the PHENIX Muon arms 59
3.1.1 PHENIX Muon arms 59
3.1.2 Select hadrons by matching track momentum and depth in MUID 60
3.1.3 Muon contamination 63
3.1.4 Background from secondary particles produced by hadronic showering in the absorber 65
3.1.5 Fiducial cut to reduce detector edge effect and beam gas . . . 73
3.1.6 Summary on cuts for selecting hadrons 74
3.2 Ratio between hadron yield in central collisions and hadron yield in peripheral collisions 74
3.2.1 Define the nuclear modification factor R_{cp} 74
3.2.2 Centrality definition in deuteron gold collisions 79
3.2.3 Modification on particle composition from absorber 81
3.3 run selection 84
3.3.1 MuID HV status 85
3.3.2 Muid blue logic trigger circuit efficiency 85
3.3.3 select good run 86
3.3.4 event statistic 88
3.4 Results 88

3.4.1 Evaluate the centrality dependence of tracking efficiency and MuID one deep trigger efficiency . . . 88
3.4.2 Results from Minbias trigger sample . . . 96
3.4.3 Results from south MuID 1-deep trigger sample . . . 100
3.4.4 Results from north MuID 1-deep trigger sample . . . 100
3.4.5 systematics . . . 101
3.4.6 summary . . . 107

4 Study of centrality bias **111**
4.1 Introduction . . . 111
4.1.1 Trigger Bias Effect . . . 112
4.1.2 Bin Shifting Effect . . . 113
4.2 What Really Defines Our Event Category? . . . 114
4.3 Modelling the Physics and Defining Our Categories . . . 116
4.4 Data Driven Input Distributions . . . 120
4.4.1 BBCS Response in Proton-Proton Collisions . . . 120
4.5 Modeling the Full Deuteron-Gold Case . . . 126
4.6 Calculating the Correction Factors . . . 128
4.7 Systematic Error Studies . . . 131
4.7.1 BBC nhit distributions . . . 132
4.7.2 Systematics on BBCLL1 trigger efficiency . . . 135
4.7.3 Systematics from assuming nbinary scaling for hard processes 140
4.8 Summary of Final Results . . . 148

5 Results and discussion **151**
5.1 Final results . . . 151
5.1.1 R_{cp} measured by hadron decay muons . . . 153
5.1.2 Compare with BRAHMS measurements . . . 156
5.2 Theoretical prospects . . . 158
5.3 Leading twist calculations . . . 161

5.3.1 EKS parametrization 162
5.3.2 Leading twist shadowing 162
5.3.3 A leading twist calculation 163
5.4 CGC calculation 165
5.5 Soft physics 167
5.6 Summary 169

List of Figures

1.1 Quark label assignments in the baryon decuplet and the observed baryons with spin-parity $\frac{3}{2}^+$. 5

1.2 Quark label assignments in the baryon octet and the observed baryons with spin-parity $\frac{1}{2}^+$. 6

1.3 Feynman diagram for a typical electron proton deep inelastic scattering. . 7

1.4 F_2 as a function of Q^2 at $x = 0.25$. The scattered electrons are measured at scattering angle $6, 10, 18, 26$ degrees [6]. The choice of $x = 0.25$ gives exact "scaling". 9

1.5 The ratio $\frac{2xF_1}{F_2}$ measured by SLAC en experiments. For $spin\frac{1}{2}$, with $g = 2$, this ratio is expected to be unity in the limit of large Q^2 [6]. 11

1.6 The F_2 structure function measured by HERA experiments. F_2 as functions of x are plotted at different Q^2. The small panels are organized such that Q^2 increases from left/top to right/bottom. F_2 as functions of Q^2 are plotted at different x on the right and x increases from top to bottom. Note Q^2 coverage is from $1.5GeV^2$ to $5000GeV^2$ and x range is down to 10^{-4}. 15

1.7 F_2 as functions of Q^2 are plotted at different x on the right and x increases from top to bottom. Note Q^2 coverage is from $1.5GeV^2$ to $5000GeV^2$ and x range is down to 10^{-4}. 16

1.8 The gluon density extracted by HERA experiments. NLO DGLAP fit is applied to 1993 and 1994 data from both ZEUS and H1 experiments. . . . 17

1.9 Gluon density as a function of x at different Q^2. 18

1.10 $\sigma_{\gamma^* P}$ as a function of $\tau = (QR_0)^2$. When $\tau \to 0$ the cross-section become flat. 19
1.11 $\frac{F_2^A}{F_2^D}$ as a function of x for different nucleus [15]. The data are from many DIS experiments. 22
1.12 Feynman diagram for the hadron structure of photon and the comparison between GVMD model calculation(the solid lines) and NMC data(the solid points). 24
1.13 Comparison between NMC data and calculations from parton recombination model. Solid points are real data. Solid line are calculations from Berger and Qiu [20]. Dashed line are calculations from Close and Robert [21] 27
1.14 Drell-Yan ratio measured by Fermi Lab. E772 experiment [23]. E772 data shows the shadowing effect and anti-shadowing effect at the same x range as EMC data. Also there is a clear A dependence of modification in E772 data. 29
1.15 Cronin effect and a calculation using Geometrical shadowing. 30
1.16 PHENIX measured R_{AA} for charged hadrons and neutral pions in different centrality classes of gold gold collisions at $\sqrt{s_{NN}} = 200$GeV. 33
1.17 PHENIX measured R_{dA} for charged hadrons and neutral pions in deuteron gold collisions at $\sqrt{s_{NN}} = 200$ GeV [33]. 34
1.18 PHENIX measured R_{AA} for charged hadrons and neutral pions in gold gold collisions at $\sqrt{s_{NN}} = 200$GeV is compared with GLV calculation. Dashed and dotted line are the calculations from X.N. Wang and his company [35]. 35
1.19 Phase diagram for CGC. The boundary of CGC is defined by Q_s [37]. . . 37
1.20 The PHENIX muon arm x coverage and the nuclear modification effects in side the PHENIX muon arm coverage. 39

2.1 Accelerator setup and the path of accelerating particles at RHIC. 41
2.2 The PHENIX detector. 44
2.3 The η and ϕ coverage for the PHENIX detector subsystems. 44
2.4 Side view of the PHENIX muon arms. 48

2.5 Invariant Mass distributions for di-muon system in dAu collisions. 53
2.6 The relations between colliding system, data rate and data sizes. The data is given for PHENIX design luminosity. 54
2.7 The schematic of one granule. 54
2.8 A simulated J/Ψ event in the detector. 58

3.1 $\frac{p_T^{\mu}-p_T^{pid}}{p_T^{\mu}}$, the peak at zero is for muons, the small bump around 0.01 is for pions and the other bump at 0.05 is for koans. 61
3.2 panel a : depth and vertex momentum for MC muons stop at different MuID gap, purple line is for tracks stop at gap2 and blue is for tracks stop at gap3. panel b: depth and vertex momentum for MC hadrons stop at gap2(red) and gap3(blue) 62
3.3 panel a : depth and vertex momentum for tracks stop at different MuID gap, red line is for tracks stop at gap2 and blue is for tracks stop at gap3. panel b: depth and station1 momentum for tracks stop at gap2(red) and gap3(blue) 63
3.4 normalized BBC vertex distribution for muons events(a) and hadron events(b). South muon arm is in negative z direction. 65
3.5 Panel a : the input p_T spectrum. Panel b : input pseudorapidity distribution 66
3.6 transverse momentum measured by detector and transverse momentum of primary particle which is given by the truth information from simulation, red dots are for primary particle dE/dx through absorber, black dots are for secondary particles. 67
3.7 panel a: polar angel difference between primary vector and measured momentum vector, dedx through (red curve) and hadronic shower(blue) and total : black; Panel b : polar angel difference between primary vector and measured momentum vector for real data 68
3.8 transverse momentum measured at vertex and transverse momentum of primary particle after cut, red dots are for primary particle de/dx through absorber, black dots are for secondary particles. 69

3.9 the probability for a primary particle produce a hadron shower(solid line) or just dEdx through absorber(dashed line) as a function of primary particle momentum. Black lines are probabilities without $\theta_{xp} < 0.03$ cut. Red lines are probabilities with $\theta_{xp} < 0.03$ cut 69
3.10 ratio between number of shower particles and number of punch-through particles as a function of measured transverse momentum at vertex . 71
3.11 primary transverse momentum distribution in different measured vertex momentum bins 72
3.12 ratio of this high p_T background to signals as a function of measured vertex momentum 73
3.13 Occupancy as a function of x and y coordinates at different gaps for each station of backward muon spectrometer. 75
3.14 Occupancy as a function of x and y coordinates at different gaps for each station of forward muon spectrometer. 76
3.15 Correlation between p_T and η 77
3.16 Cross-sections between hadrons and protons [50]. 78
3.17 Distribution of the normalized charge in the BBCS. The normalization is done in a way that the normalized charge corresponds to the number of hits 80
3.18 particles ratio measured by the PHENIX central arm in dAu collisions. Left : proton to π ratio. Right : kaon to π ratio. 83
3.19 R_{cp} measured at rapidity $y = 0$ by the PHENIX central arm for identified particles. 84
3.20 Number of disabled HV channels of MuID in run3 dAu are plotted as a function of run number. Left panel is south arm and right panel is north arm. All runs are categorized into 4 classes depended on the number of the disabled channels. We use category A in our analysis. 86
3.21 TCE of MuID trigger circuit in run3 dAu is plotted as a function of run number. Left panel is south arm and right panel is north arm. 87

3.22 Left : resolution of transverse momentum. Right : resolution of pseudo-rapidity 89
3.23 Single hadron efficiency in each (p_T, η) bins. 90
3.24 Embedded hadron efficiency in each $(p_T, centrality)$ bins for $-2.0 < \eta < -1.8$. 91
3.25 Embedded hadron efficiency in each $(p_T, centrality)$ bins for $-1.8 < \eta < -1.6$. 92
3.26 Embedded hadron efficiency in each $(p_T, centrality)$ bins for $-1.6 < \eta < -1.4$. 92
3.27 Embedded hadron efficiency in each $(p_T, centrality)$ bins for $1.4 < \eta < 1.6$. 93
3.28 Embedded hadron efficiency in each $(p_T, centrality)$ bins for $1.6 < \eta < 1.8$. 93
3.29 Embedded hadron efficiency in each $(p_T, centrality)$ bins for $1.8 < \eta < 2.0$. 94
3.30 Embedded hadron efficiency in each $(p_T, centrality)$ bins for $2.0 < \eta < 2.2$. 94
3.31 Left : The dashed line shows the MC depth distribution and the solid line shows the reconstructed depth distribution, it is clearly that many depth=3 MC hadrons are mis-reconstructed to depth=4 track. Right : The ratio between the number of reconstructed depth=3 hadrons and the number of MC depth=3 hadrons is plotted as a function of centrality, no centrality dependence is seen here. 95
3.32 Raw transverse momentum distribution for punch-through hadrons for each centralities from minbias data sample. Left : south arm. Right : north arm. 97
3.33 R_{cp} as a function of transverse momentum in each centralities. Minbias data sample and only statistic error is shown here. Left : south arm, Right north arm. 98
3.34 Road approximity distribution for south arm(red, dashedline) and north arm(black, solid) line. 98
3.35 Left : In minbias data sample, hadron η distribution for all centrality bins. Left : Hadron punch-through probability as a function of η 99

3.36 R_{cp} as a function of pseudo-rapidity in each centralities. Minbias data sample and only statistic error is shown here. 99
3.37 Left : South arm hadron raw p_T distribution for each centrality bins, south one deep trigger sample. Right : South arm hadrons R_{cp} as a function of transverse momentum in each centralities. South one deep trigger sample and only statistic error is shown here. 100
3.38 Left : South arm hadron raw η distribution for each centrality bins, south one deep trigger sample. Right : South arm hadrons R_{cp} as a function of pseudorapidity in each centralities. South one deep trigger sample and only statistic error is shown here. 101
3.39 Left : North arm hadron raw p_T distribution for each centrality bins, north one deep trigger sample. Right : North arm hadrons R_{cp} as a function of transverse momentum in each centralities. North one deep trigger sample and only statistic error is shown here. 102
3.40 Left : North arm hadron raw η distribution for each centrality bins, north one deep trigger sample. Right : North arm hadrons R_{cp} as a function of pseudorapidity in each centralities. North one deep trigger sample and only statistic error is shown here. 103
3.41 R_{cp} when change p_{tot}^{sta1} cut to $5\times\sigma$ away from muon peak at gap3. Left two panels are south arm hadron R_{cp}, right two panels are north arm hadron R_{cp}, Up is R_{cp} as a function of p_T, bottom is R_{cp} as a function of η. . . . 104
3.42 R_{cp} when change θ_{xp} cut to 0.06 away from 0.03. Left two panels are south arm hadron R_{cp}, right two panels are north arm hadron R_{cp}, Up is R_{cp} as a function of p_T, bottom is R_{cp} as a function of η. 105
3.43 R_{cp} when change d_{proxy} cut to 60 away from 30. Left is R_{cp} as a function of p_T, right is R_{cp} as a function of η. 107
3.44 R_{CP} as a function of p_T. The left panel is for the most central collisions and the centrality increases from left to right. 109

3.45 R_{CP} as a function of η. The left panel is for the most central collisions and the centrality increases from left to right. 109

4.1 Number of Participants from the Gold Nucleus (left) and Number of Binary Collisions (right) distribution from Glauber model for true minimum bias deuteron-gold reactions. 117

4.2 Comparison between the calculated deuteron-gold BBCS nhit distribution requiring BBCLL1 firing (solid line) and the experimental data distribution from deuteron-gold in real BBCLL1 selected events (open circles). . . 118

4.3 Left Biased inclusive BBC nhit distribution sliced into centrality bins according to percentage. Right the corresponding nbinary distributions. . . . 119

4.4 South BBC nhit distribution from non-BBLL1 trigger data. Open circles are the unbiased distributions. Close circles are distributions biased by requiring north BBC $nhit \geq 1$ 122

4.5 $P(nhit_{north} \geq 1 \mid nhit_{south})$ distributions for different event categories. . . 123

4.6 Difference between the PC track calculated vertex and BBC vertex. 124

4.7 South BBC nhit distribution for different events categories. The solid lines are the unbiased distributions, which are recovered from above procedures. The dashed lines are BBCLL1 biased distributions, which are taken from the BBCLL1 trigger selected data. 125

4.8 (CASE 1): South BBC nhit distributions in the case that north and south BBC are totally uncorrelated. The solid lines are unbiased distributions and the dashed lines are BBCLL1 biased distributions. 133

4.9 (CASE 2): South BBC nhit distributions in the case that north and south BBC are totally correlated. The solid lines are unbiased distributions and the dashed lines are BBCLL1 biased distributions. 134

4.10 (CASE 3): South BBC nhit distributions in the case that the correlation between north and south BBC are determined by HIJING+PISA. The solid lines are unbiased distributions and the dashed lines are BBCLL1 biased distributions. 136

4.11 (CASE 4): South BBC nhit distributions in the case that the unbiased and biased distributions are taken from HIJING+PISA simulation. The solid lines are unbiased distributions and the dashed lines are BBCLL1 biased distributions. 137
4.12 (CASE 5): South BBC nhit distributions in the case that all the unbiased and biased distributions are taken from real data without BBCLL1 trigger requirement. The solid lines are unbiased distributions and the dashed lines are BBCLL1 biased distributions. 138
4.13 South BBC nhit distributions when $\epsilon^{BBCLL1}_{inclusive} = 0.44$. The solid lines are unbiased distributions and the dashed lines are BBCLL1 biased distributions. 141
4.14 South BBC nhit distributions when $\epsilon^{BBCLL1}_{inclusive} = 0.60$. The solid lines are unbiased distributions and the dashed lines are BBCLL1 biased distributions. 142
4.15 South BBC nhit distributions when $\epsilon^{BBCLL1}_{hard} = 0.69$. The solid lines are unbiased distributions and the dashed lines are BBCLL1 biased distributions. 143
4.16 South BBC nhit distributions when $\epsilon^{BBCLL1}_{hard} = 0.81$. The solid lines are unbiased distributions and the dashed lines are BBCLL1 biased distributions. 144
4.17 R_{cp} measured in the PHENIX muon arms is plotted as a function of nbinary. 146

5.1 Nuclear Modification factor(R_{cp}) as a function of p_T. From the left panel to the right panel, the centrality percentage increases(i.e. the impact parameter increases). On the plot, PTH denotes the term of pouch-through hadron. The grey bars on each data points are point-by-point systematic errors and the black bar on the right end of the $R_{cp} = 1$ line is the common systematic errors. 152
5.2 Nuclear Modification factor(R_{cp}) as a function of η. From the left panel to the right panel, the centrality percentage increases(i.e. the impact parameter increases). On the plot, PTH denotes the term of pouch-through hadron. The grey bars on each data points are point-by-point systematic errors and the black bar on the right end of the $R_{cp} = 1$ line is the common systematic errors. 153

5.3 Collision vertex distribution for events with muons at forward rapidity, corrected for the minimum bias collision vertex distribution. 156

5.4 R_{cp} as a function of p_T for hadron decay muons(HDM) and punch-through hadrons(PTH). The error bars on each data points are the quadratic sum of systematic error and statistic error. For better vision, the HDM points are artificially shifted to the right for a quarter of the bin size. 157

5.5 R_{cp} as a function of η for hadron decay muons(HDM) and punch-through hadrons(PTH). The error bars on each data points are the quadratic sum of systematic error and statistic error. 158

5.6 comparison between the PHENIX results and the BRAHMS results. The PHENIX R_{cp} as a function of p_T at forward rapidities shown as the average of the two methods. Note that the BRAHMS centrality ranges($\frac{0-20}{60-80}$ on the left panel and $\frac{30-50}{60-80}$ on the right panel). The error bars on each data points are the quadratic sum of systematic error and statistic error. 159

5.7 Centrality selection study from PHOBOS. *Courtesy from James Nagle's Chicago DNP2004 talk.* 160

5.8 The average $\sqrt{Q^2}$ for parton parton collisions which produce hadrons with $p_T > 1.5$ GeV/c in the PHENIX muon arms is plotted as a function of x of partons in gold nuclei. 161

5.9 R_{CP} for charged hadrons in deuteron-gold collisions at $\sqrt{S_{NN}} = 200$ GeV as a function of p_T . The results for $S_{FGS,WS}$(right panel) and $S_{P,\rho}$ (left panel) are compared to the BRAHMS data in the following η bins: (a) $\eta = 0.2$; (b) $\eta = 1$; (c) $\eta = 2.2$ and (d) $\eta = 3.2 S_{P,\rho}$. The calculated ratios of the most central and semi-central to peripheral collisions are shown in the solid and dashed curves, respectively. The BRAHMS data are given by the open circles (most central) and diamonds (semi-central). 164

5.10 Comparison between FGS parametrization and the PHENIX R_{CP}. In the upper two panels, the shadowing function used in the calculation is $S_{GFS,\rho}$. In the lower two panels, $S_{FGS,WS}$ is used. Note the calculation was done for the BRAHMS R_{CP}, as we mentioned that the centrality definition were different between BRAHMS and PHENIX. 166
5.11 Nuclear modification factor R_{CP} of charged particles for different rapidities. Data is from the BRAHMS experiment. Full and open dots give the ratio of particle yields in $0-20\%$ and $30-50\%$ centrality events correspondingly divided by the yields from $60-80\%$ centrality events scaled by the mean number of binary collisions. 168
5.12 Comparison between the CGC calculation and the PHENIX R_{CP}. 169
5.13 Comparison between PHENIX $R_{cp}(\eta, p_T > 1.5\text{GeV}/c)$ with the PHOBOS $R_{cp}(\eta)$, which is calculated from $dN/d\eta$. 170
5.14 $\Delta\phi$ distributions for SC correlations (lift two panels) and NC correlations (right two panels) with $1 < p_T^{trig} < 2$ GeV/c (upper two panels) and $p_T^{trig} > 2$ GeV/c. 171

List of Tables

1.1 Summary of all fundamental particles in Standard Model. Q represents the electric charge. B is Baryon Number. S is strangeness. C is the charm quantum number. b and T are the quantum numbers for bottomness and topness. I_z is the third component of isospin and I_z^W is the third component of weak isospin. $L_{e,\mu,\tau}$ are the eletron/muon/τ lepton numbers. 2

3.1 Number of binary collisions for each centrality classes. 81

3.2 List of runs used for the analysis 88

3.3 Muon one deep trigger verse centrality. 96

3.4 Systematic Errors in percentage for south R_{cp}, where we separate the point-by-point systematics from the common systematics. 106

3.5 Systematic Errors in percentage for north R_{cp} 108

3.6 Systematic Errors in percentage for R_{cp} 110

4.1 Summary of centrality bins we used in our study. 119

4.2 Summary of centrality bias corrections 131

4.3 Summary of centrality bias corrections for different cases 139

4.4 Summary of systematic errors for different cases 140

4.5 Summary of centrality bias corrections for different BBC efficiency . 145

4.6 Summary of systematic on centrality bias corrections for varying BBC efficiency 146

4.7 Summary of centrality bias corrections for different scaling laws . . . 147

4.8 Summary of centrality bias correction factors. 149

5.1 **Summary of R_{cp} measurement.** 154

Acknowledgements

It has been my biggest achievement so far to finish this thesis, and there are many people who helped and encouraged me to accomplish it. Here I want to give my thanks to them, but there will be many I may not be able to mention their names here; nonetheless, all who have supported me over years will always be remembered with thankful thoughts.

First, I would like to thank my advisor, professor James Nagle in Colorado University at Boulder. You are like a compass for my research expedition and always directs me to the correct path ahead. Your attitude to science and the research that you have done set the standards for me to be a good physicist.

Also I want to express my deepest gratitude to my other advisor, professor William Zajc in Columbia heavy-ion group, whose leadership and guidance are critical to the success of the PHENIX experiment. Many thanks to Professors Brian Cole for many stimulating discussions about physics.

My thanks to Cheng-yi Chi, the PHENIX DCM god, not only for the electronics expertise but also for in such a long time you always take care of me.

The Columbia heavy ion group is always fun. So many great post-docs and students shared their life in the group. I own a deep debt of gratitude to my friend, Dr. Sean kelly, who taught me many things from how to write a piece of elegant C++ code to how to make cocktails and perfect steaks. To Dr. Mickey Chiu, Dr. Justin Frantz, Dr. Sotiria Batsouli, Dr. Dave Winter, Dr. David d'Enterria, Dr. Jiangyong Jia, Christine Aidala, Jiamin Jin, Xueshi Lai, your guys are the best. I will always cherish the experience I shared with you.

I want to give my thanks to all the people in PHENIX, especially to the people in the DAQ group and the Muon group, whom I spend most my time in BNL with. Many thanks to John Haggerty, Stephen Adler, Martin Purschke, Chris Pinkenburg, Ed Desmond, Sergei Belikov, and to Vince Cianciolo Mike Leitch, Hugo pereira, David Silvermy, Melynda Brooks. Thanks for all the help and it has been a lot of fun to work with all of you.

I would like to thank the staff and administration of the Columbia physics department and Nevis laboratories. In particular, I would like to thank Ms Ann Therrien and Ms Lalla Grimes. Thanks to your strength and courage to make physicists here to be able to do a better job by focusing more on teaching and research. Also thanks for your willingness for taking such good care of all the students.

To my friend in the Columbia physics department, Dr. Feng Wang, Qingbo Yang, Haitao Yu, Kaixun Ni. Thanks for the help and the friendship, which make the bitter taste of the life in graduate school almost gone.

Finally, I would like to thank my family, my mother, YanJie Zhang, my father, Qingfu Zhang and my older sister Hang Zhang. None of what I have achieved over the years would have been possible had it not been for the love and support they have given me. Most of all I would like to thank Lin, my wife, who has always been there for me.

Chapter 1

Introduction

1.1 Structure of hadrons

1.1.1 Constituents of the matters.

In ancient China, philosophers speculated that all matter was made from five fundamental elements. They are water, fire, wood, earth and gold. In the meantime, a similar concept, but closer to the modern sense, appeared on the other side of the earth. In ancient Greece, philosophers gave birth to the concept of the atom which was regarded as the unbreakable constituent of all matter. Since then technology and science have developed to allow us to have a much deeper and more complete picture of the matter. Now we know that all the matters in the universe are made from quarks and leptons. Quarks build up nucleons, nucleons build up nuclei, nuclei and electrons build up atoms. All macroscopic matter is made from atoms. Including neutrons, protons and electrons, there are over 100 particles and all these particles can be divided into two big categories. Particles which undergo strong interactions are called hadrons and the others which do not participant in strong interactions are called leptons. Besides hadrons and leptons, there are particles which mediate interactions. These particles are called bosons. All hadrons are made from quarks. Depending on how many quarks hadrons are made from, they can be called either mesons(quark and anti quark pairs) or baryons(three quarks). Analogous to electrons carrying electric charge, quarks carry color charges. There are three

Table 1.1: Summary of all fundamental particles in Standard Model. Q represents the electric charge. B is Baryon Number. S is strangeness. C is the charm quantum number. b and T are the quantum numbers for bottomness and topness. I_z is the third component of isospin and I_z^W is the third component of weak isospin. $L_{e,\mu,\tau}$ are the eletron/muon/τ lepton numbers.

	down(d)	up(u)	strange(s)	charm(c)	bottom(b)	top(t)
Q	$-\frac{1}{3}$	$+\frac{2}{3}$	$-\frac{1}{3}$	$+\frac{2}{3}$	$-\frac{1}{3}$	$+\frac{2}{3}$
I_z	$-\frac{1}{2}$	$+\frac{1}{2}$	0	0	0	0
B	$\frac{1}{3}$	$\frac{1}{3}$	$\frac{1}{3}$	$\frac{1}{3}$	$\frac{1}{3}$	$\frac{1}{3}$
S	0	0	-1	0	0	0
C	0	0	0	$+1$	0	0
b	0	0	0	0	-1	0
T	0	0	0	0	0	$+1$
Constituent mass (MeV)	360	360	540	1500	5×10^3	174×10^3
	electron (e)	e neutrino (ν_e)	muon (μ)	μ neutrino (ν_μ)	Tau (τ)	τ neutrino (ν_τ)
Q	-1	0	-1	0	-1	0
I_z^W	$-\frac{1}{2}$	$+\frac{1}{2}$	$-\frac{1}{2}$	$+\frac{1}{2}$	$-\frac{1}{2}$	$+\frac{1}{2}$
L_e	$+1$	$+1$	0	0	0	0
L_μ	0	0	$+1$	$+1$	0	0
L_τ	0	0	0	0	$+1$	$+1$
Mass (MeV)	0.511	$< 7 \times 10^{-6}$	105.7	< 0.27	1777	< 31
	photon (γ)	W boson (W^+)	W boson (W^-)	Z boson (Z^0)	gluons ($g_i(i = 1...8)$)	
Q	0	$+1$	-1	0	0	
Spin	1	1	1	1	1	
Mass (GeV)	0	80.22	80.22	91.187	0	

different color charges, i.e. RED, BLUE and GREEN. Unlike electric charges which we can directly see, color charges are confined inside hadrons. So hadrons are color neutral.

In the Standard Model, quarks, leptons and bosons are regarded as the fundamental particles. Table 1.1 summarizes all the fundamental particles in the Standard Model.

1.1.2 Strong interaction and gluons

The interaction that binds quarks together is called the strong interaction. It occurs between two particles that carry "color" charges. Gluons are the carriers of the strong interaction. Gluons, themselves, also carry color charges. We have a very good theory to describe strong interactions, it is called Quantum ChromoDynamics(QCD), a non-Abelian gauge theory. The underlying symmetry of QCD is $SU(3)$ symmetry, which means there are 8 different gluons since there are 8 independent generators in $SU(3)$ group. Unlike quarks, gluons carry a color charge and an anti-color charge. The nine different color and anti-color combinations are $R\overline{R}$, $R\overline{B}$, $R\overline{G}$, $B\overline{B}$, $B\overline{R}$, $B\overline{G}$, $G\overline{G}$, $G\overline{R}$, $G\overline{B}$. But one combination of the nine bi-color states is a colorless object, $R\overline{R} + B\overline{B} + G\overline{G}$, it is not a real gluon. The major difference between gluons and other bosons is that gluons can self-couple.

The self-coupling gluons result in the most interesting and unique phenomenon of strong interactions compared to the other three interactions, "asymptotic freedom". This phenomenon is such that the strength of the interaction between two color charges increases with the distance between the two charges. When the distance is very short, the strength of the interaction is so small that the particles carrying color charge can be regarded as free particles. This phenomenon allows perturbative calculations to be applied in small distance or high Q^2 situations. On the other hand, the increase of the interaction strength with the increase of the distance also imposes the confinement of the quarks.

The coupling constant of the strong interaction α_s, like all the other coupling constants, depends on the scale at which the interaction occurs. The solution of the renormalization group equation in leading order leads to $\alpha_s(Q^2) = \frac{4\pi}{\beta_0 \ln(\frac{Q^2}{\Lambda^2})}$, where Q^2 is the scale at which α_s is probed and $\Lambda \sim 200$ MeV is the QCD cut off parameter. β_0 depends on the number of quark flavors in the theory, N_f, $\beta_0 = 11 - \frac{2}{3}N_f$.

1.1.3 Static quark model for hadrons

In the early part of the last century, people thought nucleons(proton and neutron) were the fundamental particles and pions mediated the force between them. After the 1950's, more and more particles were discovered along with the development of new accelerators and detectors. Then people realized that nucleons and pions happened to be the lowest energy state of a series of particles. In the study of the properties of these particles, such as mass, spin etc., people found the spectra of particles indicated new symmetries. Indeed, all the hadrons can be categorized by these symmetries. In 1964, Gell-Mann and Zweig first proposed the Static Quark Model for hadron structure. According to the quark model, all hadrons are made up of a small variety of more basic entities, called quarks, bound together in different ways [1]. All the mesons we discovered so far are bound states of a quark q and an anti-quark $\overline{q'}$. All the baryons are bound states of three quarks $qq'q''$.

The strongest experimental evidence for the quark structure of nucleons comes from Deep Inelastic Scattering(DIS) experiments [2] and the observations of jets production [3]. DIS experiments measure the total inelastic cross-sections of leptons scattering from nucleons. What was found in DIS is that the cross-section is approximately independent of the Q^2 of the collisions. This fact can be understood as projectile leptons scattering from point-like objects inside the nucleons. Later when people used point-like structure functions to calculate the DIS cross-sections, the calculation fitted the data very well. In fact there are many interesting discoveries from DIS experiments and we will discuss this topic further in the next section. In the mean time, the jet production was discovered and it can only be explained as two point-like constituents scattering elastically from each other. These point-like constituents are called partons.

The early static quark model only included three generations of quarks, i.e. uds. Figure 1.1 shows the lowest mass states of baryons with spin-parity $J^P = \frac{3}{2}^+$, where we plot the strangeness S against the third component of isospin, I_3. This set of baryons is called the Baryon Decuplet. Baryons parallel with the I_3 consist of a

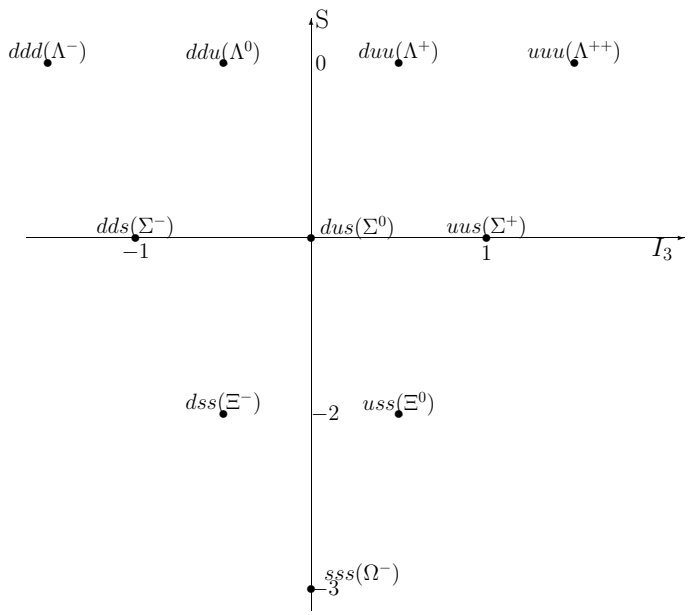

Figure 1.1: Quark label assignments in the baryon decuplet and the observed baryons with spin-parity $\frac{3}{2}^+$.

isospin multiplet and have almost the same mass. The mass differences between different isospin multiplets is approximately equal to the differences between the mass of strange quarks and the mass of up(down) quarks. Figure 1.1 was used to predicted the existence of Ω^- and indeed the Ω was discovered in 1964 at Brookhaven National Laboratory [4].

Figure 1.2 shows the lowest mass states of baryons with spin-parity $J^P = \frac{1}{2}^+$. The difference between the decuplet and octet are the wave functions of the constituent quarks. For the decuplet states, the wave functions are symmetric under interchange of either flavor or spin of any quark pair, but for the octet states, the wave functions are symmetric only under simultaneous interchange of flavor and spin of any quark pair. One should note that quarks have another quantum number, i.e. color, and all the hadrons have to be the color singlet which means the color component of the wave function is always asymmetric. Thus all other components of the wave function, e.g. flavor, spin, position, have to be collectively symmetric. In fact the structure of the hadrons is far more complicated than what we discussed here. Other than the valence quarks, there are gluons which mediate the interactions be-

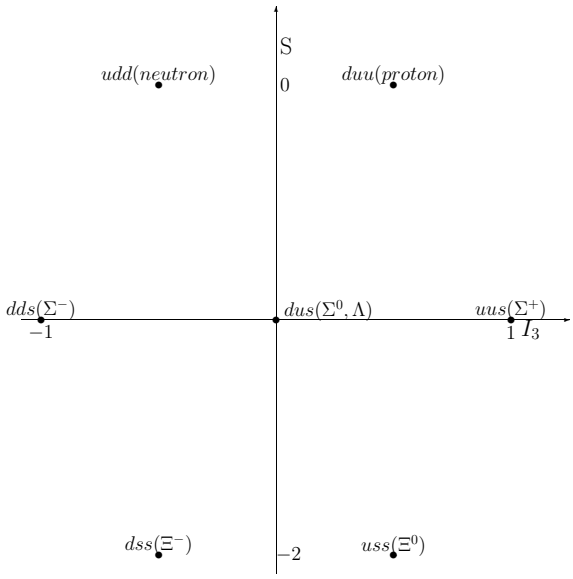

Figure 1.2: Quark label assignments in the baryon octet and the observed baryons with spin-parity $\frac{1}{2}^{+}$.

tween the valence quarks and these gluons in turn can split into quark anti-quark pairs, so called sea quarks. Sea quarks can also radiate gluons. Sea quarks, valence quarks and gluons together are called partons. The number of partons in a hadron is not constant and is dependent on the wavelength of the probes one uses to study the hadron. We will discuss the parton distributions inside nucleons and nuclei in the following sections.

1.2 Parton distribution functions in nucleons

Dynamical models of hadron structure appeared after 1968, when more experimental results came out from the DIS experiments revealing the nucleon's substructures of point-like constituents, i.e. quarks and gluons. It is found that this substructure, usually described quantitatively as Parton Distribution Function(PDF), evolves with wavelength or equivalently Q^2 of the probe one uses. Thus the static quark model for hadron structure which takes a nucleon as a compound of three valence quarks is not a precise description for hadrons, especially when high Q^2 collisions happen. The idea of using PDF which evolves with Q^2 to picture a hadron is a more precise

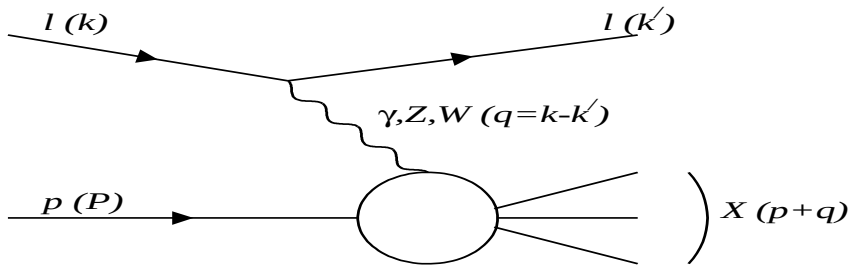

Figure 1.3: Feynman diagram for a typical electron proton deep inelastic scattering.

way.

1.2.1 DIS and Quark structure functions

A typical DIS process can be demonstrated by a Feynman diagram as in Figure 1.3. An incoming lepton exchanges a virtual photon with the target proton, then scatters off. The virtual photon has a four-momentum $q = k - k'$, where k is the four-momentum of the incoming lepton and k' is the four-momentum of the scattered lepton. In this picture, the virtual photon is the probe we use to investigate the structure of the target proton. The four momentum of the proton is denoted as P in the diagram. Some kinematic variables are often used in describing the DIS experiments such as,

- $Q^2 = -q^2 = -(k - k')^2$, the virtuality of the virtual photon.
- $s = (k + P)^2$, invariant mass of electron and proton collision system.
- $W^2 = (q + P)^2$, invariant mass of photon and proton collision system.

- $x = \frac{Q^2}{2Pq}$ Bjorken x, in infinite momentum frame $x = \frac{p_{parton}}{p_{proton}}$, the fraction of proton momentum carried by partons.
- $\nu = \frac{P \cdot q}{P^2}$, energy of virtual photon, in proton rest frame $\nu = E_e - E'_e$, where E_e and E'_e are the incident and emergent electron energies.
- $y = \frac{P \cdot q}{P \cdot k}$, in proton rest frame $y = \frac{\nu}{E_e}$, the fraction of incoming electron energy carried by virtual photon.

In DIS experiments, the energies and momenta of scattered(emergent) leptons are measured. Thus experimentally we can measure a differential DIS cross-section as a function of $q^2 = k - k'$ and $\nu = E_e - E'_e$. In the mean time, theoretically we can reconstruct a differential cross-section, if we believe that the leptons indeed are elastically scattered off of point-like objects(quarks) distributed inside the target proton, such as

$$\frac{d^2\sigma}{dq^2 d\nu} = \frac{4\pi\alpha^2}{q^4}\frac{E'_e}{E_e M}[W_2(q^2,\nu)\cos^2\frac{\theta}{2} + 2W_1(q^2,\nu)\sin^2\frac{\theta}{2}] \tag{1.1}$$

where E'_e and M are the emergent electron energy and invariant mass of proton, respectively. W_1 and W_2 are arbitrary structure functions corresponding to the two possible polarization states, transverse and longitudinal, of the virtual photon and are determined by how the quarks are distributed inside the proton relative to the process which is used in the study. By comparing the theoretical calculation and experimental results, one can actually determine W_1 and W_2.

In fact it is more convenient to use Bjorken x instead of ν to rewrite equation 1.1. The relation between x and ν is $x = \frac{Q^2}{2Pq} = \frac{Q^2}{2M\nu}$ and $\frac{dx}{x} = -\frac{d\nu}{\nu}$. In the mean time, we can define two new structure functions, F_1 and F_2 as following, $F_2 = \frac{\nu W_2}{M}$ and $F_1 = W_1$. After ν, W_1 and W_2 are replaced by x, F_1 and F_2, the equation 1.1 now looks like,

$$\frac{d^2\sigma}{dQ^2 dx} = \frac{4\pi\alpha^2}{Q^4}[(\frac{1-y}{x})F_2(Q^2,x) + \frac{y^2}{2x}2xF_1(Q^2,x)] \tag{1.2}$$

. Here we also substituted $\frac{E'_e}{E_e}$ with $1-y(1-y = 1-\frac{E_e-E'_e}{E_e})$. In most DIS experiments, the emergent electrons are measured at small angles, thus we have $\cos^2(\theta/2) \approx 1$ and

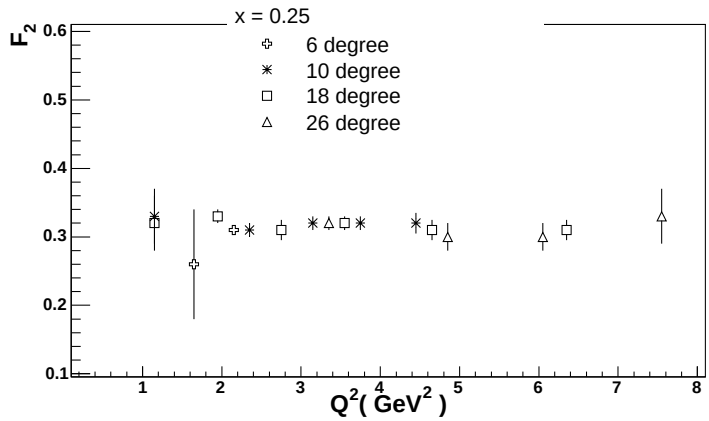

Figure 1.4: F_2 as a function of Q^2 at $x = 0.25$. The scattered electrons are measured at scattering angle $6, 10, 18, 26$ degrees [6]. The choice of $x = 0.25$ gives exact "scaling".

$\sin^2(\theta/2) \approx \frac{Q^2}{4E_e E'_e}$. Equation 1.2 is Lorentz invariant and both Q^2 and x have much clearer physics meanings. Naturally, if the lepton-parton scattering is point-like, the F_1 and F_2 can not be dependent on the Q^2 and are purely functions of x. This is the so called Bjorken scaling hypothesis [5]. Figure 1.4 shows measured F_2 structure function as a function of Q^2 at $x = 0.25$ [6] by SLAC DIS experiments. One can see there is essentially no Q^2 dependence. Bjorken scaling hypothesis mostly works in the limits $Q^2 \to \infty$ and $\nu \to \infty$. But in fact, at larger $x > 0.6$ and smaller $x < 0.01$, the Q^2 dependence starts to appear. We will talk about it later in this section.

In fact, besides exchanging a virtual photon with the target nucleon, the incoming lepton can also exchange a weak interacting boson with the target nucleon in DIS processes. In that case, equation 1.2 becomes more complex and additional structure functions need to be put in. In general there are two types of cross-sections in DIS. The neutral current cross-section is the cross-section for the process in which the incoming lepton exchanges a neutral boson(photon or Z^0 boson) with the nucleon and the charge current cross-section is the cross-section for the process in which the incident lepton exchanges a charged boson($W^{\pm}$) with the nucleon. Structure functions are process dependent and can always be determined by comparison with experimental measurements for each process. Based on Bjorken scaling hypothesis, it would be better if we put the structure function in a more general forms as

following

$$\begin{aligned} F_1(x) &= \frac{1}{2}\sum_i q_i(x)(v_i^2 + a_i^2) \\ F_2(x) &= \sum_i x q_i(x)(v_i^2 + a_i^2) \\ F_3(x) &= 2\sum_i q_i(x)(v_i a_i) \end{aligned}$$

where v_i and a_i correspond to the vector type and axial-vector type coupling between quarks and the probe. The $q_i(x)$ is the parton distribution function of quarks. It is important to realize that although both structure functions and quark parton distribution functions describe how quarks are distributed in x inside a nucleon, they are not quite the same. The structure functions are process dependent, but parton distribution functions are not. For example in the virtual photon case, $v_i = e_i$, the electric charge of the quark and for the charge current case, $v_i = a_i = 1$ for quarks and $v_i = -a_i = 1$ for anti-quarks. The relation between each structure function is mostly process dependent, but F_1 and F_2 (i.e. magnetic and electric scattering) always obey *Callan-Gross relation* i.e.

$$2xF_1(x) = F_2(x)$$

. The *Callan-Gross relation* is the natural rationale from the assumption that quark is $spin\frac{1}{2}$ and point-like particle, thus the ratio $\frac{2xF_1}{F_2}$ can be used as a test from this assumption. If quark is $spin1$ or $spin0$, this ratio will be either ∞ or 0. Figure 1.5 shows this ratio measured in SLAC electron-nucleon scattering experiments [6].

1.2.2 QCD Evolution equations

The partons inside a hadron live in a very dynamic environment. In a very short time period, a quark radiates a gluon and that gluon can split into a quark anti-quark pair. Thus the local density of partons in such a short time period can fluctuate dramatically. The parton distributions we observe depend on the timing resolution($\frac{1}{Q^2}$) of the probe we use. In other word, $F_2(x)$ is dependent on Q^2.

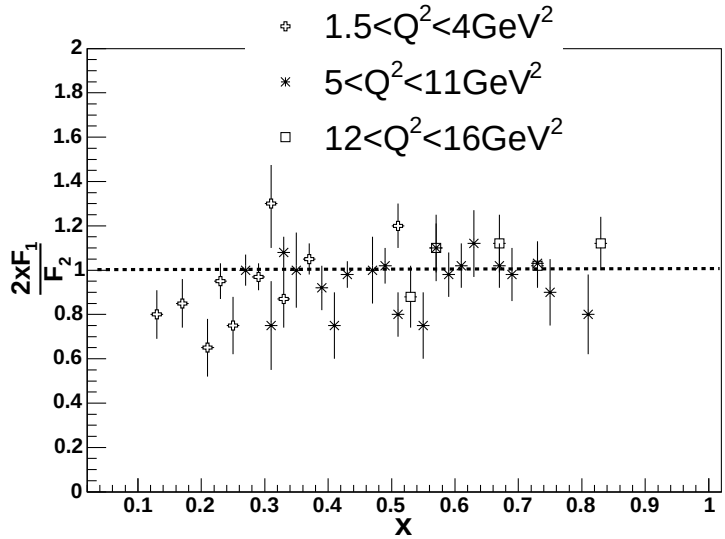

Figure 1.5: The ratio $\frac{2xF_1}{F_2}$ measured by SLAC en experiments. For $spin\frac{1}{2}$, with $g = 2$, this ratio is expected to be unity in the limit of large Q^2 [6].

The dependence is called the quantum evolution. From first principles of QCD, we can not calculate how partons are distributed inside a hadron because of the non-perturbative characteristic of QCD in long distance($> \frac{1}{M_N}$). But, fortunately, we can separate the long-range effects(small Q^2) from the short-range interactions according to the QCD factorization theorem [7]. Thus the Q^2 dependence of parton distributions can be calculated within perturbative QCD at large $Q^2(> M_N^2)$.

The QCD factorization theorem states that for a hard scattering process the cross-section can be decomposed into the flux of incoming partons and the cross-section for elastic scattering between two partons. The latter can be calculated perturbatively. For example, the cross-section of di-jet production in proton proton collisions can be written as

$$\sigma(p_1 p_2 \rightarrow 2jets) = \sum_{a,b=q,g} \int dx_1 \int dx_2 f_{p_1}(x_1^a, Q^2) f_{p_2}(x_2^b, Q^2) \hat{\sigma}(ab \rightarrow cd)$$

where $\hat{\sigma}(ab \rightarrow cd)$ is the parton parton elastic scattering cross-section that one can calculate.

The parton evolution equations built on the factorization theorem are referred to

as the Dokshitzer-Gribov-Lipatov-Altarelli-Parisi(DGLAP) evolution equations [8]. The basic processes considered in these evolution equations are

- Gluons are radiated from quarks and gluons. The number of gluons at small x increases with Q^2.
- Gluons can split into quark anti-quark pairs. The number of quarks and anti-quarks at small x increases with Q^2.

The evolution equations can are as

$$\frac{\partial}{\partial(\ln(Q^2))}\begin{pmatrix} q(x,Q^2) \\ g(x,Q^2) \end{pmatrix} = \frac{\alpha_s(Q^2)}{2\pi}\int_x^1 \frac{d\hat{x}}{\hat{x}}\begin{bmatrix} P_{qq}(\hat{x},Q^2) & P_{qg}(\hat{x},Q^2) \\ P_{gq}(\hat{x},Q^2) & P_{gg}(\hat{x},Q^2) \end{bmatrix}\begin{pmatrix} q(\hat{x},Q^2) \\ g(\hat{x},Q^2) \end{pmatrix}$$

The key ingredients of these equations are P_{jk}, the splitting functions. One can regard the splitting function as a probability of finding a k type of parton with a momentum fraction x from j type of parton with a momentum fraction $\hat{x}$ ($\hat{x} > x$). This probability can be calculated via perturbative QCD. In the DGLAP scheme, the splitting function can be written as an expansion in $\alpha_s(Q^2)$ as follows,

$$\frac{\alpha_s}{2\pi}P_{jk}(\hat{x},Q^2) = \frac{\alpha_s}{2\pi}P_{jk}^{(1)}(\hat{x}) + \left(\frac{\alpha_s}{2\pi}\right)^2 P_{jk}^{(2)}(\hat{x}) + \cdots$$

. Truncation after the first two terms in the expansion defines the next-to-leading-order(NLO) DGLAP evolution. This approach assumes that the dominant contribution to the evolution comes from subsequent parton emissions that are strongly ordered in transverse momenta k_T, the largest corresponding to the parton interacting with the probe [9]. It is noted that the *Callan-Gross* relation is broken down in the NLO.

The DGLAP equations are partial differential equations. A set of experimentally measured PDF need to be put in as initial conditions. Thus, on the $[Q^2, x]$ phase space, as long as we know the PDF in one phase space point, ideally we can always get the PDF on another point from the evolution equations. But in reality, at small x the higher-loop contributions to splitting functions are enhanced since $P_{jk}^{(n)} \sim \frac{1}{x}\ln^{(n-1)} x$ and these contributions will destroy the convergence of the

DGLAP equations. Another set of evolution equations was proposed as Balitsky-Fadin-Kuraev-Lipatov(BFKL) [10] evolution equations to allow the resummation in the splitting function expansion of leading $(\alpha_s \ln x)^n$ terms. Both DGLAP and BFKL predict a rise in PDF with decreasing x. The rise in BFKL is faster than DGLAP because the high power terms in DGLAP expansion grow faster with decreasing x than the high power terms in BFKL expansion and the high power terms are ignored in both cases.

1.2.3 Results from HERA experiments and Gluon PDF

So far the most complete and accurate PDF measurements are from HERA experiments [9]. HERA is the world's first electron proton collider. It is located at Hamburg, Germany. There are four experiments running at HERA, H1, ZEUS, HERMES and HERA-B. H1 and ZEUS started to operate earlier, they have produced lots of PDF data. HERMES studies the spin structure of the proton by colliding the polarized electron beam on polarized proton gas jet target. HERA-B is more like an upgraded experiment of H1 and ZEUS. The typical beam energies at HERA are 27.5 GeV for electrons and 820 GeV for protons. The machine has been operated since 1992.

We now discuss the proton structure functions measured by the ZEUS and H1 experiments. Before HERA experiments, the fixed target experiments, e.g. the DIS experiments at SLAC, CERN, were limited to $x > 0.01$ for $Q^2 > 10GeV$. Therefore they could not probe the proton structure down to very small x in the regime of perturbative QCD. HERA can reach to very low $x \sim 10^{-3}$ for $Q^2 \sim 10^3$ GeV^2, thus we can test perturbative QCD calculations over a much wider range. Figure 1.6 and figure 1.7 summarize the F_2 measurements at HERA, together with fixed target experimental results. These figures are too busy to be visually clear, but they give us an idea on how large the coverage in Q^2 and x HERA experiments have achieved. Also the curves on every small panels of Figure 1.6 represent the NLO DGLAP fit performed by ZEUS, the fit works well down to $Q^2 = 1.5$ GeV^2 and $x \sim 10^{-4}$. From

Figure 1.7, one can see that the scaling law is broken at very small x(on the top of the plot) and large x. F_2 increases with Q^2 at small x and slightly decreases with Q^2 at large x. This can be understood from DGLAP evolution where large x partons split into small x partons in the time period $\tau \sim \frac{1}{Q}$.

In DIS processes, the incident leptons do not directly interact with the gluons in the target hadron, but gluons can still contribute to the total DIS cross-section in the following way. A gluon can split into a quark anti-quark pair. This quark anti-quark pair can be seen by the incident lepton. The contribution from gluons has already been included into the DGLAP evolution equations by the splitting functions and by the $g(x, Q^2)$ component. It is found that the gluon contribution to the DIS cross-section starts to dominate when Q^2 is large (> 100 GeV^2) and x is small ($< 10^{-3}$) . By doing an NLO DGLAP or first order BFKL global fit on the DIS data, one can automatically get the gluon structure functions together with quark structure functions. A practical approach [9] for doing the global fit is to parameterize at a fixed $Q^2 = Q_0^2$ the x dependence of the parton density by $x\rho(x, Q^0) = Ax^\delta(1-x)^\eta P^{(n)}(\sqrt{x})$, where ρ is parton density and $P^{(n)}$ are polynomial functions. In this approach, each species of parton has a distinct set of parameters. In the end, the parameterized densities are put into DGLAP or BFKL evolution equations to perform the global fit on the DIS data. Figure 1.8 shows the extracted gluon structure functions from applying the above approach to the DIS data obtained by H1 and ZEUS from 1993 to 1994. In fact, HERA data itself is not sufficient to constrain the gluon density. The normalization A and the large-x behavior η are determined from fixed target experiments. Also the extracted gluon density depends on α_s, which evolves with Q^2 too and is taken from other experiments. Another thing one needs to keep in mind is that the gluon density is more accurate at small x.

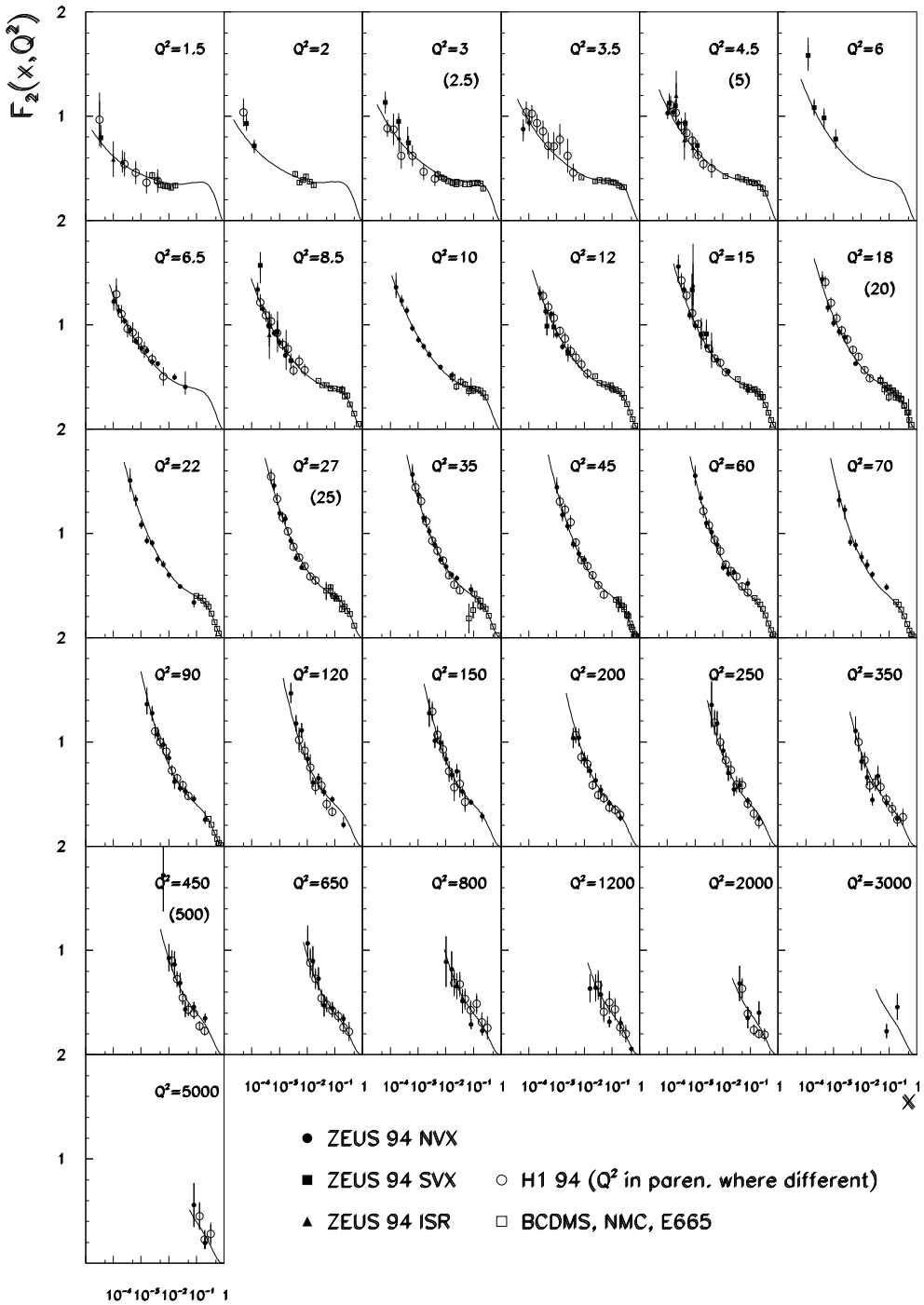

Figure 1.6: The F_2 structure function measured by HERA experiments. F_2 as functions of x are plotted at different Q^2. The small panels are organized such that Q^2 increases from left/top to right/bottom. F_2 as functions of Q^2 are plotted at different x on the right and x increases from top to bottom. Note Q^2 coverage is from $1.5GeV^2$ to $5000GeV^2$ and x range is down to 10^{-4}.

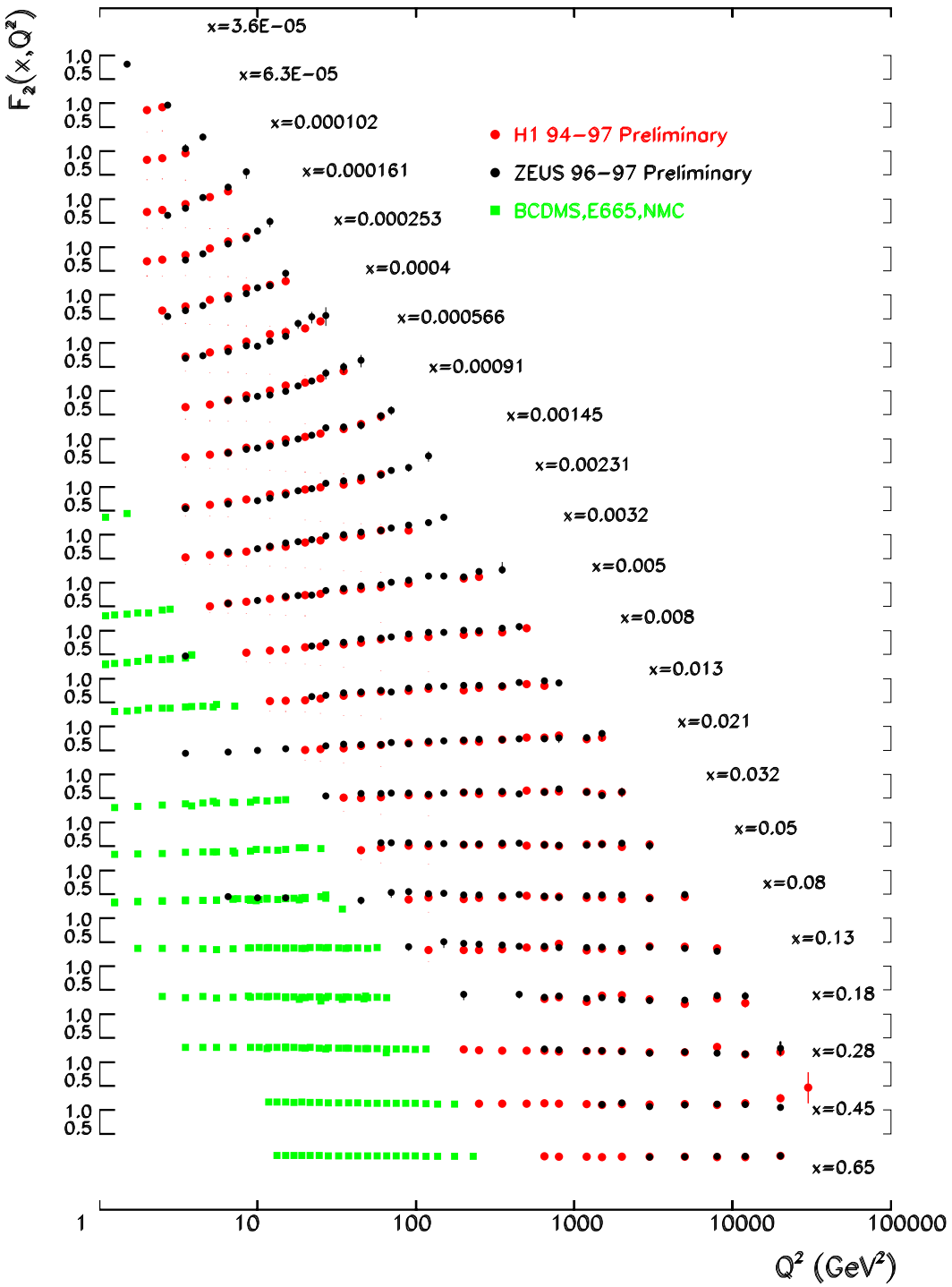

Figure 1.7: F_2 as functions of Q^2 are plotted at different x on the right and x increases from top to bottom. Note Q^2 coverage is from $1.5GeV^2$ to $5000GeV^2$ and x range is down to 10^{-4}.

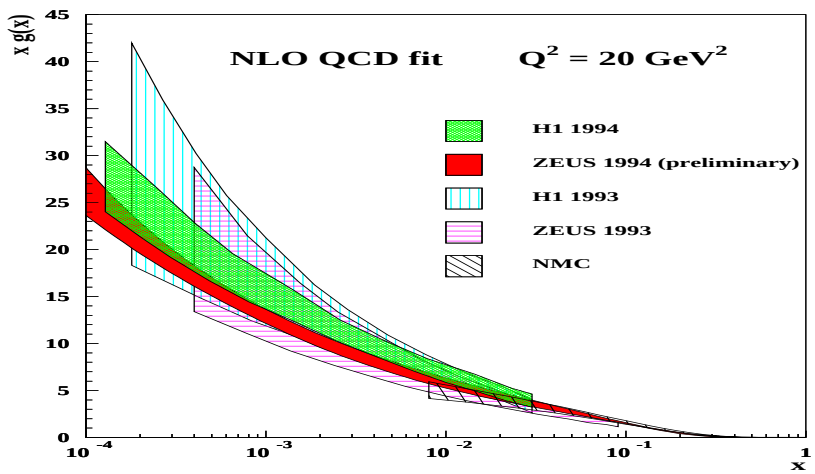

Figure 1.8: The gluon density extracted by HERA experiments. NLO DGLAP fit is applied to 1993 and 1994 data from both ZEUS and H1 experiments.

1.2.4 PDF at small x

We have learned from HERA and other DIS experiments about the PDF at small x the following

- At small Q^2, the DGLAP and BFKL QCD evolution results broke down. The extracted gluon density starts to be negative at small x as shown by figure 1.9. But at $Q^2 < 1\text{GeV}^2$, the validity of perturbative QCD itself is questionable.

- At large Q^2, the extracted gluon density increases very fast with the decrease of x as shown by figure 1.9. This observation raised question of unitarity at small x.

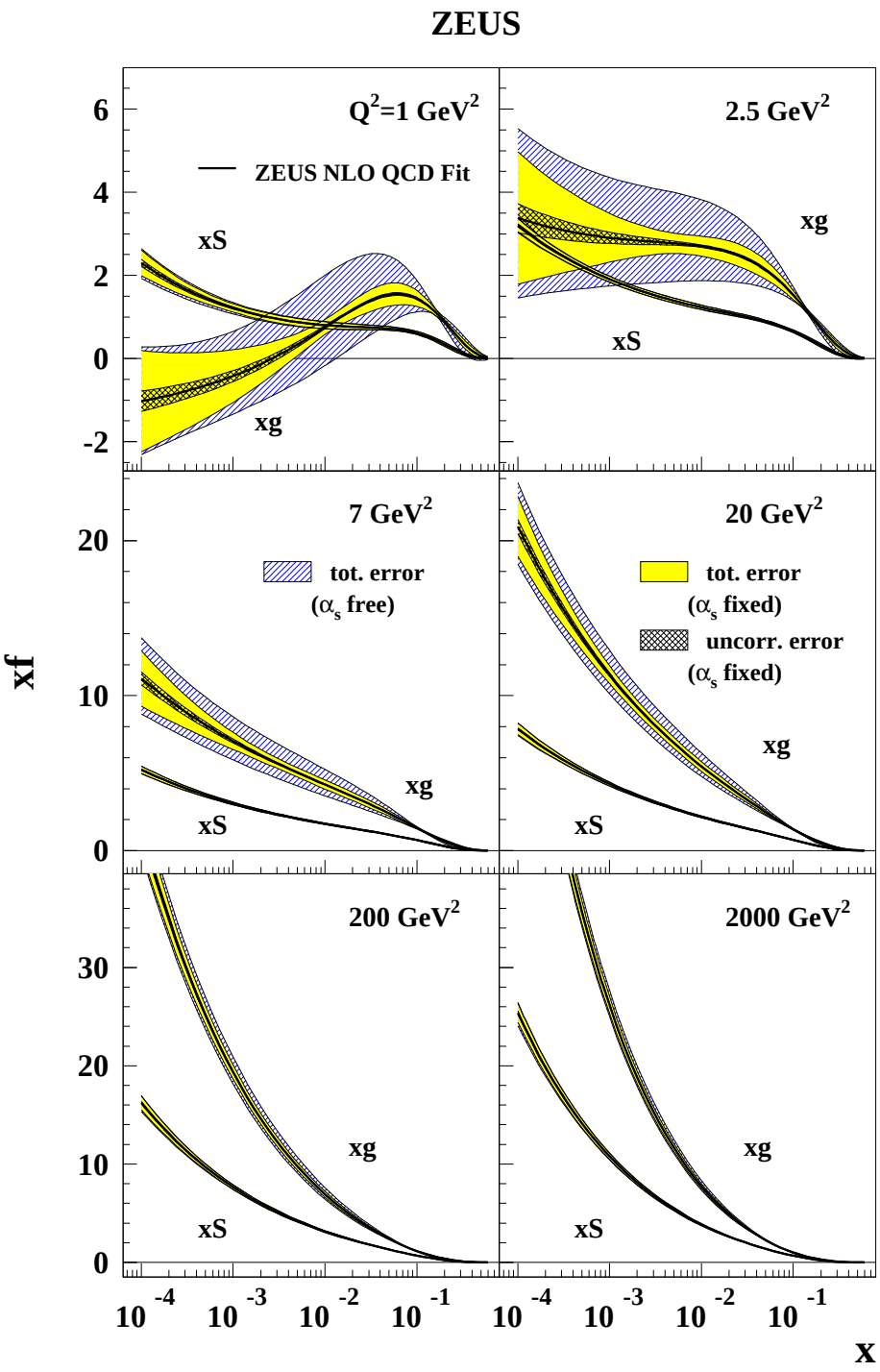

Figure 1.9: Gluon density as a function of x at different Q^2.

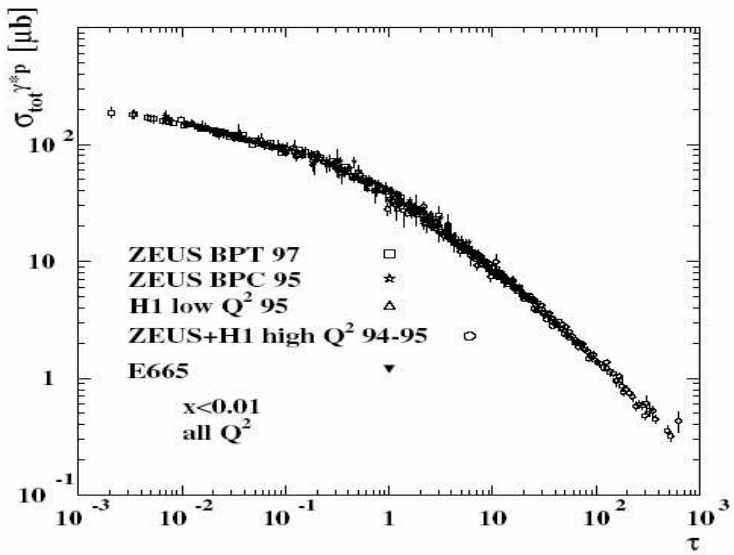

Figure 1.10: $\sigma_{\gamma^* P}$ as a function of $\tau = (QR_0)^2$. When $\tau \to 0$ the cross-section become flat.

The second point seems to be a serious problem. The fast increase of the parton density at small x may lead to the DIS cross-section going to infinity and this is not allowed. Gribov *et. al* [11] proposed that when the proton is overcrowded by partons the annihilation and recombination of partons could result in a saturation effect and would require corrections to the evolution equations.

There were also some phenomenologies that were proposed to fix the infinite cross-section problem. For example, Golec-Biernat *et. al.* [12] proposed the Geometric Scaling Model. In this model, they define a saturation radius $R_0 \sim x^\lambda$. The local parton density inside R_0 is constant. If the size of the probe $\frac{1}{Q}$ is much larger than R_0, the partons localized in R_0 can not be seen by the probe. Therefore it is equivalent to set a lower limit on x. In this model, a new scale $\tau = Q^2 R_0^2$ is defined. A saturation of the cross-section in the limit of $\tau \to 0$ is expected in the model. After re-plotting the $\gamma^* P$ cross-section measured in DIS as a function of τ, people indeed see the saturation at very small τ, as shown by figure 1.10.

1.3 Nuclear modification on PDF

Nuclear modification on PDF refers to the fact that the PDF for nucleons bound in a nucleus are different from the PDF for free nucleons, such as protons. Often the nucleons in the deuteron nucleus are also regarded as free nucleons since the deuteron is such a loose bound system. In fact, there is one bonus from using the deuteron as the free nucleon reference instead of the proton. The measurements are free of isospin effects since the deuteron nucleus is an isospin singlet. The nuclear modification on the parton distribution of nucleons comes from the fact that when nucleons are bound together, there are interactions between partons from different nucleons. Therefore the parton distributions may change due to the interactions. In general, the heavier the nucleus is, the bigger these effects are.

The most direct way to investigate the parton distributions in nuclei is measuring DIS cross-section of leptons on nuclei. In DIS, the nuclear modification effect is studied by comparing the quark structure functions in nuclei with the quark structure functions in free nucleons. Often, the proton/deuteron nucleus(p/dA) collisions are used to study the modification effects too. In p/dA collisions, the modification effects are quantified by comparing the cross-sections or yields of certain physics processes in p/dA collisions with the same cross-sections or yields in proton proton(pp) collisions scaled by the number of binary collisions in the p/dA collisons or the mass number of the target nucleus. However in the study of the nuclear modification , we can always define a thing called the nuclear modification factor, NMF. For DIS, the NMF is defined as the ratio between per nucleon structure functions for a nucleus(F_2^A) and the structure functions for proton or the per nucleon structure functions for deuteron(F_2^D), NMF= $\frac{F_2^A}{F_2^D}$. In p/dA case, following the same idea and using the Drell-Yan process as an example , we define NMF= $\frac{Y_{p/dA}^{DY}}{Y_{pp}^{DY} N_{coll}}$, where $Y_{p/dA}^{DY}$ and Y_{pp}^{DY} are the Drell-Yan yield in p/dA and in pp, respectively. N_{coll} denotes the average number of nucleon nucleon collisions in one p/dA collision. One can see that the NMF is always defined such that if there is no modification, it should be one.

It is noted that the measured NMF does not have to reflect the modification on the partonic level. Many other effects may cause the deviation of measured NMF from one. One example is Fermi motion effect. As we know that nucleons are not at rest in a nucleus, they have non zero momenta which follow Fermi distributions. Therefore, the momentum distribution for partons in bound nucleons is not identical to the parton momentum distribution in free nucleons. The net effect from Fermi motion is the NMF larger than one for processes related to partons with $x > 0.8$. In fact, all models which are used to explain nuclear modification effects always fall into two categories, contributing effects to partonic level modifications or contributing effects to nuclear level modifications. In this section, we will review the nuclear modification effects experimentally and discuss the theoretical aspects.

1.3.1 Quark Structure functions in nuclei

The first experiment that discovered the difference in structure functions between bound nucleons and free nucleons was the European Muon Collaborations(EMC) [13] at CERN. The EMC experiment was a DIS experiment using muons scattering off nuclei. Since then the effect has been extensively studied by many different DIS experiments, such as DIS experiments with electrons at SLAC, DIS experiments with neutrinos in CERN, etc. All these experiments found that F_2^A, the per nucleon structure functions measured on bound nucleons is different from F_2^D, the per nucleon structure functions measured on deuterons. The ratio, $\frac{F_2^A}{F_2^D}$, varies from less than unity or greater than unity with x.

- For $x < 0.05 - 0.1$, $\frac{F_2^A}{F_2^D} < 1.0$. This suppression is called shadowing effect.
- For $x \sim 0.1 - 0.2$, $\frac{F_2^A}{F_2^D} > 1.0$. This enhancement is called anti-shadowing effect.
- For $x \sim 0.2 - 0.8$, $\frac{F_2^A}{F_2^D} < 1.0$. This suppression is called EMC effect(*Some time people refer all the nucleon effects to EMC effect, here we exclusively refer it as the modifications in this x range.*).
- For $x > 0.8$, $\frac{F_2^A}{F_2^D} > 1.0$. Fermi motion region.

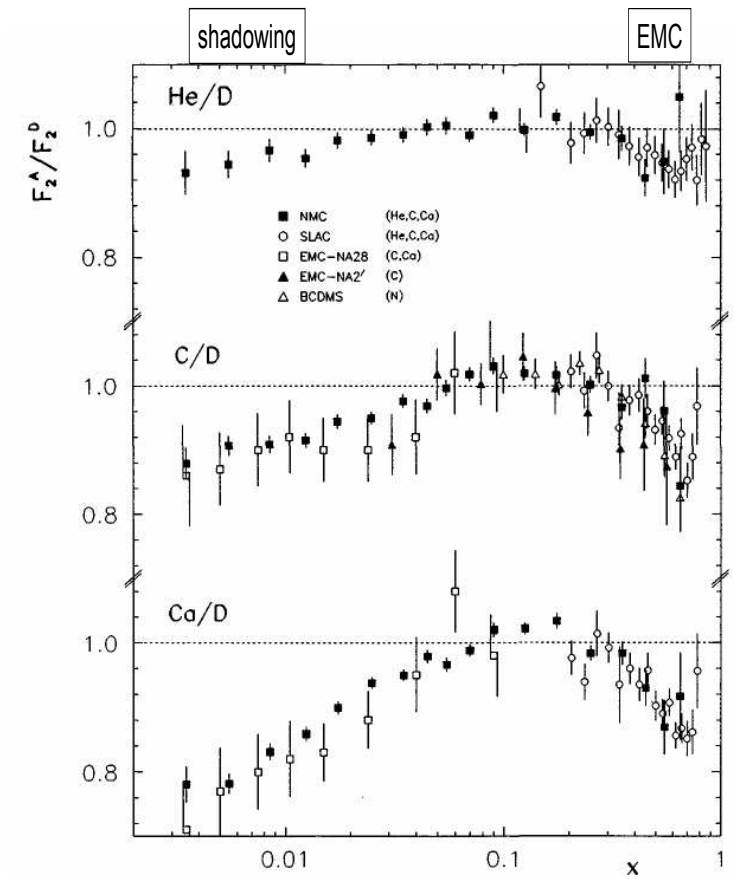

Figure 1.11: $\frac{F_2^A}{F_2^D}$ as a function of x for different nucleus [15]. The data are from many DIS experiments.

The Fermi Motion effect is somewhat trivial, so we will not spend much time on it. In the following discussion we will focus on other three effects, especially on the shadowing effect.

Figure 1.11 [15] shows $\frac{F_2^A}{F_2^D}$ as a function of x for Helium, Carbon, and Calcium nuclei. The data are from many DIS experiments, and they are consistent between

experiments. In the x range from $0.003 - 0.8$, all data show the shadowing effect, anti-shadowing effect and EMC effect. The modification increases with the increase of the mass number of the target nuclei.

To understand the fact that $\frac{F_2^A}{F_2^D} < 1$ when $x < 0.1$, Piller *et.al* [14] proposed a so-called General Vector Meson Dominance(GVMD) model. The essential idea of the GVMD is taking the hadron structures of virtual photon into account when calculating the cross-section. The incoming photon can be decomposed into a bare photon state plus lepton anti-lepton and quark anti-quark pairs. The quark anti-quark pairs form quantum states identical to vector mesons. The total cross-section between the virtual photon and the target nucleus is dominated by the cross-section between the vector meson states and the nucleus. Each vector meson state naturally has a coherence length, which roughly equals $\frac{1}{\Delta E}$. ΔE is the energy difference between the virtual photon and the vector meson state. The energy of the vector meson is

$$E_V = \sqrt{M_V^2 + k^2}$$

and the energy of the virtual photon is

$$\nu = \sqrt{-Q^2 + k^2}$$

where k is the 3 dimensional momentum of the virtual photon and M_V^2 is the mass squared of the vector meson. Thus with the limit of large ν we get

$$\Delta E = E_V - \nu = \frac{Q^2 + M_V^2}{2\nu}$$

Then since $x = \frac{Q^2}{2M_N\nu}$ and M_N is the mass of nucleon, the coherence length of the vector meson is

$$d(M_V^2, Q^2, x) = \frac{1}{M_N x}\frac{1}{1 + \frac{M_V^2}{Q^2}}$$

At the same time, the interaction between the vector meson and the target nucleon determines a mean free path $l(M_V^2) = \frac{1}{\sigma_V(M_V^2)n_0}$, where n_0 is the nucleon density and $\sigma_V(M_V^2)$ is the cross-section of the hadronic system of mass M_V with a nucleon. Under the condition $d > l$ and the size of the target nucleus $R_A > l$, the vector meson

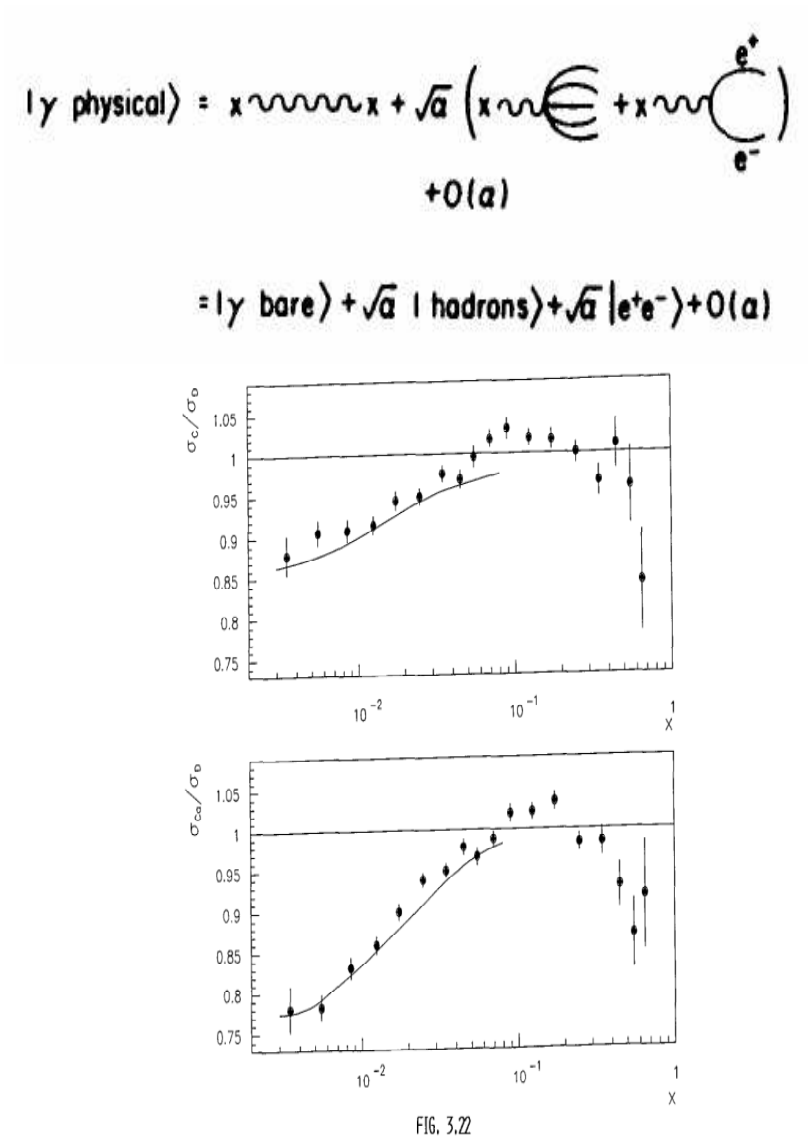

Figure 1.12: Feynman diagram for the hadron structure of photon and the comparison between GVMD model calculation(the solid lines) and NMC data(the solid points).

will interact with a nucleon before it can reach the core of the nucleus. Therefore the vector meson will not be able to see the nucleons deep inside the nucleus, fewer partons are probed. In other words, we expect a depletion of the structure function at low x since $d \propto \frac{1}{x}$. The model can be used to explain the shadowing effect and part of the EMC effect. It is noticed that at the same Q^2, the coherence length d decreases with the increase of x, when $d < l$, the shadowing effect also disappears. Figure 1.12 shows the Feynman diagram of the model. Also on the same figure, the comparison between theoretical calculation of GVMD and the data from NMC experiment [15] is shown. The calculation reproduced the shadowing effect from the data very well.

The GVMD models addresses the nuclear modifications from the aspect of nucleon level interactions between incoming virtual photons and target nuclei. There are many models following the same strategy, such as the "x rescaling" model [16] for the EMC effect. In this model, the mass of the nucleon is modified due to the effect of nuclear potential on bound nucleons, thus there will be shift of $x = \frac{Q^2}{2M_N\nu}$ to higher values and $F_2^A(x)$ is modified too. On the other hand, there are models which ascribe the nuclear modifications to the partonic level difference between free nucleons and bound nucleons. For example, F. E. Close *et.al.* proposed the "Q^2 rescaling" model [17] for the EMC effect. In this model, the valence quark confinement length of free nucleons, $\lambda_N \sim \frac{1}{\Lambda_{QCD}^N}$ is different from the valence quark confinement length of bound nucleons, $\lambda_A \sim \frac{1}{\Lambda_{QCD}^A}$. To be able to see the partons, a probe has to satisfy $Q^2 > \frac{1}{\lambda}$. Thus the difference between λ_A and λ_N implies that when one probes the parton distributions in bound nucleons, a larger Q^2 ($\Lambda_{QCD}^N < \Lambda_{QCD}^A$ because of the nuclear potential) is needed to reach the same resolution as in the free nucleon case. x rescaling and Q^2 rescaling are connected to each other in the sense that the modification on nucleon mass and the modification on the confinement length are all related to the existence of nuclear potential. Both these two models did a good job in explaining experimental data in a certain x and Q^2 range.

The model which really dealt with the modification via partonic interactions was first proposed by N.N. Nikolaev and V.I. Zakharov [18] and was later further developed by many others(e.g. A.H. Muller and J. Qiu [19]). In this model, the DIS process is considered in the Breit frame, where the 4-momentum of the virtual photon is $(0, 0, 0, -Q)$. The velocity of this frame relative to the experimental frame is $\vec{\beta} = \frac{\vec{q}+2x\vec{P}}{q_0+2xP_0}$, where $(q_0, \vec{q})$ and $(P_0, \vec{P})$ are the 4-momenta of the virtual photon and the incident nucleon in the experimental frame respectively. In the Breit frame, the outgoing partons are totally separated from the incoming nucleon and lepton by the $z = 0$ plane in space. A parton carrying a fraction x of the nucleon's momentum is localized longitudinally within a distance $\Delta z \sim \frac{1}{xP}$. At small x, Δz may be larger than the diameter of nucleons. Partons from different nucleons may overlap with each others and fuse. Therefore the parton density is reduced comparing to that of free nucleons at small x, and as a consequence of momentum conservation, the parton density at large x may be enhanced. One can define $x_N = \frac{1}{2R_N M} \sim 0.1$ and $x_R = \frac{1}{2R_A M} \approx x_N A^{-\frac{1}{3}}$. The former tells when the partons from adjacent nucleons start to overlap spatially and the latter tells when partons from all the nucleons in one nucleus start to overlap. They are essentially the parameters for the onset of the recombination. In their approach [19], Muller and Qiu calculate gluon fusion in the pQCD framework. They find that the gluon density is reduced at small x, which in turn results in a depletion of the sea quark density. Figure 1.13 shows comparison between the NMC data and the calculations done by Berger and Qiu and by Close and Robert following this parton recombination model. The calculations reproduce the data very well over a wide x-range.

Compared with GVMD, the parton recombination model addresses the nuclear modifications at a much more fundamental level. It explains the shadowing and anti-shadowing effects in the same framework. Also GVMD predicts that the nuclear modification will disappear at large enough Q^2, which is not seen by experiment . Qiu [22] also studied the Q^2 evolution of shadowing using the parton recombination model. He found the Q^2 dependence of shadowing was very weak.

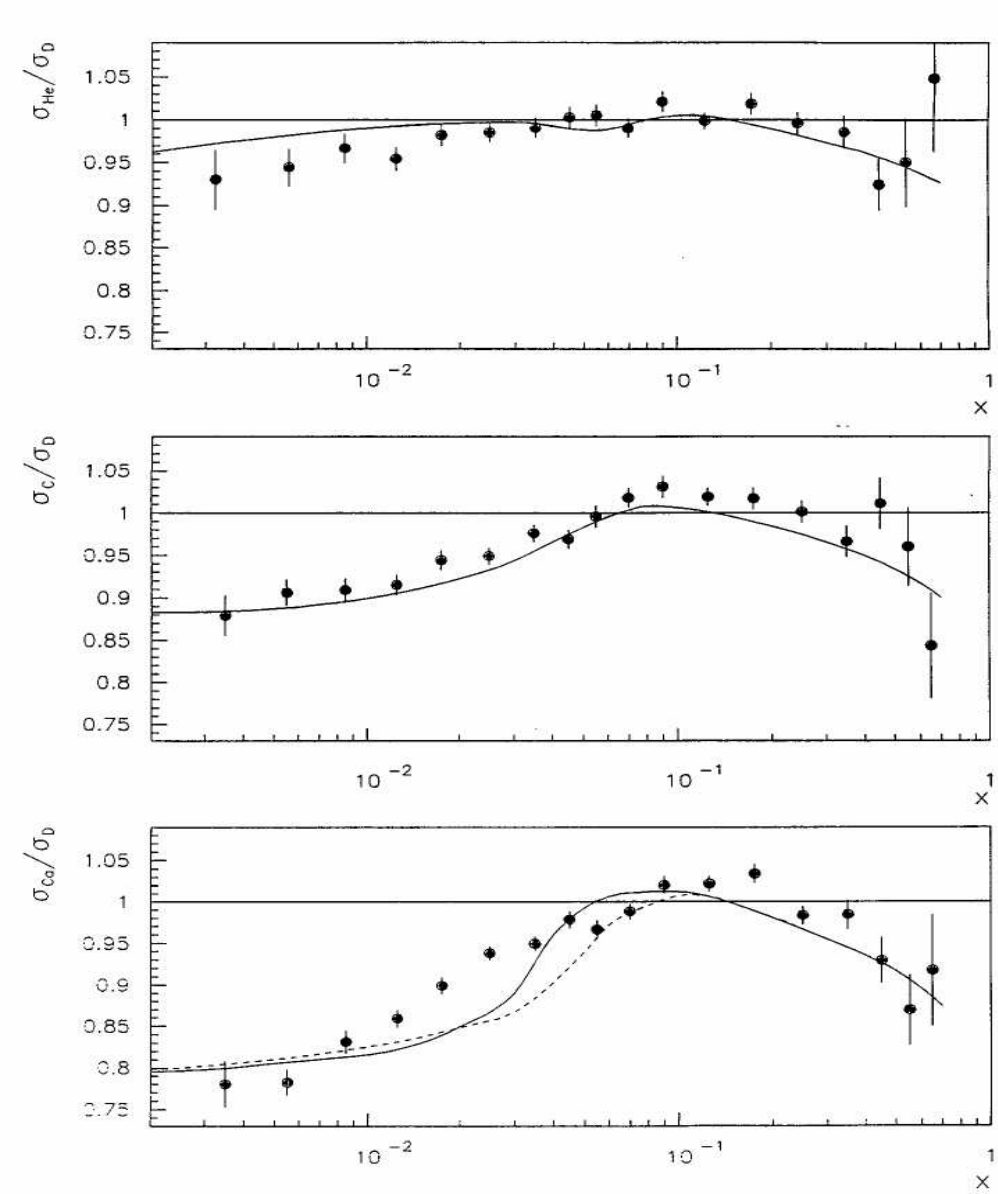

Figure 1.13: Comparison between NMC data and calculations from parton recombination model. Solid points are real data. Solid line are calculations from Berger and Qiu [20]. Dashed line are calculations from Close and Robert [21]

1.3.2 Nuclear modification in p/dA collisions

In p/dA collisions, we can use proton/deuteron as a well calibrated probe to investigate the partonic structure of the nucleus. But, unlike DIS experiments, one does not have a definite control on Q^2 and x by measuring the outgoing lepton. The final states in p/dA collisions are much more complicated. However there are some processes in p/dA collisions in which the final states are simple. Drell-Yan is such a process in which a quark from the incoming proton annihilates with an anti-quark from the target nucleon into a virtual photon, then the virtual photon splits into $\mu^+\mu^-$. In the Drell-Yan process, the $Q^2 = M_{\mu^+\mu^-}$, $x = \frac{\sqrt{M^2_{\mu^+\mu^-}+|\vec{P}_{\mu^+\mu^-}|^2}}{2P_N}$, where $M_{\mu^+\mu^-}$ is the invariant mass of muon pairs, $\vec{P}_{\mu^+\mu^-}$ is the momentum of muon pairs and P_N is the momentum of nucleons. Also the Drell-Yan process is indeed the quark antiquark annihilations, it is sensitive to the sea quark distribution in nucleons. In the study of nuclear modifications in the Drell-Yan process, people always use a variable called the Drell-Yan ratio, which is defined as the ratio between per nucleon Drell-Yan yield in p/dA collisions and the yield in proton deuteron collisions. This Drell-Yan ratio is like the $\frac{F_2^A}{F_2^D}$ in DIS. Figure 1.14 shows the Drell-Yan ratio measured by FNAL E772 experiment [23]. E772 data shows the shadowing effect and anti-shadowing effect at the same x range as the EMC data. Also there is a clear A dependence of modification in E772 data.

Besides the Drell-Yan process, J/Ψ production and high transverse momentum (p_T) particle production are also used in measuring the nuclear modifications in p/dA collisions. Gluon gluon fusion is the main J/ψ production mechanism, therefore J/Ψ production is sensitive to gluon distributions. However the mechanism of charm anti-charm pair hadronization is an unanswered question, which makes the interpretation of J/Ψ data very difficult. In high energy p/dA collisions, it is generally believed that most hadrons with $p_T > 1.0$ GeV/c are from parton parton interactions. Thus by comparing the yield of high p_T particles in p/dA collisions with the yield in proton proton(deuteron) collisions, we can also study the nuclear modifications. The most important discovery in this kind of experiments is the Cronin

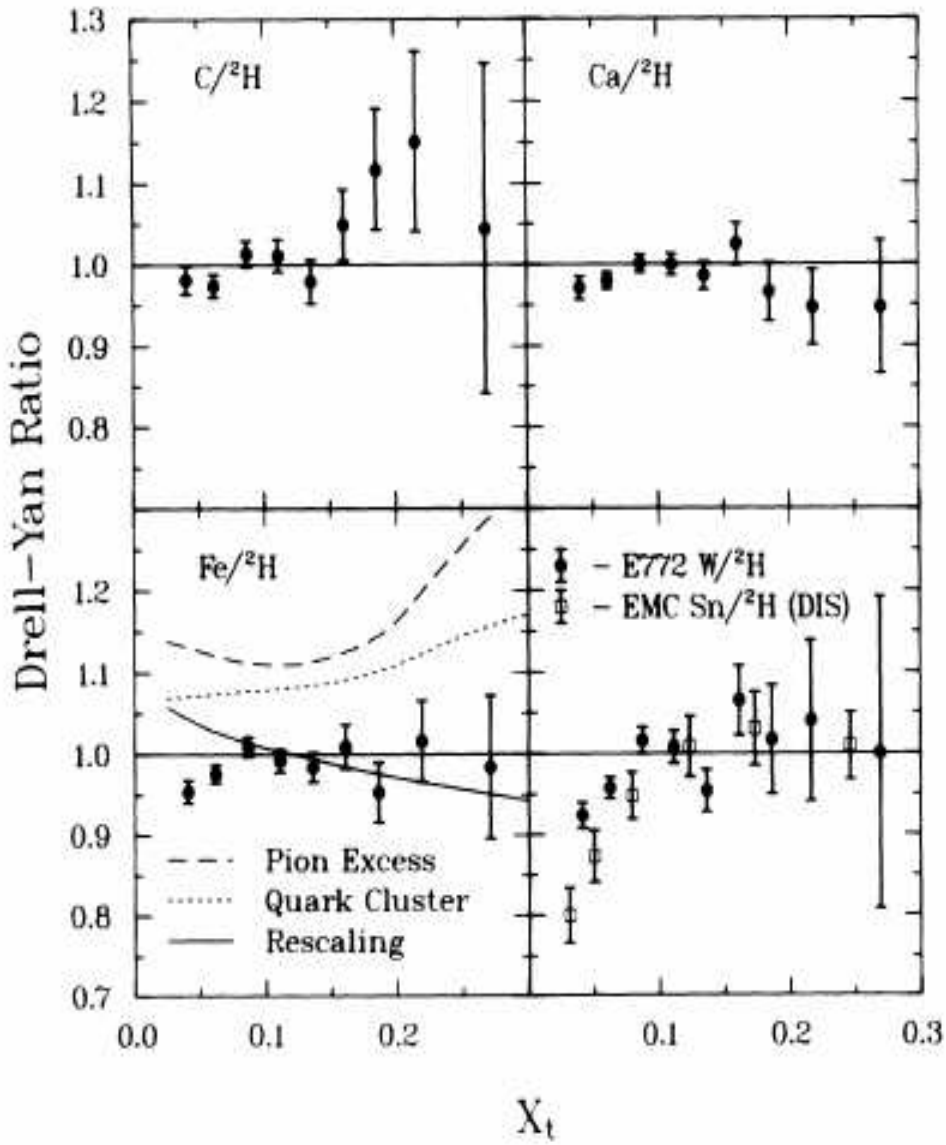

Figure 1.14: Drell-Yan ratio measured by Fermi Lab. E772 experiment [23]. E772 data shows the shadowing effect and anti-shadowing effect at the same x range as EMC data. Also there is a clear A dependence of modification in E772 data.

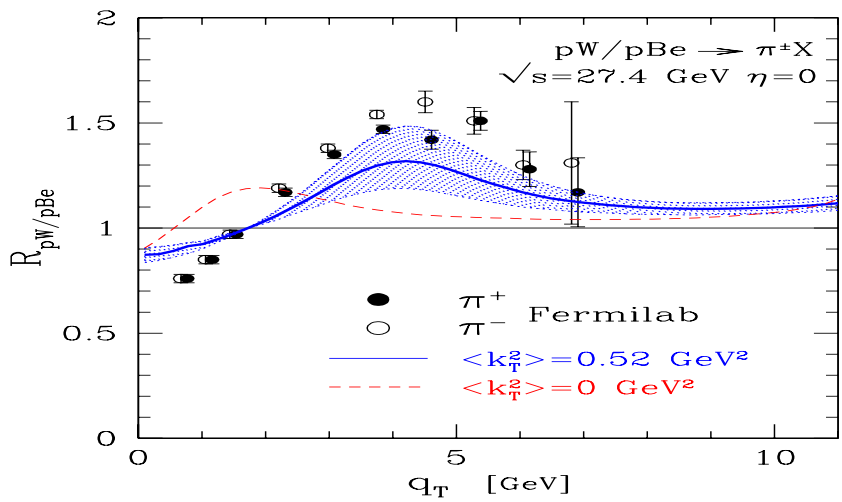

Figure 1.15: Cronin effect and a calculation using Geometrical shadowing.

Effect [24], which is the enhancement of particle production in moderate transverse momentum($p_T \sim 2 - 6$GeV/c). The theoretical explanation for the Cronin effect is generally attributed to multiple scattering of projectile partons when propagating through the target nucleus. The calculation of the multiple scattering can be formulated in the target rest frame or the infinite momentum frame. The former is also called Geometrical Shadowing [25]. In the Geometrical shadowing scheme, the series of parton multiple scattering follows the collision geometry. The calculations performed in the infinite momentum frame are also called saturation models, which was first proposed by Mclerran and Venugopalan [26]. In saturation model, the Cronin effect is a generic result from small x gluon evolution. We will come back to this topic in the next section. Figure 1.15 shows the Cronin effect from [24] and the calculation [25] by A.Accardi and M.Gyulassy using Geometrical Shadowing model.

1.4 dA collisions at RHIC

The primary goal for Relativistic Heavy Ion Collider(RHIC) at Brookhaven National Laboratory is to search for Quark Gluon Plasma(QGP). QGP is the QCD analogue of the plasma phase of ordinary atomic matter, but instead of ions and electrons, it is composed of deconfined color charges (i.e. quarks and gluons). It exists under extreme conditions, where the temperature and the energy density are very high. These conditions are believed to be satisfied only at the very early time of the universe, right after the BIG BANG. Lattice QCD calculations suggest, for a net-baryon-free matter, that the critical temperature of the QGP phase is about 170 MeV. However, we can not directly observe the QGP phase because of the confinement of quark and gluons, only the hadronic and leptonic residues from the QGP can be measured experimentally. The phase transition from QGP phase to hadronic phase has some special signals which we can use to identify the existence of the QGP. For example, the abundance of quarkonia such as J/Ψ, Ψ'. Υ etc. are sensitive to the chromo-electric field fluctuation in the QGP. It has been suggested by Matsui and Satz [27] that the yield of J/Ψ will be suppressed by the Debye screening in the QGP. Also the yield of high transverse momentum particles tells the energy density of the QGP. High p_T particles are from high p_T parton fragmentation. Before the parton hadronizes, the high p_T parton travels inside the QGP medium and interacts with the medium. Therefore, it loses energy. If the medium is dense enough, a suppression of high p_T hadrons shall be observed [28]. The spectra of direct photons are the thermometer for the initial temperature of QGP produced in heavy ion collisions. Photons do not strongly interact with the medium and preserve the original thermodynamic information of the QGP [29]

1.4.1 The suppression of high p_T particle in gold gold collisions

One of the major discoveries at RHIC is the observation of high p_T particle suppressions in gold gold collisions at $\sqrt{s_{NN}} = 200, 130$ GeV. This observation is confirmed

by all four RHIC experiments and has served as an evidence of the formation of strong coupling and dense medium in gold gold collisions. Figure 1.16 [30] shows the PHENIX measured $R_{AA} = \frac{Y^{inv}_{AuAu}}{N_{coll} Y^{inv}_{pp}}$ at $\sqrt{s_{NN}} = 200$ GeV as a function of p_T in different centrality classes, where Y^{inv}_{AuAu} and Y^{inv}_{pp} are the invariant yield of particles produced in gold gold collisions and proton proton collisions. N_{coll} is the number of binary collisions in one gold gold collision. One can see that the definition of the R_{AA} is such that with the assumption that the particle production rate scales with the number of binary collisions the R_{AA} shall be unity if there is no final state medium effect. The centrality is named such that the smaller the percentage number are, the smaller the impact parameters of the collisions are. From the plot there is a clear centrality dependence of R_{AA}. The more central the collision is (small impact parameters and more nucleons involved in the collisions), the larger the suppression. Also the p_T dependence of R_{AA} is small. But the suppression may not solely come from the final state medium effects. As we discussed in previous sections, there are also the initial state effects due to the nuclear modifications of the nucleon partonic structures which can also result in the suppression of high p_T particle yield. For example R. Vogt and S. Klein [31] calculated the R_{AA} by modifying the patron distribution functions in gold nuclei with EKS98 parametrization. They find the shadowing effects are small at mid-rapidity and can not account for the suppression we see in the data. The Color Glass Condensate model also argues that the suppression may be a consequence of gluon saturation in the CGC framework [32]. Results from CGC calculations implied that the yield of high p_T particles should scale with number of participants instead of N_{coll}.

In order to check how the initial state nuclear modifications affect the spectra of high p_T particles, RHIC collided deuteron and gold nuclei at $\sqrt{s_{NN}} = 200$GeV in Run3(from Nov. 2002 to April 2003). In deuteron gold collisions, we do not expect the formation of a hot and dense medium since the amount of nuclear matter stopped by the collisions is very little. Therefore there should be no final state medium induced effects on particle production. The measured $R_{dA} = \frac{Y^{inv}_{dAu}}{N_{coll} Y^{inv}_{pp}}$ from

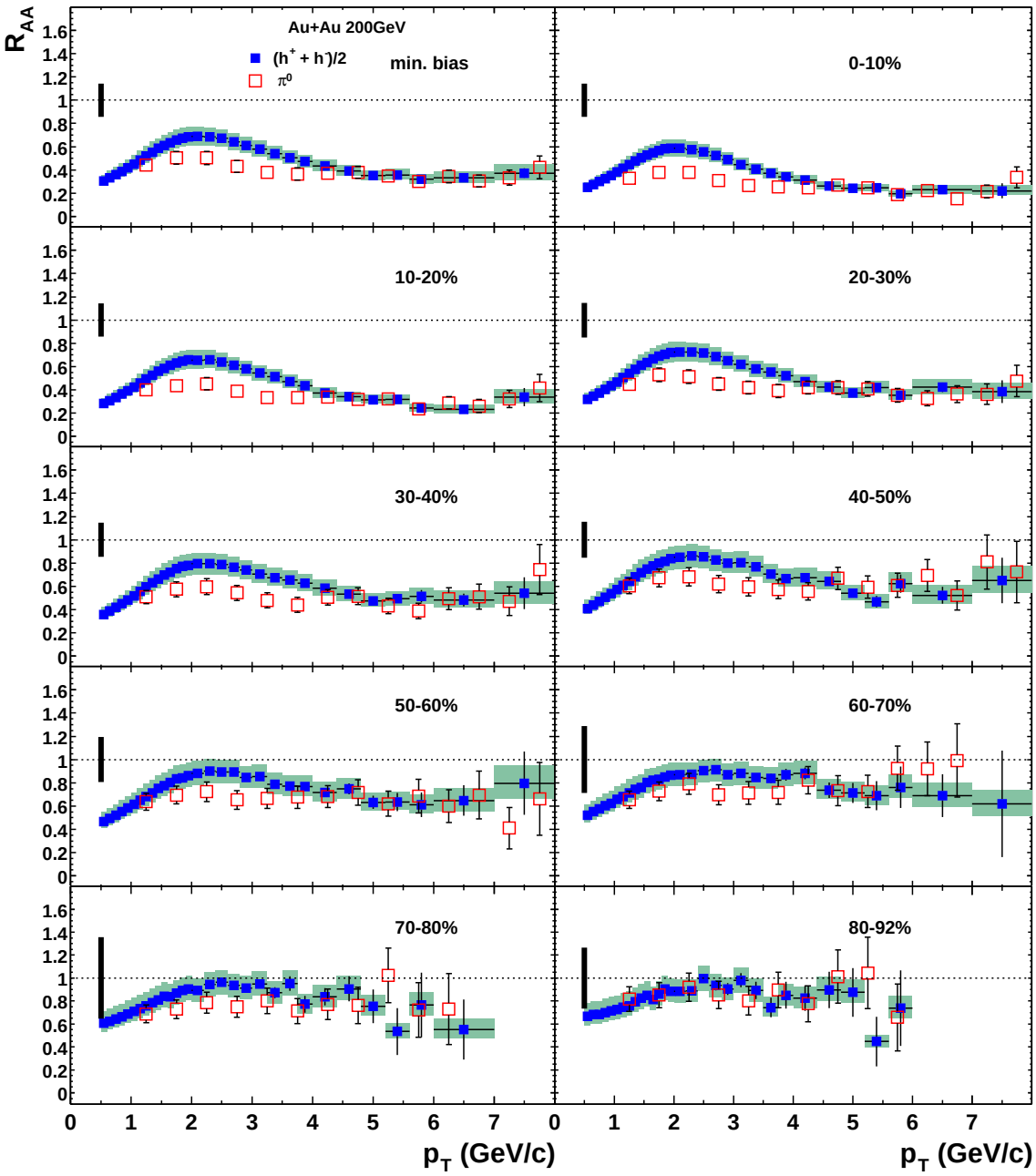

Figure 1.16: PHENIX measured R_{AA} for charged hadrons and neutral pions in different centrality classes of gold gold collisions at $\sqrt{s_{NN}} = 200$GeV.

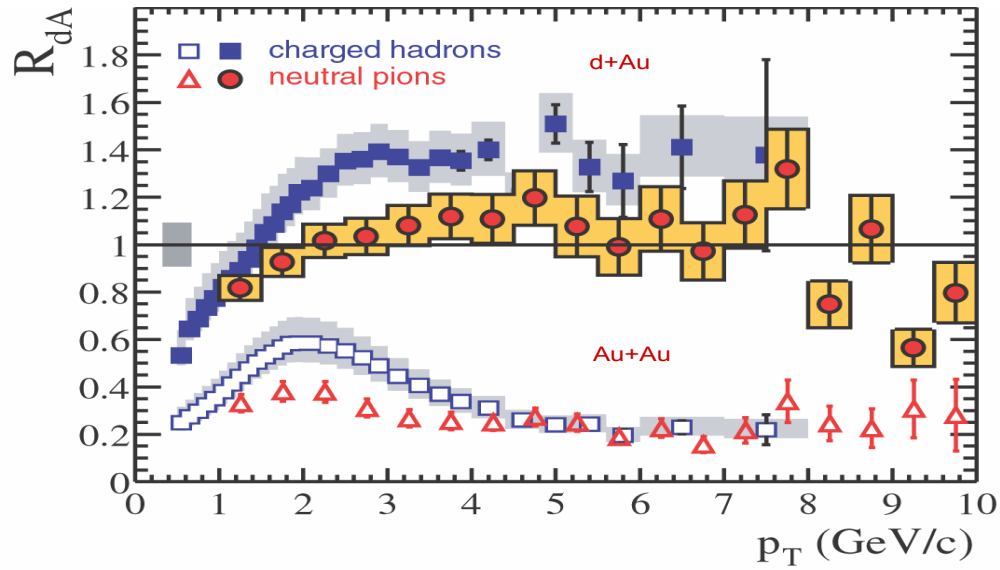

Figure 1.17: PHENIX measured R_{dA} for charged hadrons and neutral pions in deuteron gold collisions at $\sqrt{s_{NN}} = 200$ GeV [33].

all the four experiments operating at RHIC shows there is no suppression on high p_T particle production at mid-rapidity. Figure 1.17 [33] shows the results from the PHENIX experiment. To guide eyes, the results from gold gold collisions are also shown.

It is now generally believed that partons propagating in colored matter lose energy predominantly through medium-induced emission of gluon radiation. An energetic parton scatters off color charges in the high parton density medium and radiates gluon bremsstrahlung. The reduction in the parton energy translates to a reduction in the average momentum of the fragmentation hadrons, which, in turn, produces a suppression in the yield of high p_T hadrons relative to the corresponding yield in p + p collisions. In fact, the only detailed energy loss model that predicted the flat p_T dependence of R_{AA} over the p_T range covered by RHIC data was the Gyulassy-Levai-Vitev(GLV) prescription [34]. In the GLV formulation, the fractional energy loss for large jet energies varies approximately as $\frac{\log(E)}{E}$ but the

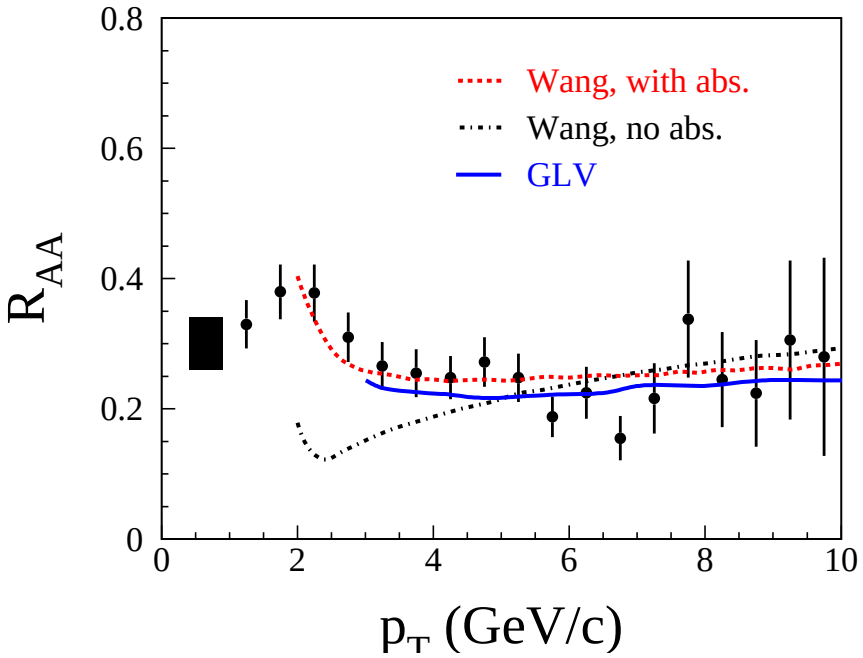

Figure 1.18: PHENIX measured R_{AA} for charged hadrons and neutral pions in gold gold collisions at $\sqrt{s_{NN}} = 200$GeV is compared with GLV calculation. Dashed and dotted line are the calculations from X.N. Wang and his company [35].

authors observe that below 20 GeV the full numerical calculation of the energy loss produces a nearly constant $\frac{\Delta E}{E}$. However, the same authors argue that the flat $R_{AA}(p_T)$ observed at high p_T at 200 GeV also requires an accidental cancellation of several different contributions including the separate p_T dependencies of the quark and gluon jet contributions, the p_T dependence of the Cronin enhancement, and shadowing/EMC effect. A comparison of the GLV results for the p_T dependence of the neutral pion suppression to the PHENIX data is shown in Figure 1.18.

1.4.2 dAu collisions at RHIC and gluon density at small x

Deuteron gold collisions conducted by RHIC mainly serves as a control experiment for understanding the initial state effects for gold gold collisions. However, deuteron gold collisions at RHIC also provide us with a very good opportunity for studying the partonic structure of heavy nuclei at high Q^2. Comparing to previous fix target p/dA experiments, the deuteron gold collisions at RHIC open a totally new era in the field in the following ways,

- RHIC is a high energy collider. It can create high Q^2 collisions between small x partons. Thus, the pQCD calculations may apply to lower x. For example, at $\sqrt{s_{NN}} = 200$GeV, Q^2 of collisions between two partons, $x_1 = 0.1$ and $x_2 = 0.001$, is about 22 GeV^2.

- RHIC can accelerate very heavy nuclei. The heavier the nuclei are, the larger the nuclear modification effect is.

- From HERA experiments, we know that the gluon density increases very fast as Q^2 increases and x decreases. Therefore, the gluon density becomes dominate in the PDF at RHIC energy.

These three points together may allow us to reveal new physics.

Now we examine the gluons at small x, high Q^2 in a heavy nucleus using the approach in reference [26]. At small x gluons, their longitudinal wavelength at the rest frame $\lambda_l \sim \frac{1}{xm_N}$ may exceed the diameter of the nucleus, therefore gluons from different nucleons may overlap each other and fuse. Because of this, one can assume that the density of the small x gluons per unit rapidity is proportional to the diameter of the nucleus, i.e. $\rho \sim A^{\frac{1}{3}}$. For a large enough nucleus, $\rho >> \Lambda^2_{QCD}$. In this case, if the following conditions are satisfied,

$$\Lambda^2_{QCD} << \alpha_s \rho << k_t^2 << \rho \tag{1.3}$$

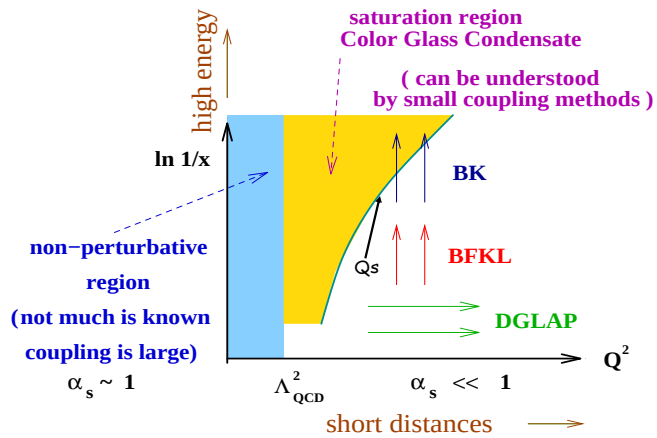

Figure 1.19: Phase diagram for CGC. The boundary of CGC is defined by Q_s [37].

then the gluon density is calculable via classical color field and it shall be of the Weiszacker-Williams form

$$\frac{1}{\pi R^2}\frac{dN_g}{dxd^2k_t} \sim \frac{\mu^2}{xk_t^2} \tag{1.4}$$

where μ is the color charge density which is proportional to $A^{\frac{1}{3}}$ and k_t is the transverse momentum of gluon. Under the condition defined by equation 1.3, the quantum evolution becomes non-linear, the recombination of gluon need to be taken into account. The gluon density $xg(x, \Lambda^2_{QCQ} < Q^2 < Q_s^2)$ at small x has at most a logarithm dependence on x [36], where $Q_s^2 \sim \mu^2$ is the saturation scale. Therefore the gluon density is saturated and unitarity of DIS cross-section at small x is recovered. This new quantum evolution defines a new phase of matter on the $[Q^2, x]$ phase space, the Color Glass Condensate(CGC) as shown by figure 1.19.

Deuteron gold collisions at RHIC have provided a test field for the CGC model. A recent CGC calculation conducted by Dmitri Kharzeev *et.al* [38] shows that the saturation scale $Q_s^2 = \Lambda^2 A^{\frac{1}{3}} e^{\lambda y} N_{coll}$ for the gluon production in deuteron gold collisions at $\sqrt{s_{NN}} = 200$GeV , where $\lambda = 0.3$ is fixed by DIS data. One can see that at large enough rapidity $y > 1$, $Q_s > 1.6$ GeV for the most central deuteron gold

collisions. This is large enough for observing the onset of the CGC gluon saturation experimentally. Therefore, by measuring the nuclear modification on hadron production at forward rapidity(deuteron beam direction), one can actually test the CGC calculations which suggest a suppression due to the gluon saturation.

Besides CGC, an approach using parameterized nuclear shadowing to calculate the initial state modification is proposed by R. Vogt [39]. In this approach, it is assumed that the nuclear parton densities, F_A^i are the product of the nucleon density in the nucleus $\rho_A(s)$, the nucleon parton density $f_N^i(x, Q^2)$, and a shadowing function $S_{P,S}^i(A, x, Q^2, \overrightarrow{r}, z)$, where $\overrightarrow{r}$ and z are the transverse and longitudinal location of the parton in position space with $s = \sqrt{r^2 + z^2}$. The first subscript, P, refers to the choice of shadowing parametrization, while the second, S, refers to the spatial dependence. All available shadowing parameterizations ignore effects in deuterium. There are two sets of parameterized shadowing functions, EKS98 and GRV LO. The calculations from this approach shows a larger shadowing effect at forward rapidities and a relative small anti-shadowing at mid-rapidities.

1.4.3 Studies in this thesis

The study presented in this thesis is to use the PHENIX detector measuring the nuclear modifications on hadron productions as a function of centrality, pseudo-rapidity(η) and p_T at forward rapidities(along the deuteron beam direction) and backward rapidities(along gold beam direction). In the purpose of studying the nuclear modification, PHENIX has unique advantages among all the four RHIC experiments. PHENIX has two muon arms placed at forward($1.2 < \eta < 2.4$) and backward ($-2.2 < \eta < -1.2$) rapidity. Figure 1.20 shows the x coverage by the PHENIX muon arms from PYTHIA simulation. By selecting hadrons at forward rapidity or at backward rapidity, we actually can study the nuclear modification effect of gold nuclei at small x or large x. Figure 1.20 highlights the PHENIX muon arm x coverage, one can see that all the interesting nuclear modification effects can be included in our study. Via this study, we hope to:

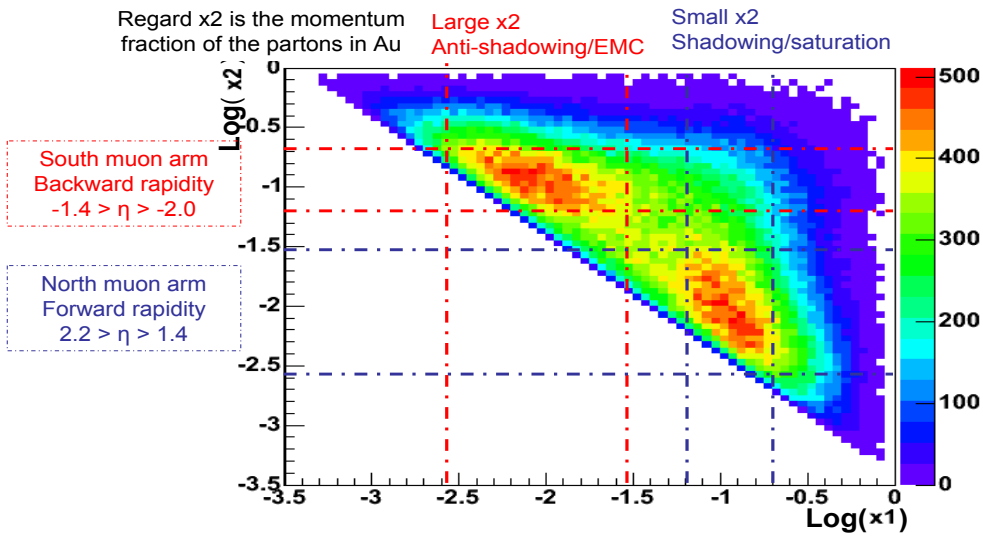

Figure 1.20: The PHENIX muon arm x coverage and the nuclear modification effects in side the PHENIX muon arm coverage.

- We can examine how nuclear modification effects evolve with centralities, p_T, and rapidity at RHIC energy.
- We can examine different theoretical models on nuclear modication by comparing our measured results with theoretical calculations.
- There is no previous measurement on nuclear modifications at the backward rapidities. Our results at the backward rapidities may provide new constraints on theoretical models.

.

Chapter 2

Experiment setup

2.1 RHIC and PHENIX detector

2.1.1 RHIC [40]

The Relativistic Heavy Ion Collider (RHIC) at Brookhaven National Laboratory is a versatile machine able to accelerate a wide variety of nuclei up to 100 GeV per nucleon and protons up to 250 GeV. It is located at the Brookhaven National Lab in Upton, NY and builds upon the previous accelerator program of the Alternating Gradient Synchrotron (AGS). The design luminosity for gold beams is $200b^{-1}sec^{-1}$ and $20\mu b^{-1}s^{-1}$ for protons averaged over a 10 hour fill. Collisions occur at the six intersections of two independent accelerator rings in which ions are grouped into bunches to increase collision rates while minimizing the average current. Each ring contains 360 RF buckets separated in time by 106 ns. Ions are injected in bunches from the AGS into these buckets one at a time. A range of 6 to 56 bunches can be injected and provided for collisions at each of the six interaction points simultaneously. To minimize intra-beam scattering the injection is performed in less than a minute. The acceleration from injection energy to up to 100GeV/u is achieved within 2 minutes. At this time the bunches are transferred to the storage RF system which limits the bunch length growth to 30 cm rms. This parameter is important because it directly impacts the size of the collision diamond at the experiments and the usable luminosity.

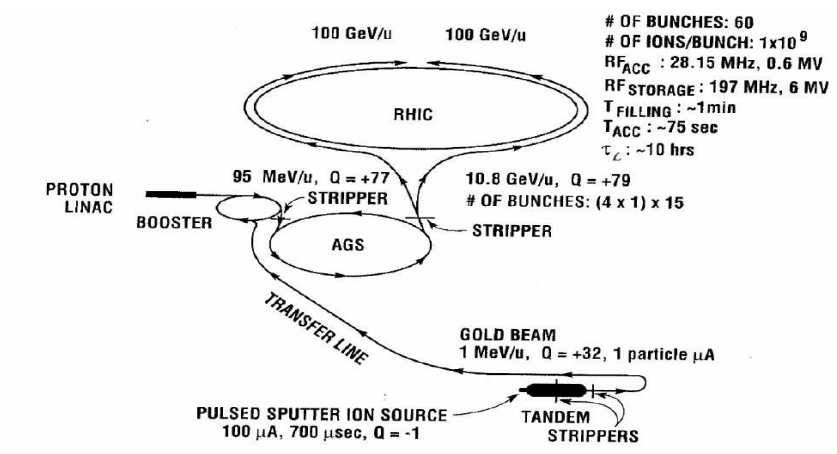

Figure 2.1: Accelerator setup and the path of accelerating particles at RHIC.

Figure 2.1 demonstrates the path of a gold ion through the accelerator complex, the Tandem - Van de Graaff, the Booster synchrotron, the AGS, and finally RHIC. The gold ions will begin their journey in the Tandem where negative gold ions are extracted from a pulsed sputter ion source and the ions with total charge $Q_T = -1$ are accelerated through 14MV potential. After the negative ions pass through the stripping foil in the positive high voltage terminal with a positive charge Q_T . The positive ions are then accelerated back to the ground potential for a gain of $14 \times Q_T$ MeV. The product of the Tandem is a beam of gold ions with a charge of +12 and 1 MeV/u kinetic energy. Upon exiting the Van de Graaff, the gold ions are further stripped to a charge of +32 before traversing the 850 meter long heavy ion transfer line to the Booster synchrotron. The gold beams are captured into six bunches and accelerated to 95 MeV/u before exiting the Booster where all but the two most tightly bound K-shell electrons are stripped. Almost half of all ions from the Tandem are successfully accelerated and stripped in the Booster. The gold ions

with charge of +79 are filled in the AGS in four Booster cycles totaling 24 bunches. They are re-bunched into four bunches before being accelerated to 8.86 GeV/u and exiting the AGS where they are fully stripped. The ions are transferred to the RHIC storage rings via the AtR beamline. There are four experiments at RHIC, PHENIX, STAR, PHOBOS, and BRAHMS.

RHIC is the world first high energy heavy ion accelerator. It can virtually accelerate all species from proton($A = 1$) to gold ions($A = 197$). By the summer 2004, RHIC has collided Au+Au at $\sqrt{s_{NN}} = 19.6, 56, 62.4, 130, 200$ GeV, d+Au at $\sqrt{s_{NN}} = 200$ GeV, and polarized p+p at $\sqrt{s_{NN}} = 200$ GeV. For the coming run at the winter 2005, RHIC is planned to collide Cu+Cu at $\sqrt{s_{NN}} = 200$ GeV and again polarized proton proton at $\sqrt{s_{NN}} = 200$ GeV.

2.1.2 PHENIX [41]

PHENIX detector is the largest detectors operating on RHIC. It is designed to meet the high multiplicity environment created in high energy heavy ion collisions. The average charged particle multiplicity in most central Au+Au collisions is $\frac{dN^{ch}}{d\eta} \sim 700$. The PHENIX tracking detectors at mid-rapidity was designed to have 10% occupancy for $\frac{dN^{ch}}{d\eta} \sim 2000$, which is the best theoretical estimation at that time when the detector was designed. The physics which drives the design of the detector are the following.

- 1. Deconfinement: $R(\Upsilon) \sim 0.13$ fm $< R(J/\Psi) \sim 0.29$ fm $< R(\Psi') \sim 0.56$ fm, *We need to measure the di-lepton decay channels of these quarkoniums.*

- 2. Chiral Symmetry Restoration : Mass, width, branching ratio of ϕ to e^+e^-, K^+K^- with $\delta M < 5$ Mev, *we need to identify electrons and koans.* Charged Hadrons Baryon susceptibility, color fluctuations, anti-baryon production. *measuring charged hadrons Charged and charged hadron PID.* Isospin fluctuations., *measuring photons and charged hadrons.*

- 3. Thermal Radiation of Hot Gas : Prompt γ and Prompt γ^* to e^+e^-, $\mu^+\mu^-$,

Photons, electrons and Muons are needed.

- 4. Strangeness and Charm Production : Production of K+, K- mesons, *koan identification.* Hadrons Production of ϕ, J/Ψ, D mesons,*Electrons and Muons are needed.*

- 5. Jet Quenching High pT jet via leading particle spectra: *Hadrons, Photons at high p_T and large azimuthal coverage.*

- 6. Space-Time Evolution: HBT Correlations of $\pi^{\pm}\pi^{\pm}$, $K^{\pm}K^{\pm}$: *Hadrons identification.*

From the list, one can see that PHENIX is a complex detector system. The detector consists of a number of subsystems. The rapidity and ϕ coverage and other features of these subsystems is given in Table2.1 and a perspective drawing of the PHENIX detector with the major subsystems labelled is shown in Figure 2.2. The east and west central arms are centered at zero rapidity and instrumented to detect electrons, photons and charged hadrons. The north and south forward arms have full azimuthal coverage and are instrumented to detect muons. The global detectors measure the start time, vertex and multiplicity of the interactions. Figure 2.3 shows the coverage in ϕ and η of different arms of PHENIX detector. Here I will go through PHENIX global detectors and central arm detectors very briefly. If interested, people can follow the references. Since the analysis in this thesis is mainly done with PHENIX Muon arms, in the next section, I will describe muon arms in details. Also with regard to the magnetic field configuration, people can refer to [44].

2.1.2.1 PHENIX global detectors [42]

In order to characterize the nature of an event following a heavy ion collision, three global detectors are employed. They consist of Zero-Degree Calorimeters (ZDC), Beam- Beam Counters (BBC) and the Multiplicity-Vertex Detector (MVD). A pair of ZDC's detect neutrons from grazing collisions and form a trigger for the most peripheral collisions. The ZDC is used by all four RHIC detectors and is discussed

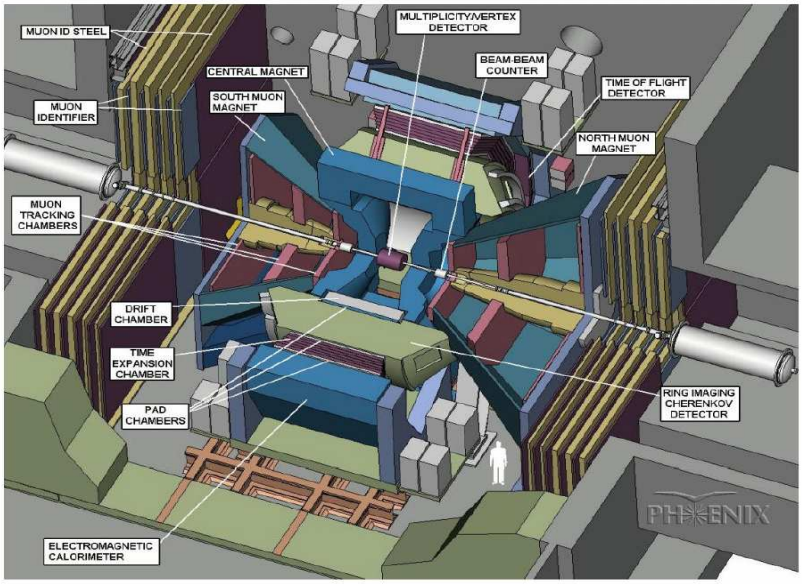

Figure 2.2: The PHENIX detector.

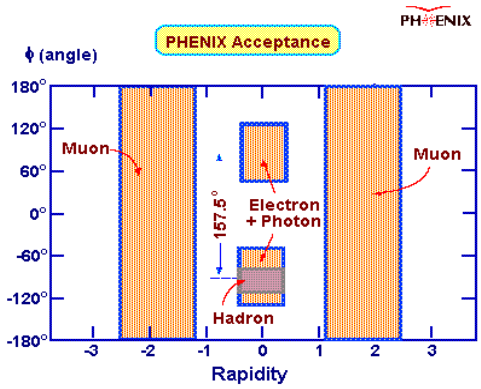

Figure 2.3: The η and ϕ coverage for the PHENIX detector subsystems.

Table2.1 PHENIX detector subsystems

Element	$\Delta\eta$	$\Delta\phi$	Purpose and Special Features
Magnet: central (CM)	± 0.35	360°	Up to 1.15 T·m.
muon (MMS)	-1.1 to -2.2	360°	0.72 T·m for $\eta = 2$
muon (MMN)	1.1 to 2.4	360°	0.72 T·m for $\eta = 2$
Silicon (MVD)	± 2.6	360°	$d^2N/d\eta d\phi$, precise vertex, reaction plane determination
Beam-beam (BBC)	$\pm$(3.1 to 3.9)	360°	Start timing, fast vertex.
NTC	$\pm$(1 to 2)	320°	Extend coverage of BBC for p-p and p-A.
ZDC	± 2 mrad	360°	Minimum bias trigger.
Drift chambers (DC)	± 0.35	90°×2	Good momentum and mass resolution, $\Delta m/m = 0.4\%$ at $m = 1$GeV.
Pad chambers (PC)	± 0.35	90°×2	Pattern recognition, tracking for nonbend direction.
TEC	± 0.35	90°	Pattern recognition, dE/dx.
RICH	± 0.35	90°×2	Electron identification.
ToF	± 0.35	45°	Good hadron identification, σ <100 ps.
T0	± 0.35	45°	Improve ToF timing for p-p and p-A.
PbSc EMCal	± 0.35	90°+45°	For both calorimeters, photon and electron detection.
PbGl EMCal	± 0.35	45°	Good $e^{\pm}/\pi^{\pm}$ separation at $p > 1$ GeV/c by EM shower and $p < 0.35$ GeV/c by ToF. $K^{\pm}/\pi^{\pm}$ separation up to 1 GeV/c by ToF.
μ tracker: (μTS)	-1.15 to -2.25	360°	Tracking for muons.
(μTN)	1.15 to 2.44	360°	Muon tracker north installed for year-3
μ identifier: (μIDS)	-1.15 to -2.25	360°	Steel absorbers and Iarocci tubes for
(μIDN)	1.15 to 2.44	360°	muon/hadron separation.

elsewhere in this volume. A pair of BBCs provide a measure of the time-of-flight of forward particles to determine the time of a collision, provide a trigger for the more central collisions and provide a measure of the collision position along the beam axis. The MVD provides a more precise determination of event position and multiplicity and measures fluctuations of the charged particle distributions. It is composed of concentric barrels of silicon-strip detectors and endcaps made of silicon pads. Recently a Normalization Trigger Counter (NTC) has been added between the MVD endcaps and the central magnet pole tips. The NTC extends the coverage of the BBC for p-p and p-A running.

2.1.2.2 PHENIX central arm detectors [43]

The magnetic field for the central spectrometer is supplied by the central magnet [44] that provides an axial field parallel to the beam and around the interaction vertex. The central arms consist of tracking systems for charged particles, particle identification detectors and electromagnetic calorimetry. The calorimeter is the outermost subsystem on the central arms and provides measurements of both photons and energetic electrons. A lead-scintillator (PbSc) calorimeter is used for good timing and a lead-glass (PbGl) calorimeter gives good energy resolution. The tracking system uses three sets of Pad Chambers (PC) to provide precise three-dimensional space points needed for pattern recognition. Separation of kaons from pions up to 2.5 GeV/c and proton identification out to 5 Gev/c. For p-p running the ToF timing resolution would be poorer than for heavy ions due to a reduced number of particles in the BBC. The ToF timing is improved by the use of a T0 counter outside the barrel of the MVD. This is needed for p-p and p-A experiments. The RICH provides separation of electrons from the large number of copiously produced pions. Using information from the RICH, the TEC and the electromagnetic calorimeter it is possible to reject pion contamination of identified electrons to one part in 10^4 over a wide range of momentum.

2.2 PHENIX muon arms

The PHENIX muon arms provide a means to study heavy ion collisions via muons. The physics relates to this are quarkonium decays, such as $J/\Psi \rightarrow \mu^+\mu^-$, Drell-Yan processes, Open charm/beauty via single muons, etc. PHENIX has two muon arms. The south muon arm is placed at $-2.2 < \eta < -1.2$ and the north muon arm is placed at $1.2 < \eta < 2.4$. Both of them have 2π coverage in ϕ direction. The average multiplicity at the PHENIX muon arm η coverage is about $\frac{dN^{ch}}{d\eta} |_{\eta=\pm 1.8} \sim 500$ [45]. Most of the 500 charge particles are light mesons such as pion and koan which are background to muons. Therefore the muon arms start with a thick hadron absorber comprising 60cm of low-carbon steel and 20cm of brass between the collision point and active detectors along the beam axis, primarily to reduce hadronic background for muon measurements. After the absorber there is the Muon Tracking Detector(MuTr) which consists of three stations of cathode strip chambers and tracks charged particles in a magnetic field. Following the muon magnet backplate(30cm steel), there is a muon identifier (MuID), which has 5 gaps per arm filled with planes of transversely oriented Iarocci tubes, interleaved with layers of steel (10cm thick in first two layers and 20cm thick for the rest two). Figure 2.4 shows the side view of the PHENIX muon arm.

2.2.1 Muon Tracker

The design requirement for muon tracking detector are the following,

- allow a clean separation of J/Ψ from Ψ', $\Upsilon(1S)$ from $\Upsilon(2S, 3S)$.
- provide a large enough signal-to-background and acceptance for vector mesons to be able to do statistically significant physics measurements in less than 1 year of RHIC running.
- 3.) have low enough occupancy to be able to reconstruct tracks efficiently in central Au-Au events.

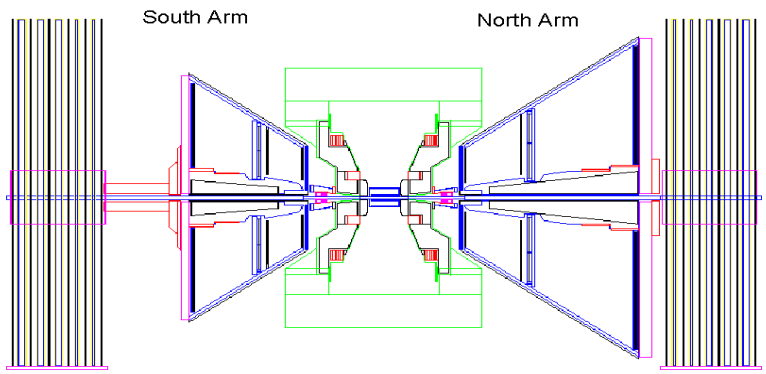

Figure 2.4: Side view of the PHENIX muon arms.

. The mass resolution is the top priority in the design. The first requirement implies that the mass resolution for muon tracker has to be $\sigma_M = \frac{\delta M}{M} = 6\%/\sqrt{M}$, where M is the mass of measured vector mesons in GeV/c^2. This is consistent with a 100μm spatial resolution for given the PHENIX muon magnet [44].

The above design requirements led to a Muon Tracker design which is comprised of three stations of cathode-strip readout tracking chambers mounted inside conical-shaped muon magnets, with multiple cathode strip orientations and readout planes in each station. The muon magnet is described in great detail in the paper on PHENIX magnets [44]. The electronics design specifications were driven by the requirement that the non-stereo cathode planes provide 100μm resolution measurements of the particle trajectories and that the readout of the system be able to meet the global PHENIX readout requirements. Test-bench measurements from production chambers and electronics combined with simulations of the full muon tracker design show that the tracker should meet the design requirements outlined above.

Each of the three stations of cathode strip chambers (CSC) presented unique design requirements. All are in the shape of octants built with a 3.175 mm half gap, 5 mm cathode strips and with alternate strips readout. For the mechanical construc-

tion, honeycomb technology was used for stations 1 and 3 and thin foil technology for station 2. Each station used a specific technology to produce a cathode pattern to an accuracy of better than 25 microns; station 1 used photolithography, station 2 used electro-mechanical etching at a facility designed specifically for this purpose and station 3 used mechanical routing. A unique wire laying apparatus was designed and implemented for each station. The anode planes are alternating structures of 20μm gold-plated W sense wires and 75μm gold-plated Cu-Be field wires with a sense wire spacing of 10 mm. Half of the cathode planes have strips perpendicular to the anode wires and the other half have strips at stereo angles between 0 and $\pm$11.25 deg with respect to the perpendicular strips. The chamber gas mixture is 50% Ar +30% CO2 + 20% CF4 with a gas recirculation system included in normal operation. The typical operating conditions for this gas are that the HV is 1850 V with a gain of approximately 2×10^4. The charge deposited by a minimum ionizing particle in the CSC is assumed to be 100 electrons. This results in a total cathode charge of 80 fC. This is an average and the charge is Landau distributed. The dimensions of three stations are different. Station 1 is the closest to the collision vertex, it is the smallest. The station 2 is the thinnest station and is only 0.1% of the radiation length. Station 3 chambers are the largest of the tracking chambers with each of the octant chambers about 2.4 m long and 2.4 m wide. Also the size of each station in south arm is smaller than the corresponding one in north arm.

To meet the design requirement of 100μm resolution, the rms noise of the front end electronics for MuTr is required to be 0.5 fC ($3125e^{-1}$) for a typical pulse of 80 fC at the input end of the pre-amplifiers, which have a capacity of 3.5 mV/fC and a dynamic range of 11 bits. The Cathode Readout Card (CROC) includes 64 channels of preamplifiers (8 Cathode Preamplifier (CPA) chips with 8 channels each) and two Analog Memory Unit/Analog to Digital Converters (AMUADC's). The ADC clock is 200 MHz so for 11 bit accuracy, 4 samples can be converted within the time constraint of 40μsec per event. Up to five events can be converted and stored locally to be transferred to the PHENIX DAQ.

A calibration system has been implemented to inject pulses into all of the chambers. Four wires in each chamber gap, which span the entire width of the cathode planes, are sent a square pulse from a digital to analog converter (DAC) thus inducing a charge on all cathode strips in a given gap simultaneously. Several different pulse amplitudes are sent to the chambers and many events are collected at each amplitude so that the relative gains of the cathode strips can be determined over the entire range of the electronics. The pedestals are monitored by collecting calibration data with the DAC amplitude set to zero.

2.2.2 Muon Identifier

The PHENIX muon identifier(MuID) is designed to be able to do the μ/π separation at a sensitivity of 2.5×10^{-4} at momentum up to 4GeV/c. To achieve this sensitivity, besides the absorber and muon magnet backplane, another 3.6(60cm) hadronic interaction lengths of steel is needed in the MuID. Thus, a muon at the vertex must have a mean energy of at least 1.9 GeV to reach the MuID system. The mean minimum original energy for a muon to penetrate completely through the MuID is 2.7 GeV.

Iarocci tubes [46] were chosen as the detector technology. We use the term Iarocci tubes to refer to planar drift tubes consisting of 100μm gold-coated CuBe anode wires at the center of long channels of a graphite-coated plastic cathode. This same physical detector when operated at higher voltage is a conventional limited streamer tube. We operate them in the proportional mode to increase longevity. Standard commercially-available Iarocci tubes have a width of 8.4 cm. Beam gas studies show that for low polar angles (20 degree or less), an effective segmentation into logical pads of approximately 13 by 13 cm is required to suppress false roads for tracks in the muon identifier. Rather than develop Iarocci tubes of greater width or use 13 cm wide external strips, the most cost effective solution is simply to use standard-width 8.4 cm tubes with all eight internal wires ganged together. This provides a readout pitch of 8.4 cm along both the x and y directions, thus providing effective

8.4 cm square hodoscopic cells (upon forming the appropriate ANDs). This most cost effective solution exceeds our requirements. This segmentation is fine enough to provide sufficient granularity for matching roads in the identifier to tracks in the muon tracker unambiguously with anticipated occupancies.

Two tubes are staged together forming a two-pack to reduce the dead area. Groups of two-packs oriented both horizontally and vertically are held inside an aluminum box. Approximately half are oriented horizontally and half are oriented vertically so that both projections are measured. This total detector element is called a muon identifier panel. There are six such panels per gap labelled A through F (counterclockwise from the upper left) arranged around the square hole left for the beam pipe to pass through. The large panels A, C, D, F are located at the 4 corners of the gap. Each contains 118 horizontal tubes of length 5200 mm and 128 vertical tubes of length 5010 m. The small panels B and E are situated above and below the square hole, respectively. Each contains 90 horizontal tubes of length 2504 mm and 52 vertical tubes of length 3821 mm. In this way, 1268 tubes per gap (6340 tubes per arm) are distributed to tile an area of 13.1 m wide by 10.7 m high in each gap. Adjacent panels overlap along their edges to eliminate deadspace.

The MuID has two separate gas volumes. The primary one is the tube gas volume. The secondary volume is the aluminum enclosure of each panel surrounding the primary volume. A mixture of CO_2 and up to $25\% i - C_4H_{10}$ is feed into the primary volume for chamber operation. N2 is feed into the secondary volume in order to keep the chamber electronics dry and clean, and to dilute the flammable gas component in the case of a primary volume leak. There are a total of 600 gas circuits for the primary volume. The total sizes of the primary and secondary volumes are 50 m^3 and 40 m^3, respectively. The gas flow rate of the primary volume is one volume exchange per day. The gas supply system can recirculate up to 50% of the flow of the primary volume.

To ensure adequate signal-to-noise performance in the unknown noise environment at RHIC we settled on a readout scheme that employs in-panel amplification

(x150) driving differential signals on 30 m twisted-pair cables to a crate-based processing system. The out-panel (post-amplifier) electronics are housed in a set of four 9U crates, each of which has two types of cards (ROC's and FEM's), described below, as well as transition cards to bring in signals and a custom backplane for communication between ROC's and FEM's. The FEM cards are analogous to a conventional crate controller, providing the interfaces between the MuID and the PHENIX online systems. The ROC cards consist of analog processing and synchronization, buffering, supplemental diagnostics and serial control. The first stage of the analog processing chain is a differential receiver for the input signals which converts the signals to single-ended and amplifies them by a factor of 3. The signals then go through a novel delay-less constant-fraction discriminator to eliminate small-signal slew. Synchronization is obtained in stages through a series of programmable delays and multiplexers that allow the operator to select the optimal clock phase for each channel (by delaying the clock and not the channel we can exchange delay lines for multiplexers, greatly reducing the cost of the system). With this scheme we can synchronize all channels if the following two restrictions are met:

- 1) all signals coming into a ROC must arrive within one RHIC cycle (106 ns).
- 2) the earliest signals into all ROC's must arrive within one RHIC cycle.

Each MuID ROC sends 96 bits of data to the Local Level One (LVL1) trigger system where an algorithm is implemented to determine if there are candidate muon tracks in the event. The algorithm finds roads pointing towards the vertex. It allows missed gaps along the road and phrases its requirements in terms of the number of deep or shallow roads in each orientation. The algorithm is "steerable" from gap to gap, meaning that the roads can vector based on the hit pattern in the two preceding gaps. The LVL1 trigger efficiency is a function of rapidity over almost the entire acceptance.

Both the Muon Trackers and muon identifiers have been taking data since 2002 fall. Most design requirements have been satisfied. Figure 2.5 shows the mass peak of J/Ψ from deuteron gold collision in run3.

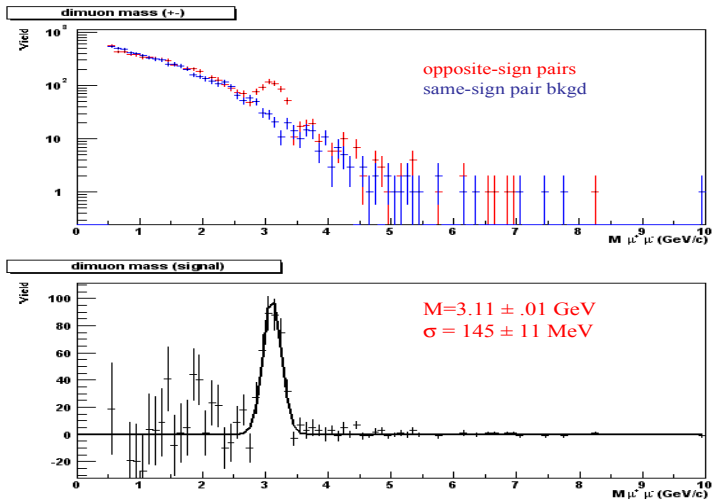

Figure 2.5: Invariant Mass distributions for di-muon system in dAu collisions.

2.3 Data Acquisition system and offline reconstruction

2.3.1 Data Acquisition [47]

The PHENIX DAQ system is designed to be able to take data for a variety of collision system and collision rate. Figure 2.6 shows the collision systems and rates our DAQ has to face. In order to keep up with the highest RHIC collision rate and in the mean time to select rare events from high background, the PHENIX On-Line system has two levels of triggering denoted as LVL1 and LVL2. The LVL1 trigger is fully pipelined, therefore the On-Line system is free of deadtime through LVL1. The LVL1 trigger and lower levels of the readout are clock- driven by bunch-crossing signals from the 9.4 MHz RHIC clock. The higher levels of readout and the LVL2 trigger are data-driven where the results of triggering and data processing propagate to the next higher level only after processing of a given event is completed.

To avoid the dependence between detectors in data taking, the whole online system is divided into small granules. One granule is a mini DAQ which can be operated without requiring any other detector in working status. In general, one detector own

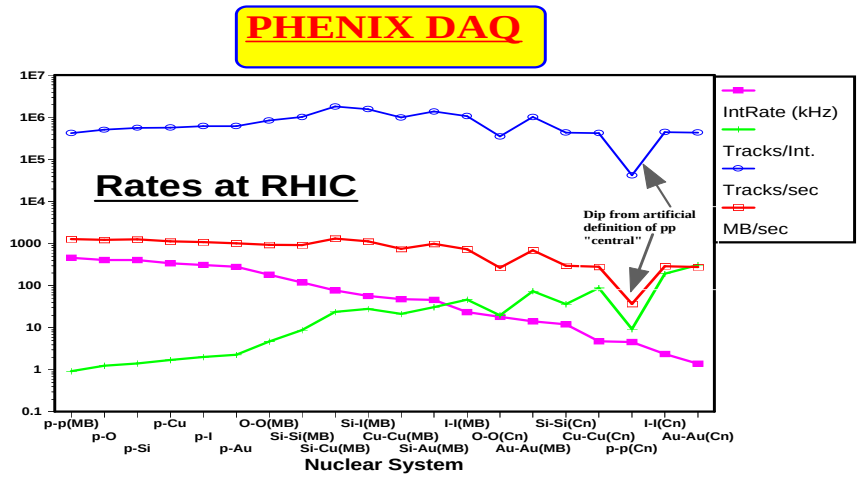

Figure 2.6: The relations between colliding system, data rate and data sizes. The data is given for PHENIX design luminosity.

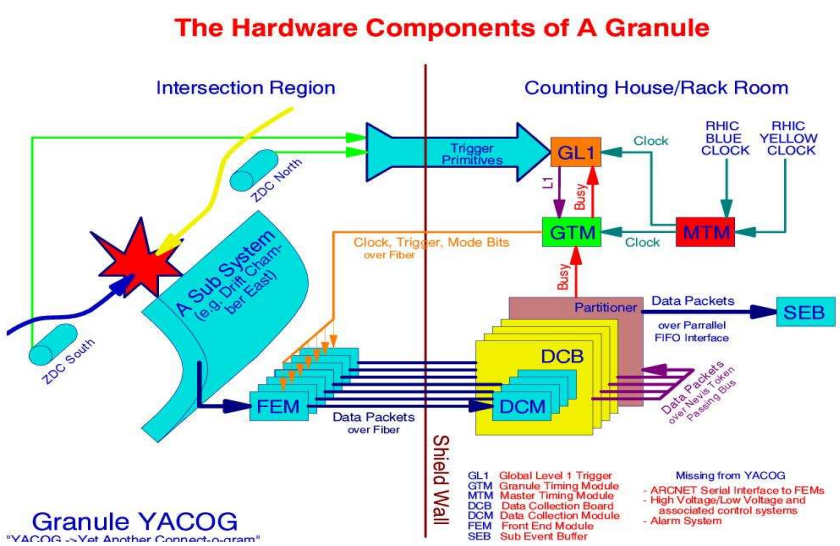

Figure 2.7: The schematic of one granule.

one or more granules. The general schematic for one granule is shown in Figure 2.7. Signals from the various PHENIX subsystems are processed by Front End Electronics (FEE) that convert detector signals into digital event fragments. This involves analog signal processing with amplification and shaping to ex- tract the optimum time and/or amplitude information, development of trigger input data and buffering to allow time for data processing by the LVL1 trigger and digitization. This is carried out for all detector elements at every beam crossing synchronously with the RHIC beam clock. The timing signal is a harmonic of the RHIC beam clock and is distributed to the FEM's by the PHENIX Master Timing System (MTS). The LVL1 trigger provides a fast filter for discarding empty beam crossings and uninteresting events before the data is fully digitized. It operates in a synchronous pipelined mode, generates a decision every 106 ns and has an adjustable latency of some 40 beam crossings. Once an event is accepted the data fragments from the FEM's and primitives from the LVL1 trigger move in parallel to the Data Collection Modules (DCM). The PHENIX architecture was designed so that all detector specific electronics end with the FEM's, so that there is a single set of DCM's that communicate with the rest of the DAQ system. The only connection between the Interaction Region (IR) where the FEM's are located and the Counting House where the DCM's are located is by fiber-optic cable. The DCM's perform zero suppression, error checking and data reformatting. Many parallel data streams from the DCM's are sent to the Event Builder (EvB). The EvB performs the final stage of event assembly and provides an environment for the LVL2 trigger to operate. In order to study the rare events for which PHENIX was designed, it is necessary to further reduce the number of accepted events by at least a factor of six. This selection is carried out by the LVL2 triggers while the events are being assembled in the Assembly and Trigger Processors (ATP) in the EvB. The EvB then sends the accepted events to the PHENIX On-line Control System (ONCS) for logging and monitoring. The data is first stored in four local hard disk, later on it is transferred to tapes. The technology used to control the many components that must work

together to successfully accumulate the data is the Common Object Request Broker Architecture (CORBA) system. CORBA makes it possible to transparently access objects on remote computers of various types throughout the network. The main control process called Run Control (RC) accesses and communicates with remote objects which in turn control a given piece of hardware. The RC process determines the configuration of the whole DAQ front-end.

2.3.2 Data reduction

One big part of the data reconstruction is to reduced the data volume. The data is first stored as PHENIX Raw Data Format(PRDF). Basically, PRDF files contain the raw detector output such as the ADC or TDC values. In PHENIX offline there are general three steps in reconstruction, first the raw outputs from the detector are calibrated and transferred into physics quantities such as time of flight, energy deposit, etc. In general, we only need to go through this step once for all. Then we need to run reconstruction softwares to look for tracks or particles in the data. The step may be repeated many times but not like every day. After step one and two, a new set of files is generated and it is called "DST". The DST file is still fairly big. The data size needs to be further reduced. In the third step, the DST file is filtered by trigger information for different physics. The filtered file contains only the track level information and only for a special interested physics. This file is called "NanoDst". The size for NanoDst is very small, people can run it in daily bases.

2.3.3 Muon arm event reconstruction

The muon tracker reconstruction for run3 dAu collisions has the following steps,

- calibrate the strip charges. For each strip, there are four charge samples read out. The total charge on one strip is obtain by fitting the four samples with a Landau distribution.

- clustering the adjacent strips into a strip cluster. Where the track which causes the strips firing pass through the cathode plane is determined by a Mathieson distribution. A one dimension coordinate is calculated. By associating two 1D coordinates from perpendicular and stereo planes in addition to the z coordinate of the gap, one can determine a 3D space point at which the track pass through the cathode strip chamber.

- pattern recognition. Find all the 3D space point for one track, ideally there should be 8, six from the first two station and two from last station.

- fit the whole track with Kalman filter in the muon magnet field.

- correct the energy loss in the absorber by using GEANT simulation.

. The MuID reconstruction is much simpler since the Iarocci tubes only gives 0/1 digital signal and the MuID track(road) is just a straight line(no magnet field in MuID). One only needs to line up all the fired two-packs to form straight tracks. When the occupancy is high, MuID track can be helpful for the pattern recongnization. One can point a road back to MuTr station 3 and look for track candidates. For run3 data analysis, this is not necessary.

The reconstruction software modules can be grouped into four general categories: low level modules for generating coordinates from raw detector signals, pattern recognition or the association of coordinates with track candidates, momentum and vertex reconstruction, and simulation and evaluation modules. The outputs of each reconstruction stage are put in so-called interface objects, such as strip clusters, tracks, etc. The container of the interface objects are STL maps. The whole architecture of the software is designed such that each stage of the reconstruction is granulated and the infra-structure is separated from user. For the consistency in the evaluation, the processes of simulation data and the real data go through exactly the same event loop. The usage of STL maps as containers of the interface objects has the advantage in organizing the objects at different reconstruction stages. For example, a track object can be associated with the strips which are fired when the

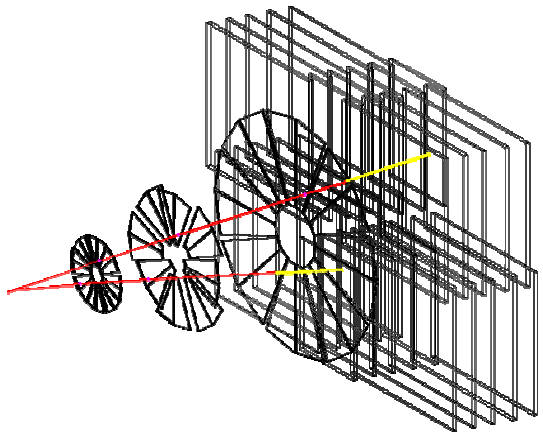

Figure 2.8: A simulated J/Ψ event in the detector.

track pass through the detector by associating the map index(key) of the track with the map index of the strips. The event display is also implemented for evaluation purpose. Figure 2.8 shows a $J\Psi$ events in the detector.

Chapter 3

Nuclear modification in dAu collisions

In this chapter, we present the analysis from PHENIX [41] on the ratios between hadron yields which were measured at forward and backward pseudo-rapidities η for different centrality(impact parameter) classes of deuteron gold interactions at $\sqrt{s_{NN}} = 200$ GeV .

3.1 Selection of Hadrons from the PHENIX Muon arms

3.1.1 PHENIX Muon arms

PHENIX has two spectrometers designed for measuring muon production over the pseudo-rapidity range $-2.2 < \eta < -1.2$(backward direction) and $1.2 < \eta < 2.4$(forward direction). [48]. Inside the spectrometers acceptance, hadrons with $p_T > 1.0 GeV/c$, if produced via semi-hard scattering of quark-gluon, are sensitive to the partonic structure of gold nuclei at x $\sim 0.004 - 0.06$ at forward η coverage or at x ~ 0.13 at backward η coverage. The spectrometers start with a thick hadron absorber comprising 60cm of low-carbon steel and 20cm of brass [44] between the collision point and active detectors along the beam axis, primarily to reduce hadronic background. After the absorber there is the Muon Tracking Detector(MuTr) which consists of three stations of cathode strip chambers and tracks charged particles

in a magnetic field. Following the muon magnet backplate(30cm steel), there is a muon identifier (MuID), which has 5 gaps per arm filled with planes of transversely oriented Iarocci tubes, interleaved with layers of steel (10cm thick in first two layers and 20cm thick for the rest two.) The MuID is used to confirm muon identification and provide fast triggering capabilities.

In order to get the vertex momentum, the track momentum measured by the MuTr is corrected for the energy loss resulted from Bethe-Bloch ionization energy loss when the track passes through the absorber. The correction is done via GEANT simulation for a given particle species. Although we do not have particle identification information from MuTr, luckily, at the energy range($1 - 100GeV/c$) we are interested, the Bethe-Bloch ionization energy loss varies very slowly with $\beta\gamma$[49], this also means the Bethe-Bloch energy loss differences between different particle species are also very small under the assumption $p_{tot} >> mass$ and this assumption is true in our case where we mostly measure pions, koans and muons with $P_{tot} > 3GeV/c$. In reality, we calculated the energy loss correction by assuming that all tracks are muons. For the Monte Carlo pions, kaons and muons, we evaluated the uncertainty raised by this approach via checking differences between the vertex momentum calculated with correct particle mass and that calculated with muon mass. The uncertainties are 1% and 5% for pions and kaons, respectively. Fig 3.1 demonstrates this point, what is plotted on Fig 3.1 is the distribution of $\frac{(p_T^{pid} - p_T^{\mu})}{p_T^{\mu}}$, where p_T^{pid} is the transverse momentum at vertex calculated with the correct mass of the particle and p_T^{μ} is the transverse momentum at vertex calculated with muon mass.

3.1.2 Select hadrons by matching track momentum and depth in MUID

Although the PHENIX Muon spectrometers were designed to detect muons, they can also be used to measure charged hadrons. Compared to muons at the same momenta, hadrons have smaller penetration power. Muons lose their energy when

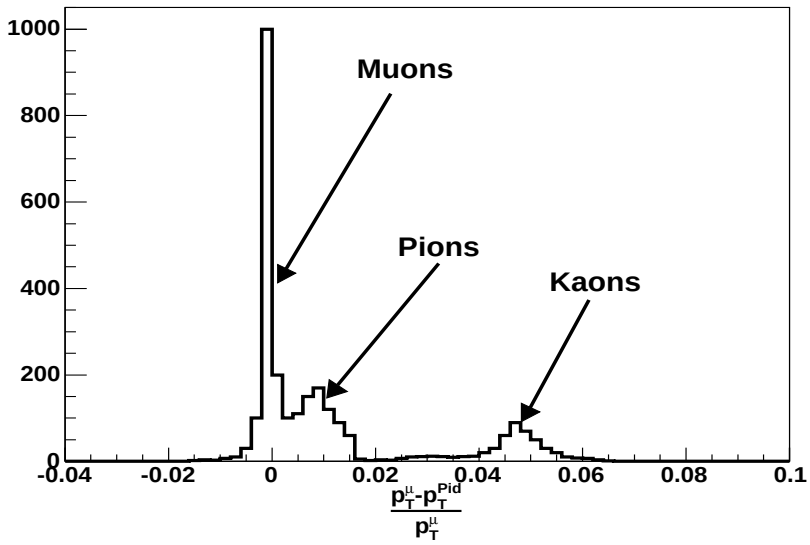

Figure 3.1: $\frac{p_T^\mu - p_T^{pid}}{p_T^\mu}$, the peak at zero is for muons, the small bump around 0.01 is for pions and the other bump at 0.05 is for koans.

passing through materials via Bethe-Bloch ionization energy loss. Hadrons suffer the same kind of energy loss, but they also have hadronic interactions that substantially reduce their ability to penetrate. In other words, a muon can go much deeper in MuID than a hadron at the same momentum. Fig. 3.2 shows the momentum distribution for muons and hadrons stopping at different MUID gaps from a GEANT simulation [51]. One can see that in general hadron has to be much more energetic to reach the same MUID gaps as muons. Also the momenta for the stopped muons are very well defined in the sense that the momentum distribution is a very narrow Gaussian shape.

Thus, hadron identification can be achieved by selecting tracks with higher momenta but only reaching shallow layers of MUID. Fig. 3.3 panel A shows the vertex momentum distribution of shallow tracks(only reaching the shallow MuID gaps, i.e the third and fourth gap) from real data. Two components are seen on both curves. A peak corresponds to the stopped muons and a long tail corresponds to stopped hadrons. The positions of the peaks are confirmed from MC simulation as shown in panel A of Fig. 3.2.

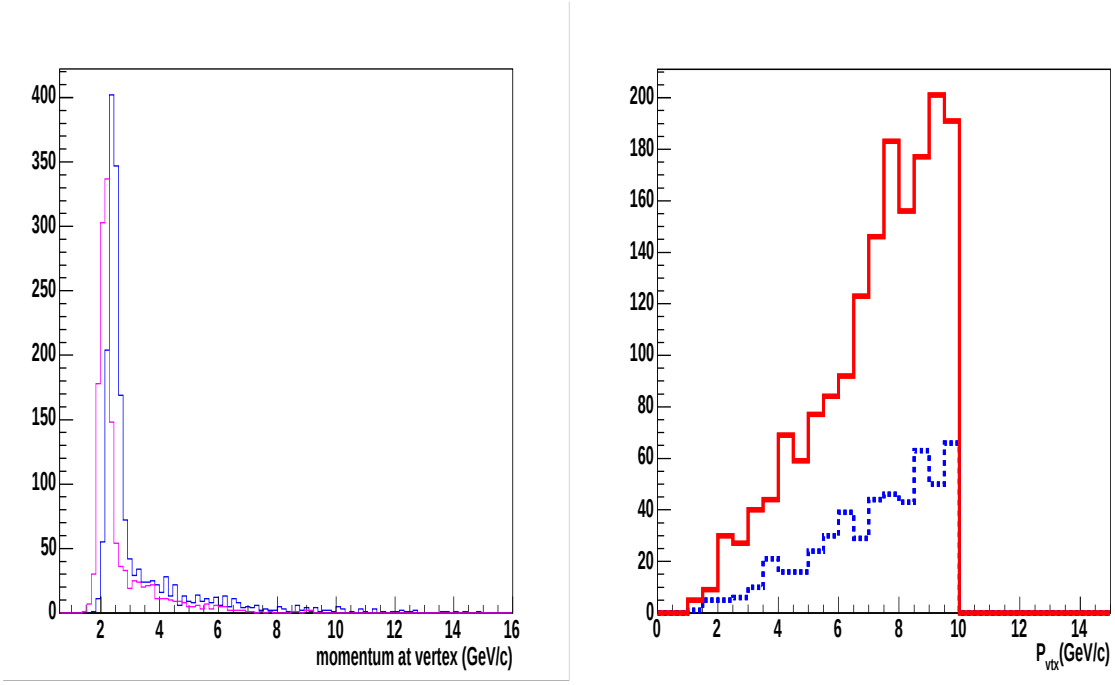

(a) (b)

Figure 3.2: panel a : depth and vertex momentum for MC muons stop at different MuID gap, purple line is for tracks stop at gap2 and blue is for tracks stop at gap3. panel b: depth and vertex momentum for MC hadrons stop at gap2(red) and gap3(blue)

In fact, the vertex momentum of a track is not a direct measurement, as we discussed before. So in the data analysis, we used the momentum measured at muon tracker station one, which is the momentum before energy loss correction. Fig. 3.3 panel B shows the uncorrected momentum distribution of shallow tracks. Here uncorrected track momentum means the momentum without energy loss correction. The distribution for tracks stopping at the fourth gap shows two components: a sharp peak around $P_{tot} = 1.2$ GeV/c and a longer tail of the stopped hadrons. The distribution of tracks stopping at third gap shows the same features, but the peak is around $P_{tot} = 1.0$ GeV/c. Both peak positions are confirmed to be stopped muons by a GEANT simulation. Thus, we select hadrons by cutting out the low momentum muons with a momentum cut $p_{total} > 1.8$ GeV/c, which is more than $3 \times \sigma$ away from the stopped muon peaks, and a MUID depth cut $depth = 2$ or 3.

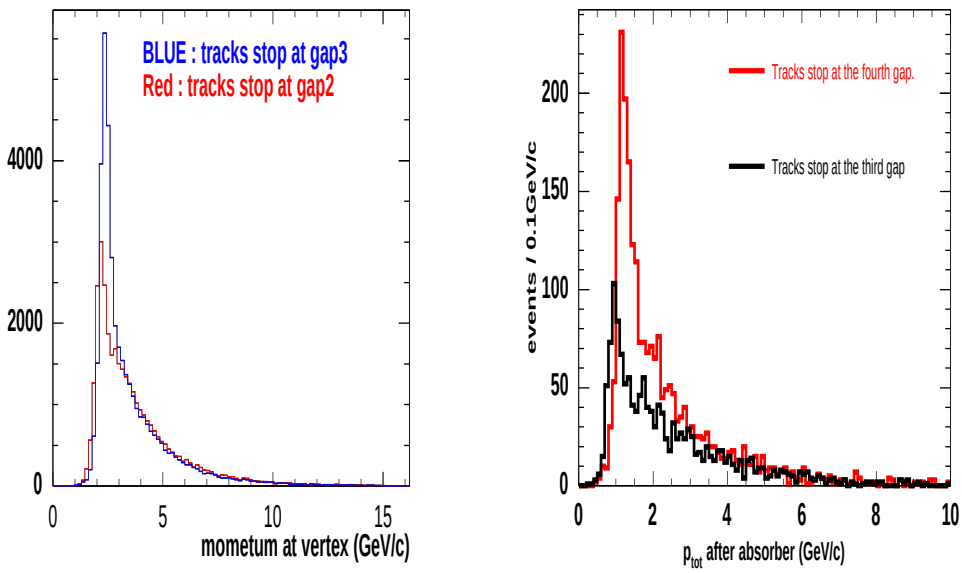

(a) (b)

Figure 3.3: panel a : depth and vertex momentum for tracks stop at different MuID gap, red line is for tracks stop at gap2 and blue is for tracks stop at gap3. panel b: depth and station1 momentum for tracks stop at gap2(red) and gap3(blue)

3.1.3 Muon contamination

In the methods we use to select hadron, there are two sources where a muon can be mis-identified as a hadron,

- muons in the high momentum tail as shown in panel a of Fig 3.2.
- Deep muons can be reconstructed as shallow tracks due to the inefficiency of the muon identifier detector.

So, the number of hadrons in our samples $N_h = N_h^{true} + N_\mu^{true} \times \varepsilon_h^m$, where N_h^{true} and N_μ^{true} are the true numbers of hadrons and muons in the detector, ε_h^μ is the probability of a muon is mis-identified as a hadron due to above two reasons and it can be calculated from simulation as long as we have the detector real efficiency and geometry implemented. But the difficulty is how to estimate the ratio $\frac{N_h^{true}}{N_\mu^{true}}$. In the first order, we assume that all muons we detect in the detector are from light meson

decays, i.e. kaons and pions. Therefore we can use Monte Carlo single kaon events to study both sources of the muon contamination. We generated single kaons into our detector and the koans will decay into muons or punch through the absorbers. The ratio $\frac{N_h^{true}}{N_\mu^{true}}$ is naturally fixed by the probabilities of decay and punch-through of kaons. By applying the hadron selection criteria to the decay muons, then counting how many decay muons were misidentified as hadrons, we can actually calculate ε_h^m. The first source of contamination is built in the GEANT simulation and the tracking software. The second source is simulated by assigning a realistic MUID two-pack efficiency to each two-pack according to the run averaged MUID HV status, we will discuss more about how to generate the two-pack efficiency in the "result" section. The muon contamination is determined by this study to be less than 4% in $4.0 > p_T > 0.5 GeV/c$ momentum range.

As we mentioned, there are absorbers before each muon arms to reduce hadronic background. Most pions and kaons produced at collision vertex are stopped at absorber, but some of them may decay to muon before they hit into absorbers, and others just punch through the absorber. Since both pions and kaons have long life time, they will fly a distance before the decay happens. If pions/kaons decay to muon before they get into absorber, the detector will see the muons. Thus the probability of a decay muon being detected is dependent on the collision vertex. The further a collision is from the absorber, the more likely we see a decay muon in the detector. This vertex dependence of decay muon events can be utilized by us for checking how well we can reject muons by the hadron selection method. Panel A of Fig 3.4 shows the normalized collision vertex distribution for the events where tracks are measured in south muon arm. This vertex dependence provides us a way to check the method we used to select hadrons. Panel B of Fig 3.4 shows the vertex distribution for the events in which we find punch-through hadrons from south muon arm. We can clearly see that decay muon are taken out by applying hadron cuts.

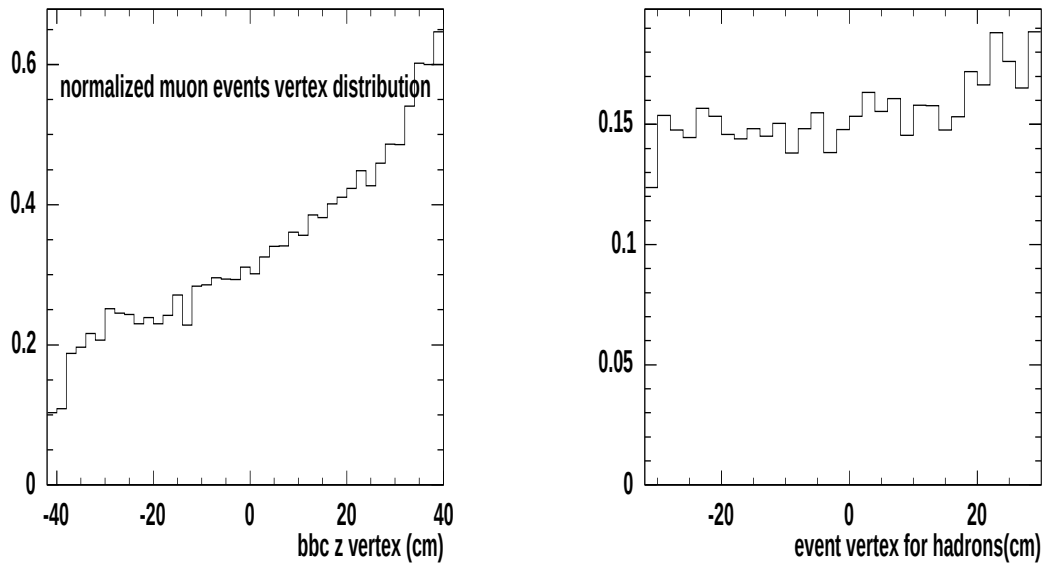

(a) (b)

Figure 3.4: normalized BBC vertex distribution for muons events(a) and hadron events(b). South muon arm is in negative z direction.

3.1.4 Background from secondary particles produced by hadronic showering in the absorber

Another source of background is the secondary particles produced from hadronic showering in the absorber. For a hadron produced at collision vertex, there are three ways that it can result in a measured track in the muon tracker.

- Decay into a muon before absorber, then the muon is measured in muon tracker, it is called hadron-decay-muons.
- All the way Bethe-Bloch dE/dx through absorber, then measured in muon tracker. We call them punch-through hadrons
- Produce hadronic showers in absorber, then the secondary particles from the showers are measured in muon tracker.

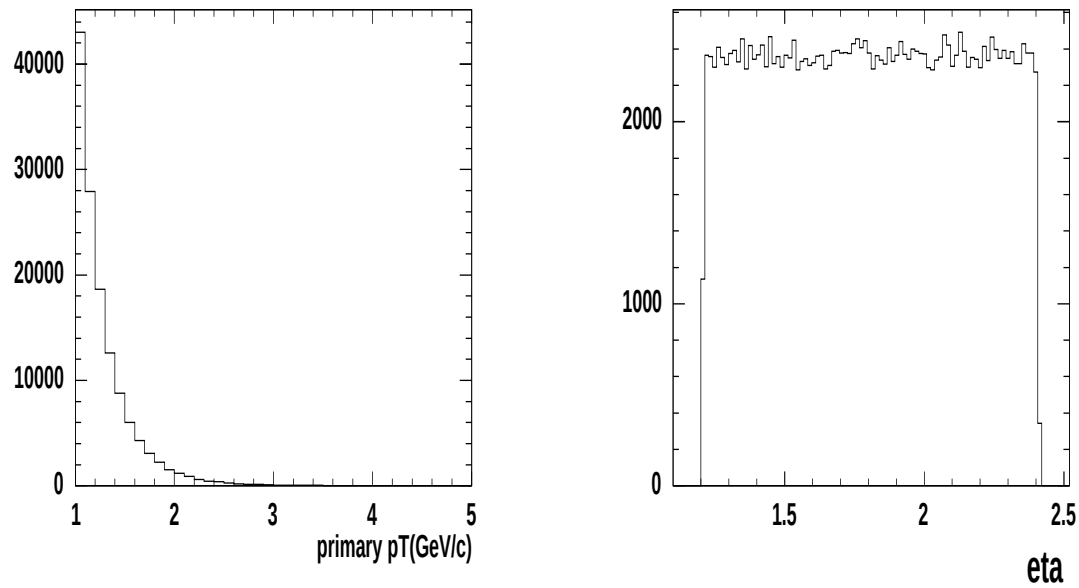

Figure 3.5: Panel a : the input p_T spectrum. Panel b : input pseudorapidity distribution

After the hadron selection as described in last two sections, only the punch-through hadrons and secondary hadrons are left.

To study secondary particle, we did single pion simulation with PISA, a PHENIX detector simulator based on GEANT. For input to the simulation, we used a parameterized power-law spectrum for transverse momentum and a flat pseudo-rapidity distribution. The parameters for this power-law input are taken from the PHENIX π^0 measurement in run3 dAu data at mid-rapidity and are listed below,

- $A = 6.411873e + 01 \pm 3.985085e + 00$
- $p^0 = 1.2200 \pm 0.0000$
- $n = 9.8562 \pm 0.0448$

. Fig 3.5 shows the input transverse momentum and the pseudo-rapidity distribution.

For primary hadrons, their energy loss in absorber can be recovered by using GEANT simulation with a given particle species. For secondary particles, since they

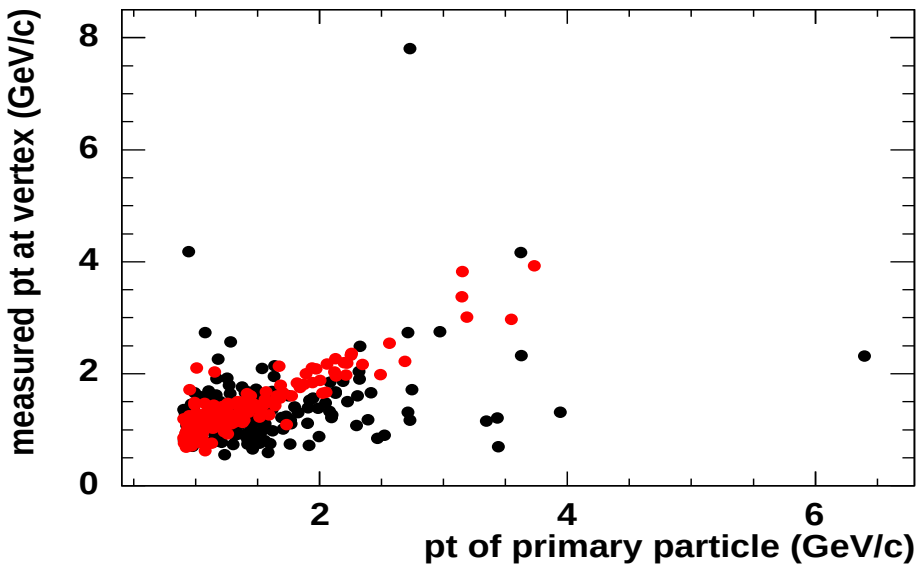

Figure 3.6: transverse momentum measured by detector and transverse momentum of primary particle which is given by the truth information from simulation, red dots are for primary particle dE/dx through absorber, black dots are for secondary particles.

are produced from hadronic showers, they can have a very different momenta from their primary particles, thus they will modify the spectrum produced at collision vertices, which is what we indeed want to measure. Fig 3.6 shows Monte Carlo simulation of the correlation between the transverse momentum we measured for a track and the transverse momentum we generated at vertex. The Black dots are for secondary particles and the red dots are for primary hadrons, which suffer ionization energy loss through absorber, i.e. dE/dx through.

When particle dE/dx through the absorber, the interaction between the particle and media is mainly elastic scattering on electrons, the direction of the particle changes very little. On the other hand, hadronic showers happen when the incoming particle scatters on a nucleus inelastically, the direction of secondary particle can be very different from the primary particle. This could potentially give us some handles on separating secondary particles. Since there is no momentum measurement before absorber, we use collision vertex(measured by the PHENIX BBC) and

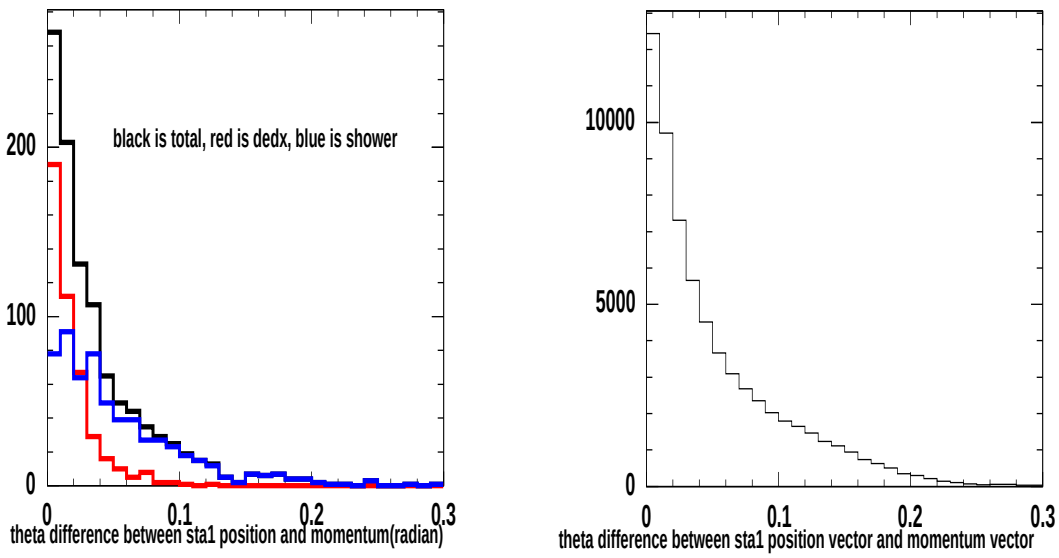

Figure 3.7: panel a: polar angel difference between primary vector and measured momentum vector, dedx through (red curve) and hadronic shower(blue) and total : black; Panel b : polar angel difference between primary vector and measured momentum vector for real data

the first measurement point in muon tracker to construct a vector. This vector, to some extents, represents the direction of the momentum of the primary particle at produced at vertex and we call it **primary vector**. Panel a of Fig 3.7 shows distribution of the polar angle difference between primary vector and momentum vector measured inside the MuTr. The red curve represents punch-through hadrons and it has a narrow peak around zero. The blue curve represents secondary particles and it has a very wide distribution. The black curve represents the sum of these two distributions. Panel b of Fig 3.7 shows the distribution of the same quantity from real data. The nice thing is that the distribution from simulation(black curve in panel a) reproduces the shape of distribution from real data(panel b), therefore it can be serve as a good analysis cut to get ride of secondary particle. We define it as θ_{xp}. From Fig 3.7, we can see that by applying $\theta_{xp} < 0.03$ radians, we can cut off most secondary particles.

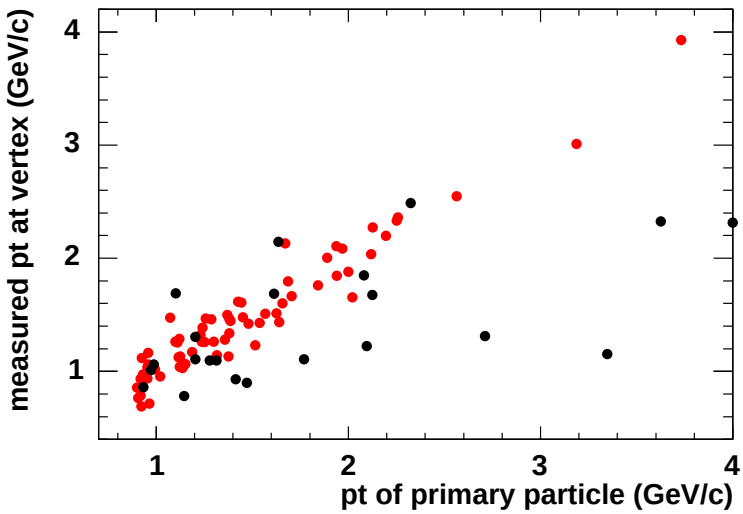

Figure 3.8: transverse momentum measured at vertex and transverse momentum of primary particle after cut, red dots are for primary particle de/dx through absorber, black dots are for secondary particles.

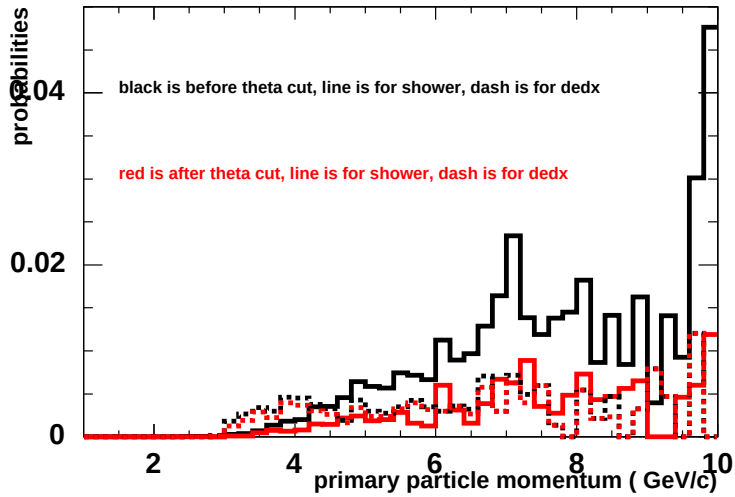

Figure 3.9: the probability for a primary particle produce a hadron shower(solid line) or just dEdx through absorber(dashed line) as a function of primary particle momentum. Black lines are probabilities without $\theta_{xp} < 0.03$ cut. Red lines are probabilities with $\theta_{xp} < 0.03$ cut

Now we can go back to check how this θ_{xp} cut affects our p_T measurement. Fig 3.8 shows the correlation between generated vertex momentum and measured transverse momentum after we applied this cut. Now we see very nice correlation between these two. In fact, the usefulness of this cut is twofold. First it really reduces the number of secondary particles, as we see from Fig 3.7 and from later part of this section. Second, the secondary particles surviving from this cut are those which are very close with their primary particles in phase space, this point will be seen in the later part of this section.

Also we checked the probability for a primary particle produce a hadron shower or just dEdx through absorber as a function of total momentum of primary particles. This is summarized by Fig 3.9. The probability of producing hadronic showers and later being seen by MuTr was significantly reduced by the $\theta_{xp} < 0.03$ cut, in the mean time the probability of punch-through was not affected much. Fig 3.10 shows the ratio between number of shower particles and number of punch-through particles in different p_T bins. Again the cut brings the ratio down by a factor of ~ 2.

Although the phase space distortion from secondary particle brings a lot of uncertainties in our vertex momentum measurement, things are not that bad because if one looks at Fig 3.8, one can realize that those secondary particles which pass the θ_{xp} cut may be very close to their primary particles in phase space, we have mention this point early in this section. Now let's take a close look at this. As we know from energy conservation, almost all the secondary particles have less transverse momenta than their primary particles do. This fact can also been seen from Fig 3.8. $\delta p_T = p_T^{primary} - p_T^{measured}$ defines the distortion in phase space, where $p_T^{primary}$ is the transverse momentum for primary particle we generated at vertex in our simulation and $p_T^{measured}$ is what we measured for a track which may either be from the hadronic shower produced by it's primary particle or simply be a punch-through hadron. Then by plotting the $p_T^{primary}$ distribution in a given $p_T^{measured}$ bin, we can see how large the distortion is. The plots are shown as Fig 3.11. In the meantime, the tracking software we are using gives $\sigma \sim 14\% \times p_T$ transverse momentum reso-

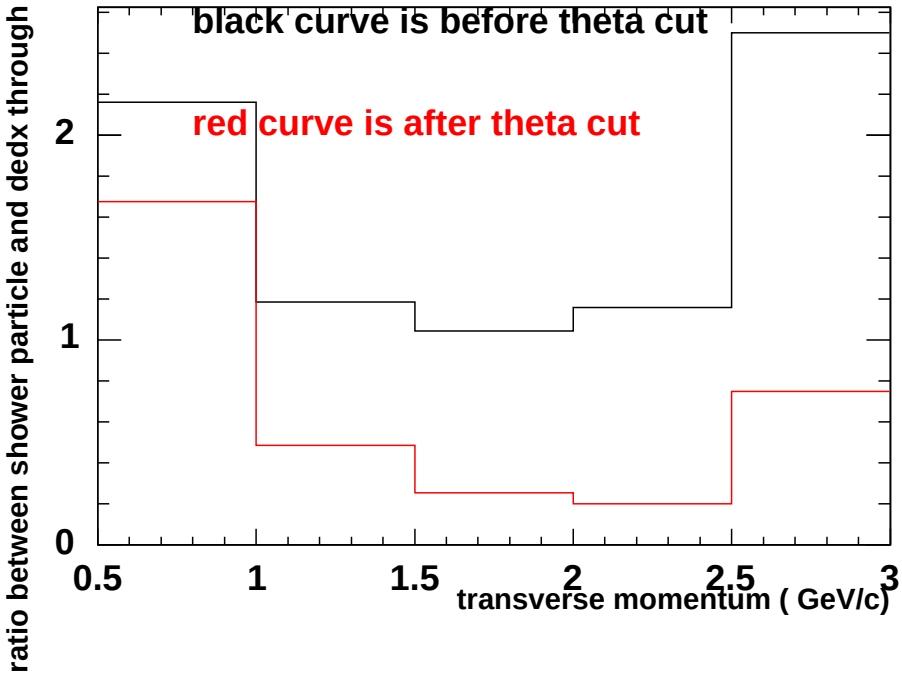

Figure 3.10: ratio between number of shower particles and number of punch-through particles as a function of measured transverse momentum at vertex

lution. For each above momentum bins, We can define high p_T background based on the momentum resolution. If in a measured transverse momentum bin, the true transverse momentum of a track is $3 \times \sigma$ larger than the up boundary of the bin, we regard this track as high p_T backgrounds. Otherwise it would be regarded as signal. Fig 3.12 shows the ratio between high p_T backgrounds to signals in each measured transverse momentum bin. Again, we see the ratio is reduced a lot by the θ_{xp} cut. The ratio of high p_T backgrounds from secondary particles to signals varies as a function of p_T and is typically around $1 - 5\%$ for $1 < p_T < 2.5 GeV/c$. For $4.0 GeV/c > p_T > 2.5 GeV/c$, the ratio is zero within the statistics we used for this study.

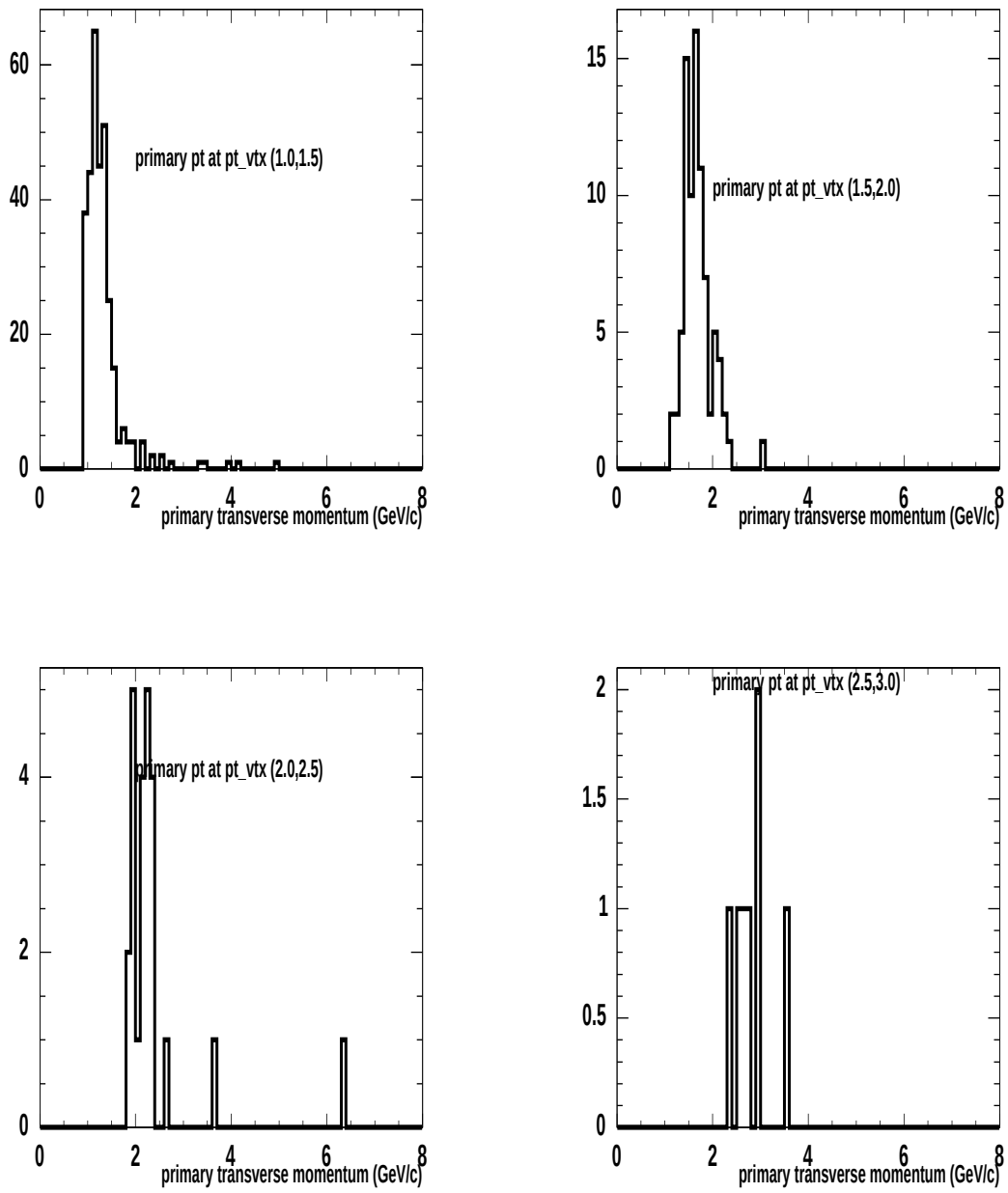

Figure 3.11: primary transverse momentum distribution in different measured vertex momentum bins

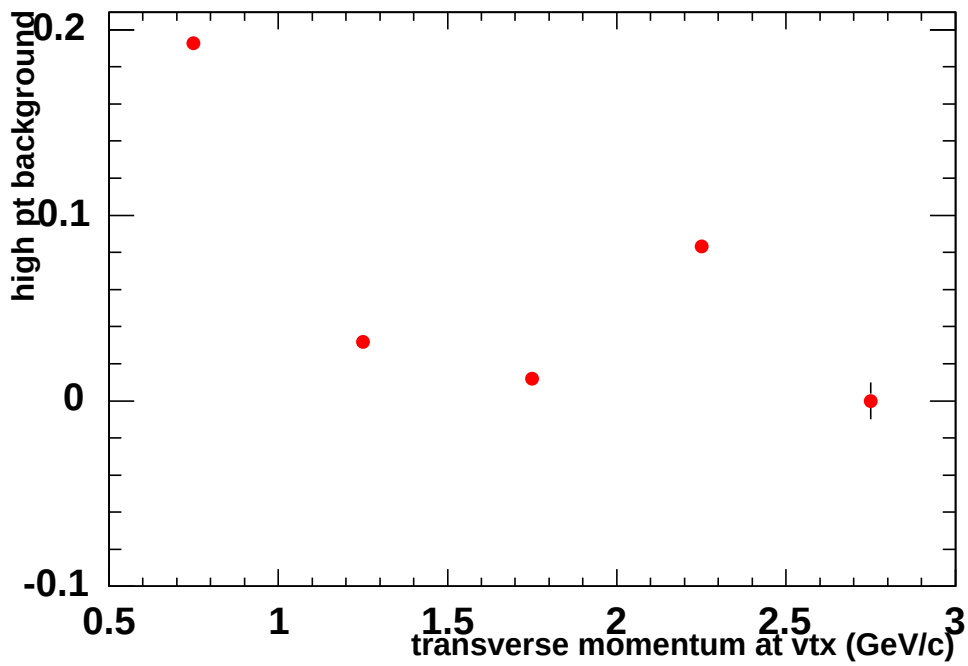

Figure 3.12: ratio of this high p_T background to signals as a function of measured vertex momentum

3.1.5 Fiducial cut to reduce detector edge effect and beam gas

Both of the PHENIX Muon spectrometers are in the pseudo-rapidity range close to the beam rapidity. Especially the first station of each arm is very close to beam pipe. For example the inner part of station1 south muon arm is only $20 \sim 50cm$ away from beam pipes. Thus the beam gas can produce relatively high occupancy in the inner part of the detector. Fig 3.13 and Fig 3.14 show the variation of the occupancy with x and y coordinates in the backward(south) muon spectrometer and forward(north) muon spectrometer, respectively. One can notice that at small $\sqrt{x^2+y^2}$ area of the first station of each spectrometer the occupancy is higher than the rest areas. But for the other two stations the occupancy is much more uniform with x and y. This is because they are far from the beam pipes. To get ride of

the beam gas, we required that the pseudorapidity of each track has to be larger than -2.0 in backward muon spectrometer and smaller than 2.2 in forward muon spectrometer.

On the other hand, in the hadron selections, we required that the vertex momentum of a hadron has to be larger than $3.1GeV/c$, which is equivalent to applying an low p_T cut in each pseudo-rapidity bins. This point can be seen clearly in Fig 3.15. Thus, if we want to have an uniform acceptance for tracks with $p_T > p_T^{min}$, we have to apply a cut-off point in pseudo-rapidity. For this analysis we optimize our acceptance for $p_T^{min} = 1.5GeV/c$, which corresponds a cut-off of $\mid \eta \mid > 1.4$.

3.1.6 Summary on cuts for selecting hadrons

Here is a summary of all the cuts we used so far to select hadrons,

- χ^2 per degree of freedom less than 20.
- Momentum measured at station one $p_{tot}^{sta1} > 1.8GeV/c$.
- Depth in MuID equals to 2 or 3.
- $-1.4 > \eta > -2.0$ for tracks measured in the backward muon spectrometer, $2.2 > \eta > 1.4$ for tracks measured in forward muon spectrometer.
- BBC vertex $\mid z_{vtx} \mid < 28$ cm

3.2 Ratio between hadron yield in central collisions and hadron yield in peripheral collisions

3.2.1 Define the nuclear modification factor R_{cp}

In proton nucleus reactions, the nuclear modification factor has always quantified as the ratio between the cross-section for a certain process measured in pA collisions and the corresponding cross-section measured in proton proton(deuteron) collisions scaled up by A, the mass number of the nucleus. This ratio, itself, often is called

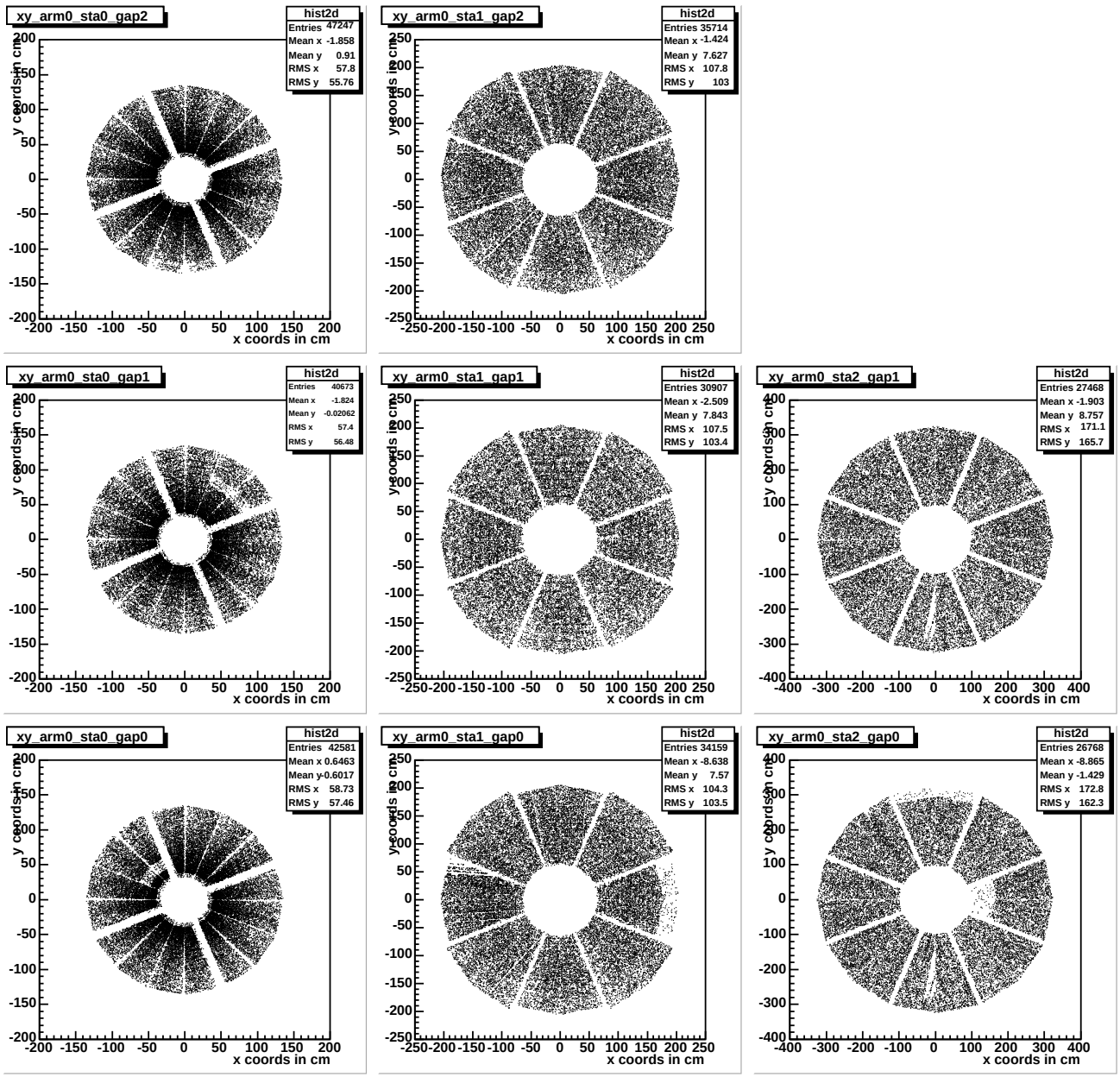

Figure 3.13: Occupancy as a function of x and y coordinates at different gaps for each station of backward muon spectrometer.

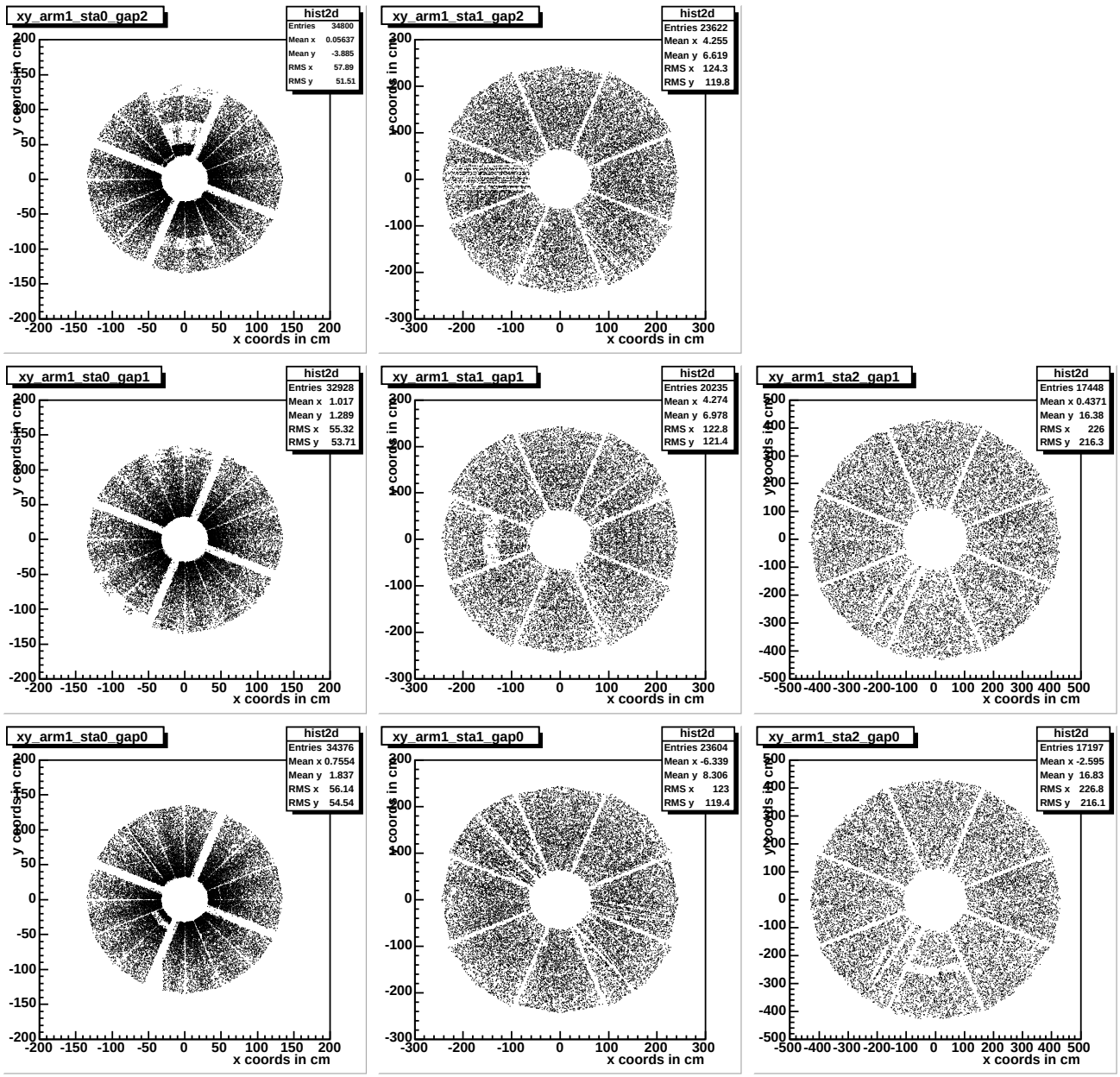

Figure 3.14: Occupancy as a function of x and y coordinates at different gaps for each station of forward muon spectrometer.

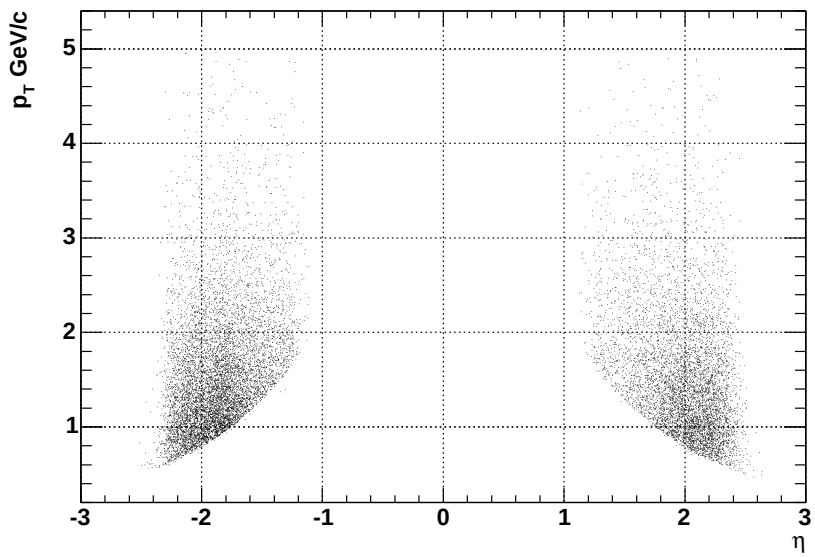

Figure 3.15: Correlation between p_T and η

the nuclear modification factor . But some time, the measurement in proton proton collisions is not always available or the measurement on absolute yield or cross-section is too difficult to be achieved. Then alternatively, one can try to divide the whole pA event sample into different event classes, each event class corresponds to a range of the impact parameters of collisions. Thus under the assumption that the most peripheral event class(largest impact parameter event class) behaves like pp collisions, we can measure the nuclear modification by comparing the relative yields in central event classes with the relative yield in the most peripheral bin.

The probability of hadrons to punch through the absorber is $\sim 10^{-3} - 10^{-4}$, which is mostly determined by the inelastic scattering cross-sections between the incoming hadrons and the nucleons in the absorber. Fig 3.16 shows the total cross-section between different hadrons with protons. From the plot, we can see that, from $3GeV/c \sim 20\text{GeV}/c$ which is the momentum range we are interested, the cross-sections are relatively constant. However, the plot also shows large variations in the cross-sections for different hadrons at that momentum range. The particle species dependence of the cross-sections makes the measurement of the absolute

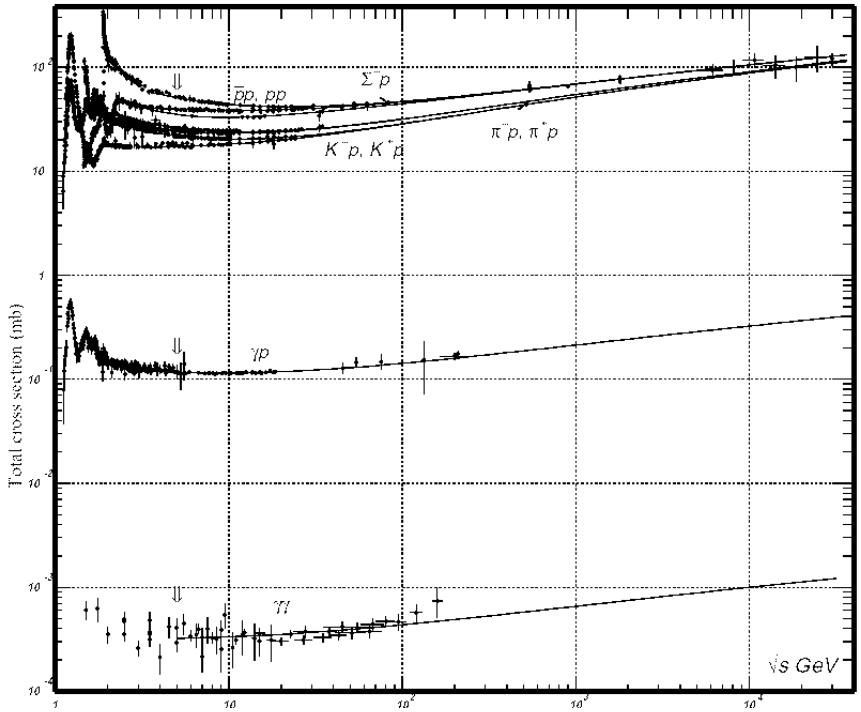

Figure 3.16: Cross-sections between hadrons and protons [50].

charge particle yield heavily replying on the knowledge of particle composition. Unfortunately, there is no particle identification detectors in forward and backward rapidity at PHENIX. Currently, there is no available experimental results from other experiments too. But, for the purpose of measuring the nuclear modification effects, we can study how the ratios of the hadronic yields between different impact parameter classes of deuteron gold collisions varies with transverse momentum and pseudo-rapidity. We don't really need the absolute charge particle yields to calculate ratios. Most systematics related to acceptance, efficiencies are concealed out via the ratio. Further more, we will see in the following sections that the uncertainties from the particle compositions are also be reduced. Thus we can make a relatively clean measurement. The *nuclear modification factor* R_{cp} is then defined as the ratio of the particle yield in central collisions with the particle yield in peripheral collisions,

each normalized by number of nucleon nucleon inelastic scattering (N_{coll}):

$$R_{cp} = \frac{\left(\frac{dN}{d\sigma dp_T}\right)^{Central} / N_{coll}^{Central}}{\left(\frac{dN}{d\sigma dp_T}\right)^{Peripheral} / N_{coll}^{Peripheral}} \tag{3.1}$$

3.2.2 Centrality definition in deuteron gold collisions

In the deuteron gold collisions, PHENIX uses its south Beam Beam Counter(BBCS) to decide the event classes in term of centrality. BBCS locates at the gold nuclei going direction. The charge multiplicities seen by BBCS is proportional to the number of participants in the gold nuclei [52]. Fig 3.17 shows the distribution of the normalized charge measured by BBCS. BBC also serves as a minbias trigger detector, with a trigger requirement such as at least one tube is hit($BBC \geq 1$) on each side of BBC, the minbias trigger covers $(88 \pm 4)\%$ of total dAu inelastic cross-section. The distribution of normalized charge is divided into four areas. They correspond to centrality classes which represent certain percentiles of the total inelastic cross-section of dAu collisions, namely $0-20$, $20-40$, $40-60$ and $60-88$. The smaller of the percentile is, the smaller the impact parameter of the collision is.

The underlying idea of using south BBC measuring the centrality is summarized in PHENIX analysis note 210 [52] as the following,

- 1.) Number of hits seen by BBC south is proportional to the number of Au participants.

- 2.) Number of hits seen by BBC south obeys the statistics of Negative Binomial Distributions(NBD). Below is the formula for NBD.

$$P(n, \mu, k) = \frac{\Gamma(n+k)}{(\Gamma(k)n!)} \times \frac{(\mu/k)^n}{(1++\mu/k)^{n+k}}$$

  where k and μ are the NBD parameters, which are related to the width of the distribution σ as,

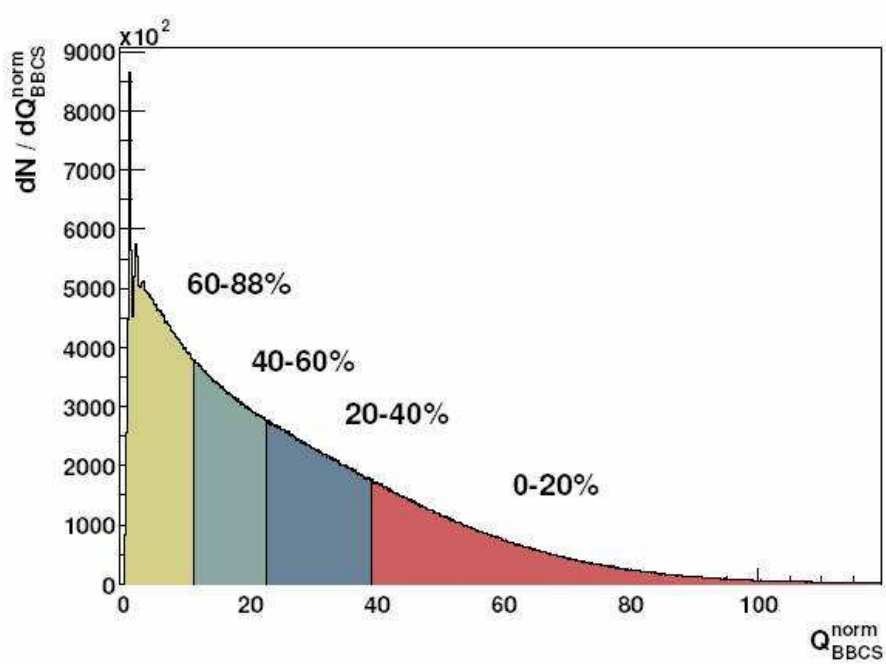

Figure 3.17: Distribution of the normalized charge in the BBCS. The normalization is done in a way that the normalized charge corresponds to the number of hits

$$(\frac{\sigma}{\mu})^2 = \frac{1}{k} + \frac{1}{\mu}$$

- Under assumption 1 and the assumption that every hit seen by BBC south are is correlated, both μ and k are proportional to the number of Au participants.

In the calculation, the distributions of the number of Au participants(N_{part}) and the number of binary collisions are taken from Glauber model [53]. By minimizing the difference between calculated distribution and the distribution from real data, one can actually determine the k and μ parameters when $N_{part} = 1$ for minbias events(BBCLL1 trigger selected).

In the collisions where the number of nucleon nucleon collisions is small, such as peripheral dAu collisions and pp collisions, the BBCS only accepts a part of the total cross-section, the particle yield of this part of the cross-section is generally higher than that averaging over the total cross-section. For example, in pp collisions, BBC only sees 50% of the total pp inelastic cross-section, but this half cross-section contains 75% all the π^0 produced in pp collisions. Thus, the measured π^0 yield by

Table 3.1: Number of binary collisions for each centrality classes.

centrality bin	N_{coll}	ratio to most peripheral bin	trigger bias
$0-20\%$	15.0 ± 1.0	4.6 ± 0.5	1.000 ± 0.0008
$20-40\%$	10.4 ± 0.7	3.2 ± 0.3	0.995 ± 0.003
$40-60\%$	6.9 ± 0.6	2.1 ± 0.1	0.974 ± 0.01
$60-88\%$	3.2 ± 0.3	1.0 ± 0.0	0.885 ± 0.04

the minbias trigger has to been corrected by a factor of $\frac{2}{3}$ to get the true π^0 yield of pp collisions. This fact is called trigger bias. One can calculate the trigger bias for each dAu centrality class by assuming that each centrality class of the dAu collisions corresponds to an ensemble of binary nucleon nucleon collisions [54]. The result is listed in the fourth column in Table 3.1.

The centrality and N_{coll} determined here do not take into account the correlation between the BBC south multiplicity and the underlying event category. This effect in fact is not small and will bring a centrality bias for high p_T events. In the next chapter we will study it in detail and a set of final correction factors on centrality bias will be given. Through this chapter, we are keeping the above centrality definition since the correction factor just scales up/down the results we get here.

3.2.3 Modification on particle composition from absorber

It has been discussed that the presence of the absorber will modify the particle composition due the difference of hadronic interaction cross-section of different particle species. Here, I will show a simple estimation about how much it may affect our R_{cp} measurement. In this estimation, we will only consider three particle species, namely pion, kaon and proton, then the R_{cp} before absorber can be written as,

$$R_{cp}\mid_{z=0} = \frac{Y_{\pi}^{cent}\mid_{z=0} + Y_{K}^{cent}\mid_{z=0} + Y_{P}^{cent}\mid_{z=0}}{Y_{\pi}^{peri}\mid_{z=0} + Y_{K}^{peri}\mid_{z=0} + Y_{P}^{peri}\mid_{z=0}} \tag{3.2}$$

. Where the $\mid_{z=0}$ indicates the value is evaluated at collision vertex(i.e. before absorber). Y_{π}^{cent} represents the yield of pions in the central collisions, the superscript (i.e. cent or peri) indicates the event classes and subscript indicates the particle

species. In the mean time, the R_{cp} of individual particle species can be written as,

$$R_{cp}^{\pi} \mid_{z=0} = \frac{Y_{\pi}^{cent} \mid_{z=0}}{Y_{\pi}^{peri} \mid_{z=0}} = \frac{Y_{\pi}^{cent} \mid_{z=0}}{Y_{\pi}^{peri} \mid_{z=0} + Y_{K}^{peri} \mid_{z=0} + Y_{P}^{peri} \mid_{z=0}} \times \frac{1}{R_{\pi}^{peri} \mid_{z=0}} \tag{3.3}$$

. Where $R_{\pi}^{peri} \mid_{z=0} = \frac{Y_{\pi}^{peri}|_{z=0}}{Y_{\pi}^{peri}|_{z=0} + Y_{K}^{peri}|_{z=0} + Y_{P}^{peri}|_{z=0}}$, is the ratio of pion yield to all charged particle yield in most peripheral collisions. Thus, equation 3.2 can be re-written as,

$$R_{cp} \mid_{z=0} = R_{cp}^{\pi} \times R_{\pi}^{peri} \mid_{z=0} + R_{cp}^{K} \times R_{K}^{peri} \mid_{z=0} + R_{cp}^{P} \times R_{P}^{peri} \mid_{z=0} \tag{3.4}$$

. We neglect the $\mid_{z=0}$ on the R_{cp} for each particle species because we believe that the probabilities of absorption for each particle species would not change with centralities, thus absorber would not change the R_{cp} value for individual particle species. According to the same principle, the R_{cp} after absorber can be written as,

$$R_{cp} \mid_{z\neq 0} = R_{cp}^{\pi} \times R_{\pi}^{peri} \mid_{z\neq 0} + R_{cp}^{K} \times R_{K}^{peri} \mid_{z\neq 0} + R_{cp}^{P} \times R_{P}^{peri} \mid_{z\neq 0} \tag{3.5}$$

. Where $z \neq 0$ indicates the value is evaluated after absorber. From previous section, we know that positive kaons have the smallest absorption cross-section in absorber, so we can consider an extreme case in which the absorber is large enough that all the pions and protons are stopped inside the absorber completely and the only left particles that we can measure in Muon Trackers are positive koans. In the case, it is equivalent to say that the $R_{\pi}^{peri} \mid_{z\neq 0}$ and $R_{P}^{peri} \mid_{z\neq 0}$ are equal to zero in equation 3.5. Then,

$$R_{cp} \mid_{z\neq 0} = R_{cp}^{K} \tag{3.6}$$

As it has already been mentioned that there is no available measurement yet on the identified particle R_{cp} and particle composition at the rapidity ranges covered by the PHENIX muon arms at RHIC energy in deuteron gold collisions, so we can only use the PHENIX central arm identified particle measurements. Fig 3.18

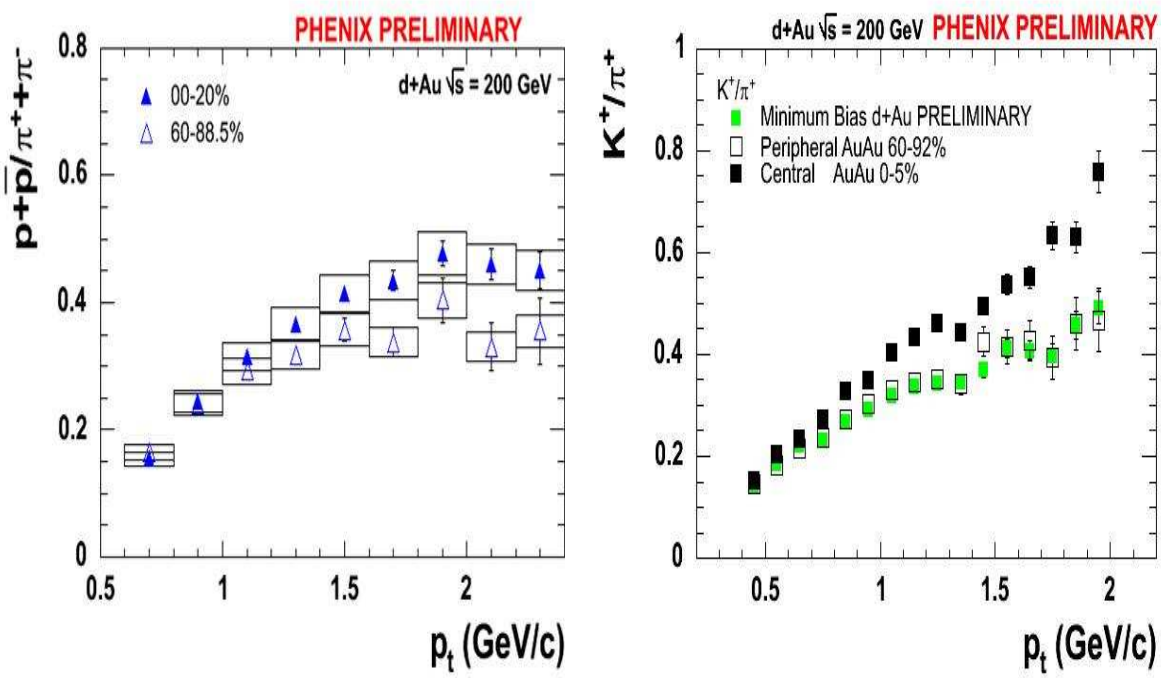

Figure 3.18: particles ratio measured by the PHENIX central arm in dAu collisions. Left : proton to π ratio. Right : kaon to π ratio.

shows ratio between protons/kaons and pions measured by the PHENIX central arm for deuteron gold collisions at rapidity $y = 0$. One can see that, for peripheral collisions, the maximum protons/kaons to pions ratio is 40%. Fig 3.19 shows the R_{cp} for different particle species. On the plots, the R_{cp} for pions and kaons are very close to each other, one can consider that $R_{cp}^{\pi} \approx R_{cp}^{K}$, but proton R_{cp}^{P} are higher than R_{cp}^{π}, the difference is about 20% of pion R_{cp}.

Based on the information from the PHENIX central arm measurement, we can calculated the difference between $R_{cp} \mid_{z=0}$ and $R_{cp} \mid_{z\neq 0}$ by assuming that $R_{cp}^{\pi} = R_{cp}^{K} = \frac{1}{1.2} \times R_{cp}^{P}$ and $0.4 \times R_{\pi}^{peri} \mid_{z=0} = R_{K}^{peri} \mid_{z=0} = R_{P}^{peri} \mid_{z=0}$,

$$R_{cp} \mid_{z=0} = R_{cp}^{K} \times (R_{\pi}^{peri} \mid_{z=0} + R_{K}^{peri} \mid_{z=0} + 1.2 \times R_{P}^{peri} \mid_{z=0}) \tag{3.7}$$

. From equation 3.6, $R_{\pi}^{peri} \mid_{z=0} + R_{K}^{peri} \mid_{z=0} + R_{P}^{peri} \mid_{z=0} = 1$ and $R_{P}^{peri} \mid_{z=0} = \frac{0.4}{0.4+0.4+1} \approx 0.2$, we get

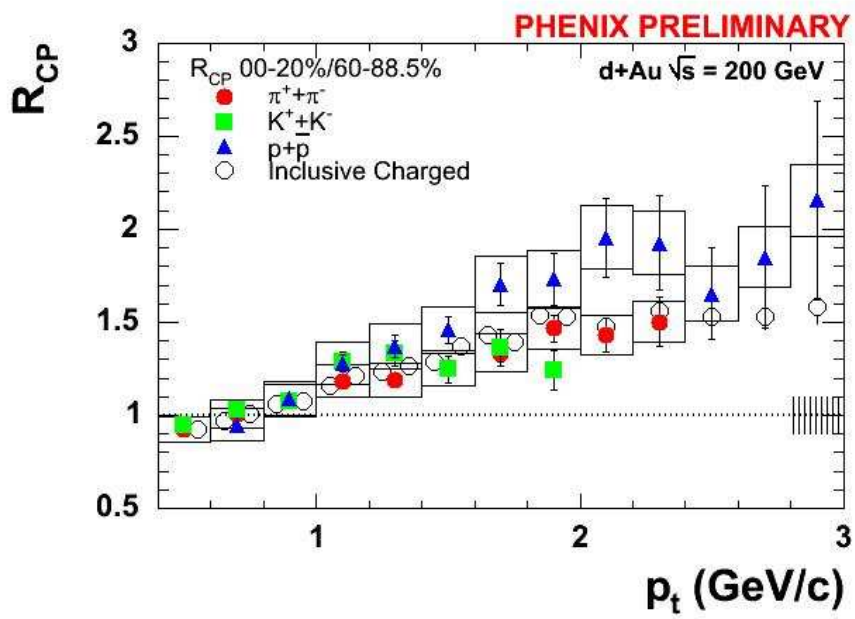

Figure 3.19: R_{cp} measured at rapidity $y = 0$ by the PHENIX central arm for identified particles.

$$R_{cp} \mid_{z=0} = R_{cp} \mid_{z\neq 0} \times (1 + 0.2 \times 0.2) = 1.04 \times R_{cp} \mid_{z\neq 0} \tag{3.8}$$

. We can see the difference is about 4% and it is an up-limit.

3.3 run selection

In this analysis, the data we used was taken from RHIC run3 deuteron gold collision at $\sqrt{s_{NN}} = 200$ GeV. There are two different trigger samples. One is the minbias trigger sample, which required at least 1 PMT tuber on each side of the PHENIX BBC fired during the collisions to record events. This trigger covers 88% of the total dAu inelastic scattering cross-section. Another trigger sample is so called MuID one deep trigger sample. MuID one deep trigger is an analogue circuit determined trigger. The basic logic is to select the events in which at least one online deep road was found in muon identifier. An online deep road is defined as that at least 7 out of 8 Iarocci tube planes from the first four gaps in the same quadrant of MuID

were fired. The whole MuID detector is divided into four quadrants in XY plane. During the data taking, this MuID one deep trigger is set as a level1 trigger on top of Minbias trigger. In section, we will outline how we choose good runs from this two trigger samples.

3.3.1 MuID HV status

In the hadron identification, we rely on the MuID detector to provide the how deep a track penetrates in the detector and we veto the tracks which have associated hits in the last gap of MuID. But during the data taking, there was lots of beam background coming from back of the MuID and the background tripped the High Voltage(HV) of the last MuID gap, sometime, we had to turn of the HV. Under this situation, the last gap veto is essentially useless, so in the data analysis we only use the runs from the data taking period during which the beam background was small that the HV on last gap was on.

In the mean time, if during data taking there are too many MuID HV channels tripped, the tube efficiency will be very low, so in the run selections, we also exclude those runs which have more than 20 HV channels disabled in north arm and 60 HV channels disabled in south arm. Fig 3.20 shows the number of disabled HV channels as a function of run number for both muon arms and we only keep the category A runs for our analysis.

3.3.2 Muid blue logic trigger circuit efficiency

In off-line analysis, we also have a MuID trigger emulator to simulate the logic of MuID trigger circuit. The basic ideal is to use the MuID raw hits information to re-calculate the trigger decision according to logic of MuID trigger circuit. This emulator can serve as a cross check for the trigger circuit. In fact, during the data taking, we picked up some deficits of the circuit hardware by using the emulator to crosscheck the online trigger decisions. The Trigger Circuit Efficiency(TCE) is

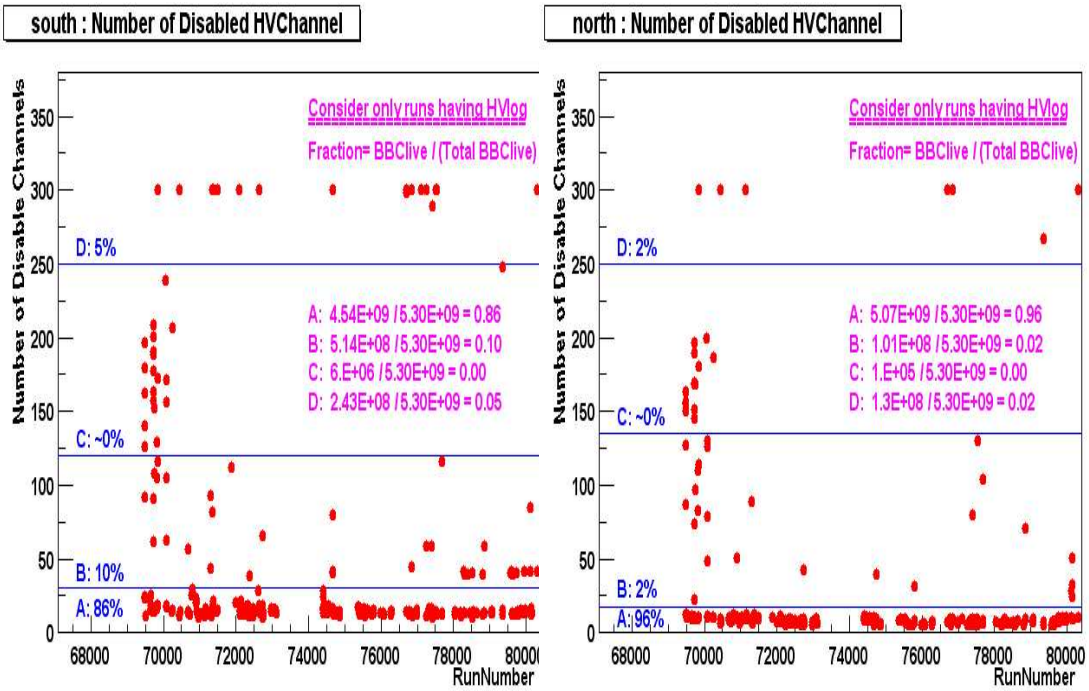

Figure 3.20: Number of disabled HV channels of MuID in run3 dAu are plotted as a function of run number. Left panel is south arm and right panel is north arm. All runs are categorized into 4 classes depended on the number of the disabled channels. We use category A in our analysis.

defined as

$$TCE = \frac{N_{circuit}}{N_{emulator}} \tag{3.9}$$

,where $N_{circuit}$ is the number of events fired by MuID trigger circuit and $N_{emulator}$ is the number of event fired by the emulator. If the trigger circuit worked at 100% of time, then the TCE should be one. But during the data taking, the trigger circuit sometimes failed to function correctly. Here we want to exclude those runs for which the TCE is less than 95% for both arms. Fig 3.21 shows the TCE as a function of run number.

3.3.3 select good run

Here is the list of the most of the criteria we used to select good runs,

- Full magnet fields were operated.

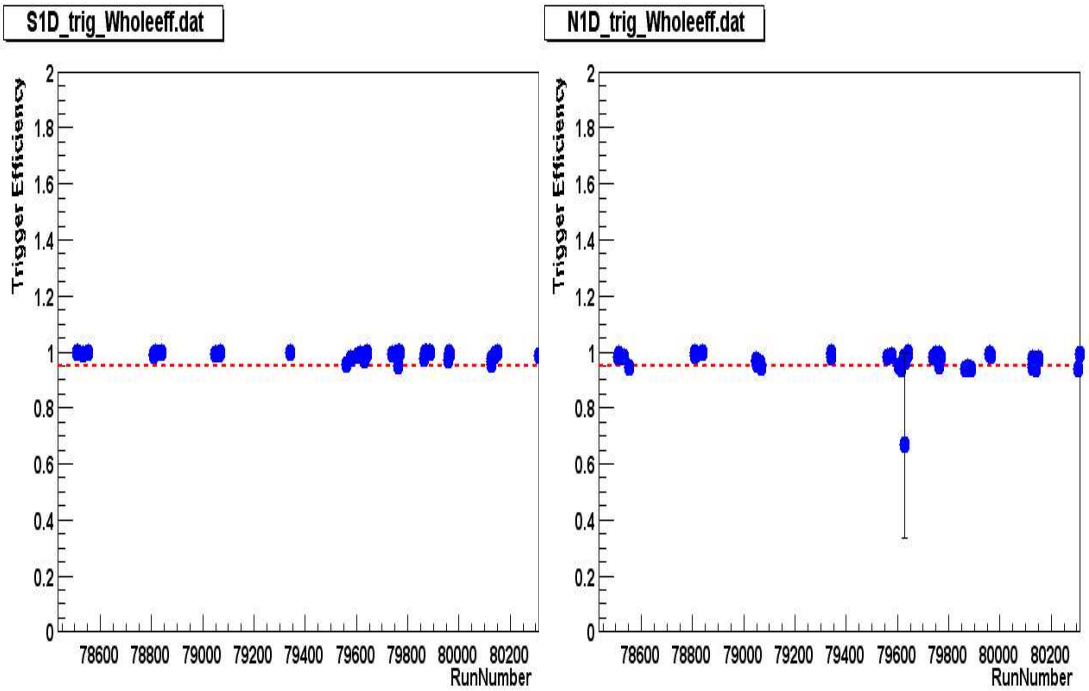

Figure 3.21: TCE of MuID trigger circuit in run3 dAu is plotted as a function of run number. Left panel is south arm and right panel is north arm.

- Both detector and accelerator are stable, which means the run lasted more than half an hour.
- Beam background is low enough that HV of last MuID gap was able to be turned on.
- Number of disabled MuID HV channels is less than 20 for north arm and less then 60 for south arm.
- TCE is larger than 95%.

. The first two items are basic information one can get from the run control log book.

Thus the run which are satisfied above all criteria are list as Table 3.2,

. To avoid double counting events in our analysis, we always required the scaled trigger bits for each trigger, and the rate for double counting under this requirement is less than $\frac{1}{100000}$. Also for one deep trigger sample, we always look at tracks at the

75403	75549	75587	75619	75622	75631	75636	75747	75794	76284
76852	76853	76864	76981	76983	76985	76995	77096	77247	77255
77256	77266	77312	77313	77314	77319	77320	77322	77324	77326
77530	78509	79047	79641	80127	77678	78510	79050	79642	78508
80128	77687	78511	79066	79740	80139	77688	78512	79067	78839
79762	80141	78035	78532	79340	79872	80150	78181	78549	79632
79341	79875	80152	78182	78553	79560	79885	80304	78207	80126
78578	79579	79888	80312	78208	78632	79603	79960	78210	78633
79615	79961	78269	78808	79626	79962	78306	78817	79629	79963
78402	78838	79630	79964						

Table 3.2: List of runs used for the analysis

same side with the fired trigger, i.e, only look at south arm tracks in south MuID one deep trigger sample, or only look at the north arm tracks in north one deep trigger sample.

3.3.4 event statistic

We always count the number of corresponding minbias raw trigger for each selected trigger sample. So the total statistic we have is given by corresponding minbias raw trigger events. For the minbias trigger sample, we have 67 million minbias events, and for 1D trigger sample, we sampled 5.3 billion minimal bias events.

3.4 Results

3.4.1 Evaluate the centrality dependence of tracking efficiency and MuID one deep trigger efficiency

Single tracking efficiency is evaluated by comparing the reconstructible MC single hadrons and the reconstructed hadrons. First we need to decide if a hadron one throws at vertex is reconstructible, since we do not care about the acceptance in R_{cp} measurement, we only want to know the percentages of reconstructible tracks are able to be reconstructed correctly. The requirements for reconstructible hadron type tracks are

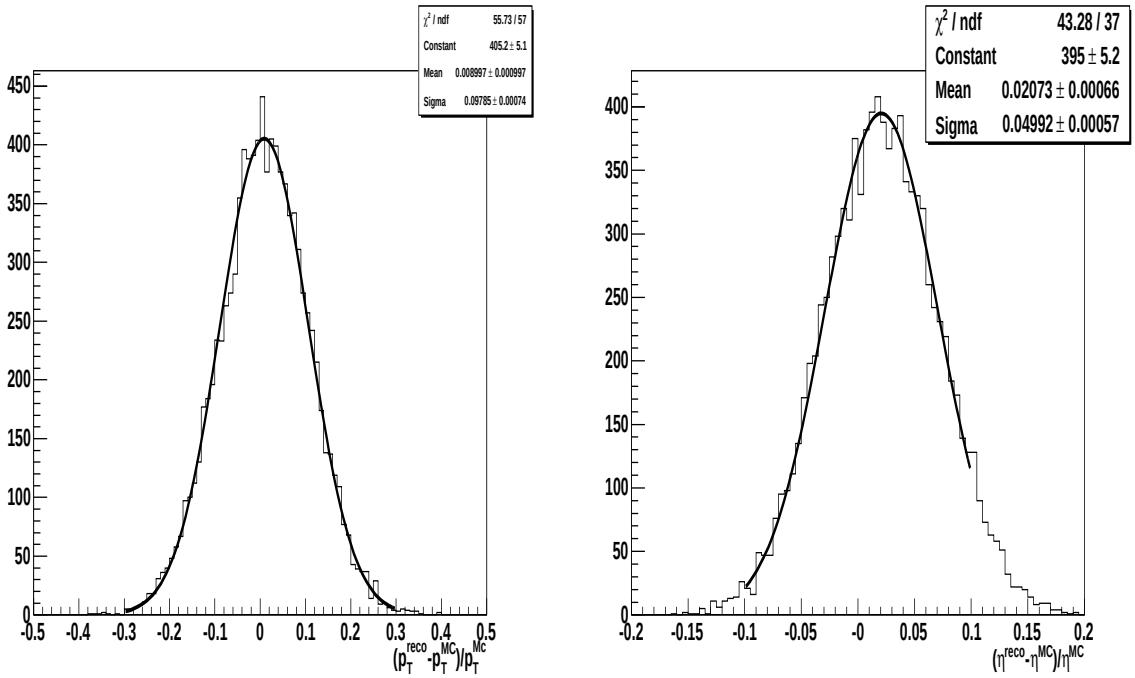

Figure 3.22: Left : resolution of transverse momentum. Right : resolution of pseudorapidity

- Tracks leaves at least one Monte Carlo hit at each station of MuTr.
- Tracks leaves at least one Monte Carlo hit at each gap of the first four/three gaps for hadrons stopped at the fourth/third gap (gap3/gap2 counting from zero).
- The true MC momentum at station on is larger than 1.8 GeV/c.

. In the mean time, a hadron is a successfully reconstructed hadron means,

- The reconstructed transverse momentum is within $3\times\sigma_{p_T}$ from true MC transverse momentum, where σ_{p_T} is shown as in the left panel of Fig 3.22
- The reconstructed pseudo-rapidity is within $3 \times \sigma_\eta$ from true MC pseudo-rapidity, where σ_η is shown as in the right panel of Fig 3.22

. Thus the single hadron efficiency is defined as

$$EFF_{single} = \frac{N_{reco}}{N_{MC}} \tag{3.10}$$

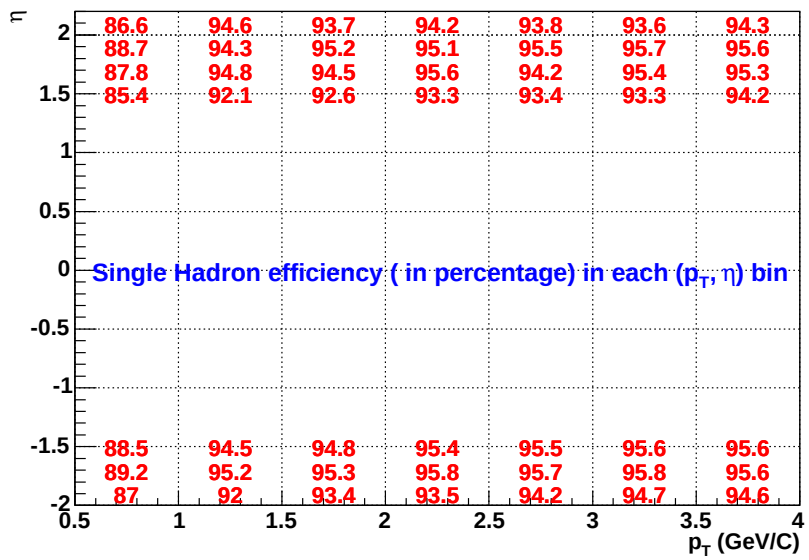

Figure 3.23: Single hadron efficiency in each (p_T, η) bins.

, where N_{reco} is the number of successfully reconstructed hadrons and N_{MC} is the number of reconstructible MC hadrons. Fig 3.23 shows the single hadron efficiency in each (p_T, η) bins for perfect detector configurations, i.e. no detector inefficiency.

In fact, the numbers listed in Fig 3.23 are the so-called bench mark numbers. They tell us how well our tracking software can do. We are really interested in the efficiencies calculated in real detector environment and their variances with the centralities. For MuTr, the way to implement the real detector environment is to mask out strips which are corresponding to the disabled FEM(Front End electric Modules) during data taking. For MuID, each two-pack in Monte Carlo simulation is assigned a realistic efficiency number. The method to determine the efficiency number is following. First, for each Iarocci tube panel, we select a sample of good roads. These good roads have to fire all panels at different depth except for the panel we are examining. Then we open a searching window on the examined panel to look for fired two-packs. Therefor the two-pack efficiency is the ratio between the number of times that the check has been made and the number of times that a fired two-pack is found. To evaluate the variation of efficiency with centralities,

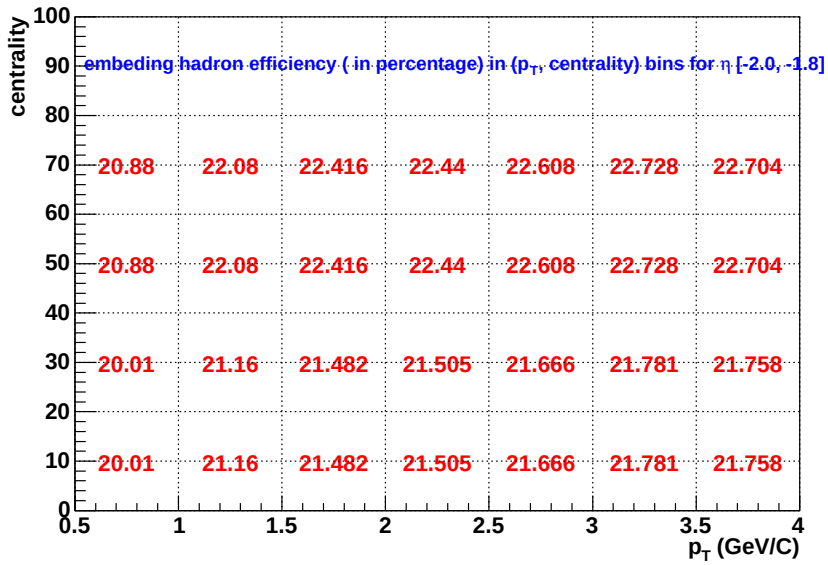

Figure 3.24: Embedded hadron efficiency in each $(p_T, centrality)$ bins for $-2.0 < \eta < -1.8$.

we embedded the reconstructible single hadron tracks into real events of different centrality classes, then try to reconstruct the embedded hadrons. We did the embedding study together with the real detector environment. The results are shows in Fig 3.24 for η in [-2.0, -1.8] bin, Fig 3.25for η in [-1.8, -1.6] bin, Fig 3.26 for η in [-1.6, -1.4] bin, Fig 3.27 for η in [1.4, 1.6] bin, Fig 3.28 for η in [1.6, 1.8] bin, Fig 3.29 for η in [1.8, 2.0] bin, Fig 3.30 for η in [2.0, 2.2] bin. From the plots, we can see that variation of the efficiency with centralities is $\sim 4\%$ in all the (p_T, η) bins.

The large difference between the single hadron efficiency and the embedding hadron efficiency is because of two reasons. The first is the MUID detector inefficiency. Especially for south arm, the average panel efficiency is around 80%, the low panel efficiency does most harm on the shallow roads (depth == 2). This is because shallow roads do not have so many hits to begin with as deep roads do and this is also because of the algorithm we used for searching MuID roads. The road finding algorithm includes two steps. First, we look for a one dimensional track among one orientation tube planes, then we combine two one dimensional tracks into one road. The requirement for shallow 1D tracks is 2 out of 3 planes fired, which has an effi-

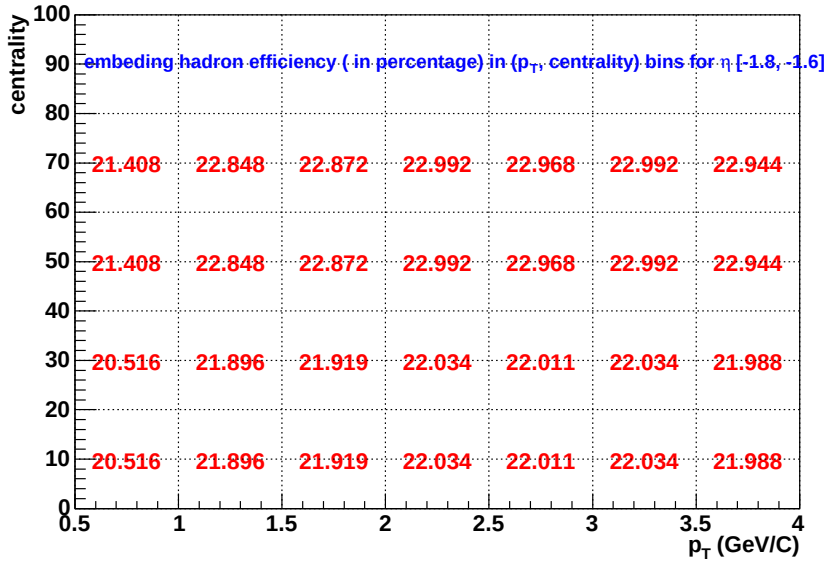

Figure 3.25: Embedded hadron efficiency in each $(p_T, centrality)$ bins for $-1.8 < \eta < -1.6$.

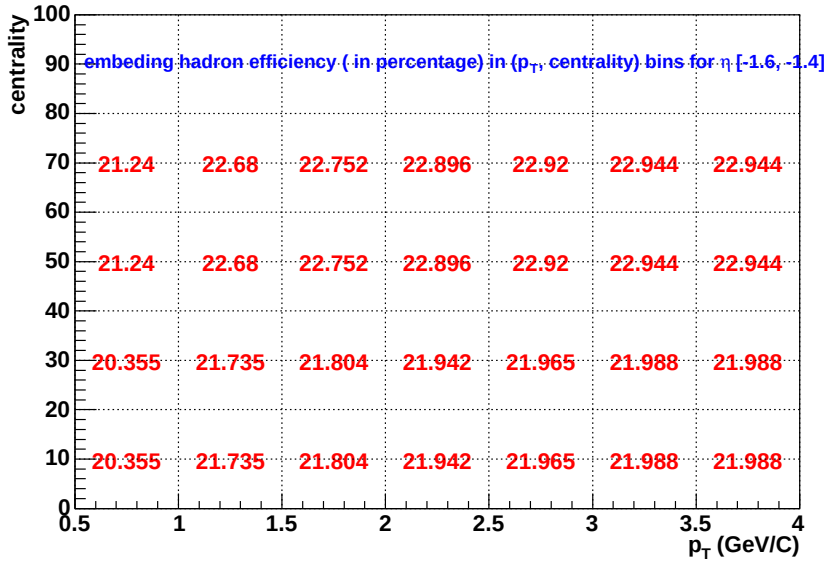

Figure 3.26: Embedded hadron efficiency in each $(p_T, centrality)$ bins for $-1.6 < \eta < -1.4$.

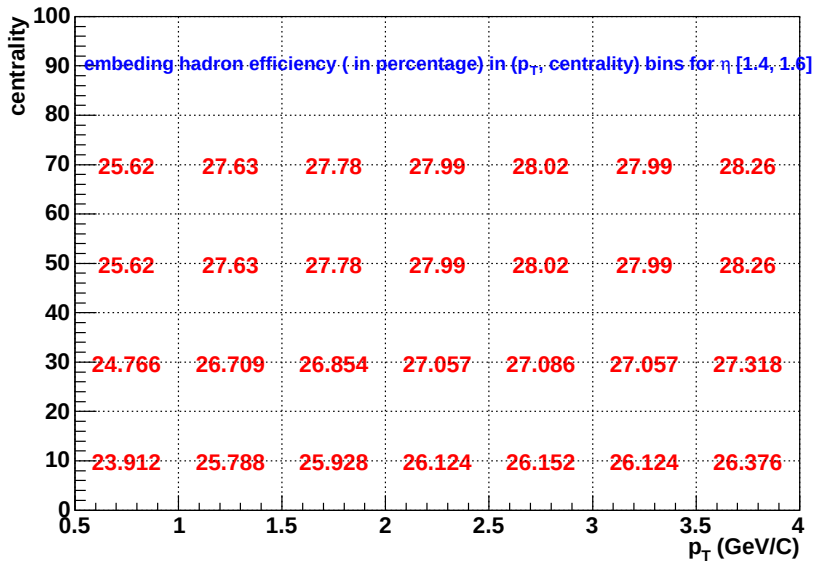

Figure 3.27: Embedded hadron efficiency in each $(p_T, centrality)$ bins for $1.4 < \eta < 1.6$.

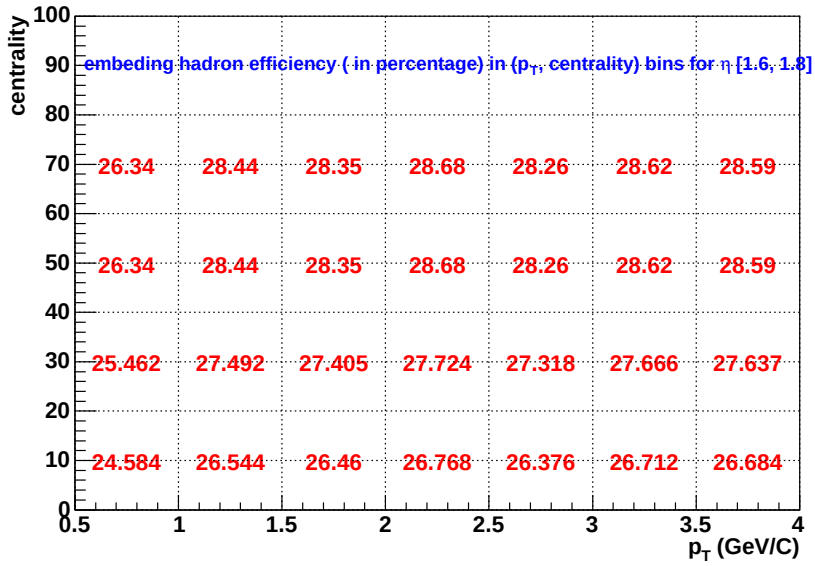

Figure 3.28: Embedded hadron efficiency in each $(p_T, centrality)$ bins for $1.6 < \eta < 1.8$.

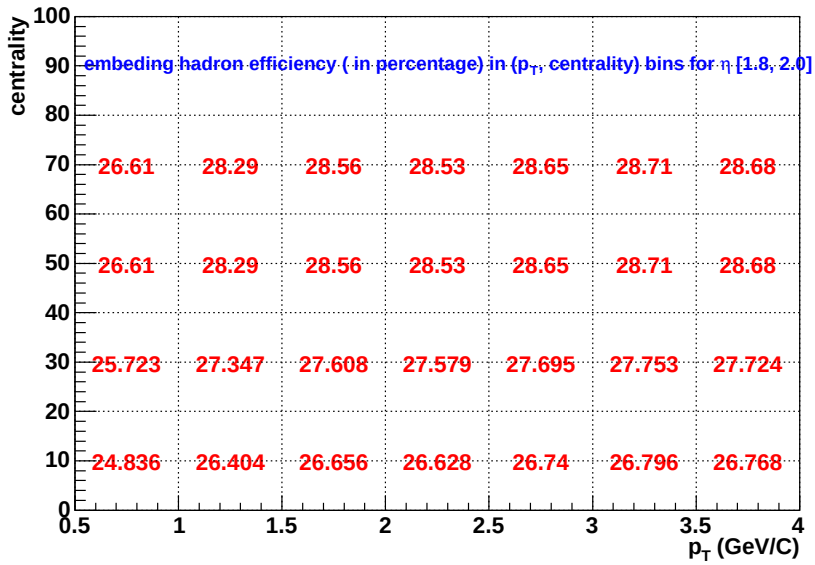

Figure 3.29: Embedded hadron efficiency in each $(p_T, centrality)$ bins for $1.8 < \eta < 2.0$.

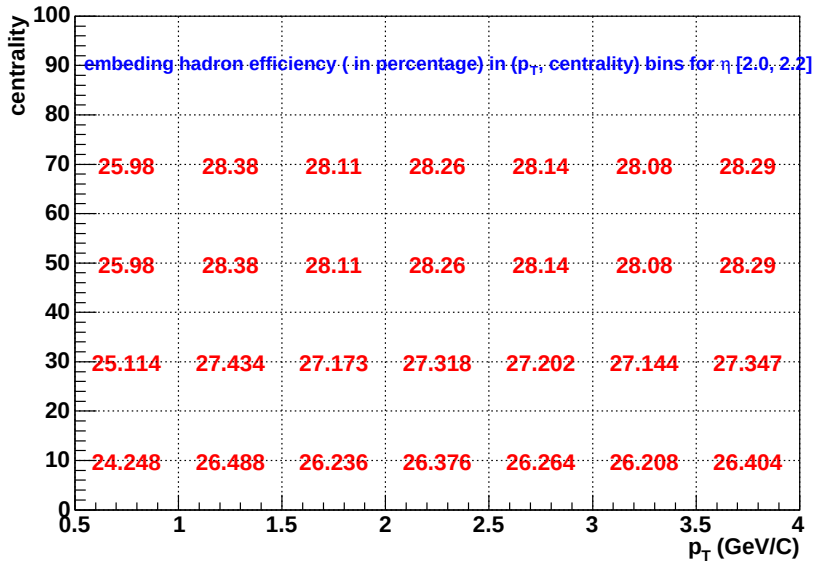

Figure 3.30: Embedded hadron efficiency in each $(p_T, centrality)$ bins for $2.0 < \eta < 2.2$.

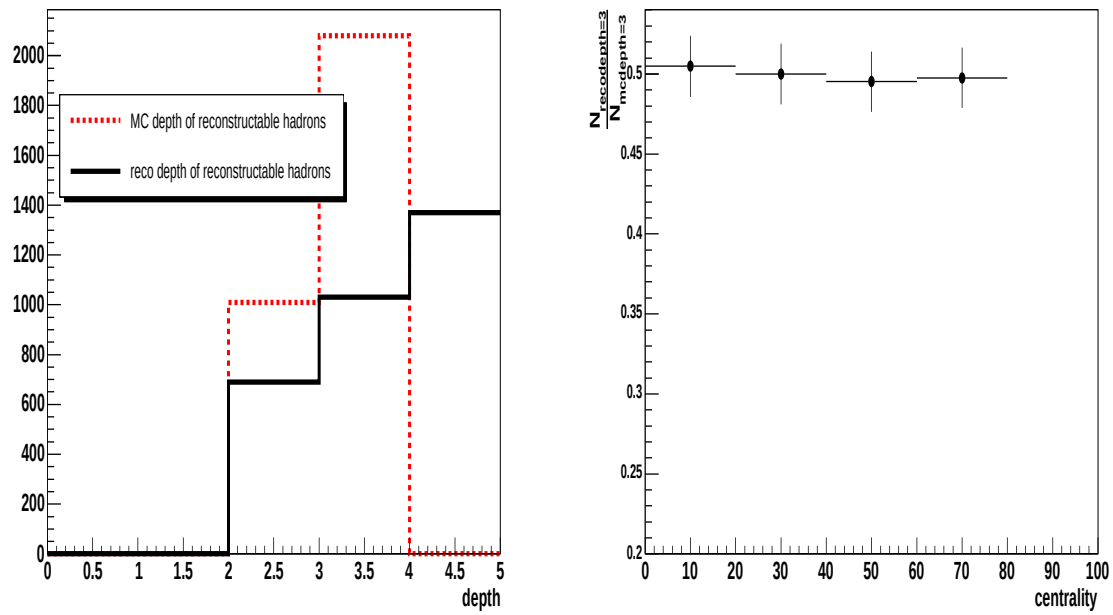

Figure 3.31: Left : The dashed line shows the MC depth distribution and the solid line shows the reconstructed depth distribution, it is clearly that many depth=3 MC hadrons are mis-reconstructed to depth=4 track. Right : The ratio between the number of reconstructed depth=3 hadrons and the number of MC depth=3 hadrons is plotted as a function of centrality, no centrality dependence is seen here.

ciency $\epsilon_{1Droad} = \epsilon^3_{plane} + C^2_3\epsilon^2_{plane}(1-\epsilon_{plane})$. if the single plane efficiency $\epsilon_{plane} = 0.8$, then $\epsilon_{1Droad} = 0.88$. The efficiency for shallow roads is $\epsilon_{road} = \epsilon_{1Droad}\epsilon_{1Droad} = 0.77$. The second reason is the random benefit from the last gap hits which are associated with the beam background. This random benefit will make sheep roads (depth==3) become fake deep road (depth ==4), which will be vetoed by our hadron selection. Embedding studies show that almost 50% of sheep roads were reconstructed to deep roads, and the percentage does not vary with centralities, which indicates the background has no connection with centralities. Fig 3.31 shows the results from the studies. The left panel shows how much the MC depth is modified and the right panel shows that this modification is independent with centralities.

The centrality dependence of one deep MuID trigger is also evaluated by embedding deep and sheep tracks into real minbias events of each centrality classes.

Table 3.3: Muon one deep trigger verse centrality.

trigger eff vs centrality bin	$0-20\%$	$20-40\%$	$40-60\%$	$60-88\%$
south one deep efficiency	$64 \pm 4\%$	$61 \pm 3\%$	$61 \pm 3\%$	$62 \pm 3\%$
north one deep efficiency	$91 \pm 6\%$	$89 \pm 6\%$	$90 \pm 6\%$	$90 \pm 6\%$

The embedded data samples are analyzed by trigger emulator. If the tube efficiency is 100%, trigger emulator should fire on every embedded event. Since we used the real two-pack efficiency in the simulation, trigger emulator only fires a fraction of the events. The centrality dependence of trigger efficiency comes from the random benefit related to the occupancy of the detector. The result of this study is summarized as Table 3.3. From the table, we can see that the trigger efficiency almost have no dependence on centrality.

3.4.2 Results from Minbias trigger sample

Since we have known the tracking efficiency is independent with centrality and all the acceptance will the same in all the centralities, then the R_{cp} calculation is just plugging the raw spectrum into equation 3.1. Fig 3.32 shows the raw transverse momentum distribution for minbias event sample and for all centrality bins. Fig 3.33 shows the R_{cp} as a function of transverse momentum. One important thing we need to mention here is that the acceptance for the hadrons in the lowest two p_T bins only covers $\mid \eta \mid > 1.8$, so the R_{cp} measured at these two bins does not count to the physics covered by the rest part of the detector.

In fact, to produced above plots, we use yet another cut to reduce the background from random MuID road and MuTr track matching. This cut is called road approximity cut, and the quantity we cut on is the distance between the extrapolated point on MuID first fired gap from MuTr track and the gap0 point of associated MuID road. It tells us how well the track is associated with road and we require this distance has to be less than 30cm for selected hadrons. Fig 3.34 shows the road approximity cut for south and north arm. One can see that the distribution for south arm is much wider, it can be understood that the tube efficiency in south arm

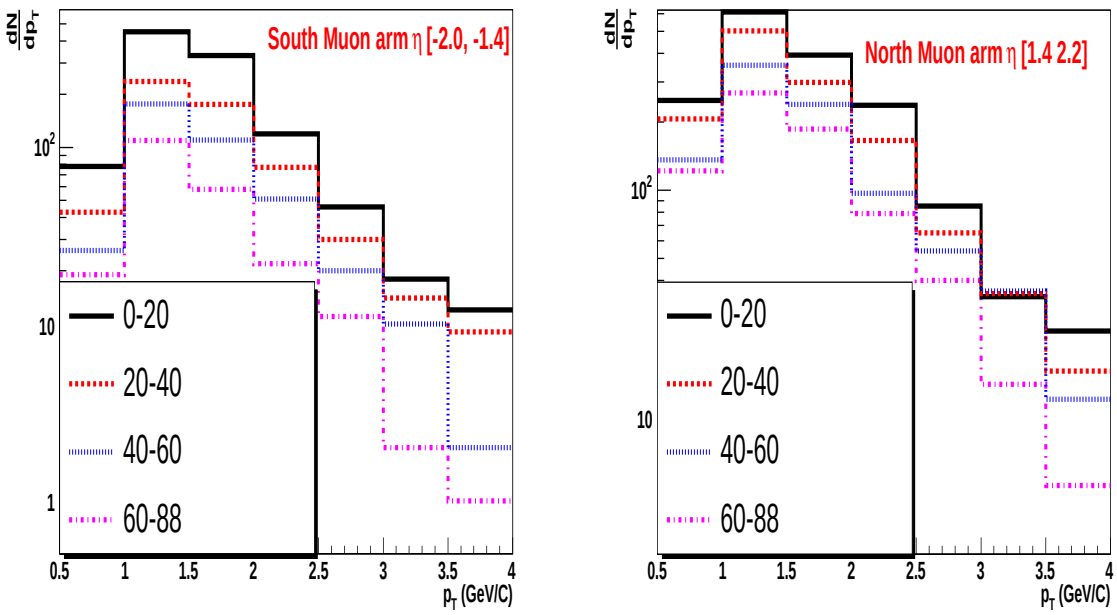

Figure 3.32: Raw transverse momentum distribution for punch-through hadrons for each centralities from minbias data sample. Left : south arm. Right : north arm.

is low and one gets more random associations. This is even worse for the shallow roads in south arm. So in our analysis, we exclude the tracks in south arm which stop at gap2 of south MuID.

In Fig 3.35, left panel shows the raw η distribution of the punch-through hadrons. In order to produce this plots, we need to have a $p_T > 1.5$ GeV/c cut to make all the η bins have the same phase space coverage. The shape of the η distribution is mainly determined by the hadron punch-through probability. For the hadrons in the rapidity bins close to central rapidity, they need to go through a longer path in the absorber and, therefor have more chances to produce hadronic showers than to punch through. The right panel of Fig 3.35 shows the MC hadrons punch-through probability as a function of η. The input MC p_T spectrum is taken from PHENIX central arm π^0 measurement and the η is a flat distribution.

Fig 3.36 shows the hadron R_{cp} as a function of η.

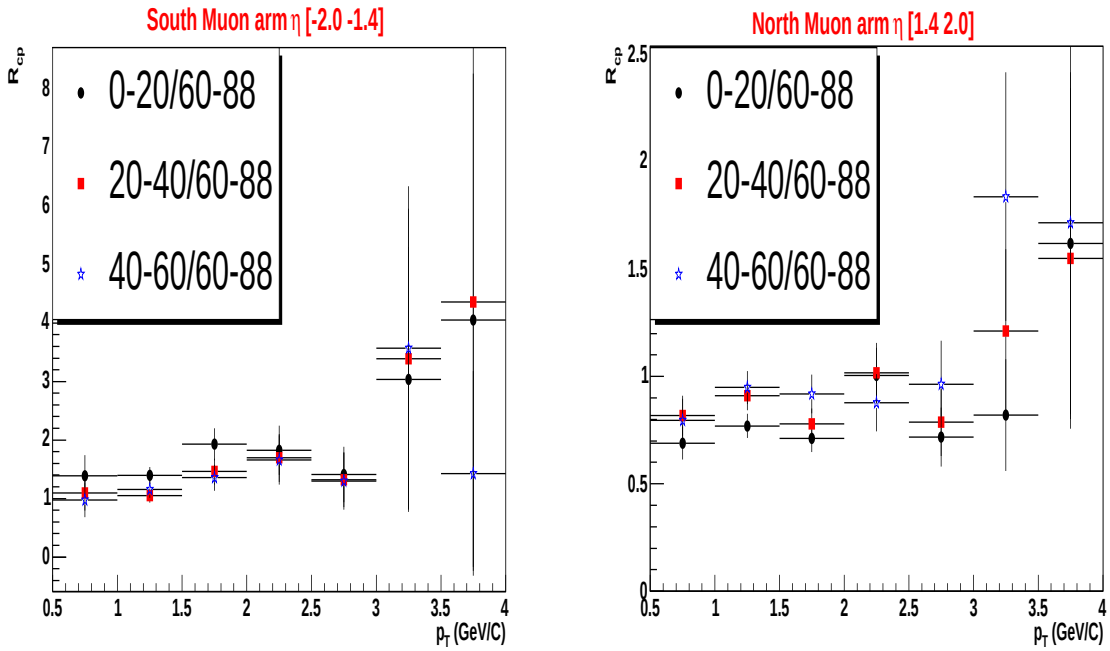

Figure 3.33: R_{cp} as a function of transverse momentum in each centralities. Minbias data sample and only statistic error is shown here. Left : south arm, Right north arm.

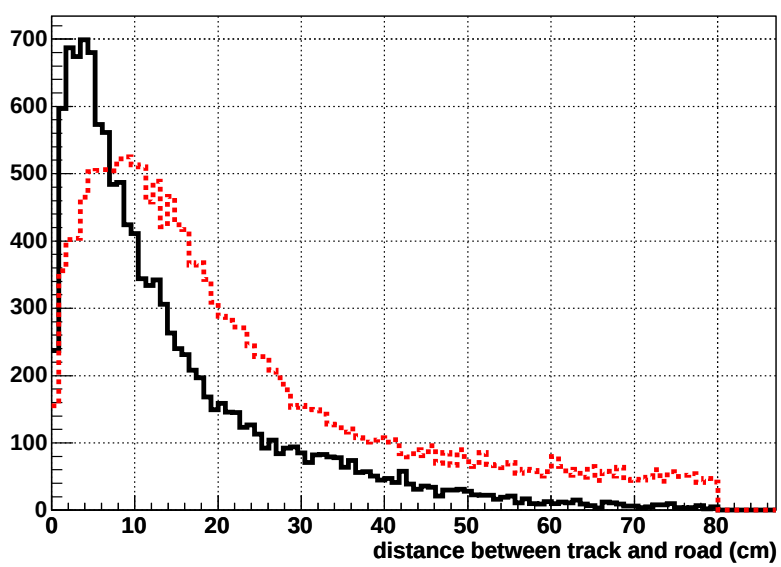

Figure 3.34: Road approximity distribution for south arm(red, dashedline) and north arm(black, solid) line.

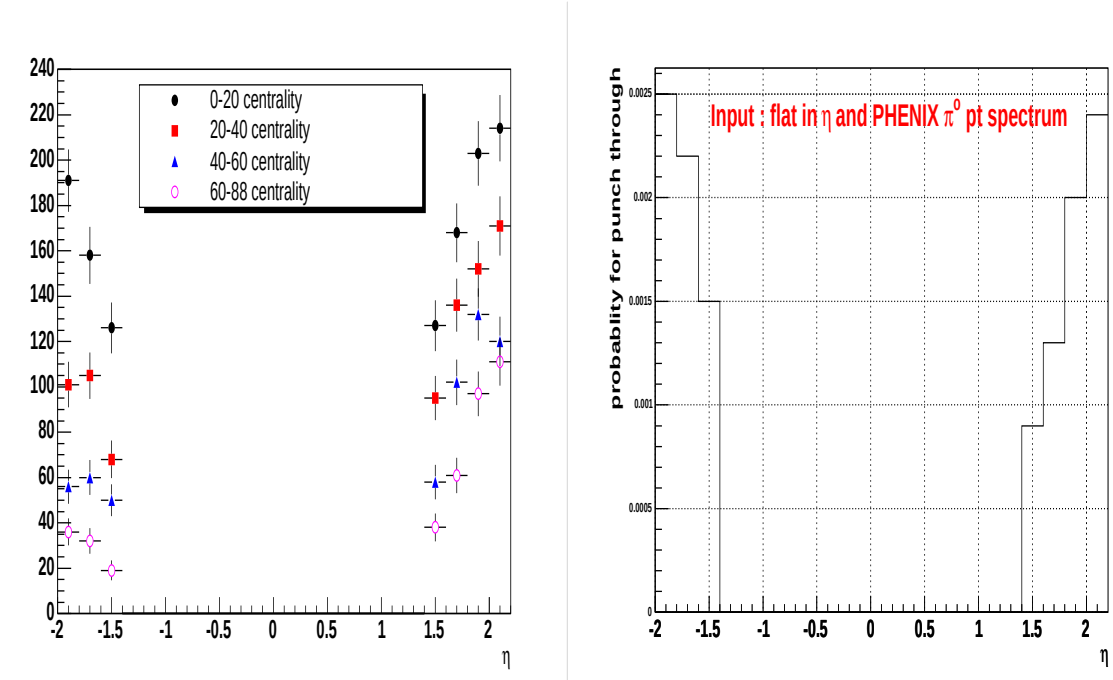

Figure 3.35: Left : In minbias data sample, hadron η distribution for all centrality bins. Left : Hadron punch-through probability as a function of η

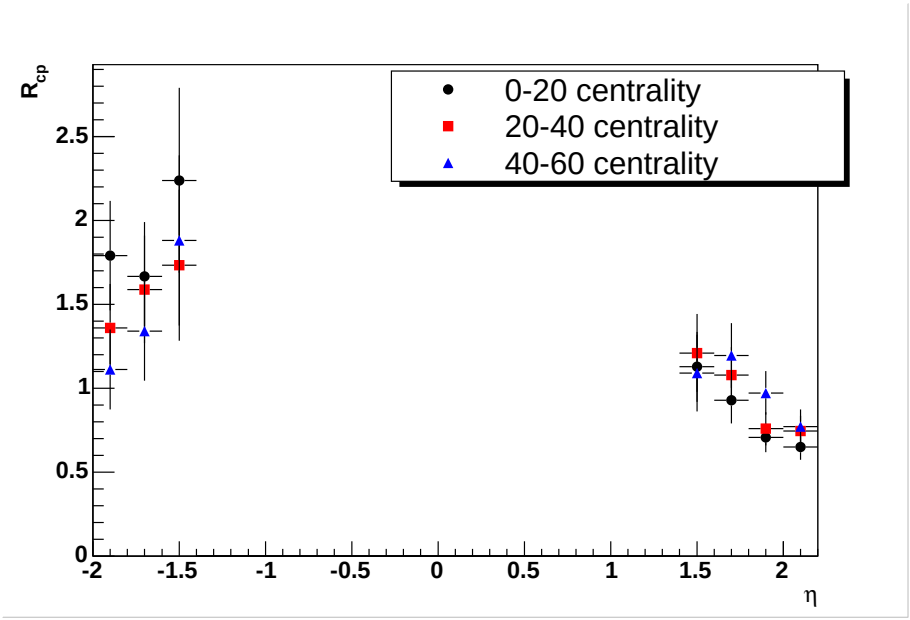

Figure 3.36: R_{cp} as a function of pseudo-rapidity in each centralities. Minbias data sample and only statistic error is shown here.

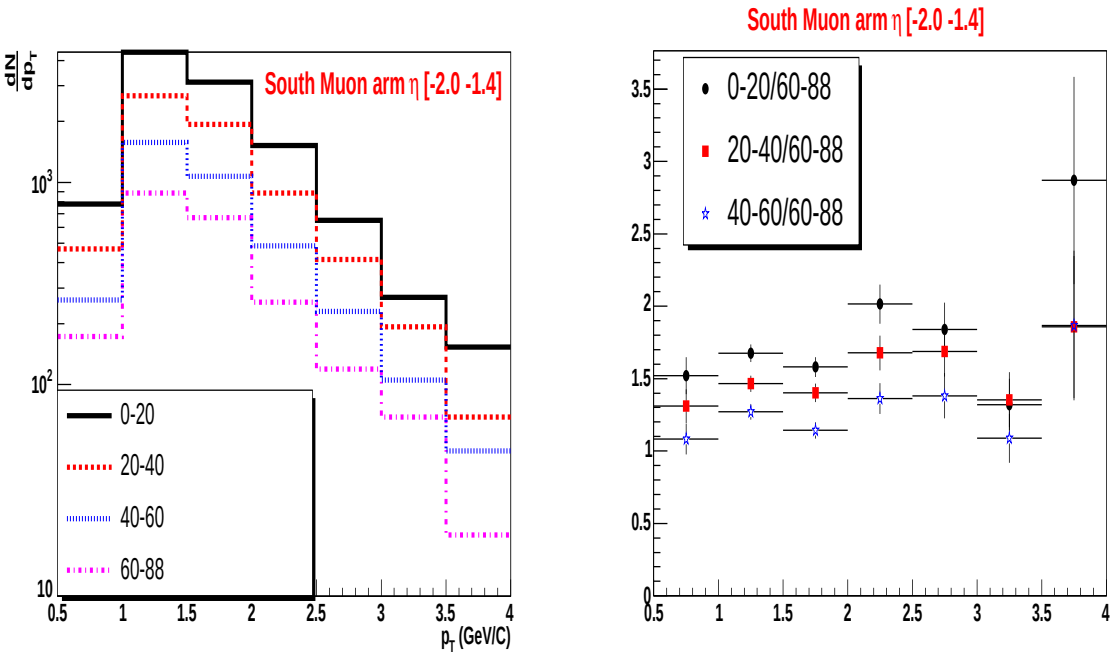

Figure 3.37: Left : South arm hadron raw p_T distribution for each centrality bins, south one deep trigger sample. Right : South arm hadrons R_{cp} as a function of transverse momentum in each centralities. South one deep trigger sample and only statistic error is shown here.

3.4.3 Results from south MuID 1-deep trigger sample

In Fig 3.37, left panel shows the raw transverse momentum distribution of south arm reconstructed hadrons from south MuID one deep trigger sample for each centrality bins. The right panel of Fig 3.37 shows the R_{cp} as a function of p_T for south arm hadrons from south MuID one deep trigger. In Fig 3.38, left panel shows the raw pseudo-rapidity distribution of south arm reconstructed hadrons from south MuID one deep trigger sample for each centrality bins. The right panel of Fig 3.38 shows the R_{cp} as a function of η for south arm hadrons from south MuID one deep trigger.

3.4.4 Results from north MuID 1-deep trigger sample

In Fig 3.39, left panel shows the raw transverse momentum distribution of north arm reconstructed hadrons from north MuID one deep trigger sample for each centrality

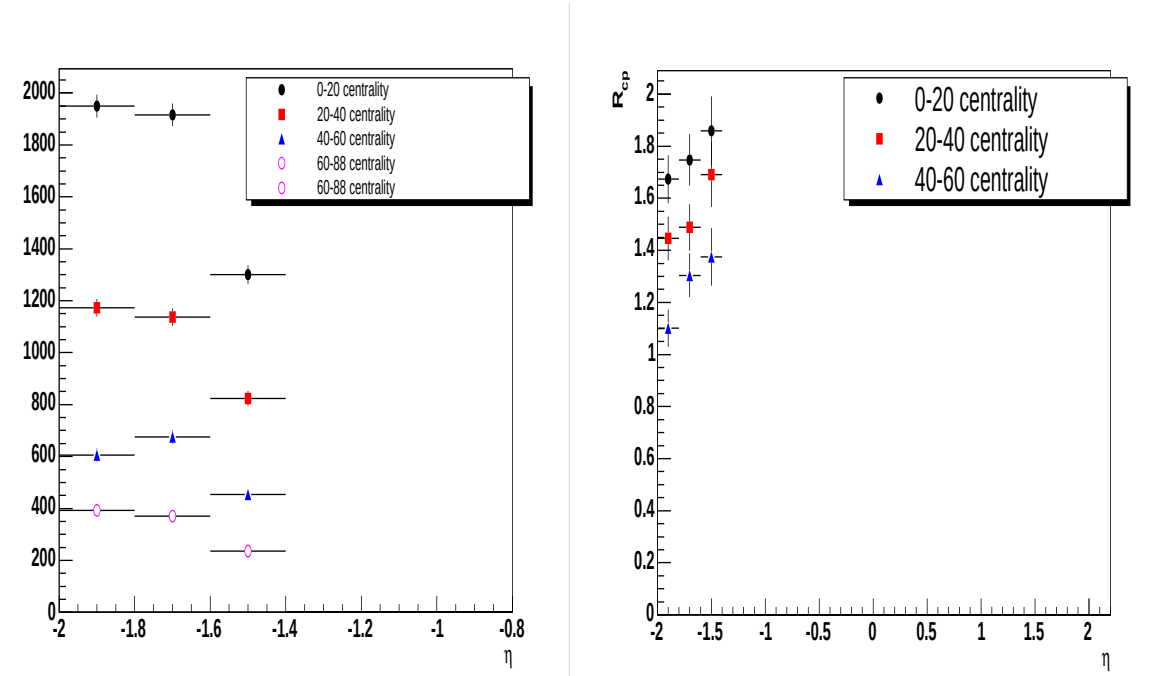

Figure 3.38: Left : South arm hadron raw η distribution for each centrality bins, south one deep trigger sample. Right : South arm hadrons R_{cp} as a function of pseudorapidity in each centralities. South one deep trigger sample and only statistic error is shown here.

bins. The right panel of Fig 3.39 shows the R_{cp} as a function of p_T for north arm hadrons from north MuID one deep trigger. In Fig 3.40, left panel shows the raw pseudo-rapidity distribution of north arm reconstructed hadrons from north MuID one deep trigger sample for each centrality bins. The right panel of Fig 3.40 shows the R_{cp} as a function of η for north arm hadrons from north MuID one deep trigger.

3.4.5 systematics

By reconstructing R_{cp}, most systematics which are not related to centralities and are detector wise, such as detector acceptance, particle absorption by absorber, are concealed out, so they do not need to be considered in the analysis. But things like tracking efficiency and trigger efficiency which are in principle depended on the centralities need to be evaluated. As we discussed at beginning of this section , centrality dependence of tracking efficiency is very small, here we quota 4%. In the

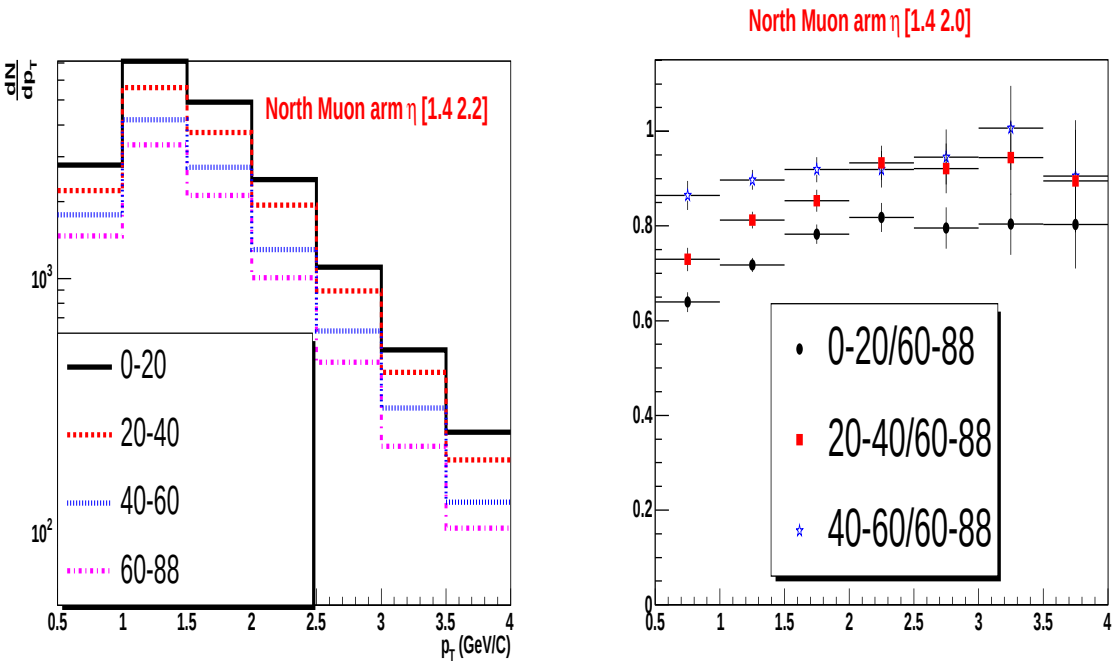

Figure 3.39: Left : North arm hadron raw p_T distribution for each centrality bins, north one deep trigger sample. Right : North arm hadrons R_{cp} as a function of transverse momentum in each centralities. North one deep trigger sample and only statistic error is shown here.

mean time, to get the final R_{cp} values, we have applied many analysis cuts either to select good hadron candidates or to get ride of background contamination. we also need to evaluate how these analysis cuts affect our final R_{cp} values by varying the cuts.

The first cut we applied to is the total station1 momentum cut when we select hadrons. This cut is essential to get ride of muon contaminations. In the first place, we chose this cut to be as far from the muon peak at gap3 as possible, which is $3 \times \sigma$ away. To estimate the its contribution to systematics, we changed it to $5 \times \sigma$ away, then re-calculated the R_{cp}, as shown by Fig 3.41. One can see the R_{cp} values are not changed very much.

The θ_{xp} cut is used to get ride of the secondary particles from hadronic showers. Fig 3.42 shows how much the R_{cp} changes when we change the cut from < 0.03 to < 0.06.

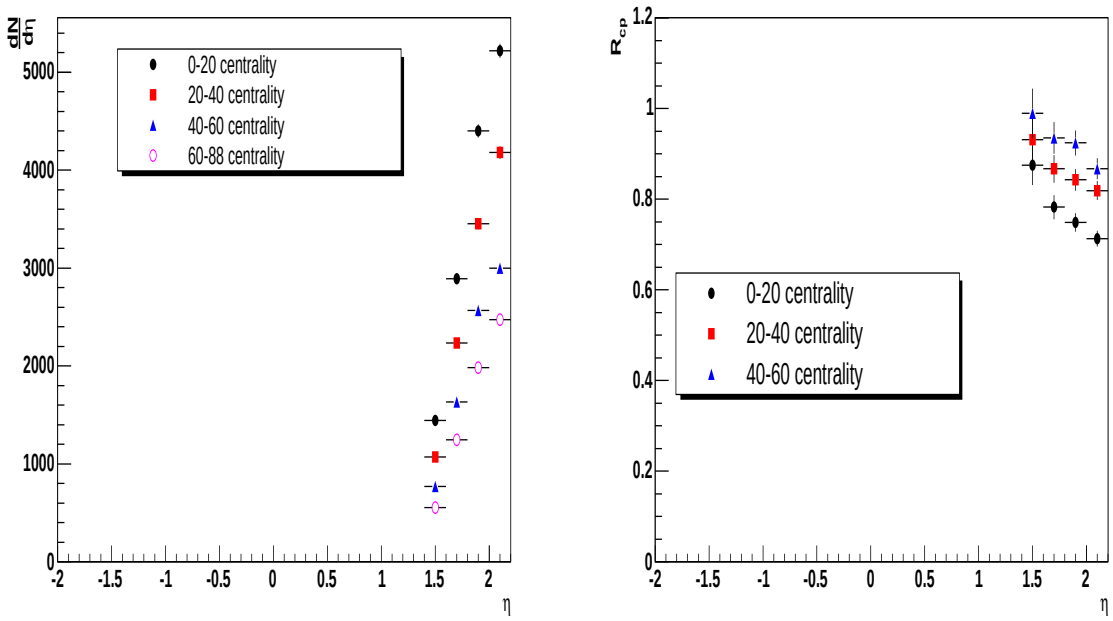

Figure 3.40: Left : North arm hadron raw η distribution for each centrality bins, north one deep trigger sample. Right : North arm hadrons R_{cp} as a function of pseudorapidity in each centralities. North one deep trigger sample and only statistic error is shown here.

Also we applied the road approximity cut $d_{proxy} < 30cm$ in the analysis. This cut mainly affect south arm analysis. In fact this cut is the reason why there has been a difference between QM04 analysis and our new analysis(presented here) for south arm hadrons. Fig 3.43 shows the R_{cp} after we changed $d_{proxy} < 30cm$ to $d_{proxy} < 60cm$

In the mean time, we also changed all the other cuts such as, single track χ^2, vertex cut, fiducial cut. All results are summarized in the following tables. In the table, the systematics is divided into two categories, points by points varied errors and common systematic errors. Point by point errors are from all the analysis cuts, and the common systematic errors are from the ratio of number of binary collisions from different centralities and the 4% uncertainty on the centrality dependence of tracking efficiency. Also in each table we have a "sub total systematics", which is the quadratic sum of all the point by point errors.

Table 3.4 shows the systematics errors in each p_T bins of south R_{cp}.

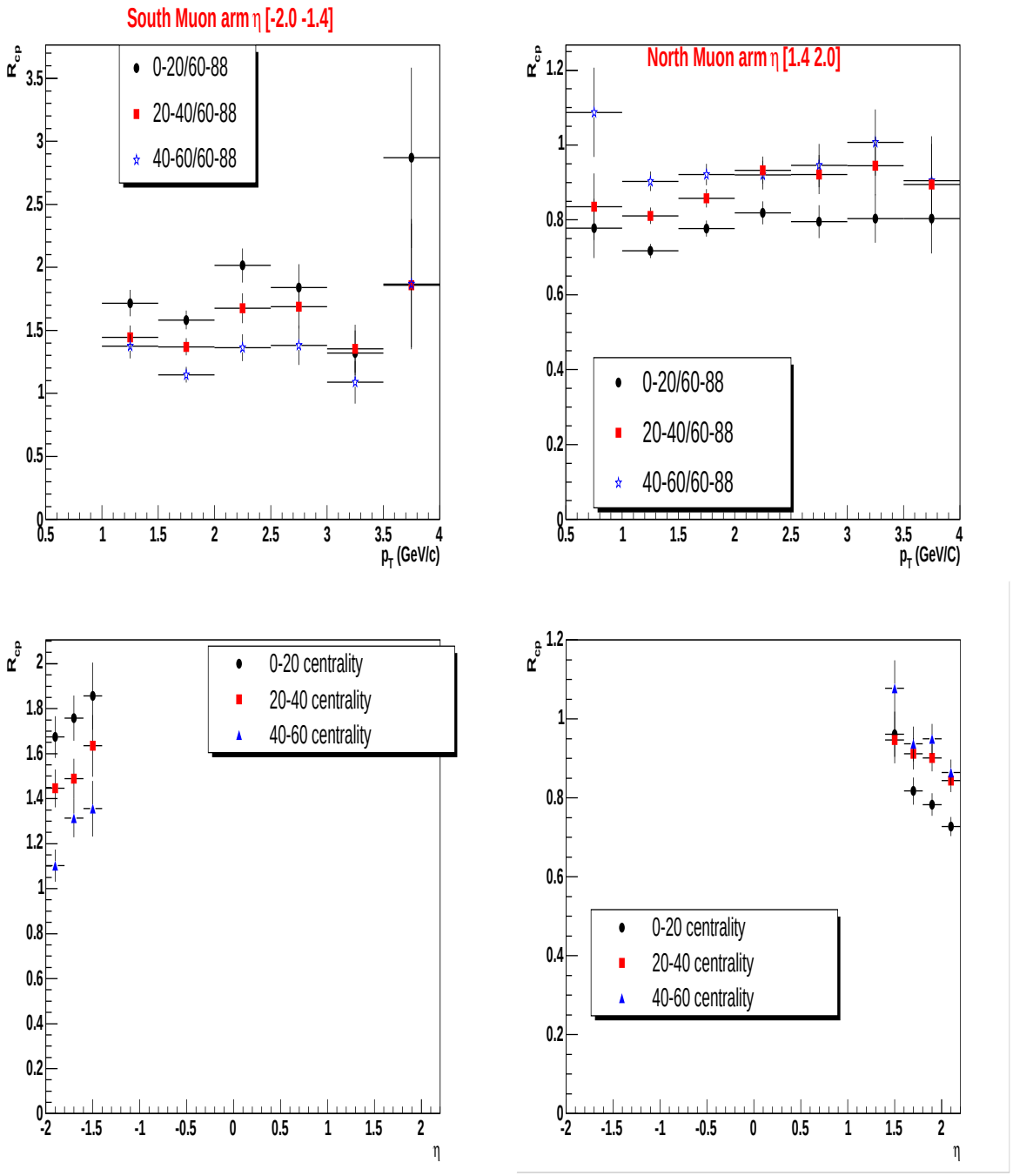

Figure 3.41: R_{cp} when change p_{tot}^{sta1} cut to $5 \times \sigma$ away from muon peak at gap3. Left two panels are south arm hadron R_{cp}, right two panels are north arm hadron R_{cp}, Up is R_{cp} as a function of p_T, bottom is R_{cp} as a function of η.

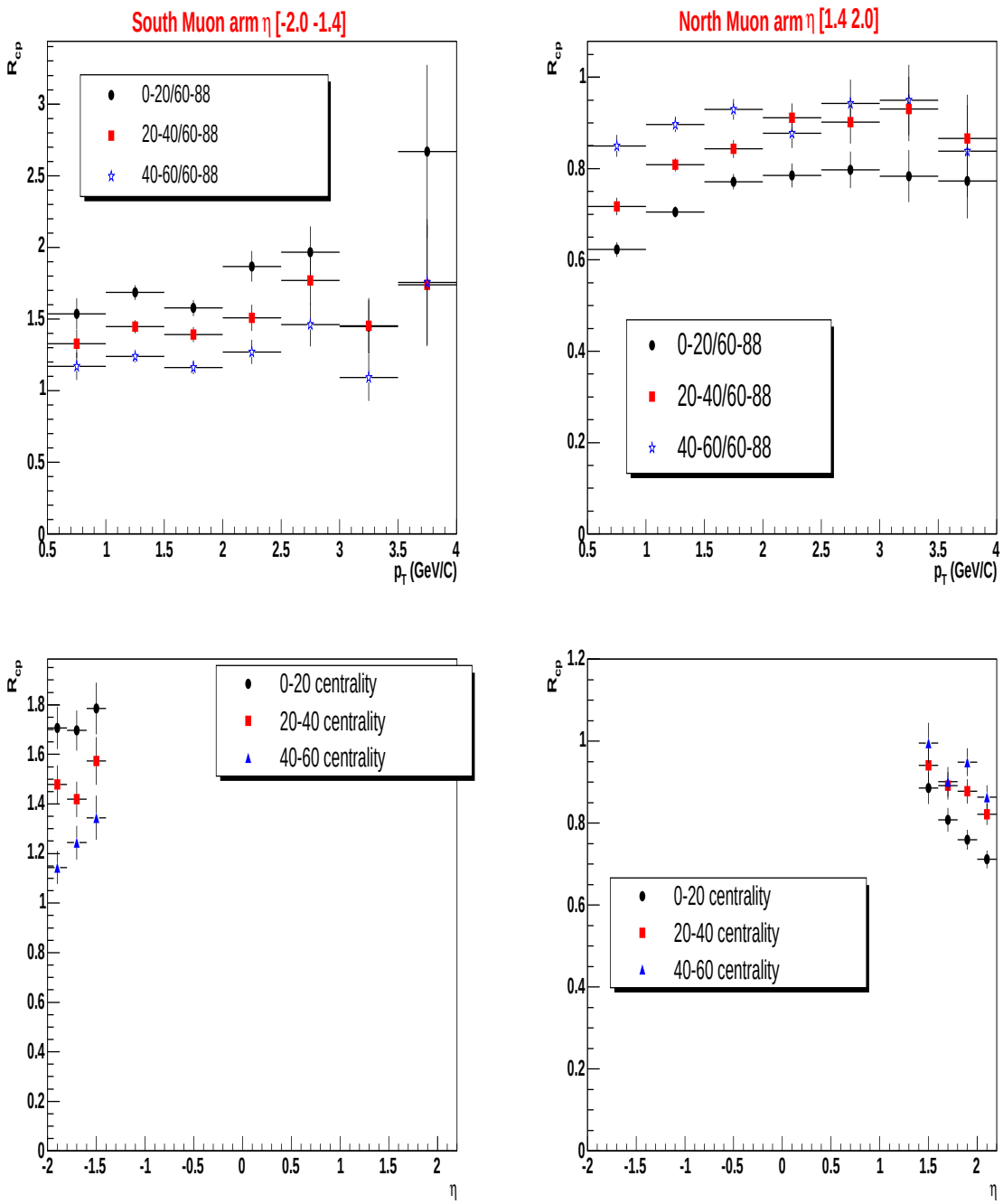

Figure 3.42: R_{cp} when change θ_{xp} cut to 0.06 away from 0.03. Left two panels are south arm hadron R_{cp}, right two panels are north arm hadron R_{cp}, Up is R_{cp} as a function of p_T, bottom is R_{cp} as a function of η.

Table 3.4: Systematic Errors in percentage for south R_{cp}, where we separate the point-by-point systematics from the common systematics.

centrality	p_T (GeV/c)	0.5–1.0	1.0–1.5	1.5–2.0	2.0–2.5	2.5–3.0	3.0–3.5	3.5–4.0
$\frac{0-20}{60-88}$	n_{coll} ratio	10.8	10.8	10.8	10.8	10.8	10.8	10.8
	tracking/ road finding	4	4	4	4	4	4	4
	acceptance	3.4	3.4	2.0	2.1	3.2	3.3	3.8
	χ^2	4	3.1	1.0	2.2	1.7	4.2	4.1
	θ_{xp}	3	3.7	2.3	4.0	4.3	4.4	4.3
	approximity	6	6	6.2	6.1	6.8	6.3	6.3
	p_{tot}^{sta1}	-	1.0	1.1	1.0	0.9	0.9	1.0
	vertex cut	1.2	2.0	2.0	1.8	1.8	1.9	2.2
	subtotal systematics	8.6	8.7	7.7	8.2	9.0	9.6	9.8
$\frac{20-40}{60-88}$	n_{coll} ratio	9.4	9.4	9.4	9.4	9.4	9.4	9.4
	tracking/ road finding	4	4	4	4	4	4	4
	acceptance	3.3	3.1	2.2	2.1	3.1	3.1	3.7
	χ^2	4.2	3.2	1.1	2.1	1.8	4.3	4.2
	θ_{xp}	3.1	3.4	2.4	4.1	4.3	4.3	4.4
	approximity	6	6	6.2	6.1	6.8	6.3	6.3
	p_{tot}^{sta1}	-	1.0	1.1	1.0	0.9	0.9	1.0
	vertex cut	1.2	2.2	2.1	1.8	1.8	2.0	2.1
	subtotal systematics	8.5	8.5	7.5	7.7	9.8	9.5	9.7
$\frac{40-60}{60-88}$	n_{coll} ratio	4.8	4.8	4.8	4.8	4.8	4.8	4.8
	tracking/ road finding	4	4	4	4	4	4	4
	acceptance	3.5	3.5	2.1	2.1	3.2	3.3	3.8
	χ^2	4.1	3.3	1.2	2.2	1.9	4.4	4.2
	θ_{xp}	3.1	3.5	2.2	3.8	4.2	4.1	4.0
	approximity	3	3	3	3.2	3.3	3.1	3.1
	p_{tot}^{sta1}	-	1.0	1.1	1.0	0.9	0.9	1.0
	vertex cut	1.2	2.0	2.3	1.8	2.0	1.9	2.2
	subtotal systematics	6.9	6.3	5.2	5.4	6.3	6.4	6.6

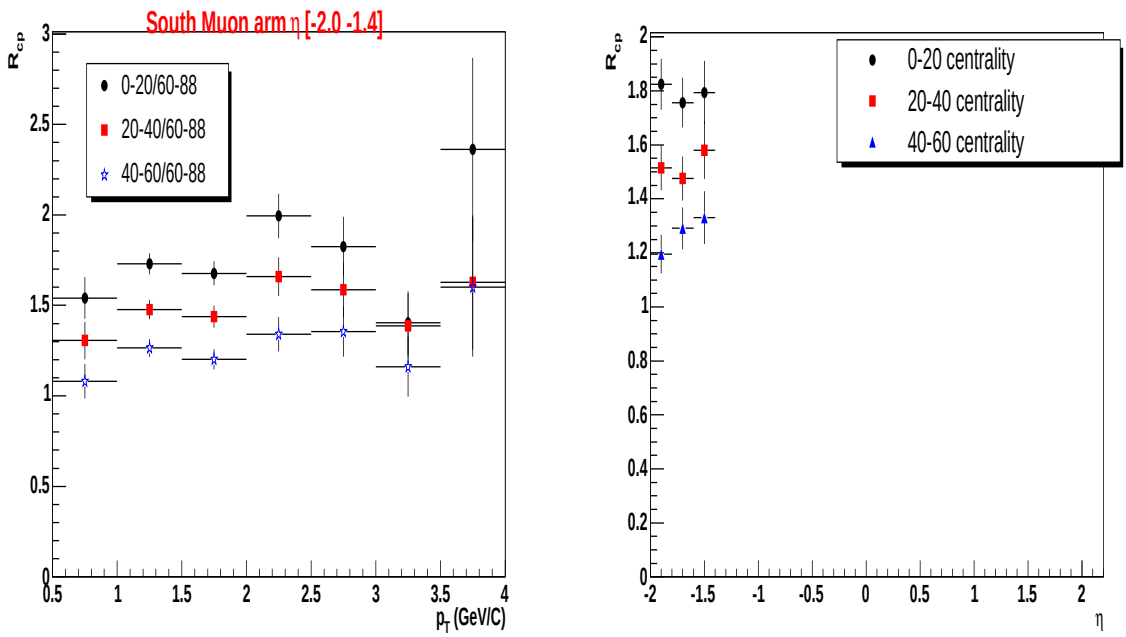

Figure 3.43: R_{cp} when change d_{proxy} cut to 60 away from 30. Left is R_{cp} as a function of p_T, right is R_{cp} as a function of η.

Table 3.5 shows the systematics errors in each p_T bins of north R_{cp}.

Table 3.6 shows the systematics errors in each η bins of R_{cp} and $p_T > 1.5$ GeV/c.

3.4.6 summary

The results of our measurement are summarized as the following plots. Fig 3.44 summarizes the R_{CP} as a function of p_T and Fig 3.45 summarizes the R_{CP} as a function of η. The hadron results are the combined results with minbias and trigger sample. The combination is made by averaging the results with the weights determined by statistic errors. The point to point systematic errors are shown as shaded bars and the common systematic error is shown as the color bar at the right end of $R_{cp} = 1$ line on each panel.

Table 3.5: Systematic Errors in percentage for north R_{cp}

centrality	p_T (GeV/c)	0.5–1.0	1.0–1.5	1.5–2.0	2.0–2.5	2.5–3.0	3.0–3.5	3.5–4.0
$\frac{0-20}{60-88}$	n_{coll} ratio	10.8	10.8	10.8	10.8	10.8	10.8	10.8
	tracking/ road finding	4	4	4	4	4	4	4
	acceptance	4.1	4.4	4.1	4.1	4.2	4.7	4.7
	χ^2	4	3.1	1.0	2.2	1.7	3.2	3.1
	θ_{xp}	2.9	3.3	2.8	4.1	4.4	4.4	4.2
	approximity	1.3	1.2	1.5	2.0	1.5	1.3	1.3
	p_{tot}^{sta1}	3.0	1.4	1.1	1.1	1.1	1.4	1.6
	vertex cut	3.2	3.0	3.0	2.8	3.5	3.4	4.2
	subtotal systematics	7.9	7.2	6.7	7.2	7.4	7.6	8.4
$\frac{20-40}{60-88}$	n_{coll} ratio	9.4	9.4	9.4	9.4	9.4	9.4	9.4
	tracking/ road finding	4	4	4	4	4	4	4
	acceptance	4.0	4.3	4.0	3.9	3.9	4.4	4.7
	χ^2	3.8	3.3	1.2	2.4	1.8	3.1	3.1
	θ_{xp}	3.0	3.3	2.9	4.1	4.2	4.2	4.3
	approximity	1.4	1.3	1.7	2.1	1.6	1.5	1.4
	p_{tot}^{sta1}	3.1	1.5	1.2	1.2	1.2	1.3	1.7
	vertex cut	3.2	3.1	4.1	2.9	3.3	3.5	4.1
	subtotal systematics	7.4	7.1	6.5	7.1	7.3	7.2	8.1
$\frac{40-60}{60-88}$	n_{coll} ratio	4.8	4.8	4.8	4.8	4.8	4.8	4.8
	tracking/ road finding	4	4	4	4	4	4	4
	acceptance	3.1	4.0	3.2	3.4	4.1	4.2	4.2
	χ^2	4	3.1	1.0	2.2	1.7	3.2	3.1
	θ_{xp}	2.9	3.3	2.8	4.1	4.4	4.4	4.2
	approximity	1.0	1.1	1.0	1.0	1.0	1.3	1.3
	p_{tot}^{sta1}	2.1	1.5	1.2	1.2	1.2	1.4	1.6
	vertex cut	3.4	3.2	3.0	2.8	3.3	3.0	4.0
	subtotal systematics	7.4	7.3	6.6	7.2	7.3	7.7	7.4

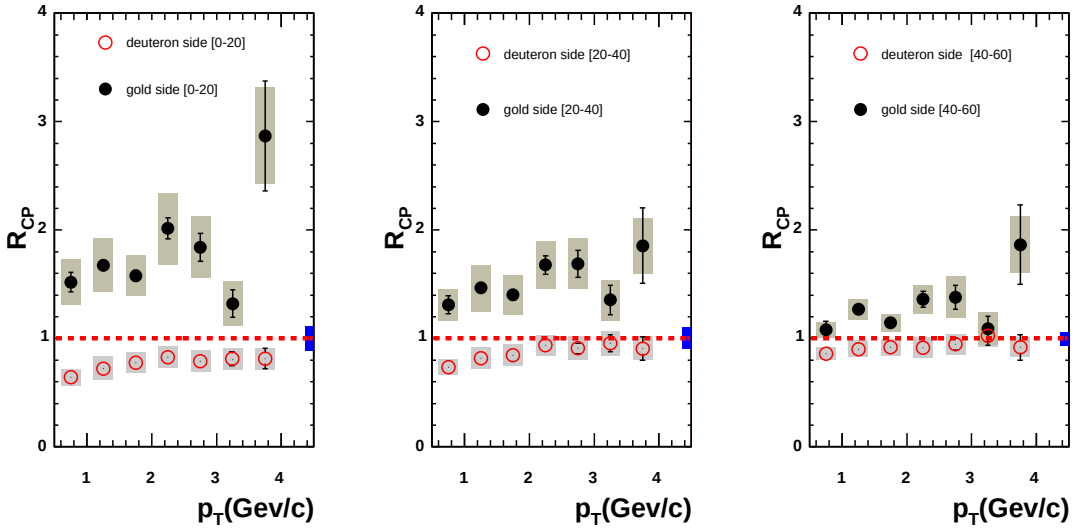

Figure 3.44: R_{CP} as a function of p_T. The left panel is for the most central collisions and the centrality increases from left to right.

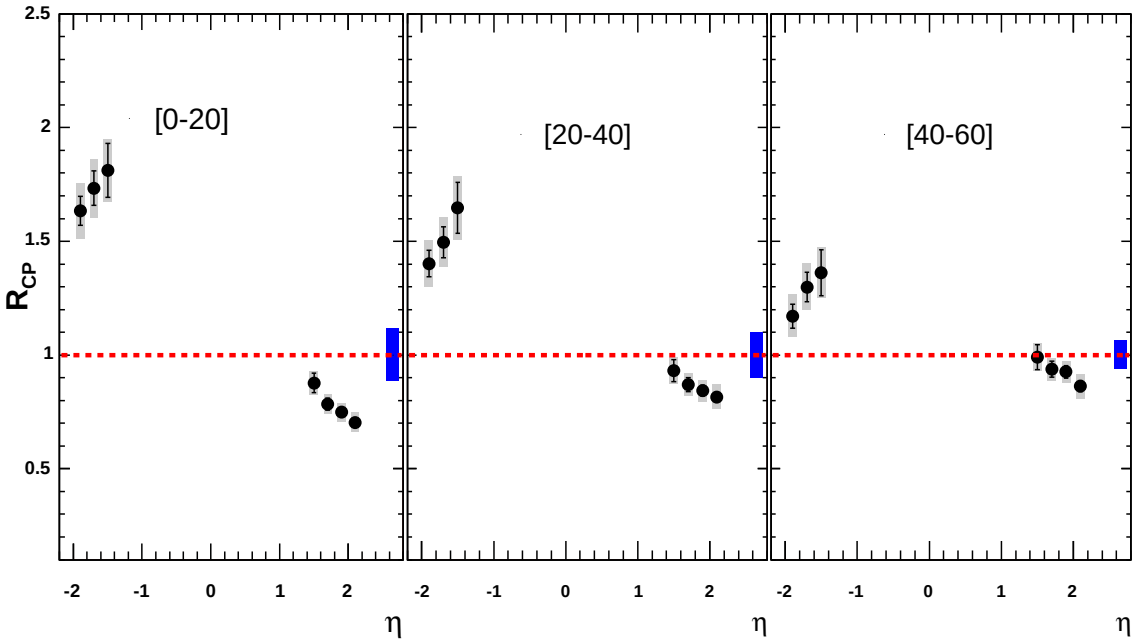

Figure 3.45: R_{CP} as a function of η. The left panel is for the most central collisions and the centrality increases from left to right.

Table 3.6: Systematic Errors in percentage for R_{cp}

centrality	η	-1.9	-1.7	-1.5	1.5	1.7	1.9	2.1
$\frac{0-20}{60-88}$	n_{coll} ratio	10.8	10.8	10.8	10.8	10.8	10.8	10.8
	racking/road finding	4	4	4	4	4	4	4
	χ^2	2.7	2.6	2.6	3.0	2.9	2.9	3.1
	θ_{xp}	3.0	3.3	3.1	4.0	4.3	4.4	4.3
	approximity	6.1	6.2	6.1	1.1	0.8	0.8	1.2
	p_{tot}^{sta1}	1.0	1.0	1.1	1.0	0.9	0.9	1.0
	vertex cut	1.7	1.7	2.0	2.8	2.4	2.2	2.7
	subtotal systematics	7.6	7.6	7.8	5.9	5.8	5.8	6.0
$\frac{20-40}{60-88}$	n_{coll} ratio	9.4	9.4	9.4	9.4	9.4	9.4	9.4
	racking/road finding	4	4	4	4	4	4	4
	χ^2	3.0	2.5	2.6	3.1	2.9	3.0	3.2
	θ_{xp}	3.1	3.2	3.2	3.8	4.3	4.4	4.3
	approximity	5.8	5.8	5.9	1.1	0.8	0.8	1.3
	p_{tot}^{sta1}	1.0	1.2	1.1	1.0	0.9	1.0	1.0
	vertex cut	1.9	1.7	2.0	2.8	2.3	2.2	2.6
	subtotal systematics	7.4	7.6	7.7	5.7	5.8	5.8	6.0
$\frac{40-60}{60-88}$	n_{coll} ratio	4.8	4.8	4.8	4.8	4.8	4.8	4.8
	racking/road finding	4	4	4	4	4	4	4
	χ^2	3.0	2.8	2.7	2.8	2.7	2.9	3.2
	θ_{xp}	3.0	3.0	3.1	3.8	3.6	3.8	4.0
	approximity	4.1	4.2	4.1	1.1	0.8	0.8	1.4
	p_{tot}^{sta1}	1.0	1.0	1.2	1.0	0.9	0.9	1.2
	vertex cut	1.7	1.7	2.0	2.7	2.6	2.4	2.7
	subtotal systematics	6.4	6.6	6.3	5.3	5.1	5.2	5.8

Chapter 4

Study of centrality bias

The study of proton-nucleus or similarly deuteron-nucleus reactions at high energy is a critical part of the relativistic heavy ion program. They allow us to probe "cold nuclear" or initial state nuclear effects in a cleaner environment than in nucleus-nucleus reactions. Many initial state effects are expected to vary as a function of the impact parameter of the collision or as a function of the number of collisions suffered by the incoming projectile. Thus, a crucial manner of extending our sensitivity to these effects is to experimentally categorize different "centrality" classes of deuteron-gold reactions. In this note we outline a method, building upon previous work detailed in PHENIX Analysis Notes 209 [54] and 210 [52], for selecting different centrality classes and how to categorize them in terms of the underlying distribution of binary nucleon-nucleon collisions (including the average $< N_{binary} >$).

4.1 Introduction

In this analysis, we have decided to use the response of the south (gold going-direction) Beam-Beam Counter (BBCS) for categorizing events into various deuteron-gold centrality classes. From previous proton-nucleus experimental results and from simulations, it is expected that the number of charged particles in the backward (gold going-direction) rapidity should be roughly proportional to the number of participating nucleons in the gold nucleus. Thus, it has been proposed to select event categories on the real data by dividing the BBCS hit distribution into percentiles

(with discrete BBCS nhit ranges). Then one can model the BBCS response as a superposition of nucleon-nucleon collisions and attempt to determine the underlying distribution of the number of binary collisions that each percentile represents.

Ideally the physics used to determine the centrality class would be completely independent (factorizable) from the physics signal we are interested in. Looking at recoil nucleons from the gold nucleus may be a possible observable for doing this. The forward calorimeter (FCAL) was constructed for this purpose, but has not been available for analysis on the time scale of this analysis note. The BBCS counter is good in the sense that it is separated in rapidity from the central arms by almost 3 units and by more than 1 unit from the small angle part of the south muon arm acceptance. However, what has been observed by PHENIX and other experiments in proton-proton reactions, is that there is an "underlying" event correlation with specific physics processes. In reactions with a parton-parton hard scattering, the charged particle multiplicity over a broad range of rapidities is increased. Within a narrow cone one would also expect an increase from correlated jet fragmentation products, but this "underlying" event correlation cannot be removed by a large rapidity gap between the BBCS and central arm detectors. It is also notable that this correlation may be different for different physics processes.

There are two significant effects that arise from this physics process - BBCS response correlation.

4.1.1 Trigger Bias Effect

One is referred to as a trigger bias effect, and was originally discussed in PHENIX Analysis Note 209. We prefer to think in terms of invariant yields rather than cross sections, and so the proceeding discussion will use that language. In a proton-proton reaction we want to measure the the true number of produced pions (for example) divided by the number of true inelastic reactions.

$$Y_{\pi}^{true} = \frac{N_{\pi}^{true}}{N_{inel.coll}^{true}} \tag{4.1}$$

However, what we often measure is the number of pions in events where the BBCLL1 trigger fires and the number of inelastic collisions where the BBCLL1 trigger fires. We realize that for pions in the central arms we have also measured pions without the BBCLL1, but we continue with the pion case as our example to make the point clear.

$$Y_{\pi}^{measured} = \frac{N_{\pi}^{measured}}{N_{inel.coll}^{measured}} \tag{4.2}$$

From simulation and real data studies with alternate triggers without BBCLL1, we know that we measure 0.75 of the true pions with $p_T > 1.5$ GeV by the requirement of BBCLL1. We also know that we measure 0.52 of the true inelastic reactions by the requirement of BBCLL1. In this formalism we must correct the measured pions by 1.0/0.75 and the number of reactions by 1.0/0.5. This results in a multiplicative correction of $0.52/0.75 = 0.693$ applied to the $Y_{\pi}^{measured}$ to obtain Y_{π}^{true}. The trigger bias comes from the fact that hard parton-parton reactions that produce high p_T pions fire the BBCLL1 more easily simply because they produce more charged particles, on average, that can hit the BBC. A similar effect occurs in deuteron-gold reactions and needs to be corrected for. We expect this trigger bias to be smaller for deuteron-gold reactions and only a significant effect in the most peripheral reactions.

4.1.2 Bin Shifting Effect

A second bias occurs in deuteron-gold centrality selected analysis that is not there in proton-proton reactions. This bias is related to how we categorize reactions into different centrality classes using the BBCS. The true invariant yield in each category is:

$$Y_{\pi}^{true}(i) = \frac{N_{\pi}^{true}(i)}{N_{coll}^{true}(i)} \tag{4.3}$$

where i is the index over 1,2,3,4 for the centrality categories. Again, what we measure experimentally is:

$$Y_{\pi}^{meas}(j) = \frac{N_{\pi}^{meas}(j)}{N_{coll}^{meas}(j)} \tag{4.4}$$

where j is the index over 1,2,3,4 for the measured centrality categories. However, in the measurement case the centrality category is not guaranteed to be correct (unbiased) since it is based on the real BBCS detector.

As an example of this bias, an interaction with nbinary=3 may normally fall into the peripheral centrality category. However, it may have an enhanced probability for larger BBCS if the event contains a high p_T pion and thus has a larger probability to land into the next higher centrality - mid-central - category. Therefore, more measured pions are shifting out of the peripheral bin relative to regular events. From this effect we expect to see an artificial reduction in $Y_{\pi}^{meas}(j = 1)$ relative to $Y_{\pi}^{true}(i = 1)$. Thus for the peripheral category, this bin shifting effect gives an opposite bias than the trigger bias effect mentioned in the previous section. For the most central category, we expect more pions shifting into that category from the mid-central and thus see an artificial enhancement of $Y_{\pi}^{meas}(j = 4)$ relative to $Y_{\pi}^{true}(i = 4)$.

4.2 What Really Defines Our Event Category?

One point that often raises much confusion is what really defines our event categories (which gives us our definition for the "truth"). In fact, there are multiple ways of approaching this problem. We argue that one good method is to define the true event category in terms of a true distribution of nbinary collisions. In this manner, one can run a Monte Carlo Glauber simulation and a modelling of the BBCS response. Knowing the true nbinary for each event, one can calculate the "true" yield where every event is put exactly correctly into its event category. Then one can use the

simulation of the BBCS response (and its correlation with physics processes) to calculate the "measured" yield where every event is not necessarily put into its correct event category and not every event gets put into a category at all due to the BBCLL1 trigger requirement. Then one can simply calculate the correction factor to convert our measured yield into the "true" yield.

For completeness, we outline below other possible options that have been discussed. 1. We calculate invariant yield as the number of produced pions divided by number of events for a given BBCS hit range. This means using the BBCS hit range to fundamentally define the centrality category. We apply no corrections to pions or events and tell theorists where to find our full GEANT simulation of the BBC. There is nothing incorrect in this option, but it is not viable to maximize the impact of our results in the community.

2. We decide that the BBCS hit range (say 45-100 for most central) defines the event category. We thus calculate the invariant yield with no correction to the pions or events. However, our category has no meaning outside of PHENIX and people with the GEANT simulation. Thus, we attempt as best we can to characterize this category in terms of a distribution of nbinary (or just a mean value). Since there are correlations between different processes and the BBC hits (as has been clearly demonstrated), the characterization of a category defined as BBC South Hits 45-100 will actually be different depending on whether our measure is of high pt pions, low pt pions, J/ψ or otherwise. Thus the 00-20% central for high pt pions may have a different $< Nbinary >$ than the 00-20% central for low pt pions.

3. This is the method we started with and will use in this analysis note. We decide that a fixed distribution of nbinary with a given mean nbinary defines our event category. What we measure as 00-20% central with the BBC cannot exactly match this category for all processes. Thus, we correct the measured yield per event to be the equivalent of the yield per event in our nbinary defined event category. That way we have corrected the yield for all processes to a common set of event category definitions. These nbinary distribution as our category definition should

be published (not just the mean values).

In fact, the label 00-20% is not really needed and in many ways is confusing. It only represents something with true meaning with the full PHENIX GEANT of BBC. The real meaning is in the nbinary distribution that defines the category. Of course, we use an nbinary distribution to define the category that is close to that expected from BBC in an attempt to minimize the correction factors.

4.3 Modelling the Physics and Defining Our Categories

In this section we give all details on the procedure for modelling the BBC response (in a data driven manner) and determining the definitions of our event categories. Here we follow many of the details and assumptions of PHENIX Analysis Note 210, except to use proton-proton data instead of a tuned negative binomial distribution input.

We use a Glauber model [53] of deuteron-gold reactions with identical parameters from PHENIX Analysis Note 210. The true minimum bias distribution of the number of participants from the gold nucleus and the number of binary collisions are shown in Figure 4.1.

We hypothesize that the number of charged particles firing the BBC South is proportional to the number of participants from the gold nucleus in the reaction. This is the same assumption used in PHENIX Analysis Note 210. Note that there is not a large difference if one included the deuteron participants as well. Thus, here we view the BBCS response as a superposition of the response from N_{targ} independent proton-proton type reactions, where N_{targ} is the number of gold target participants.

In order to complete the modelling, we need to know the BBCS response in proton-proton inelastic reactions with no bias, and also the BBCS response in proton-proton inelastic reactions where the BBCLL1 has fired. We then need to determine these same two distributions in the case of a proton-proton reaction that produces a high p_T pion, for example. We will discuss how we determine these four

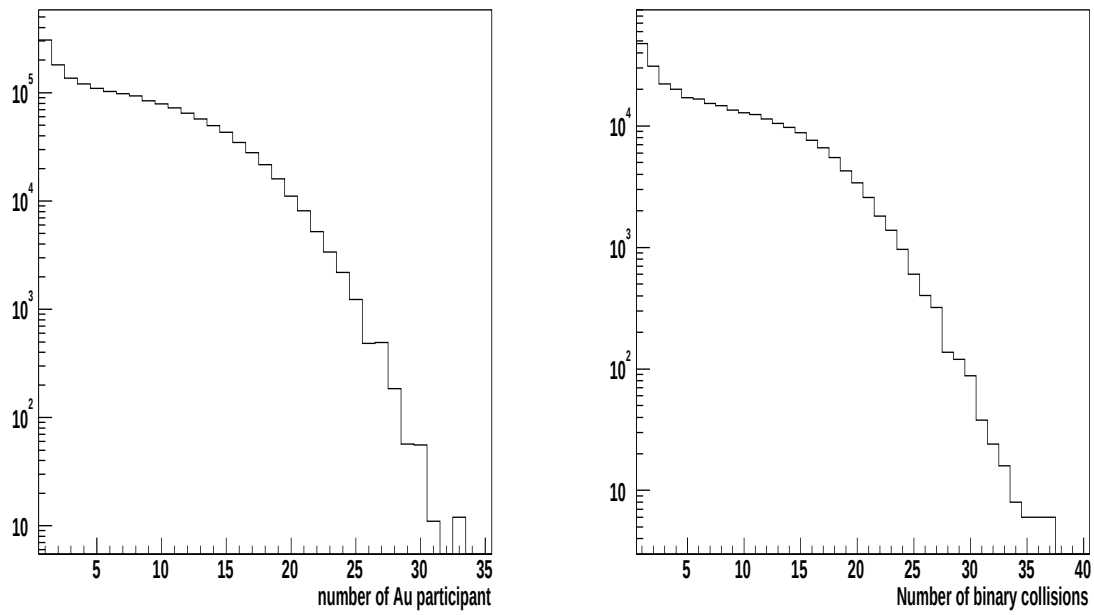

(a) (b)

Figure 4.1: Number of Participants from the Gold Nucleus (left) and Number of Binary Collisions (right) distribution from Glauber model for true minimum bias deuteron-gold reactions.

distributions in the next section. We can then calculate the distribution of BBCS hits for deuteron-gold reactions that fire the BBCLL1. We simply run through the Glauber events, sample BBCS hits for each N_{targ}, sum them, and require that at least one of the N_{targ} scaled reactions fired the BBCLL1 trigger. The resulting distribution compared with experimental data from deuteron-gold BBCLL1 events is shown in Figure 4.2. Although the agreement is certainly not perfect, the calculation appears to follow the general features of the data distribution on a log scale. Recall that we are using this data driven modelling to determine the bias corrections. In the end we will compare our results with those from PHENIX Analysis Note 210 for the $< nbinary >$ and in the last section of this note vary different parameters to set appropriate systematic errors.

From previous studies - and confirmed in our study - the BBCLL1 trigger fired on 88% of the deuteron-gold inelastic cross section. Thus, consistent with previous

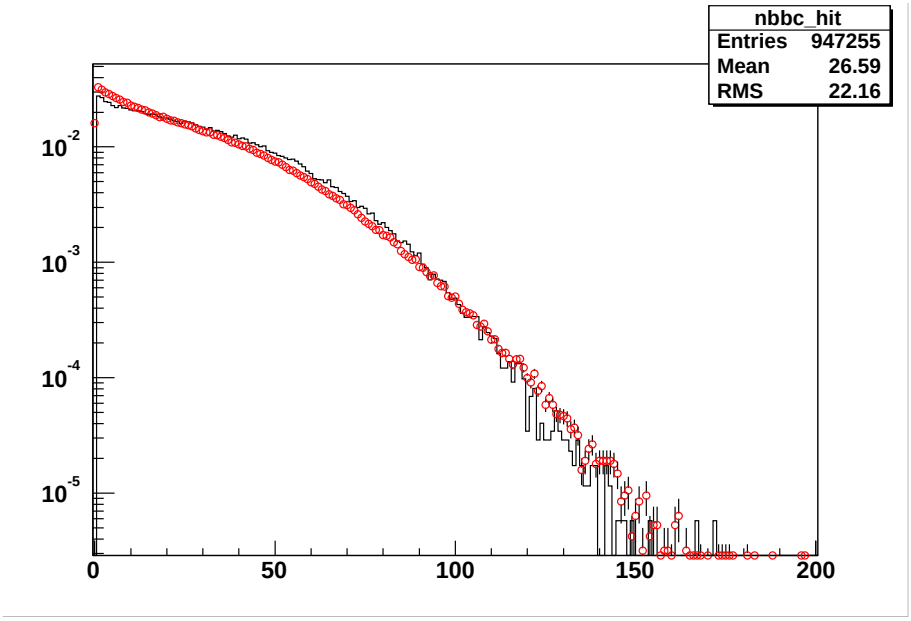

Figure 4.2: Comparison between the calculated deuteron-gold BBCS nhit distribution requiring BBCLL1 firing (solid line) and the experimental data distribution from deuteron-gold in real BBCLL1 selected events (open circles).

computations, we divide our results into four centrality bins 00-20%, 20-40%, 40-60%, 60-88%. These percentages refer to fractions of the BBCS distribution within a specified range of BBCS cut values. Shown in Figure 4.3 (left panel) is the modelled BBCS distribution as divided up into these four bins. Although we have used the N_{targ} for scaling our BBCS distribution, in the Glauber calculation for each event we know the N_{targ} and the N_{binary}. Thus, we can perfectly calculate the N_{binary} distribution that is associated with each of these centrality selections. These distributions are shown in Figure 4.3 (right panel).

Table 4.3 shows the $< nbinary >$ for each category and the lower and upper BBCS selection on our simulation.

At this point, we define our "true" centrality categories in terms of these N_{binary} distributions. This choice of definition is arbitrary, but as long as we use this definition consistently it provides what we believe is a good choice. We have chosen this "true" categorization to closely match the "measured categories" for BBCLL1 real data events. Now for each specific physics process, the correlations with BBCS

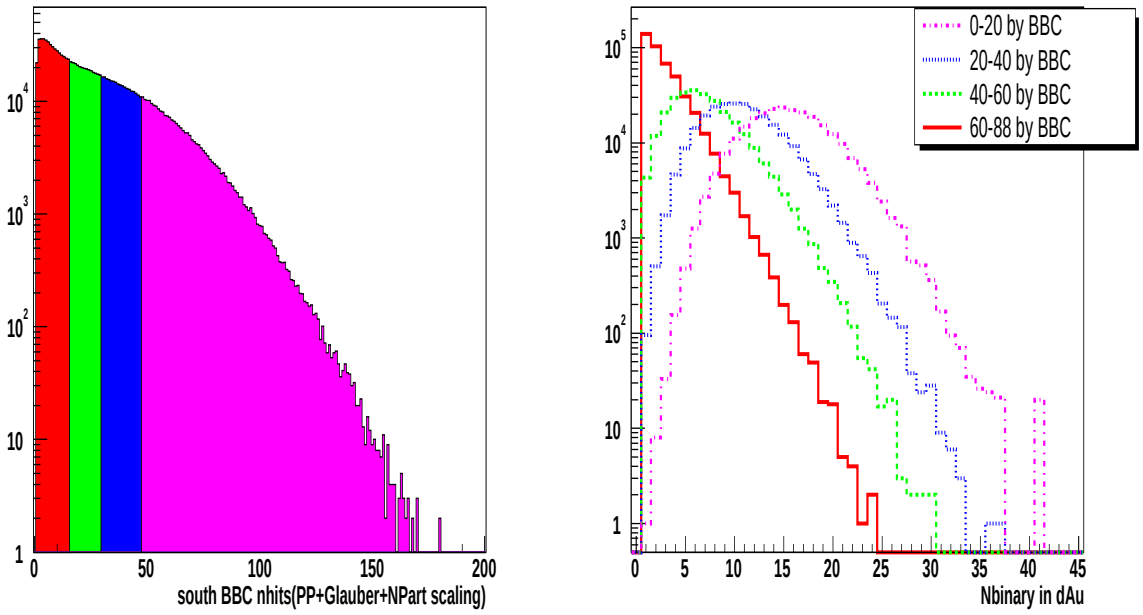

(a) (b)

Figure 4.3: Left Biased inclusive BBC nhit distribution sliced into centrality bins according to percentage. Right the corresponding nbinary distributions.

Table 4.1: Summary of centrality bins we used in our study.

BBC defined centrality	$0-20\%$	$20-40\%$	$40-60\%$	$60-88\%$
nbinary for inclusive	15.64	10.86	7.0	2.94
minimal nhit	48	30	16	1
maximum nhit	∞	47	29	15
nbinary for Process C	16.51	10.92	6.80	2.83
nbinary for Process S	16.51	10.92	6.77	2.80
nbinary for Process N	16.29	10.92	6.80	2.88

will induce a bias in each measurement relative to our "true" category which we need to calculate and then correct for. Again, this leads to the situation where all PHENIX results will have a completely common definition in terms of N_{binary} for each centrality bin.

For completeness, we include the biased $< N_{binary} >$ values for different processes in Table 1. Thus, if we had wanted to follow through with method 2, we could have re-categorized each centrality bin, instead of correcting the yield. One can use these numbers to prove that the corrections are equivalent.

4.4 Data Driven Input Distributions

As mentioned in the previous section, for determining the correction factors we require the BBCS distribution in unbiased events, BBCLL1 fired events and the same two distributions for each physics process we are interested in.

In this analysis note, we are interested in three categories of physics processes.

- High $p_T(> 1.5 Gev/c)$ charge particle produced in the PHENIX Central Arm. We call it Process C.
- High $p_T(> 1.5 Gev/c)$ charge particle produced in the PHENIX South Muon Arm. We call it Process S.
- High $p_T(> 1.5 Gev/c)$ charge particle produced in the PHENIX North Muon Arm. We call it Process N.

Here we define a few terms that we will continue to use in our discussion. Processes C/S/N are all "hard processes", so we call them "hard events". Any inelastic collision which can be hard or soft, we will refer to as "inclusive events".

4.4.1 BBCS Response in Proton-Proton Collisions

The two types of BBCS distributions we need are unbiased and BBCLL1 biased. The BBCLL1 biased BBCS nhit distribution can be obtained straightforwardly. We

have plenty of statistics from BBCLL1 trigger selected data. However, it is not so straightforward to reconstruct the unbiased BBCS nhit distribution. One can examine clock triggered data to study these distributions. But, the reason it is difficult is that for those events which do not satisfy the BBCLL1 trigger, it means that either the North BBC or South BBC has no hit at all (or the z-vertex is not in range). In these events it is difficult to evaluate the noise contribution to the BBC nhit distribution, especially for the $nhit = 1$ bin (i.e. one tube hit in one BBC and no tube hit on the other side BBC).

We are able to minimize this problem in the following manner:

- Use the non-BBCLL1 trigger data (e.g. clock triggers) to determine the correlation between the south BBC and north BBC for $nhit \geq 1$. This correlation can be represented by the probability of north BBC firing as a function of south BBC nhit, $P(nhit_{north} \geq 1 \mid nhit_{south})$.

- Since we know from previous studies that the BBCLL1 trigger fires on 0.52 of the inelastic proton-proton events and the BBCLL1 trigger fires on 0.75 of the inelastic proton-proton events with a hard process (e.g. high p_T pion), we normalize the BBCLL1 biased distribution for inclusive events to 0.52, and the distribution for hard events to 0.75.

- Divide the normalized BBCLL1 biased distribution by the $P(nhit_{north} \geq 1 \mid nhit_{south})$. Thus, we reconstructed the unbiased distributions for $nhit \geq 1$.

- Then the $nhit = 0$ bin for each unbiased distribution is determined by the the total normalization of the unbiased distribution to one.

Figure 4.4 shows the BBCLL1 biased and unbiased south BBC nhit distributions for inclusive events and hard events from non-BBCLL1 trigger data. Figure 4.5 shows how $P(nhit_{north} \geq 1 \mid nhit_{south})$ varies with south BBC nhit.

In order to determine these distributions we used the $CLOCK$ trigger data for the inclusive case, ERT_GAMMA2 trigger data for the process C case, $MUIDS_1D1S\&NTCS$

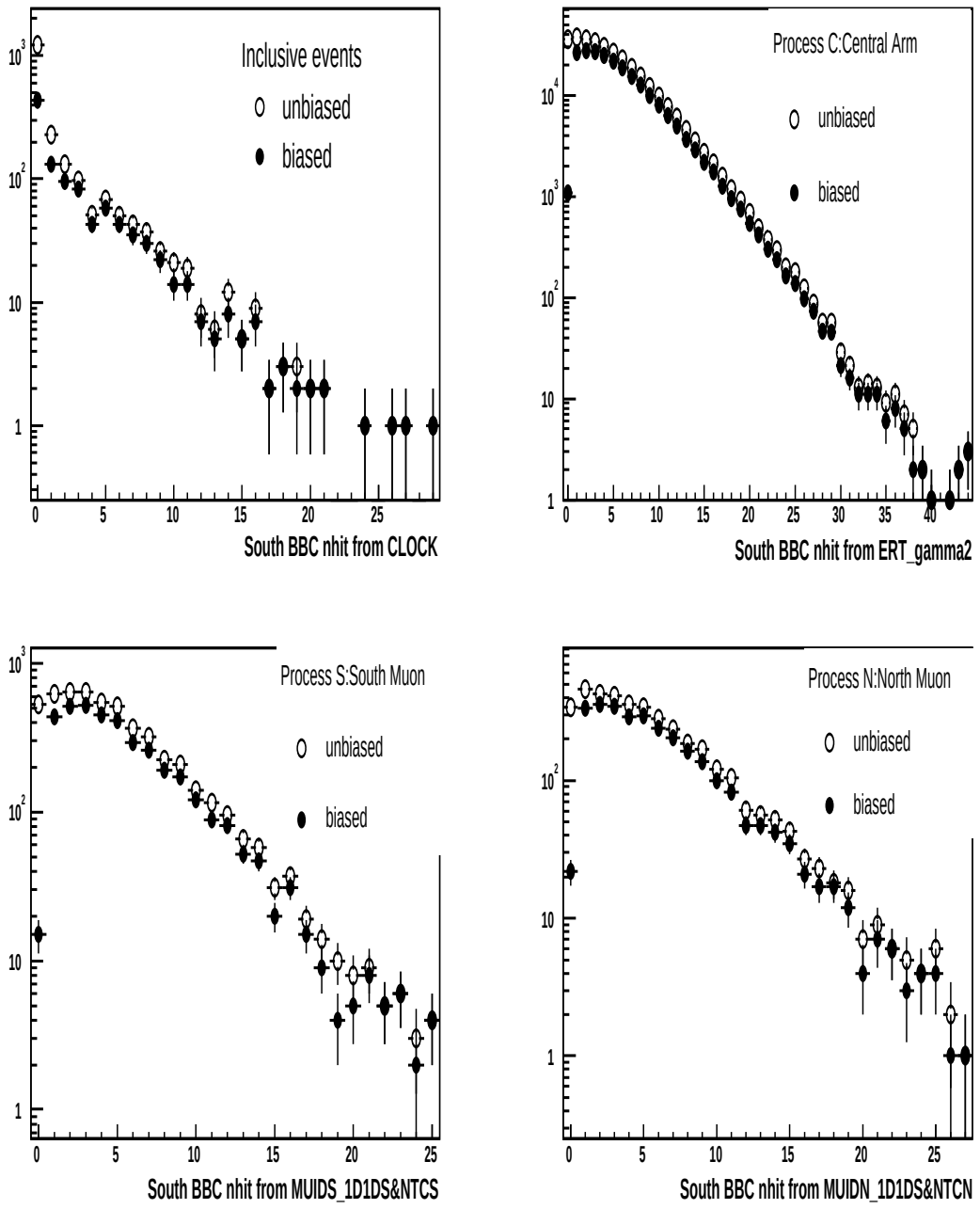

Figure 4.4: South BBC nhit distribution from non-BBLL1 trigger data. Open circles are the unbiased distributions. Close circles are distributions biased by requiring north BBC $nhit \geq 1$

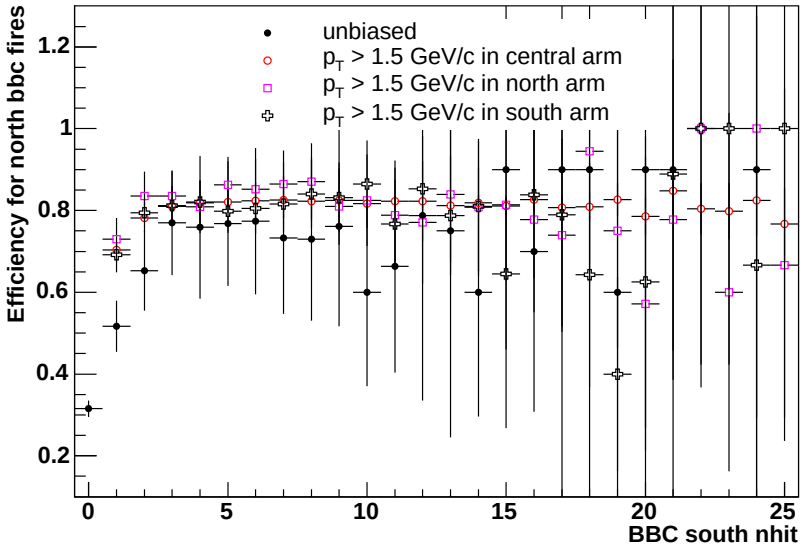

Figure 4.5: $P(nhit_{north} \geq 1 \mid nhit_{south})$ distributions for different event categories.

trigger data for the process S case and $MUIDN_1D1S\&NTC$ trigger data for the process N case.

For non-BBCLL1 trigger events, there is no guarantee for having BBC vertex information in the events. Thus we use the PHENIX Pad Chamber(PC) tracks to reconstruct the collision vertex. We call this vertex vtx_{PC}. vtx_{PC} is a relatively good approximation for collision vertex which is normally reconstruction by BBC vertex(vtx_{BBC}). The tracks used to reconstruct vtx_{PC} are selected by the following criteria.

- Track quality has to be 31 or 63 if a BBC vertex is found, otherwise it can also be 7.
- $\mid pc3sdz \mid < 2.5$ cm if a BBC vertex is found.
- $\mid pc3dphi \mid < 2.5$

Figure 4.6 shows the difference between vtx_{PC} and BBC vertex. Here is a list of all the criteria for selecting inclusive events, central arm tracks and muon are tracks.

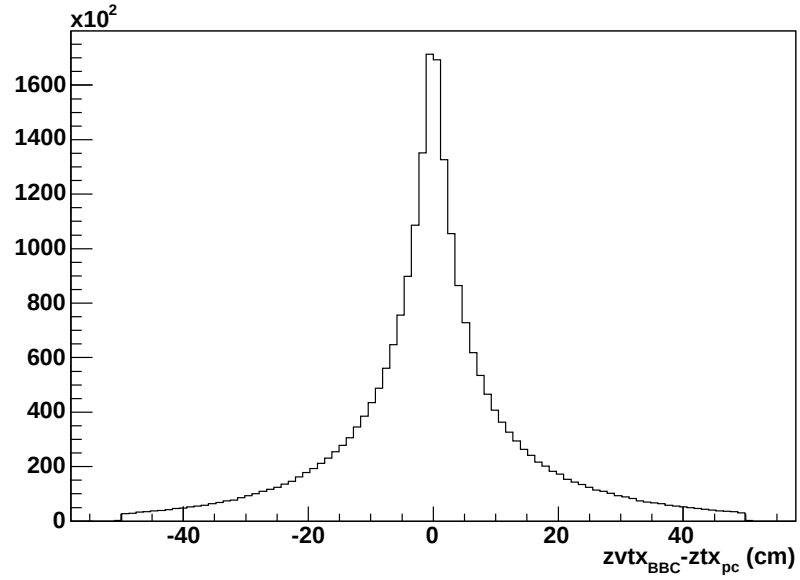

Figure 4.6: Difference between the PC track calculated vertex and BBC vertex.

- Inclusive events, $\mid vtx_{PC} \mid < 30$ cm.
- Process C events, $\mid vtx_{PC} \mid < 30$ cm and at least one track, which passes the same criteria as those applied when we calculated vtx_{PC}, has $p_T > 1.5 GeV/c$
- Process N/S events, $\mid vtx_{PC} \mid < 30$ cm, and at least have one track with $\chi^2 < 20$, depth in MUID ≥ 2 as well as $p_T > 1.5$GeV/c.

For Muon arm tracks, we can also calculate a vertex(vtx_{muon}) in the same way as we do for central arm tracks. For process N/S events, besides the criteria listed above, we further require that $\mid vtx_{muon} \mid < 30$ cm. Here we assume the BBCLL1 covers the same fraction of total cross section for the process C/S/N. In fact this is not a bad assumption because the difference in $P(nhit_{north} \geq 1 \mid nhit_{south})$ between different processes is less than 10%. Figure 4.7 summarizes the results from this procedure. Again, we will vary this in determining final systematic errors.

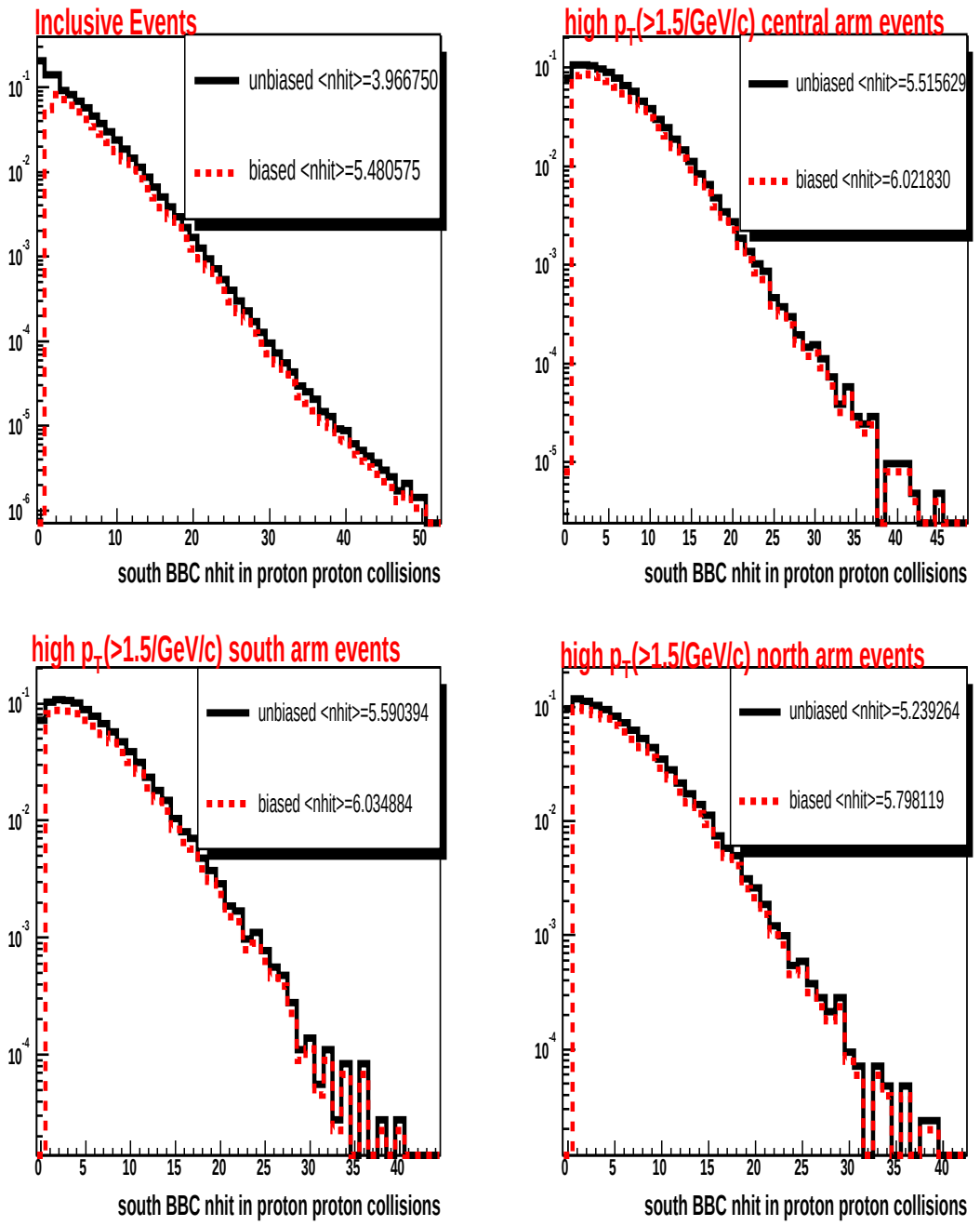

Figure 4.7: South BBC nhit distribution for different events categories. The solid lines are the unbiased distributions, which are recovered from above procedures. The dashed lines are BBCLL1 biased distributions, which are taken from the BBCLL1 trigger selected data.

4.5 Modeling the Full Deuteron-Gold Case

In order to simulate the BBCS and BBCLL1 response in deuteron-gold collisions, we need the following input:

- N_{targ} and N_{binary} distribution from the Glauber Model (or the Glauber model contained in HIJING [56]).
- BBC response in proton-proton collisions (i.e. the south BBC nhit distributions in $nbinary = 1$ collisions). Two kinds BBC nhit distributions are needed here. And we need them for all the three physics processes in addition to inclusive events. One is the distribution without BBCLL1 trigger fire condition, so called unbiased distributions. The other one is the distribution with BBCLL1 trigger fire condition, so called BBCLL1 biased distributions.
- We assume the BBC South response in deuteron-gold collisions for inclusive events follows the N_{targ} scaling.
- We assume hard processes follow N_{binary} scaling, but then vary this assumption for determining systematic errors.
- The probability for having a hard collision is so small that no more than one hard NN collision is considered to occur in one deuteron-gold reaction. Considering cases with more than one hard NN collision is a very small higher order effect.
- The BBCLL1 covers 52% of the total inelastic cross section for NN reactions, but covers 75% of the NN reactions that contain at least one high $p_T(> 1.5GeV/c)$ particle. We consider variations of these numbers as part of our systematic errors.

We use a Monte Carlo method to simulate the deuteron-gold BBC response. The program follows the steps outlined below.

- 1.) We sample N_{targ} and N_{binary} on an event by event basis from the PHENIX standard Glauber model.

- 2.) For the inclusive process, we sample the inclusive unbiased BBC nhit distribution (shown in the previous

  section) N_{targ} times, then sum all the BBCS nhits.

$$nhit_{dAu}^{inclusive} = \sum_{i=1}^{N_{part}} nhit_{i_{th}NN}^{inclusive}$$

- 3.) For hard process, we sample the inclusive unbiased BBC nhit distribution $N_{part} - 1$ times and sample the corresponding hard process unbiased BBC once. Then we sum all the sampled nhits.

$$nhit_{dAu}^{hard} = \sum_{i=1}^{N_{part}-1} nhit_{i_{th}NN}^{inclusive} + nhit_{NN}^{hard}$$

- 4.) We determine if any of the individual modeled NN reactions would fire the BBCLL1 trigger. If at least one would fire the trigger, then the deuteron-gold reaction is considered to have fired the BBCLL1 trigger. Note that this ignores the probability that one NN reaction fires just BBCN and one other NN reaction fires just BBCS, and thus combined they fire the trigger.

- 5.) The probability for having a hard process in the deuteron-gold reaction is given by a probability for a hard process in proton-proton times the number of binary collisions. In the final correction factors, the probability for a hard process in proton-proton reactions drops out of the equation.

In the above procedure, the decision of whether a Monte Carlo event fires the BBCLL1 trigger or not is done as follows. For each NN collision, after a BBCS nhit is sampled from the unbiased distributions, the ratio between the content of nhit bin in the biased distribution and content of the same bin on unbiased distributions is compared with an random number uniformly distributed from 0 to 1. If the ratio

is larger than the random number, this NN collision fires the trigger. As long as one NN collision fires the trigger, the Monte Carlo deuteron-gold event fires the trigger.

4.6 Calculating the Correction Factors

We want to calculate in the Glauber Monte Carlo the "true" yield and the "measured" yield for each centrality bin. The correction factor $C.F.$ is then the multiplicative correction to equate the two.

$$Y_{\pi}^{true}(i) = C.F. \times Y_{\pi}^{meas}(i) \tag{4.5}$$

Below we give an outline of the code algorithm. The code itself is checked into CVS.

- 1. Int Num-True-Events[event-class] = 0
- 2. Int Num-Meas-Events[event-class] = 0
- 3.
- 4. Loop over all Glauber MC Events
- 5. [
- 6. Determine from number of binary collisions the true-event-class
- 7. Num-True-Events[true-event-class]++;
- 8.
- 9. Model BBCS Response using proton-proton distributions summed over N_{targ}
- 10. Determine meas-event-class from modeled BBCS response
- 11. Determine if this event would fire the BBCLL1 trigger (Bool trig-fire)

- 12.
- 13. if (trig-fire) {
- 14. Num-Meas-Events[meas-event-class]++;
- 15. }
- 16.
- 17.]

Then we do a second loop over events for the pions (for examle).

- 18. Float Num-True-Pions[event-class] = 0
- 19. Float Num-Meas-Pions[event-class] = 0
- 20.
- 21. Float prob-pion-per-nbinary = some-value (this cancels out at the end anyway)
- 22.
- 23. Loop again over all Glauber MC Events
- 24. [
- 25. Determine from number of binary collisions the true-event-class
- 26. Num-True-Pions[true-event-class] += prob-pion-per-nbinary * nbinary
- 27.
- 28. Model BBCS response using proton-proton distributions summed over N_{targ}

- 29. *For one ntarg used BBCS response for hard process event and for all others use unbiased inclusive
- 30.
- 31. Determine meas-event-class form modeled BBCS response
- 32. Determine if this event would fire the BBCLL1 trigger (Bool trig-fire)
- 33.
- 34. if (trig-fire) {
- 35. Num-Meas-Pions[meas-event-class] += prob-pion-per-nbinary* nbinary
- 36. }
- 37.
- 38.]

And then for the final correction factor:

- 39. Yield-True[i] = Num-True-Pions[i] / Num-True-Events[i]
- 40. Yield-Meas[i] = Num-Meas-Pions[i] / Num-Meas-Events[i]
- 41. Yield-True[i] = C.F. $\times$ Yield-Meas[i]

The results for the Correction Factors (C.F.) for different processes are summarized in Table 4.2. The corrections have already combined both the trigger bias effect and the bin shifting effect as detailed above.In the table the column for correction implies the types of the correction factor listed in the table. We list the trigger bias correction factor besides the total correction factor (bin shifting + trigger bias). Note that only the total correction factor is applied, and we show the trigger bias separately just for completeness.

Table 4.2: Summary of centrality bias corrections

Processes	correction	$0-20\%$	$20-40\%$	$40-60\%$	$60-88\%$	$0-88\%$
Process C	total	0.95	0.99	1.03	1.04	0.94
Central arm	trigger bias	1.00	0.99	0.97	0.85	0.94
Process S	total	0.95	0.99	1.04	1.05	0.94
South arm	trigger bias	1.00	0.99	0.97	0.85	0.94
Process N	total	0.96	0.99	1.03	1.02	0.94
North arm	trigger bias	1.00	0.99	0.97	0.85	0.94

Some people have noted that the correction for the most central events of order 5% seems large given that only one NN collision out of perhaps ten in the deuteron-gold reaction is biased. The key to understanding this effect is that on a linear scale the BBCS distribution is falling exponentially with increasing BBCS. For the 00-20% central bin, events are required to have $BBCS \geq 48$ hits. However, if only one NN reaction were biased such that it gave just one extra BBCS hit, this would mean that all events with a high p_T pion that would have had $BBCS \geq 47$ would get included in the central bin. If one integrates the real data BBCS hit distribution from 47 and up compared with 48 and up, it makes a 4% difference. This is quite consistent with the level of bias we thus expect and is reflected in our correction factors.

4.7 Systematic Error Studies

In our study, the possible sources contributing to the systematic are listed as following.

- The BBC nhit distributions for the input to our simulation. Especially the unbiased ones since they are estimated from the biased ones and the correlations between north BBC and south BBC.
- The BBC efficiency for inclusive and hard processes, i.e. the 0.52 and 0.75. These numbers determine the $nhit = 0$ bin of the unbiased distributions.
- The uncertainty on nbinary scaling law for hard processes.

In this section, we discuss the contributions from each of the above three sources to the total systematic of our calculated corrections.

4.7.1 BBC nhit distributions

In the calculation of the centrality bias correction, we use a set of BBC nhit distributions in NN collisions as the input for our simulation. This set of distributions is determined by the data driven method we discussed in the previous sections. From the calculation, it is realized that both the trigger bias and the bin shifting effect are quite sensitive to the difference between the unbiased distributions of hard processes and the distribution of inclusive processes. In our method, one of the key factors in the determination of unbiased nhit distributions is the correlations between the PHENIX north BBC and the PHENIX south BBC. These correlations are obtained from non-BBCLL1 trigger data and we do not have perfect handling of the noise contributions. To estimate how the correction varies when the south-north correlation changes, we regenerate the unbiased nhit distributions under the following extreme cases of south-north correlation, then repeat the correction calculations for each cases.

Case 1. Assume that the north and south BBC are totally uncorrelated. Thus the probability that north or south BBC fires for inclusive events is just $\sqrt{0.52} = 0.72$ since the probability that both BBCs fire is 0.52. In the same spirit, the probability that north or south BBC fires for hard events is $\sqrt{0.75} = 0.87$. In this case, the unbiased nhit distributions for the PHENIX south BBC can be obtained via scaling up the BBCLL1 biased distribution by $\frac{0.72}{0.52} = 1.38$ for inclusive processes and by $\frac{0.87}{0.75} = 1.16$ for hard processes, The $nhit = 0$ bins are thus determined. Figure 4.8 shows the nhit distributions for this case.

Case 2. Assume that the north and south BBC are totally correlated. Thus the probability that north or south BBC fires is 0.52 for inclusive events and 0.75 for hard events, respectively. Figure 4.9 shows the nhit distributions for this case.

Case 3. Determine the correlation between north and south BBC by using HI-

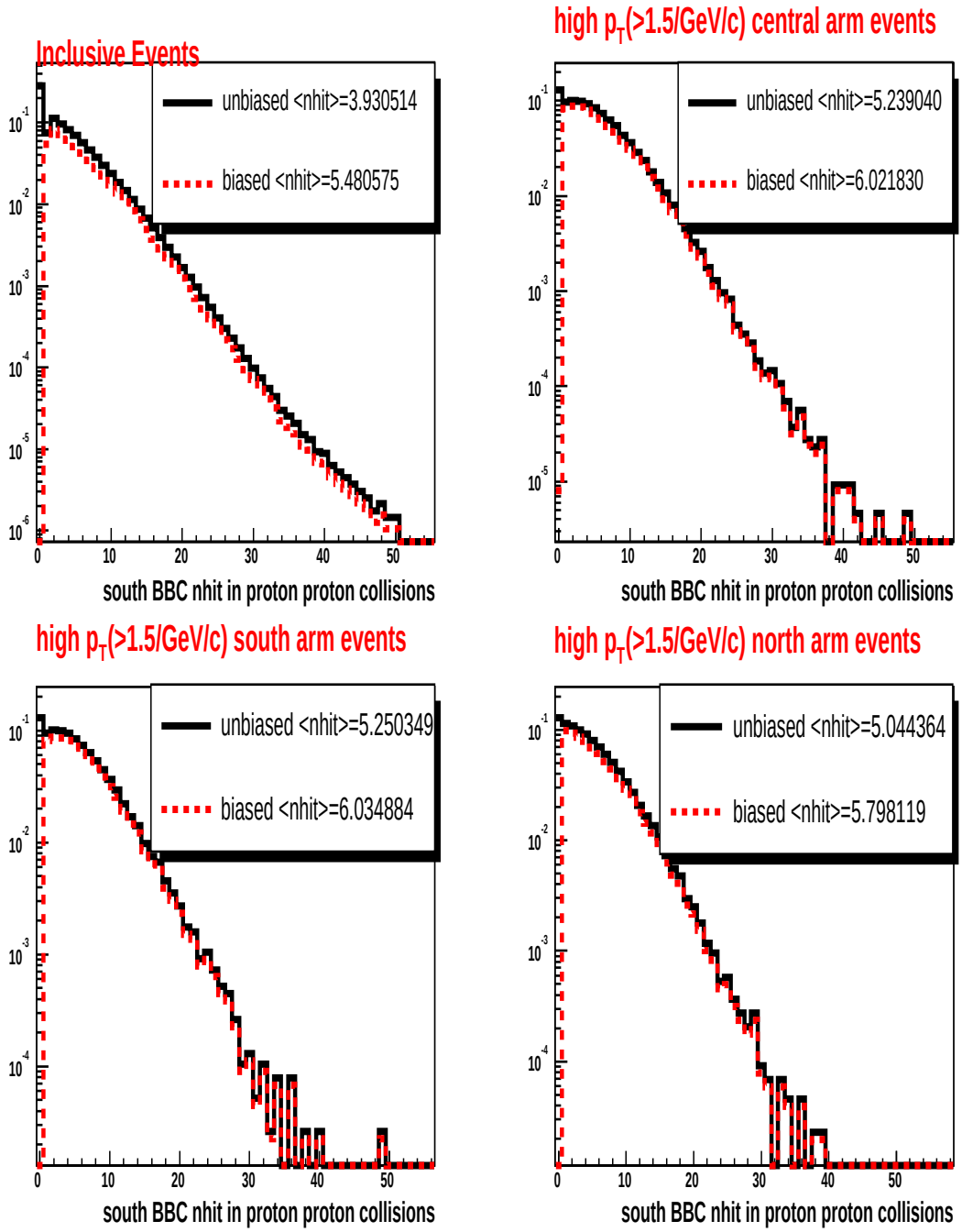

Figure 4.8: (CASE 1): South BBC nhit distributions in the case that north and south BBC are totally uncorrelated. The solid lines are unbiased distributions and the dashed lines are BBCLL1 biased distributions.

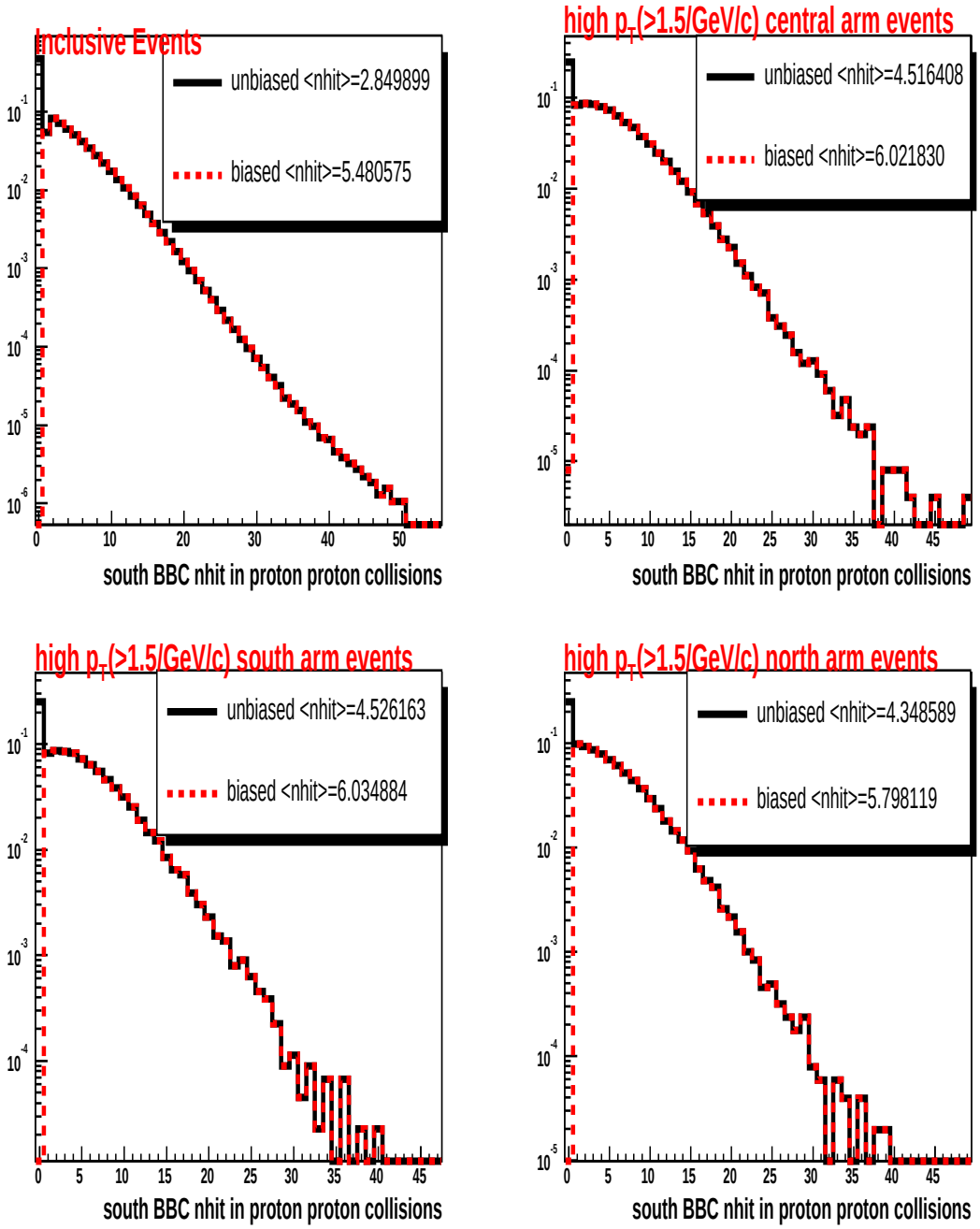

Figure 4.9: (CASE 2): South BBC nhit distributions in the case that north and south BBC are totally correlated. The solid lines are unbiased distributions and the dashed lines are BBCLL1 biased distributions.

JNG+PISA [55] simulation. Then scale up the BBCLL1 biased BBC nhit distributions from real dAu data by the correlation function. Figure 4.10 shows the nhit distributions for this case.

Case4. Alternatively, we can get both biased and unbiased distributions from HIJING+PISA simulation. Figure 4.11 shows the nhit distributions for this case.

Case5. Instead of recalculating the $nhit = 0$ bin for the unbiased distributions by renormalizing, we can just believe that the events we selected are purely from the real collisions and there is no noise contribution to all the distributions, then directly reconstruct the unbiased distributions from the non-BBCLL1 trigger data. Figure 4.12 shows the nhit distributions for this case.

Table 4.3 summarizes the centrality bias correction calculated in all these cases. For comparison purpose, the "Case 0" in the table is the canonical corrections as we listed in Table 4.2. In the table the column for correction implies the types of the correction factor listed in the table. We list the trigger bias correction factor in addition to the total correction factor (bin shifting + trigger bias).

From Table 4.3, we take the maximum and minimum values of the correction factors in each processes and centrality bins as the upper and low limits. These ranges are shown in Table 4.4.

4.7.2 Systematics on BBCLL1 trigger efficiency

In the modelling of the BBC response, two BBCLL1 efficiency numbers play very important roles. They are BBCLL1 trigger efficiency for inclusive events in proton proton collisions, $\epsilon^{BBCLL1}_{inclusive}$ and BBCLL1 trigger efficiency for hard events in proton proton collisions, ϵ^{BBCLL1}_{hard}. $\epsilon^{BBCLL1}_{inclusive}$ was measured to be 0.516 ± 0.04 [57] and ϵ^{BBCLL1}_{hard} was measured to be 0.75 ± 0.02 [58] for central arm charge hadron and π^0 analysis in RHIC RUN2 proton proton collisions. In order to evaluate of our systematics on these two efficiencies, we rerun our simulations and recalculate the final corrections for $\epsilon^{BBCLL1}_{inclusive} = 0.44$, $\epsilon^{BBCLL1}_{inclusive} = 0.60$, $\epsilon^{BBCLL1}_{hard} = 0.69$ as well as $\epsilon^{BBCLL1}_{inclusive} = 0.81$. The variation for $\epsilon^{BBCLL1}_{inclusive}$ is $2 \times \sigma$ and the variation for ϵ^{BBCLL1}_{hard}

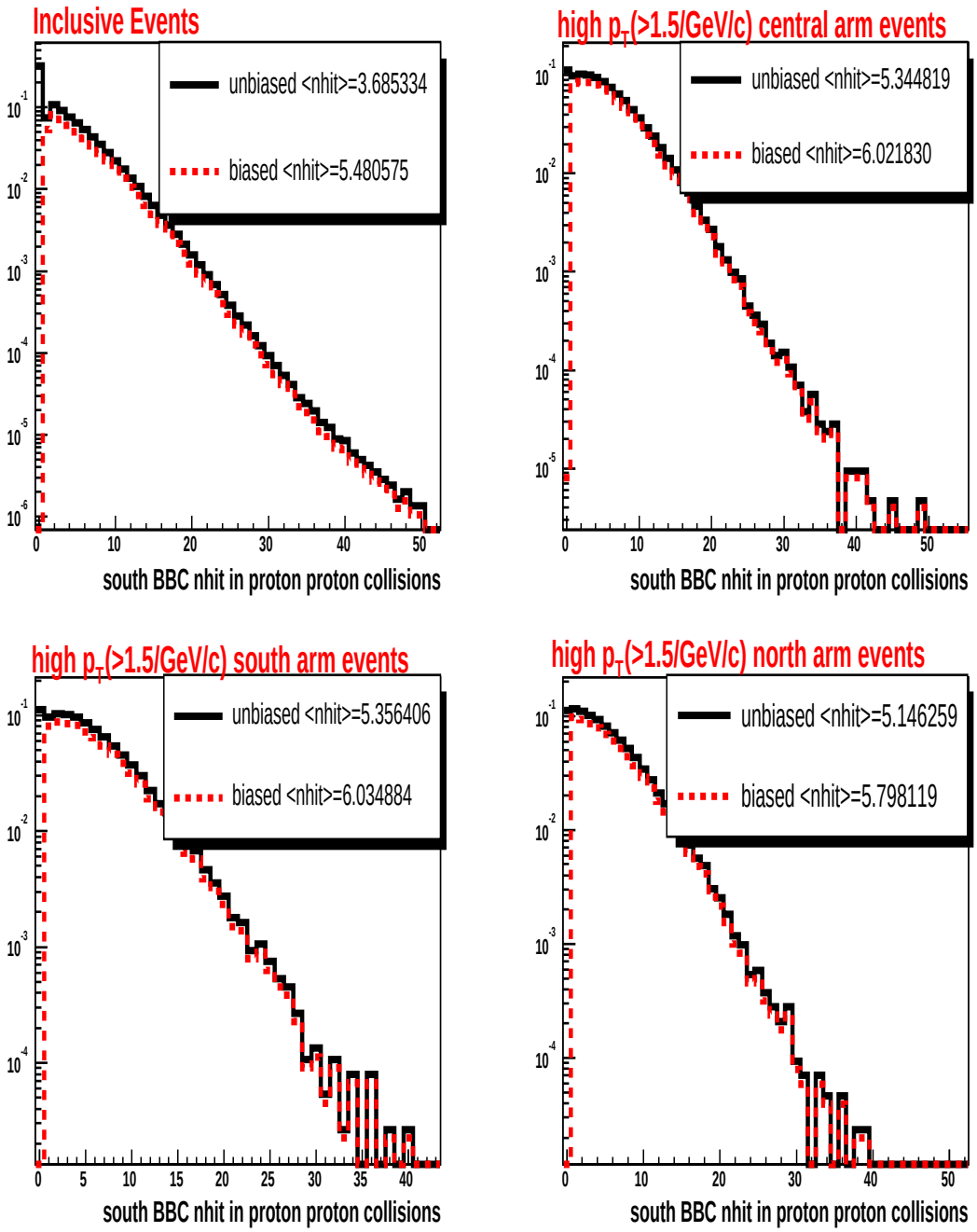

Figure 4.10: (CASE 3): South BBC nhit distributions in the case that the correlation between north and south BBC are determined by HIJING+PISA. The solid lines are unbiased distributions and the dashed lines are BBCLL1 biased distributions.

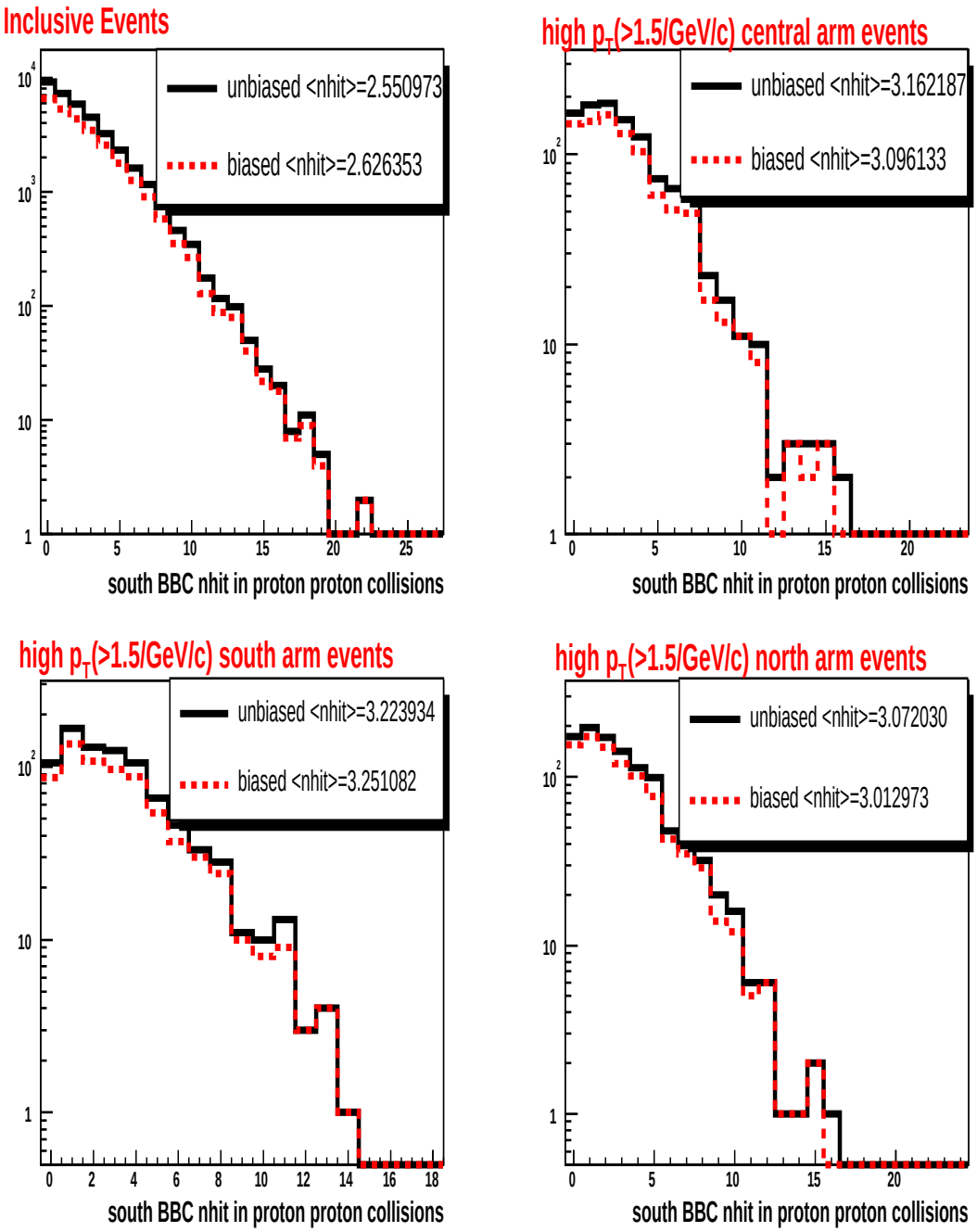

Figure 4.11: (CASE 4): South BBC nhit distributions in the case that the unbiased and biased distributions are taken from HIJING+PISA simulation. The solid lines are unbiased distributions and the dashed lines are BBCLL1 biased distributions.

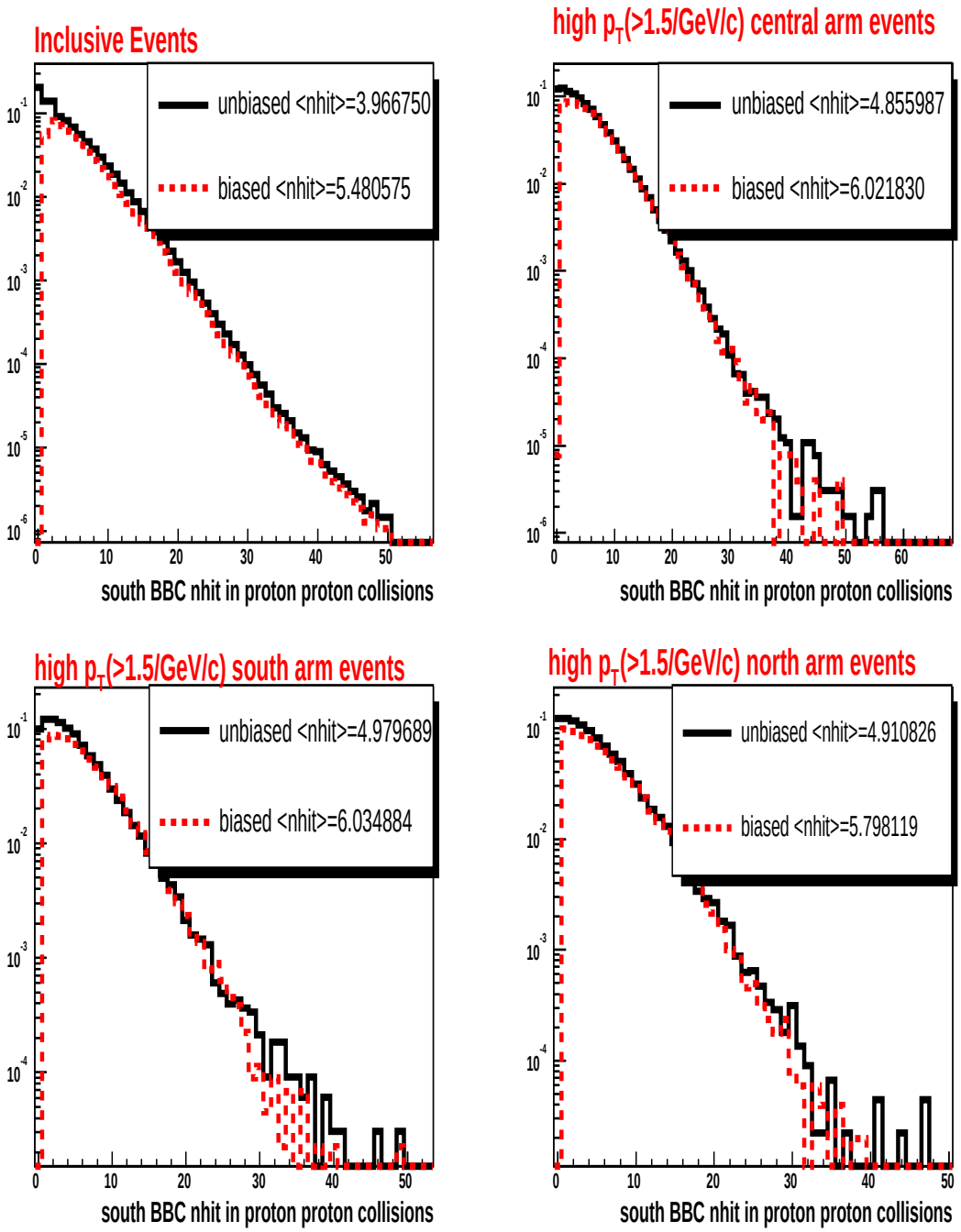

Figure 4.12: (CASE 5): South BBC nhit distributions in the case that all the unbiased and biased distributions are taken from real data without BBCLL1 trigger requirement. The solid lines are unbiased distributions and the dashed lines are BBCLL1 biased distributions.

Table 4.3: Summary of centrality bias corrections for different cases

Processes	cases	correction	$0-20\%$	$20-40\%$	$40-60\%$	$60-88\%$	$0-88\%$
Process C Central arm	case 0	total	0.95	0.99	1.03	1.04	
		trigger bias	1.00	0.99	0.97	0.85	0.94
	case 1	total	0.96	1.00	1.02	1.03	
		trigger bias	1.00	0.99	0.97	0.86	0.95
	case 2	total	0.93	0.98	1.02	1.10	
		trigger bias	1.00	0.99	0.97	0.87	0.95
	case 3	total	0.94	0.99	1.03	1.06	
		trigger bias	1.00	0.99	0.97	0.86	0.95
	case 4	total	0.97	0.99	1.02	1.04	
		trigger bias	1.00	1.00	0.99	0.92	0.97
	case 5	total	0.97	0.99	1.02	0.99	
		trigger bias	1.00	1.00	0.97	0.85	0.94
Process S South arm	case 0	total	0.95	0.99	1.04	1.05	
		trigger bias	1.00	0.99	0.97	0.85	0.94
	case 1	total	0.96	0.99	1.02	1.03	
		trigger bias	1.00	0.99	0.98	0.86	0.95
	case 2	total	0.93	0.98	1.02	1.10	
		trigger bias	1.00	0.99	0.97	0.87	0.95
	case 3	total	0.94	0.99	1.03	1.06	
		trigger bias	1.00	0.99	0.97	0.86	0.95
	case 4	total	0.97	0.99	1.02	1.05	
		trigger bias	1.00	1.00	0.99	0.91	0.97
	case 5	total	0.97	0.99	1.02	0.99	
		trigger bias	1.00	1.00	0.97	0.85	0.94
Process N North arm	case 0	total	0.96	0.99	1.03	1.02	
		trigger bias	1.00	0.99	0.97	0.85	0.94
	case 1	total	0.96	1.00	1.02	1.01	
		trigger bias	1.00	1.00	0.98	0.86	0.95
	case 2	total	0.94	0.98	1.02	1.08	
		trigger bias	1.00	1.00	0.97	0.87	0.95
	case 3	total	0.95	0.99	1.03	1.04	
		trigger bias	1.00	1.00	0.97	0.86	0.95
	case 4	total	0.97	0.99	1.02	1.02	
		trigger bias	1.00	1.00	0.99	0.91	0.97
	case 5	total	0.97	1.00	1.02	0.99	
		trigger bias	1.00	0.99	0.97	0.85	0.94

Table 4.4: Summary of systematic errors for different cases

Processes	correction	$0-20\%$	$20-40\%$	$40-60\%$	$60-88\%$	$0-88\%$
Process C	total	$^{+0.02}_{-0.02}$	$^{+0.01}_{-0.01}$	$^{+0.002}_{-0.01}$	$^{+0.06}_{-0.05}$	
Central arm	trigger bias	$^{+0.001}_{-0.001}$	$^{+0.01}_{-0.003}$	$^{+0.02}_{-0.002}$	$^{+0.07}_{-0.002}$	$^{+0.03}_{-0.001}$
Process S	total	$^{+0.02}_{-0.02}$	$^{+0.004}_{-0.01}$	$^{+0.003}_{-0.02}$	$^{+0.05}_{-0.06}$	
South arm	trigger bias	$^{+0.001}_{-0.001}$	$^{+0.01}_{-0.002}$	$^{+0.02}_{-0.001}$	$^{+0.06}_{-0.002}$	$^{+0.03}_{-0.001}$
Process N	total	$^{+0.01}_{-0.02}$	$^{+0.01}_{-0.01}$	$^{+0.004}_{-0.01}$	$^{+0.06}_{-0.03}$	
North arm	trigger bias	$^{+0.001}_{-0.001}$	$^{+0.01}_{-0.001}$	$^{+0.02}_{-0.002}$	$^{+0.06}_{-0.001}$	$^{+0.03}_{-0.001}$

is $3 \times \sigma$. Figure 4.13 shows the unbiased and biased south BBC nhit distributions for different processes when $\epsilon^{BBCLL1}_{inclusive} = 0.44$. Figure 4.14 shows the unbiased and biased south BBC nhit distributions for different processes when $\epsilon^{BBCLL1}_{inclusive} = 0.60$. Figure 4.15 shows the unbiased and biased south BBC nhit distributions for different processes when $\epsilon^{BBCLL1}_{hard} = 0.69$. Figure 4.16 shows the unbiased and biased south BBC nhit distributions for different processes when $\epsilon^{BBCLL1}_{inclusive} = 0.81$.

The results of the trigger bias corrections calculated based on these distributions are listed in Table 4.5. In the table the column for correction implies the types of the correction factor listed in the table. We list the trigger bias correction factor besides the total correction factor (bin shifting + trigger bias). The raw 0.52/0.75 is listed for reference. This time the range of upper and low limits for each bbc_{eff} values are calculated and are summarized in Table 4.6. In the table, the 0.75 and 0.52 that those raw shows the systematic errors contributed from ϵ^{BBCLL1}_{hard} and $\epsilon^{BBCLL1}_{inclusive}$, respectively.

4.7.3 Systematics from assuming nbinary scaling for hard processes

In our calculation of high p_T particle yields, we assumed that the probabilities of producing high p_T particles scale with nbinary. But we know that in reality there are nuclear effects modifying the production of particles. Thus, the nbinary scaling law for sure will be broken. In fact, from our particle yield measurements without these correction applied, we are already able to approximately determined how the physics process scales with nbinary. We can use the preliminary R_{cp} measurement

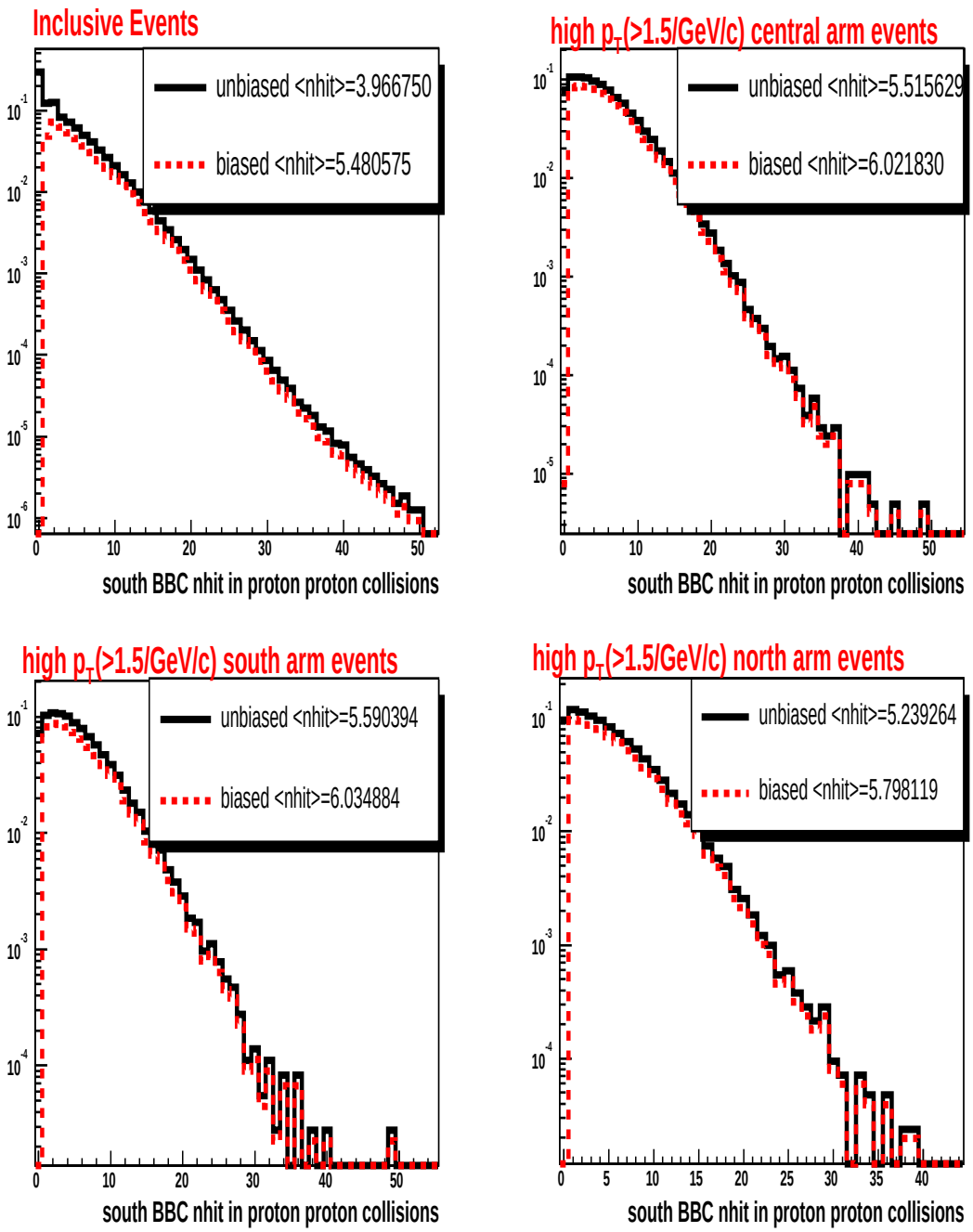

Figure 4.13: South BBC nhit distributions when $\epsilon_{inclusive}^{BBCLL1} = 0.44$. The solid lines are unbiased distributions and the dashed lines are BBCLL1 biased distributions.

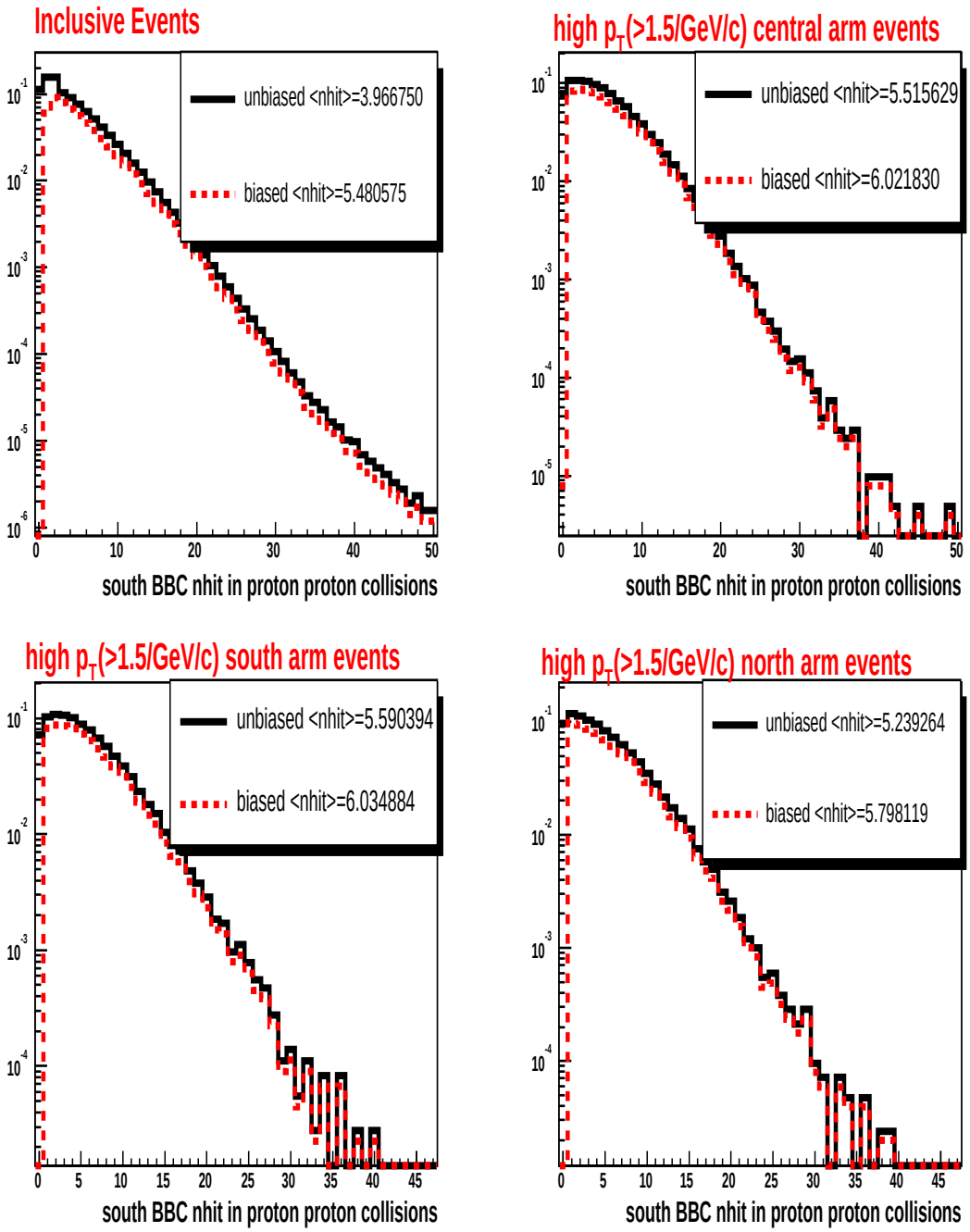

Figure 4.14: South BBC nhit distributions when $\epsilon_{inclusive}^{BBCLL1} = 0.60$. The solid lines are unbiased distributions and the dashed lines are BBCLL1 biased distributions.

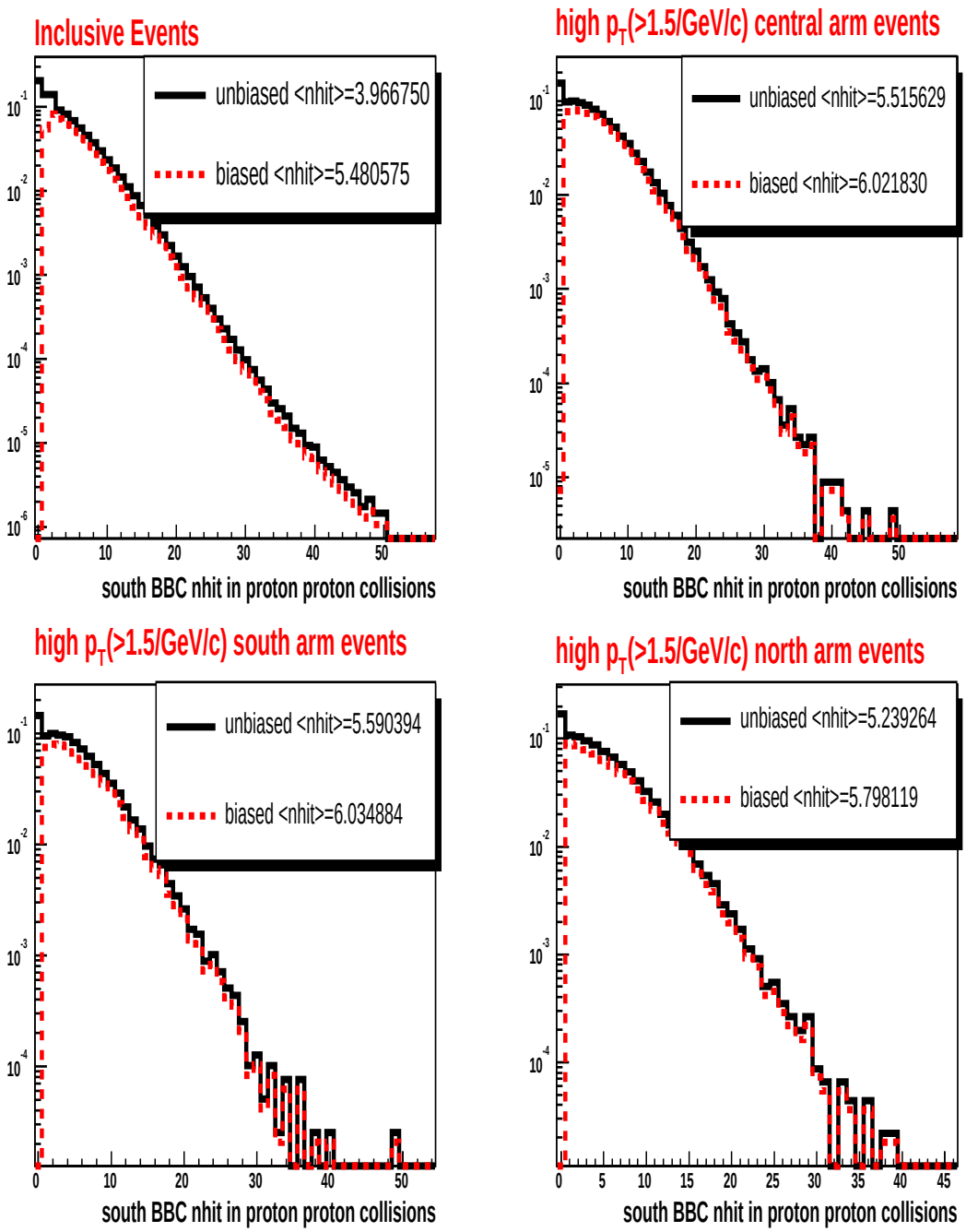

Figure 4.15: South BBC nhit distributions when $\epsilon_{hard}^{BBCLL1} = 0.69$. The solid lines are unbiased distributions and the dashed lines are BBCLL1 biased distributions.

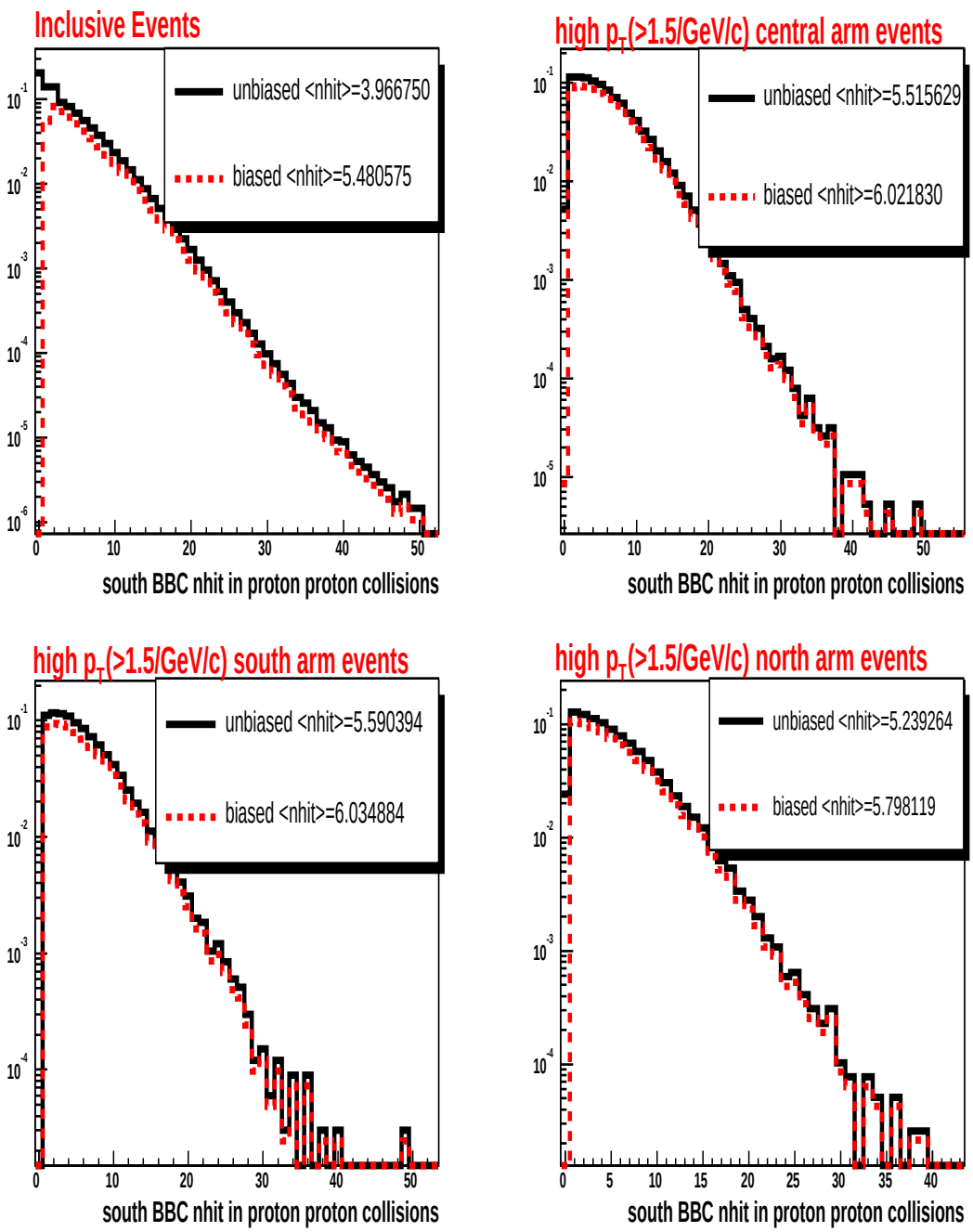

Figure 4.16: South BBC nhit distributions when $\epsilon_{hard}^{BBCLL1} = 0.81$. The solid lines are unbiased distributions and the dashed lines are BBCLL1 biased distributions.

Table 4.5: Summary of centrality bias corrections for different BBC efficiency

Processes	bbc_{eff}	correction	$0-20\%$	$20-40\%$	$40-60\%$	$60-88\%$	$0-88\%$
Process C	0.52 /0.75	total	0.95	0.99	1.03	1.04	
Central arm		trigger bias	1.00	0.99	0.97	0.85	0.94
	0.44	total	0.93	0.99	1.04	1.06	
		trigger bias	1.00	0.99	0.97	0.80	0.93
	0.60	total	0.97	1.00	1.02	1.03	
		trigger bias	1.00	1.00	0.98	0.89	0.96
	0.69	total	0.96	1.00	1.02	1.03	
		trigger bias	1.00	1.00	0.98	0.88	0.96
	0.81	total	0.94	0.99	1.04	1.06	
		trigger bias	1.00	0.99	0.97	0.81	0.93
Process S	0.52 /0.75	total	0.95	0.99	1.04	1.05	
South arm		trigger bias	1.00	0.99	0.97	0.85	0.94
	0.44	total	0.92	0.99	1.04	1.07	
		trigger bias	1.00	0.99	0.96	0.80	0.93
	0.60	total	0.96	1.00	1.03	1.03	
		trigger bias	1.00	1.00	0.98	0.89	0.96
	0.69	total	0.96	1.00	1.03	1.04	
		trigger bias	1.00	1.00	0.98	0.88	0.96
	0.81	total	0.93	0.99	1.04	1.07	
		trigger bias	1.00	0.99	0.97	0.81	0.93
Process N	0.52 /0.75	total	0.96	0.99	1.03	1.02	
North arm		trigger bias	1.00	0.99	0.97	0.85	0.94
	0.44	total	0.94	0.99	1.03	1.04	
		trigger bias	1.00	0.99	0.96	0.80	0.93
	0.60	total	0.98	1.00	1.02	1.00	
		trigger bias	1.00	1.00	0.98	0.89	0.96
	0.69	total	0.97	1.00	1.02	1.00	
		trigger bias	1.00	1.00	0.98	0.88	0.96
	0.81	total	0.94	0.99	1.04	1.03	
		trigger bias	1.00	0.99	0.97	0.81	0.93

Table 4.6: Summary of systematic on centrality bias corrections for varying BBC efficiency

Processes	bbc_{eff}	correction	$0-20\%$	$20-40\%$	$40-60\%$	$60-88\%$	$0-88\%$
Process C Central arm	0.52	total	$^{+0.02}_{-0.02}$	$^{+0.01}_{-0.002}$	$^{+0.01}_{-0.01}$	$^{+0.02}_{-0.01}$	
		trigger bias	$^{+0.001}_{-0.001}$	$^{+0.01}_{-0.001}$	$^{+0.01}_{-0.002}$	$^{+0.04}_{-0.05}$	$^{+0.02}_{-0.01}$
	0.75	total	$^{+0.01}_{-0.01}$	$^{+0.01}_{-0.004}$	$^{+0.01}_{-0.01}$	$^{+0.02}_{-0.01}$	
		trigger bias	$^{+0.001}_{-0.001}$	$^{+0.01}_{-0.005}$	$^{+0.01}_{-0.001}$	$^{+0.03}_{-0.04}$	$^{+0.02}_{-0.01}$
Process S South arm	0.52	total	$^{+0.01}_{-0.03}$	$^{+0.01}_{-0.002}$	$^{+0.002}_{-0.01}$	$^{+0.02}_{-0.02}$	
		trigger bias	$^{+0.001}_{-0.001}$	$^{+0.01}_{-0.001}$	$^{+0.01}_{-0.01}$	$^{+0.04}_{-0.05}$	$^{+0.02}_{-0.01}$
	0.75	total	$^{+0.01}_{-0.02}$	$^{+0.01}_{-0.001}$	$^{+0.002}_{-0.01}$	$^{+0.02}_{-0.01}$	
		trigger bias	$^{+0.001}_{-0.001}$	$^{+0.01}_{-0.004}$	$^{+0.01}_{-0.002}$	$^{+0.03}_{-0.04}$	$^{+0.02}_{-0.01}$
Process N North arm	0.52	total	$^{+0.02}_{-0.02}$	$^{+0.01}_{-0.005}$	$^{+0.002}_{-0.01}$	$^{+0.02}_{-0.02}$	
		trigger bias	$^{+0.001}_{-0.001}$	$^{+0.01}_{-0.003}$	$^{+0.01}_{-0.01}$	$^{+0.04}_{-0.05}$	$^{+0.02}_{-0.01}$
	0.75	total	$^{+0.01}_{-0.02}$	$^{+0.01}_{-0.001}$	$^{+0.01}_{-0.01}$	$^{+0.01}_{-0.02}$	
		trigger bias	$^{+0.001}_{-0.001}$	$^{+0.01}_{-0.001}$	$^{+0.01}_{-0.003}$	$^{+0.03}_{-0.04}$	$^{+0.02}_{-0.01}$

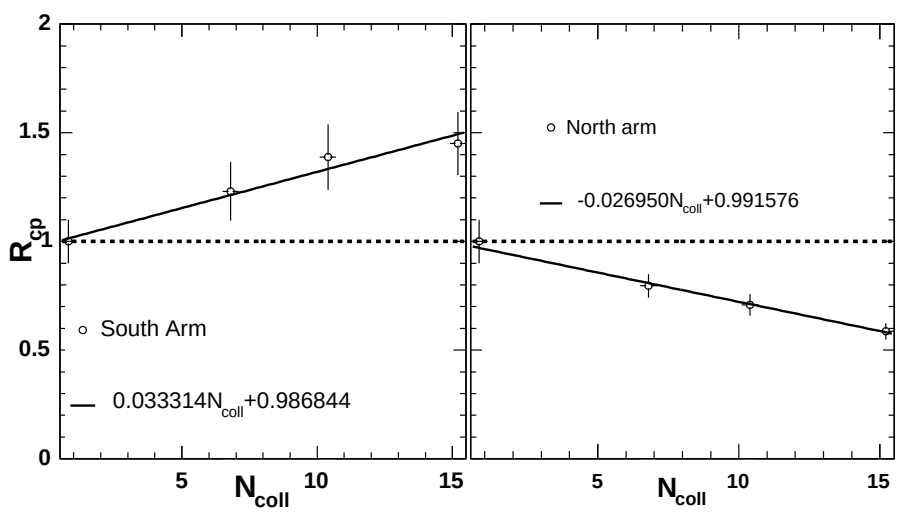

Figure 4.17: R_{cp} measured in the PHENIX muon arms is plotted as a function of nbinary.

in the PHENIX muon arms to set up the limits on how fast the yield changes with centrality, then use this information to gauge the systematics from the nbinary scaling assumption. Figure 4.17 shows the R_{cp} for charge hadrons measured in muon arms as a function of nbinary.

We fit the data with a linear function of nbinary. The fitted linear function for south arm hadrons is $Y_{south}(N_{coll}) = 0.033314 \times N_{coll} + 0.986844$ and the function

Table 4.7: Summary of centrality bias corrections for different scaling laws

Processes	$Y(N_{coll})$	$0-20\%$	$20-40\%$	$40-60\%$	$60-88\%$
Process C	nbinary	0.95	0.99	1.03	1.04
Central	south	0.93	0.987	1.035	1.042
arm	north	0.99	0.997	1.026	1.035
C errors		$^{+0.04}_{-0.02}$	$^{+0.007}_{-0.003}$	$^{+0.005}_{-0.004}$	$^{+0.002}_{-0.005}$
Process S	nbinary	0.95	0.99	1.04	1.05
South	south	0.93	0.987	1.042	1.054
arm	north	0.99	0.997	1.026	1.045
S errors		$^{+0.04}_{-0.02}$	$^{+0.007}_{-0.003}$	$^{+0.002}_{-0.014}$	$^{+0.004}_{-0.005}$
Process N	nbinary	0.96	0.99	1.03	1.02
North	south	0.95	0.987	1.035	1.03
arm	north	1.00	0.997	1.022	1.019
C errors		$^{+0.04}_{-0.01}$	$^{+0.007}_{-0.003}$	$^{+0.005}_{-0.008}$	$^{+0.01}_{-0.001}$

for north arm hadrons is $Y_{south}(N_{coll}) = -0.02695 \times N_{coll} + 0.991576$. We can see that the increase in particle production with nbinary is faster than nbianry scaling in south muon arm coverage and is slower than nbinary scaling in north muon arm coverage. This observation provide us upper and lower limits on varying the relation between the yields and the centralities. The upper and lower limits on the correction factor K is calculated as

$$K_{up} = \frac{Y_{south}(N_{coll}^{true})}{Y_{south}(N_{coll}^{BBC})} \tag{4.6}$$

$$K_{low} = \frac{Y_{north}(N_{coll}^{true})}{Y_{north}(N_{coll}^{BBC})} \tag{4.7}$$

, where N_{coll}^{true} is the $\langle nbinary \rangle$ in nbinary defined centrality bins and N_{coll}^{BBC} is the $\langle nbinary \rangle$ in BBC defined centrality bins, as listed in Table 4.3. Note that N_{coll}^{BBC} is process dependent. The results of the calculation are listed in Table 4.7. The $Y(N_{coll})$ column in the table represents different scaling of yields. "nbinary" means nbinary scaling. "south"("north") means the yield changes with nbinary according to the linear function we got from south(north) arm measurements.

4.8 Summary of Final Results

There are two observations from the systematic studies we describe in the last section.

- 1.) We found that the results from varying the correlations between south and north BBC are correlated with the results from varying the BBCLL1 trigger efficiency in the sense that they both modify the unbiased BBC nhit distributions. Thus, the Cases 0-5 and the variations on the BBCLL1 trigger efficiency are as if we performed the calculation eight times with slightly different unbiased BBC nhit distributions. We calculate the systematic error by taking the RMS of these 8 calculations.

- 2.) Since we know, roughly, from our preliminary R_{cp} measurement (as shown in Figure 4.17) that the relation between the yield per binary collision and $\langle nbinary \rangle$, we use the correction factor (C.F.) calculated from south scaling relation for south arm analysis and the correction factor calculated from north scaling relation for north arm analysis. For central arm, we will still use the nbinary scaling. Then the error on each C.F. is the RMS of the results from the three different scaling law considerations. This gives us the most likely mean correction factor and a reasonable systematic error.

Table 4.8 summarizes the results of this centrality bias study and the systematic errors on the correction factors are calculated by summing up each systematic errors from observation 1 and 2 in quadrature.

The final correction factors are listed for each process and each centrality in Table 4.8. Please note that these are multiplicative correction factors to the measured yields. Also, the previously applied correction factor of 0.88, is no longer necessary as that effect is included in our factor.

There is a small issue in that in PHENIX Analysis Note 210, they have also determined the $< N_{binary} >$ for the same centrality bins, but using the tuned negative

Table 4.8: Summary of centrality bias correction factors.

Processes	$0-20\%$	$20-40\%$	$40-60\%$	$60-88\%$	$0-88\%$	$0-100\%$
Process C Central arm	0.95 ±0.029	0.99 ±0.007	1.03 ±0.009	1.04 ±0.027	0.98 ±0.01	0.94 ±0.02
Process S South arm	0.93 ±0.030	0.99 ±0.007	1.04 ±0.011	1.05 ±0.028	0.98 ±0.01	0.94 ±0.02
Process N North arm	1.00 ±0.026	1.00 ±0.008	1.02 ±0.008	1.02 ±0.025	0.98 ±0.01	0.94 ±0.02
nbinary	15.37 ±1.0	10.63 ±0.7	6.95 ±0.6	3.07 ±0.3	8.42 ±0.3	7.58 ±0.3
nbinary ratio to periperial	5.01 ±0.51	3.46 ±0.27	2.26 ±0.09	1.00 ±0.00		

binomial distribution as input. Their quoted values are 15.0±1.0, 10.4±0.7, 6.9±0.6, and 3.2 ± 0.3 for bins 0-20%, 20-40%, 40-60%, and 60-88% respectively. All of these values agree within systematic errors of our $< N_{binary} >$ values determined here. It should be noted that our calculation on the correction factors is not very sensitive to this slight difference. In principle one could use either set of values for the final result. For the best result, we quote in Table 4.8 the average between the two sets of numbers.

Also in the Table, we quote the correction factors for $0-88\%$ and $0-100\%$. The first 00-88% is applicable only if one is interested in the physics which is selected by BBCLL1 and the underlying true nbinary distribution is determined by BBCLL1 selected Glauber events. The later one is for correcting your measured yield back to the true particle yield produced in the minimum bias deuteron-gold inelastic collisions and the underlying nbinary distribution is given by the pure Glauber model. One should use it for deuteron-gold inclusive measurements.

Note that we have not explicitly studied other processes in this Analysis Note, including J/ψ and a more detailed p_T dependence of the correction factors. We have strong reason to believe that the north and south arm (N and S) correction factors should apply for the J/ψ within systematic errors in the same respect arm. Also, at low p_T we expect these correction factors to smoothly trend towards one. Since the existing corrections include 1.0 within the systematic errors, there appears to be no reason to do an interpolation towards one. Again, these are suggestions that have not been studied in detail in this analysis.

Chapter 5

Results and discussion

5.1 Final results

In Chapter 3 we discussed how we measured the charged hadrons in the PHENIX muon arms in dAu collisions and how we constructed the nuclear modification factors, R_{cp}. Then in Chapter 4 we outlined the centrality bias correction for our R_{cp} measurements. The PHENIX south muon arm covers $-2.0 < \eta < -1.4$ in this measurement. Since this η coverage is close to the RHIC gold ion beam going direction, it is called backward rapidity. On the other hand, the PHENIX north muon arm covers $1.4 < \eta < 2.2$, the forward rapidity(the RHIC deuteron beam going direction). This broad kinematic coverage gives the unique importance of our measurement. The final corrected R_{cp} as a function of transverse momentum are shown in figure 5.1. On the plots, we distinguished the measurement at forward rapidity and the measurement at backward rapidity by solid squares and circles, respectively. Two features can be seen from the plots. First, an enhancement is seen at the backward rapidity and a suppression is seen at the forward rapidity. Both the enhancement and suppression are centrality dependent. The more central(smaller impact parameter) the collisions are, the bigger the enhancement/suppression is. Second the p_T dependence is small, especially at the forward rapidity. The suppression we see at the forward rapidity is much bigger comparing to the enhancement at the backward rapidity. For most central collisions, there is almost $40 - 50\%$ sup-

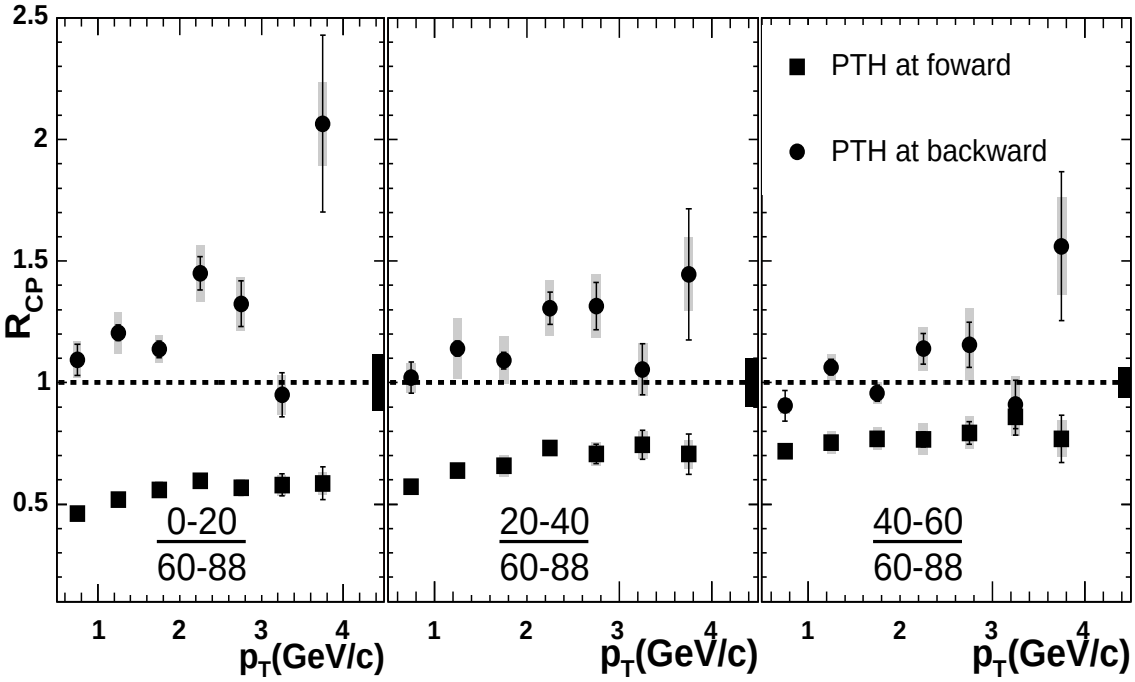

Figure 5.1: Nuclear Modification factor(R_{cp}) as a function of p_T. From the left panel to the right panel, the centrality percentage increases(i.e. the impact parameter increases). On the plot, PTH denotes the term of pouch-through hadron. The grey bars on each data points are point-by-point systematic errors and the black bar on the right end of the $R_{cp} = 1$ line is the common systematic errors.

pression relative to the most peripheral collisions at the forward rapidity, however in comparison there is only a 20% enhancement at the backward rapidity.

We can look more closely at the pseudo-rapidity dependence of the R_{cp} by dividing our measurement into small η bins. Since we are most interested in the hard or semi-hard collisions, which is in general believed to dominate the high p_T particle productions, we also applied a $p_T > 1.5\text{GeV}/c$ cut when we divide the R_{cp} in each η bins. Figure 5.2 shows R_{cp} as a function of η. One striking feature is that there is a strong η dependence at forward rapidity, but within our errors, it is not very clear whether there is an η dependence at all at the backward rapidity. In the mean time, although the suppression at the forward becomes smaller as one goes to peripheral collisions, but the η dependence seems to be persistent.

Table 5.1 summarizes our results. In the column where R_{cp} is listed, the first

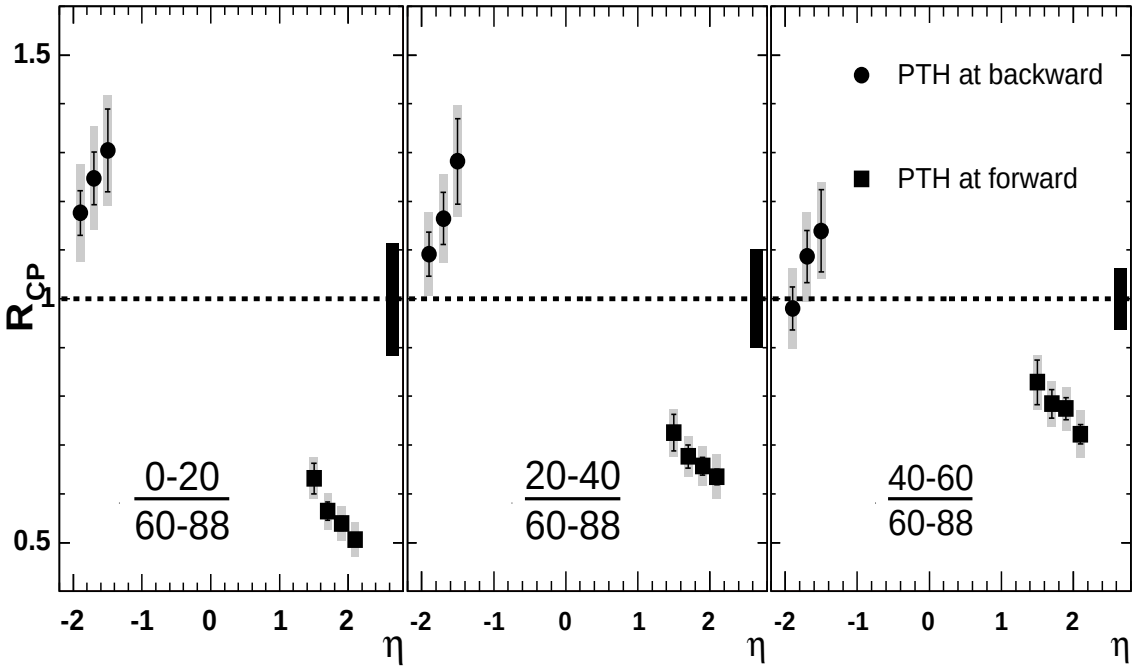

Figure 5.2: Nuclear Modification factor(R_{cp}) as a function of η. From the left panel to the right panel, the centrality percentage increases(i.e. the impact parameter increases). On the plot, PTH denotes the term of pouch-through hadron. The grey bars on each data points are point-by-point systematic errors and the black bar on the right end of the $R_{cp} = 1$ line is the common systematic errors.

error is the statistical error and the second error is the point to point systematic error. The common systematic errors, i.e. errors on the determination of the number of binary collisions for each centrality class, are not listed and can been found in Chapter 3. The middle value of η for each η(binwidth is 0.2) is listed in η column of the table. .

5.1.1 R_{cp} measured by hadron decay muons

In fact, there are two independent methods which we can use to measure hadrons in the PHENIX muon arms. One is measuring the punch-through hadrons and it is discussed at length in this thesis. The other is via measuring hadron decay muons. Some hadrons will decay into muons before the absorber, and the decay muons are then measured by the muon spectrometers. Muons can result from many sources

Table 5.1: **Summary of R_{cp} measurement.**

centrality	p_T (GeV/c)	$R_{cp}(p_T)$ $1.4 < \eta < 2.2$	$R_{cp}(p_T)$ $-2.0 < \eta < -1.4$	η	$R_{cp}(\eta)$ $p_T > 1.5$GeV/c
$\frac{0-20}{60-88}$	$0.5-1.0$	0.462 $\pm 0.014 \pm 0.023$	1.09 $\pm 0.06 \pm 0.07$	-1.9 -1.9	1.18 $\pm 0.04 \pm 0.10$
	$1.0-1.5$	0.519 $\pm 0.010 \pm 0.025$	1.21 $\pm 0.03 \pm 0.08$	-1.7 -1.7	1.25 $\pm 0.05 \pm 0.11$
	$1.5-2.0$	0.559 $\pm 0.014 \pm 0.034$	1.14 $\pm 0.03 \pm 0.06$	-1.5 -1.5	1.3 $\pm 0.08 \pm 0.11$
	$2.0-2.5$	0.596 $\pm 0.022 \pm 0.028$	1.45 $\pm 0.07 \pm 0.12$	1.5 1.5	0.631 $\pm 0.031 \pm 0.041$
	$2.5-3.0$	0.567 $\pm 0.030 \pm 0.033$	1.32 $\pm 0.09 \pm 0.11$	1.7 1.7	0.564 $\pm 0.021 \pm 0.044$
	$3.0-3.5$	0.579 $\pm 0.045 \pm 0.042$	0.95 $\pm 0.09 \pm 0.08$	1.9 1.9	0.539 $\pm 0.019 \pm 0.043$
	$3.5-4.0$	0.586 $\pm 0.067 \pm 0.045$	2.06 $\pm 0.36 \pm 0.17$	2.1 2.1	0.506 $\pm 0.013 \pm 0.045$
$\frac{20-40}{60-88}$	$0.5-1.0$	0.572 $\pm 0.018 \pm 0.016$	1.02 $\pm 0.06 \pm 0.06$	-1.9 -1.9	1.09 $\pm 0.04 \pm 0.09$
	$1.0-1.5$	0.637 $\pm 0.013 \pm 0.022$	1.14 $\pm 0.03 \pm 0.12$	-1.7 -1.7	1.16 $\pm 0.05 \pm 0.09$
	$1.5-2.0$	0.659 $\pm 0.017 \pm 0.044$	1.09 $\pm 0.03 \pm 0.10$	-1.5 -1.5	1.28 $\pm 0.09 \pm 0.11$
	$2.0-2.5$	0.731 $\pm 0.027 \pm 0.023$	1.31 $\pm 0.06 \pm 0.12$	1.5 1.5	0.725 $\pm 0.043 \pm 0.049$
	$2.5-3.0$	0.707 $\pm 0.039 \pm 0.048$	1.32 $\pm 0.10 \pm 0.13$	1.7 1.7	0.677 $\pm 0.021 \pm 0.042$
	$3.0-3.5$	0.744 $\pm 0.060 \pm 0.056$	1.05 $\pm 0.10 \pm 0.11$	1.9 1.9	0.657 $\pm 0.022 \pm 0.041$
	$3.5-4.0$	0.706 $\pm 0.084 \pm 0.059$	1.45 $\pm 0.27 \pm 0.15$	2.1 2.1	0.635 $\pm 0.024 \pm 0.045$
$\frac{40-60}{60-88}$	$0.5-1.0$	0.718 $\pm 0.024 \pm 0.032$	0.905 $\pm 0.06 \pm 0.03$	-1.9 -1.9	0.98 $\pm 0.04 \pm 0.08$
	$1.0-1.5$	0.754 $\pm 0.017 \pm 0.046$	1.06 $\pm 0.03 \pm 0.05$	-1.7 -1.7	1.09 $\pm 0.05 \pm 0.09$
	$1.5-2.0$	0.769 $\pm 0.021 \pm 0.047$	0.956 $\pm 0.03 \pm 0.04$	-1.5 -1.5	1.14 $\pm 0.08 \pm 0.10$
	$2.0-2.5$	0.767 $\pm 0.031 \pm 0.064$	1.14 $\pm 0.06 \pm 0.09$	1.5 1.5	0.829 $\pm 0.052 \pm 0.055$
	$2.5-3.0$	0.792 $\pm 0.046 \pm 0.066$	1.16 $\pm 0.09 \pm 0.15$	1.7 1.7	0.785 $\pm 0.028 \pm 0.046$
	$3.0-3.5$	0.858 $\pm 0.073 \pm 0.075$	0.91 $\pm 0.10 \pm 0.12$	1.9 1.9	0.775 $\pm 0.021 \pm 0.044$
	$3.5-4.0$	0.768 $\pm 0.098 \pm 0.075$	1.56 $\pm 0.31 \pm 0.20$	2.1 2.1	0.722 $\pm 0.033 \pm 0.049$

including decays of π, K, D mesons, and J/Ψ. These particles have a finite decay probability P_{decay} before they reach the absorber $P_{decay}(p, L) = 1 - e^{-\frac{L \cdot m}{\tau \cdot p}}$, where m and τ are the rest mass and the proper life time of the parent particle. In the PHENIX detector setup, $L \sim 41$cm, is the distance from the collision vertex to the absorber; p is the momentum of the parent particle. Thus, collisions that occur far from the absorber will be more likely to have muons from light meson decays than those that occur close to the absorber. Charm hadrons, however, due to their very short proper decay lengths, $e^{-\frac{L \cdot m}{\tau \cdot p}} << 1$, will have minimal collision vertex dependence. Thus there will be a collision vertex dependence on the probability of detecting muons from light meson decay. Figure 5.3 shows the collision vertex distribution from events in which muons are detected at forward rapidity, corrected for the minimum bias collision vertex distribution. The large vertex dependence indicates a significant fraction of the muons are from pion and kaon decay. Using this distribution, we can separate the muons from pion and kaon decay from other contributions. It should be noted that the measured muon p_T is approximately 15% lower on average than the parent hadron p_T.

The measured nuclear modification factor from hadron decay muons (HDM) are plotted on Figure 5.4 and Figure 5.5 as the open symbols. For comparison, the results from punch-through hadrons(PTH) are plotted too as the closed symbols. One can see from the plots that the results from two independent methods are very consistent. It is notable that our two measurement methods have different sensitivity to different hadrons. The particle composition ($\pi/K/p$ ratio) we measure is modified relative to the particle composition at the collision vertex due to species-dependent nuclear interaction cross-sections affecting the punch-through hadrons and due to species-dependent decay lifetimes affecting the hadron decay muons. Both effects enhance the kaon contribution to our R_{cp} measurements. However, in PTH case, it is the negative kaon contribution that is enhanced, while in HDM case, both positive and negative kaon contributions are enhanced. The fact that almost identical results are obtained from the two methods may indicate that the nuclear modification

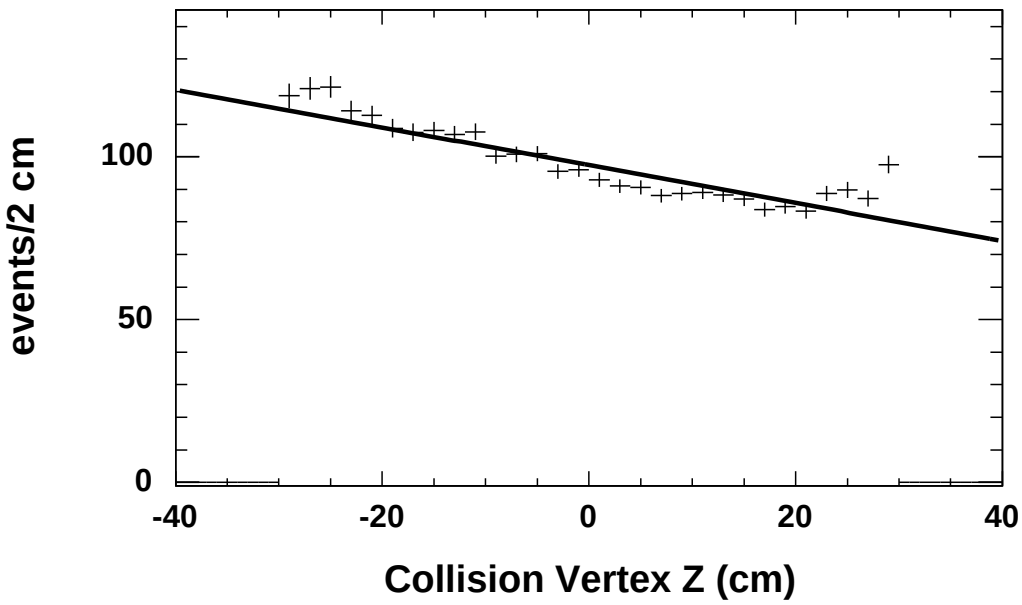

Figure 5.3: Collision vertex distribution for events with muons at forward rapidity, corrected for the minimum bias collision vertex distribution.

observed here has no obvious charge dependence.

5.1.2 Compare with BRAHMS measurements

The BRAHMS experiment has also measured the R_{cp} as a function of p_T for negative charged hadrons at three forward pseudo-rapidity bins, i.e. $\eta = 1, 2.2, 3.2$ [59]. Their results also show a strong suppression at the forward rapidity. In figure 5.6, we compare results from the BRAHMS experiment with our results at forward rapidity. The PHENIX data and the BRAHMS data are in agreement within systematic uncertainties. However the centrality definition for the BRAHMS experiment is somewhat different from the PHENIX definition. Their reference bin(most peripheral) is $60 - 80\%$ and they only have two central bins $0 - 20\%$ and $30 - 50\%$. To make the plot less busy, the PHENIX R_{cp} is the error-weighted average results of the PTH and HDM methods.

Although the two experiment's results are consistent in systematic errors, ide-

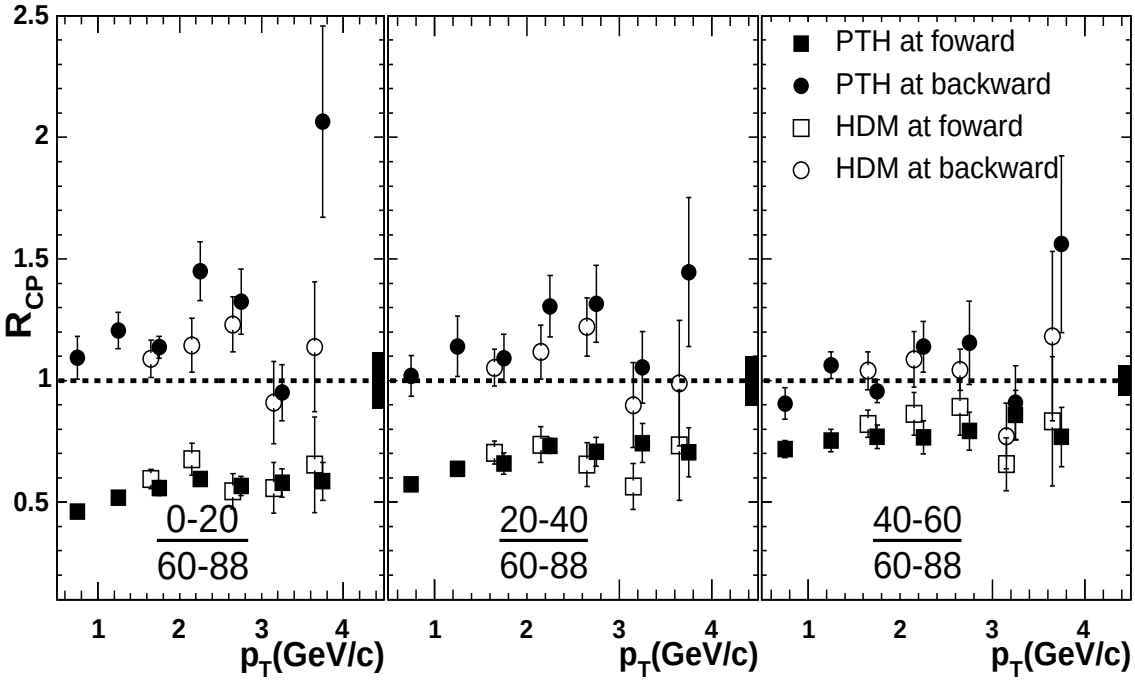

Figure 5.4: R_{cp} as a function of p_T for hadron decay muons(HDM) and punch-through hadrons(PTH). The error bars on each data points are the quadratic sum of systematic error and statistic error. For better vision, the HDM points are artificially shifted to the right for a quarter of the bin size.

ally the PHENIX data points should fall in between the BRAHMS R_{cp} at $\eta = 1$ and at $\eta = 2.2$ since the PHENIX forward rapidity coverage is $1.4 < \eta < 2.2$. One may realize from figure 5.6 that the PHENIX data points are systematically lower than the BRAHMS R_{cp} at $\eta = 2.2$. However, we note that BRAHMS calculates centrality by counting the particle multiplicity in the pseudo-rapidity range $-2.2 < \eta < 2.2$ [64]. From our centrality bias study, we find that there is very big auto-correlation between the track multiplicity and the event categories(such as forward high p_T events). This auto-correlation may introduce a significant bias in determination of centrality for events where hard binary collisions happen. From the study discussed in Chapter 4, we believe that the net effect of the auto-correlation is to enhance the high p_T particle yield in central event classes and deplete the yield in peripheral event classes. Therefore, the BRAHMS R_{cp} may be artificially high due to this effect. The PHOBOS experiment did the same centrality bias study

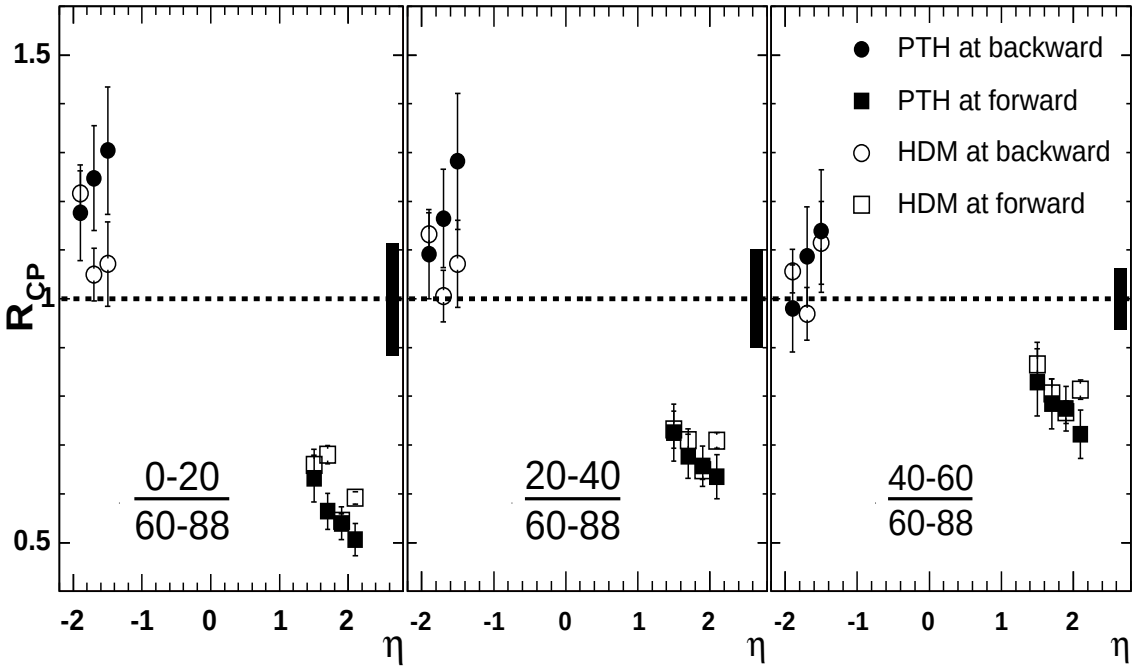

Figure 5.5: R_{cp} as a function of η for hadron decay muons(HDM) and punch-through hadrons(PTH). The error bars on each data points are the quadratic sum of systematic error and statistic error.

by using HIJING, they came to the same conclusion as we did. Figure 5.7 are the results from PHOBOS's centrality study. The plot on the right panel shows possible η ranges one can use for centrality measurement. The plot on the right panel shows the $dN/d\eta/N_{part}$ as a function of the number of participants(N_{part}) in gold nuclei. For example , if one wants to measure $dN/d\eta$ at the red area with black tilted lines($0 < \eta < 1$) and measure centrality at whole red area ($-2 < \eta < 2$), the measured results as the red dots on the right panel will be at almost 50% deviation from the truth as the blue dots.

5.2 Theoretical prospects

Since BRAHMS nuclear modification measurements at forward rapidity were first reported, lots of theoretical effort has been conducted to understanding the results. Currently there are two main theoretical approaches. The first one is the Color

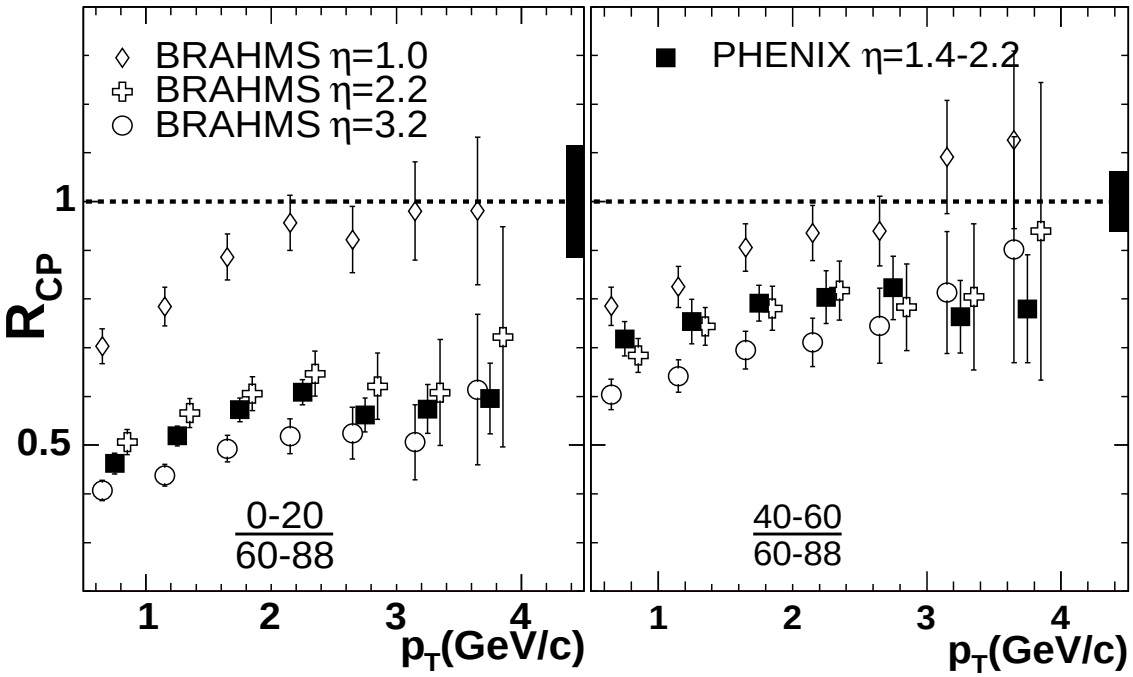

Figure 5.6: comparison between the PHENIX results and the BRAHMS results. The PHENIX R_{cp} as a function of p_T at forward rapidities shown as the average of the two methods. Note that the BRAHMS centrality ranges($\frac{0-20}{60-80}$ on the left panel and $\frac{30-50}{60-80}$ on the right panel). The error bars on each data points are the quadratic sum of systematic error and statistic error.

Glass Condensate model, which emphasizes variously the role of small x physics in nuclear production. The other uses leading-twist shadowing to account for the observed suppression. In both of these two approaches, the anti-shadowing effect at large x comes from momentum re-summation, which requires an enhancement at large x to balance the depletion at small x. We shall discuss the two approaches, but before we jump into them, let's first take a look at where our measurements stand in the Q^2, x phase space.

We measure the inclusive hadron production, $d + Au \rightarrow h + X$. By measuring the kinematic information of h, we do not have all the necessary information to reconstruct the x_1, x_2, and the Q^2 of the initial parton parton collision. Thus we use the PYTHIA simulation. Figure 5.8 shows the correlation between x of the parton in gold nuclei and the average Q^2 of the parton parton collision in which charged

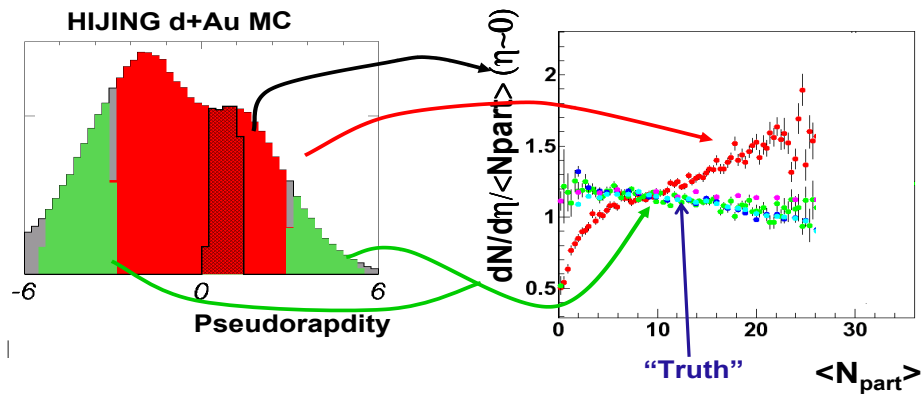

Figure 5.7: Centrality selection study from PHOBOS. *Courtesy from James Nagle's Chicago DNP2004 talk.*

hadrons with a minimal p_T cut at 1.5 GeV/c are produced into the PHENIX forward and backward muon arm coverage. At forward rapidity, our measurement explores the $x \sim 10^{-3}$ at an average $\sqrt{Q^2} = 5$ GeV. This indicates two things, which we already mentioned in Chapter 1,

- pQCD calculations are applicable for our measurements.
- Gluon density is large and may dominate the PDF.

The Color Glass Condensate model requires both high Q^2 and small x, therefore, its calculation may be applicable for our measurement. In the mean time, DGLAP quantum evolution which is based on pQCD may also be valid in our coverage. Note that the leading twist shadowing calculations use leading twist DGLAP quantum evolution in their approach. In the following two sections, we shall discuss the leading twist shadowing and the CGC in detail.

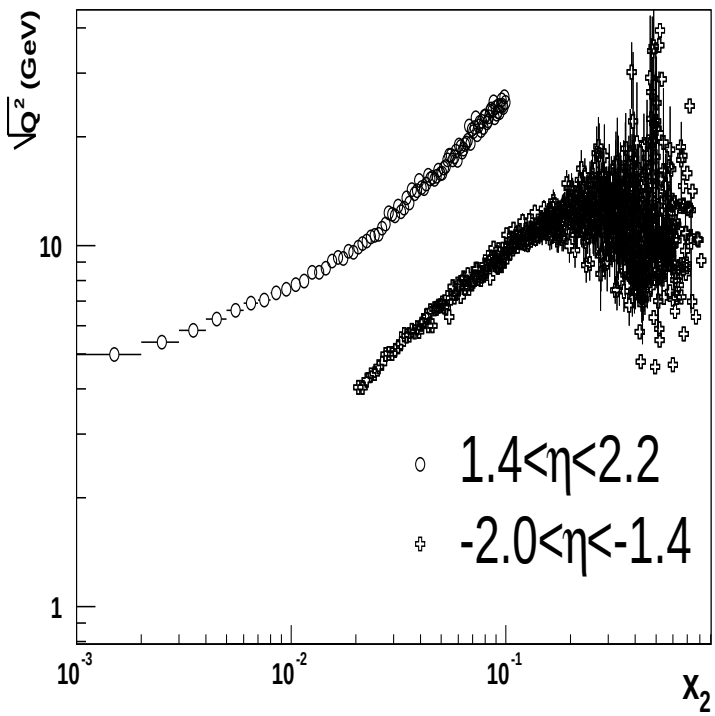

Figure 5.8: The average $\sqrt{Q^2}$ for parton parton collisions which produce hadrons with $p_T > 1.5$ GeV/c in the PHENIX muon arms is plotted as a function of x of partons in gold nuclei.

5.3 Leading twist calculations

In the leading twist approximation, the inclusive cross-sections for hadron processes $A + B- > c + X$ can be write as

$$\sigma(A + B \rightarrow c + X) = \sum_{a,b=q,g} \int dx_1 \int dx_2 f_A(x_1^a, Q^2) f_B(x_2^b, Q^2) \hat{\sigma}(ab \rightarrow c + X)$$

where the f_A is the parton distribution function in nucleus A, often called nPDF. The nuclear modification results from the difference between the f_A and the parton distribution function f_N of free nucleons. Like f_N, f_A can not be calculated via pQCD. Thus non-perturbative input from data on various hadron production processes is needed for the extraction of the nPDF. Currently, in the leading twist framework, there are two approaches that are used in extracting nPDF,

- At a given $Q_0^2 >> \Lambda_{QCD}$, one can use the available nuclear DIS, Drell Yan and charm production data to parameterize a nuclear parton distribution function. Then use the DGLAP equations to determine the nPDF at any $Q^2 > Q_0^2$. The most referenced example of this approach is the EKS parametrization.

- Use leading twist to calculate the leading twist shadowing as a correction on the free nucleon PDF. The data input to this approach is from lepton diffraction scattering experiments, such as at HERA.

5.3.1 EKS parametrization

In the EKS parametrization approach [60], the nPDF is defined through a ratio such as:

$$R_i^A = \frac{f_i^{p/A}(x,Q^2)}{f_i^p(x,Q^2)}$$

where the PDF of the free proton f_i^p are from a standard computed set, e.g. CTEQ, MRS, GRV. Isospin symmetry is invoked for constructing the PDF of bound neutrons, i.e. $f_{u(\overline{u})}^{n/A} = f_{d(\overline{d})}^{p/A}$, etc. Also to simplify the determination of the input nuclear effects for the valence and sea quarks, the following flavor-independent initial modifications(the ratio above) are assumed: $R_{u_V}^A(x,Q^2) \approx R_{d_V}^A(x,Q^2) \approx R_V^A(x,Q^2)$, and $R_{\overline{u}}^A(x,Q^2) \approx R_{\overline{d}}^A(x,Q^2) \approx R_s^A(x,Q^2) \approx R_S^A(x,Q^2)$. Thus there are only three independent ratios, R_V^A, R_S^A, R_G^A, which are the modifications for valence quarks, sea quarks and gluons, respectively. These three ratios are determined at $Q_0^2 = 2.25\text{GeV}^2$ from data. It is noted that the approximation for the relations between each ratio are only needed at the Q_0^2 for the initial determination. At other Q^2, DGLAP evolution equations are used to evolve the nPDF and it is found that all the relations above are roughly kept.

5.3.2 Leading twist shadowing

The underlying idea of the leading twist shadowing is that the incoming probe may not just interact with one nucleon at one time, it may interact with multiple

nucleons simultaneously. Such coherent effects reduce the resolution of the probe, in turn result in shadowing. Therefore the probed parton density is expressed as following,

$$f_i^A/A = f_i^N - \delta f_i^A \tag{5.1}$$

δf_i^A reflects the reduction of PDF from the coherent effects. Gribov first realized δf_i^A can be calculated by relating it to the hard diffractive scattering process in lepton proton collisions [61]. Frankfurt, Guzey and Strikman [62] proposed the following formula,

$$\delta f_i^A(x, Q^2) \approx \frac{A(A-1)}{2}(1-\eta^2)\sigma_{eff}^i f_i^N(x, Q^2) \int d^2b dz_1 dz_2 \rho_A(b, z_1)\rho_A(b, z_2)$$

and

$$\sigma_{eff}^i(x, Q^2) \propto \int dx_P f_i^D(\beta, Q^2, x_P, t) \mid_{t=t_{min}}$$

The σ_{eff}^i has the meaning of the re-scattering cross-sections, which determines the amount of shadowing. f_i^D is the so-called diffraction PDF of free nucleons, one can extract it from HERA diffraction measurements.

With the above two equations plus f_i^N and f_i^D as inputs, one can actually calculate the δf at a given Q_0^2 and plug it into equation 5.1 to calculated the nPDF at the Q_0^2. Then again applying DGLAP equation to obtain the nPDF at other Q^2. The nPDF calculated in this procedure is often called FGS parametrization.

5.3.3 A leading twist calculation

Recently, R. Vogt published a calculation [39] of the nuclear suppression factor, R_{dAu} and R_{cp} for dAu collisions at RHIC. In her calculation, she treats the deuteron PDF as the PDF of free nucleons and applies EKS and FGS parametrization on the PDF of Gold nuclei in terms of a shadowing function, $S_{P,S}^i(A, x, Q^2, \overrightarrow{r}, z)$, where $\overrightarrow{r}$ and z are the transverse and longitudinal location of the parton in position space with $s = \sqrt{r^2 + z^2}$. The first subscript, P, refers to the choice of shadowing parametrization, while the second, S, refers to the spatial dependence. The centrality dependence of the shadowing comes from the spatial dependence of the shadowing function. In this calculation Vogt uses two different spatial dependencies. The first is $S_{P,WS}$, which assumes that shadowing is proportional to the local density.

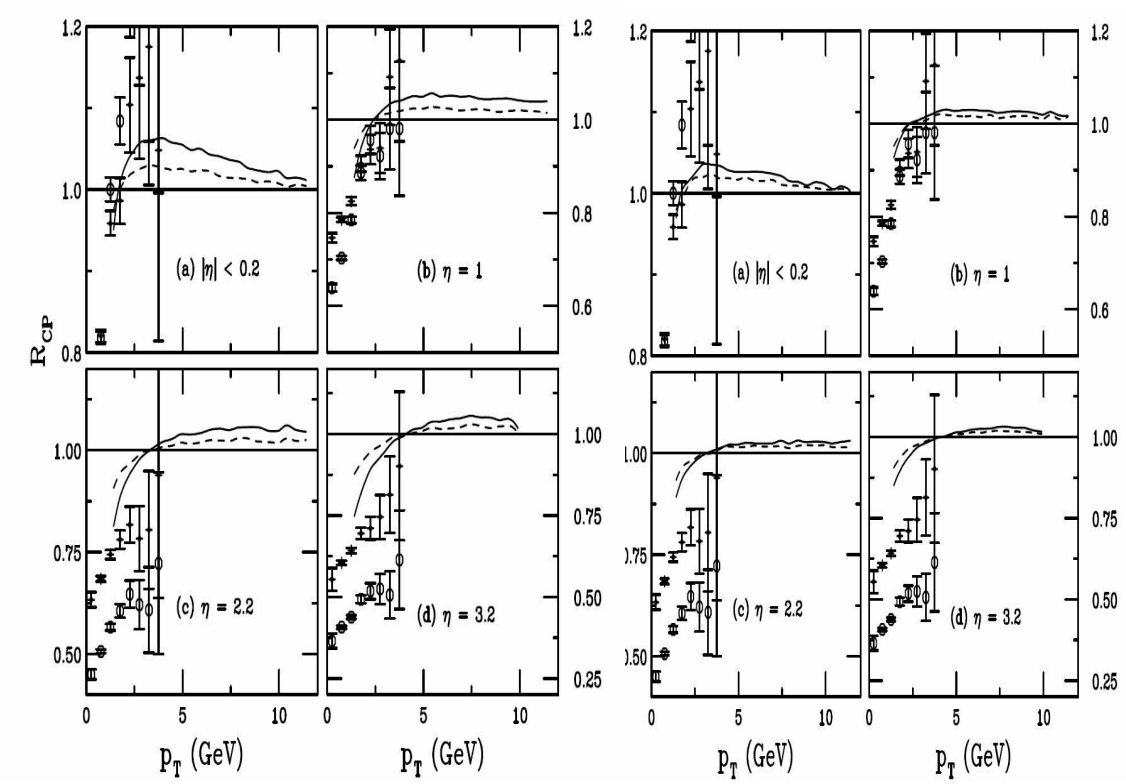

Figure 5.9: R_{CP} for charged hadrons in deuteron-gold collisions at $\sqrt{S_{NN}} = 200$ GeV as a function of p_T . The results for $S_{FGS,WS}$(right panel) and $S_{P,\rho}$ (left panel) are compared to the BRAHMS data in the following η bins: (a) $\eta = 0.2$; (b) $\eta = 1$; (c) $\eta = 2.2$ and (d) $\eta = 3.2 S_{P,\rho}$. The calculated ratios of the most central and semi-central to peripheral collisions are shown in the solid and dashed curves, respectively. The BRAHMS data are given by the open circles (most central) and diamonds (semi-central).

The other is $S_{P,\rho}$, which assumes shadowing stems from the multiple interactions of the incident partons. The calculations are done for the BRAHMS pseudo-rapidity coverage and are compared with BRAHMS results. For the EKS parametrization, the calculation seems to underestimate the suppress in R_{dAu} except for mid-rapidity, while the FGS parametrization has a better consistency with the BRAHMS R_{dAu} , but definitely underestimates the suppression in R_{cp} at very forward rapidity too. Figure 5.9 shows the results from the FGS parametrization.

As we mentioned at the end the last section, the BRAHMS R_{cp} may underesti-

mate the real suppression due to the centrality bias and our PHENIX results show a stronger suppression than the BRAHMS's result, this also indicates that the FGS shadowing is not able to reproduced PHENIX results too. In Figure 5.10 we compared the FGS parametrization with the PHENIX R_{CP} at forward rapidity. The calculation is not able to reproduce the suppression in all the centrality bins seen by PHENIX, as we expected. Although the $S_{FGS,\rho}$ gives larger centrality dependence relative to $S_{FGS,WS}$, its centrality dependence are still much smaller than what appears in data. Another observation is that the η dependence in the calculation seems very small. This also contradicts with the strong η dependence seen by data.

5.4 CGC calculation

We have described the CGC model in the introduction chapter. Here we will discuss a CGC calculation by Dmitri Kharzeev and his company [38] for the forward suppression observed by the BRAHMS experiment.

In this special CGC calculation, the cross-sections for hadron production are determined by the fragmentation of gluons and quarks which are produced in the collisions. The gluon production cross-section is given by,

$$\frac{d\sigma_G^{dAu}}{d^2kdy} = \frac{C_F S_A S_d}{\alpha_s \pi (2\pi)^3} \frac{1}{\underline{k}^2} \int d^2z \Delta_z^2 n_G(\underline{z}, Y-y) e^{-i\underline{k}\cdot\underline{z}} \Delta_z^2 N_G(\underline{z}, y)$$

where S_A and S_d are cross sectional areas of the gold and deuteron nuclei correspondingly and Y is the total rapidity interval. $\underline{z}$ is the size of the gluon dipole and n_G and N_G are the gluon dipole scattering amplitude on deuteron nuclei and gold nuclei. In the calculation, n_G is obtained in a simple form by the analogy with the two-gluon exchange processes. But in the determination of N_G, the asymptotic behavior at $z_T << 1/Q_s(y)$ and at $z_T >> 1/Q_s(y)$ are used to avoid the difficulty of solving the non-linear evolution equations, where z_T is the transverse size of the gluon dipole and $Q_s(y)$ is the saturation scale. A Glauber-like formula is given for N_G as following

$$N_G(z_T, y) = 1 - e^{[-\frac{1}{4}(z_T^2 Q_s^2)^\gamma (y, z_T^2)]}$$

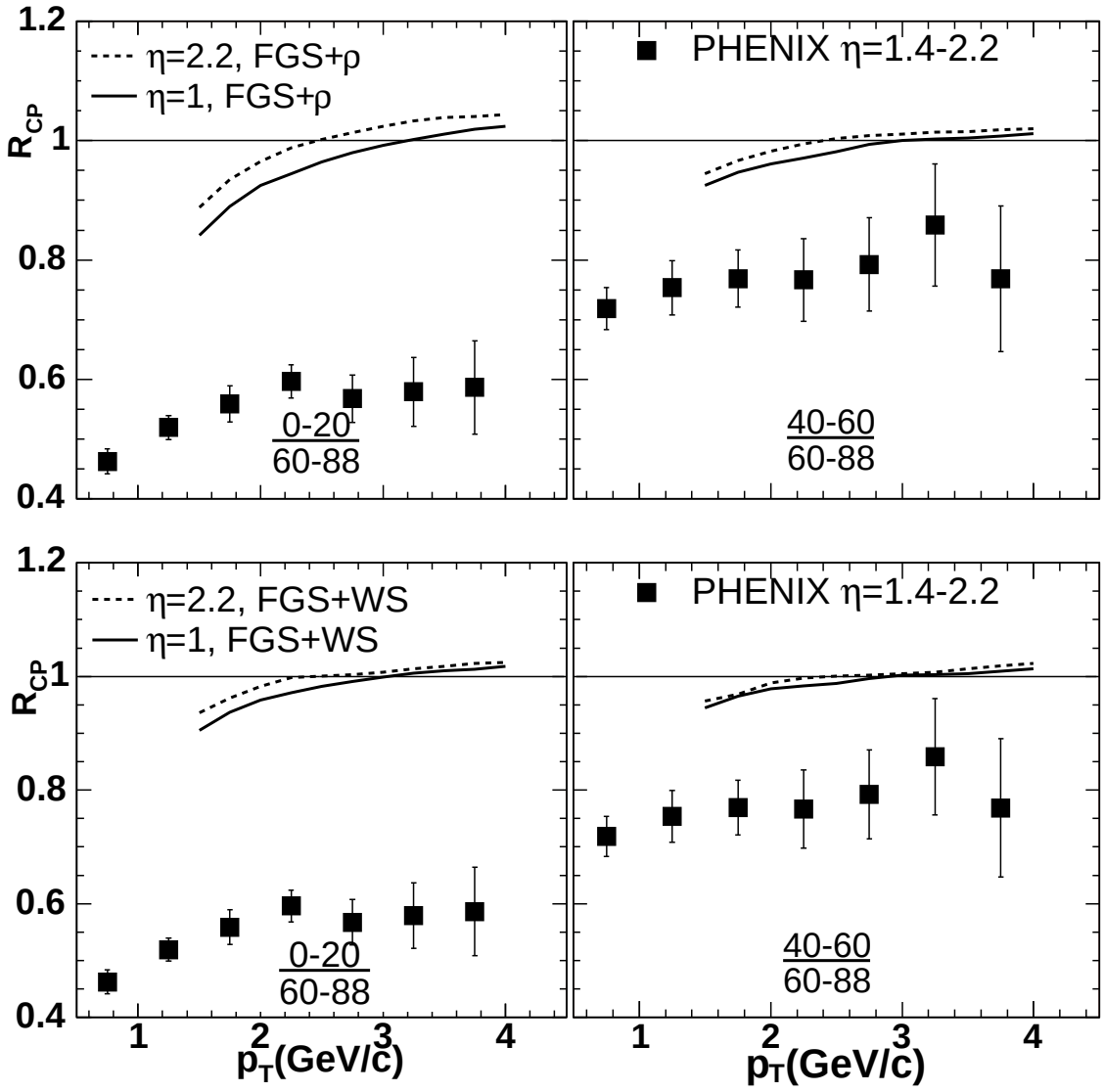

Figure 5.10: Comparison between FGS parametrization and the PHENIX R_{CP}. In the upper two panels, the shadowing function used in the calculation is $S_{GFS,\rho}$. In the lower two panels, $S_{FGS,WS}$ is used. Note the calculation was done for the BRAHMS R_{CP}, as we mentioned that the centrality definition were different between BRAHMS and PHENIX.

where $\gamma(y, z_T^2)$ is the anomalous dimension and can be written as

$$\gamma(y, z_T^2) = 0.5(1 + \frac{\xi(y, z_T^2)}{\xi(y, z_T^2) + \sqrt{2\xi(y, z_T^2)} + 7\zeta(3)c})$$

In the formula $\xi(y, z_T^2) = \frac{\ln(1/(z_T^2 Q_s^2))}{(\lambda/2)(y-y_0)}$ and c is a constant to be determined from data. The quark production cross-section is similar to the gluon production cross-section. Thus, the hadron production cross-section can be calculated.

The saturation scale is given by, $Q_s^2(y) = \Lambda^2 A^{\frac{1}{3}} e^{\lambda y} = 0.13 GeV^2 e^{\lambda y} N_{coll}$. Here N_{coll} is the number of binary collisions at a given centrality in a dAu collision. Parameters $\Lambda = 0.6$ GeV and $\lambda = 0.3$ are fixed by HERA DIS data. Figure 5.11 shows the R_{cp} calculated at $\eta = 0, 1, 2.2, 3.2$. And for comparison, BRAHMS data is also plotted. Figure 5.12 shows the comparison between this CGC calculation and the PHENIX R_{CP}.

The calculation does not reproduce the PHENIX R_{CP} as well as it reproduces the BRAHMS R_{cp}. However, we note that there are two free parameters c, y_0 in the calculation of ξ. They are fixed by fitting the BRAHMS data. Although the authors of the calculation claim that their results are not sensitive to these two parameters, the calculation may be biased by the BRAHMS results and we know that the BRAHMS results underestimate the suppression due to the centrality bias. Also, this calculation uses the same centrality definition as the BRAHMS experiment, which is different from the PHENIX's centrality too.

Overall, it seems this CGC calculations predicts a much stronger shadowing effect than the leading twist calculation by Vogt does. Moreover, it also gets the centrality and rapidity dependence roughly right comparing to data.

5.5 Soft physics

It is important to note that in the transverse momentum range of this measurement, $0.5 < p_T < 4.0$GeV/c, hadron production is also sensitive to soft physics phenomena which are determined by coherent hadron-hadron interactions. In p + A reactions at lower energies soft hadron production shifts from forward to backward rapidity, with

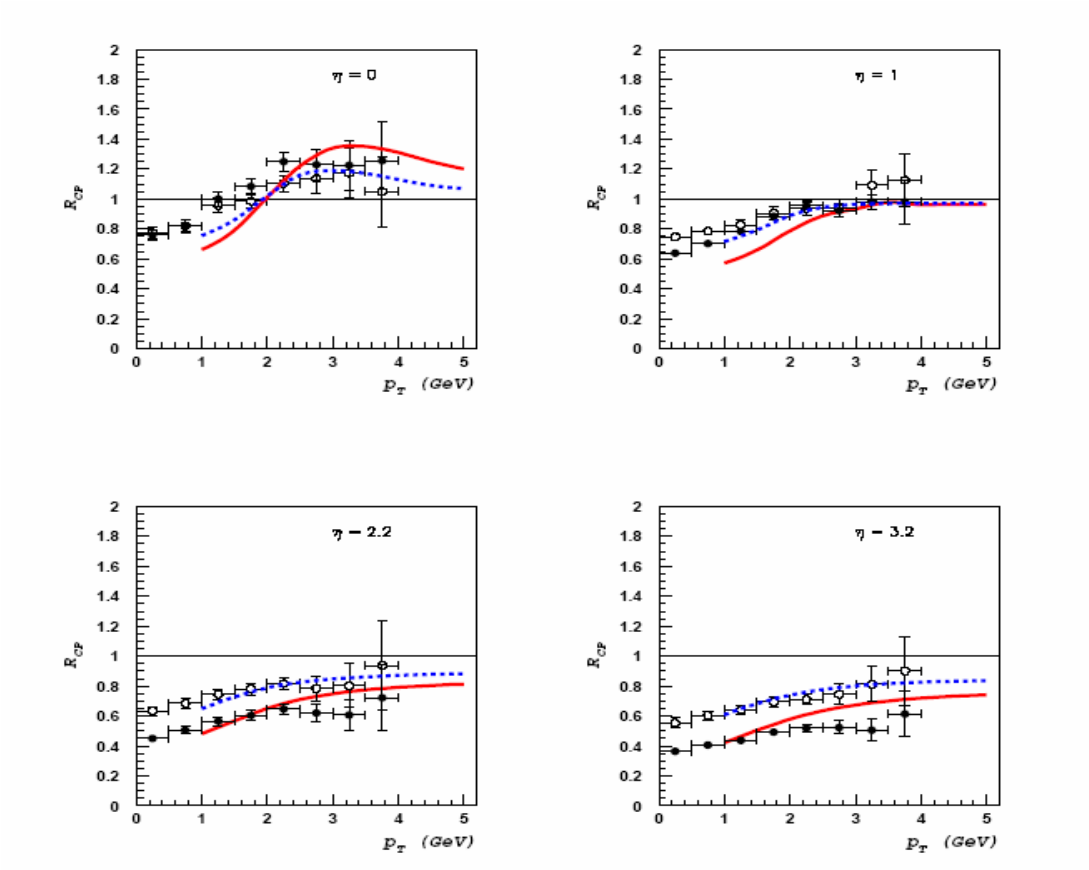

Figure 5.11: Nuclear modification factor R_{CP} of charged particles for different rapidities. Data is from the BRAHMS experiment. Full and open dots give the ratio of particle yields in $0-20\%$ and $30-50\%$ centrality events correspondingly divided by the yields from $60-80\%$ centrality events scaled by the mean number of binary collisions.

a larger shift for larger nuclear targets. This can be understood as rapidity exchange between incident and target nucleons. One study [63] suggests that for a 100GeV/c proton incident on a lead nucleus at rest, the proton suffers an average rapidity loss of $\Delta y \sim 2.5$. This rapidity loss at RHIC energies is quite similar, as determined in Au + Au reactions [64]. The PHOBOS experiment measured inclusive charged hadron $dN/d\eta$ over a wide rapidity range at different dAu centralities [65]. The mean p_T for their measurement is less than 500 MeV. At such low p_T, the hadron production is dominated by soft physics. We can calculate the R_{cp} as a function of η using the PHOBOS $dn/d\eta$. It would be interesting if we make a comparison

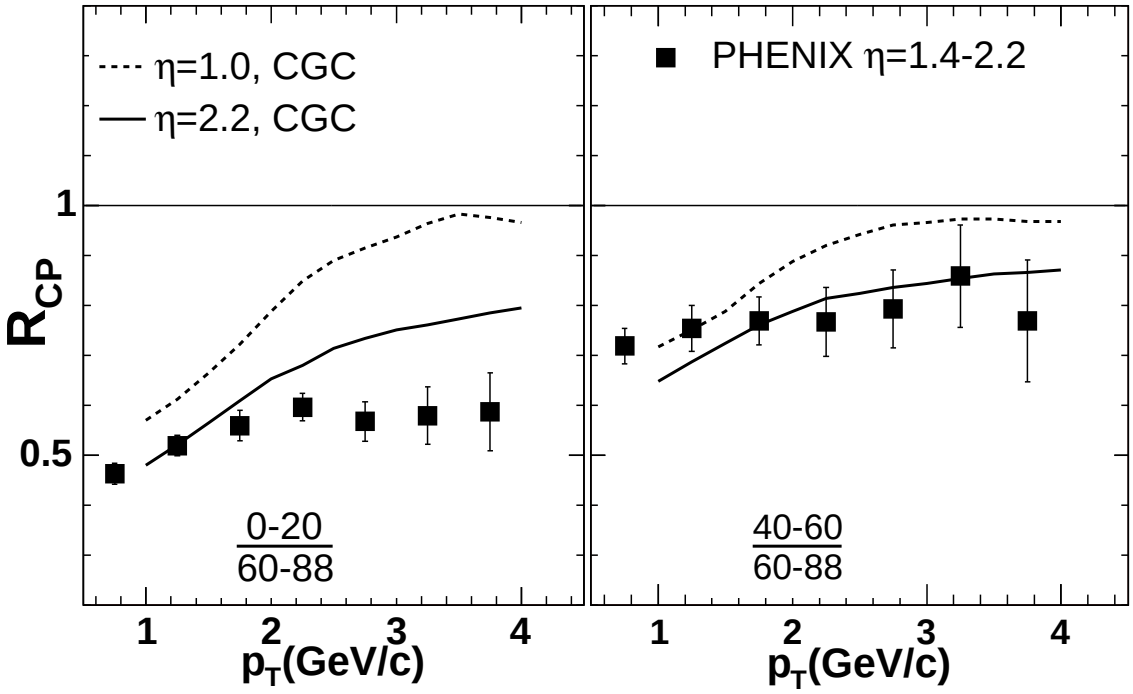

Figure 5.12: Comparison between the CGC calculation and the PHENIX R_{CP}.

of our R_{cp} ($p_T > 1.5$ GeV/c) as a function of η with it. Figure 5.13 shows the comparison. From the plot, we can see that at $-1.2 > \eta > -2.0$, the PHENIX R_{cp} has a totally different behavior from the PHOBOS R_{cp}. This may indicates that the enhancement in the backward rapidity is not so trivial as soft physics productions. On the other hand, at $2.2 > \eta > 1.4$, the two R_{cp} almost overlap on each other regardless the difference in the p_T ranges. This is somehow also surprising, and needs to be understood.

5.6 Summary

The suppression of hadron yields relative to binary collision scaling at forward rapidity seen in this analysis is expected from initial state nuclear effects. However, detailed comparisons with various theoretical approaches is necessary in order to discriminate between various models. More detailed analysis will also help in resolving the discrimination between models. For example, the CGC model also predicts the

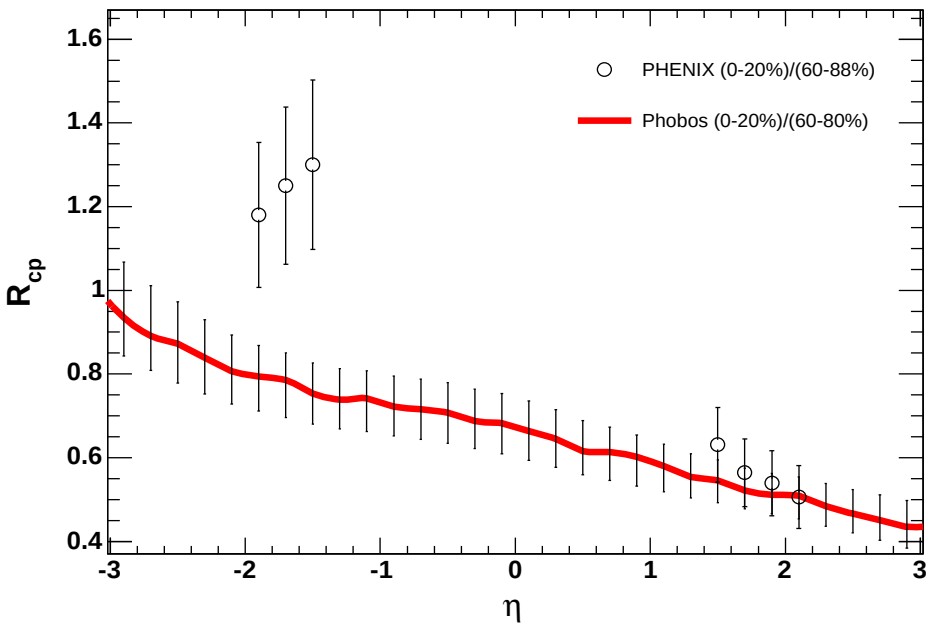

Figure 5.13: Comparison between PHENIX $R_{cp}(\eta, p_T > 1.5\text{GeV}/c)$ with the PHOBOS $R_{cp}(\eta)$, which is calculated from $dN/d\eta$.

mono-jet in the forward rapidity [66].

We have already started the two particle correlation analysis using the PHENIX muon arms and the PHENIX central arm. In the correlation analysis, we trigger on the high p_T hadrons in the PHENIX muon arm and look for the azimuthal (i.e. ϕ angles) correlation between the trigger particle and the associated particles in the PHENIX central arm. Figure 5.14 shows the $\Delta\phi = \phi_{trigger} - \phi_{associate}$ distributions in different trigger particle p_T bins. The azimuthal correlation between the south muon arm (backward rapidity) and the central arm(middle rapidity), called SC correlation, is sensitive to the jet production from high x partons in gold nuclei and the azimuthal correlation between the north muon arm (forward rapidity) and the central arm, called NC correlation, is sensitive to the jet production from low x partons in gold nuclei. *Note, since we are looking for the azimuthal correlation from different rapidities, there is no near side associated particles(i.e. no signal at* $\Delta\phi = 0$ *).* If the mono-jet prediction from CGC is right, we should be able to see a

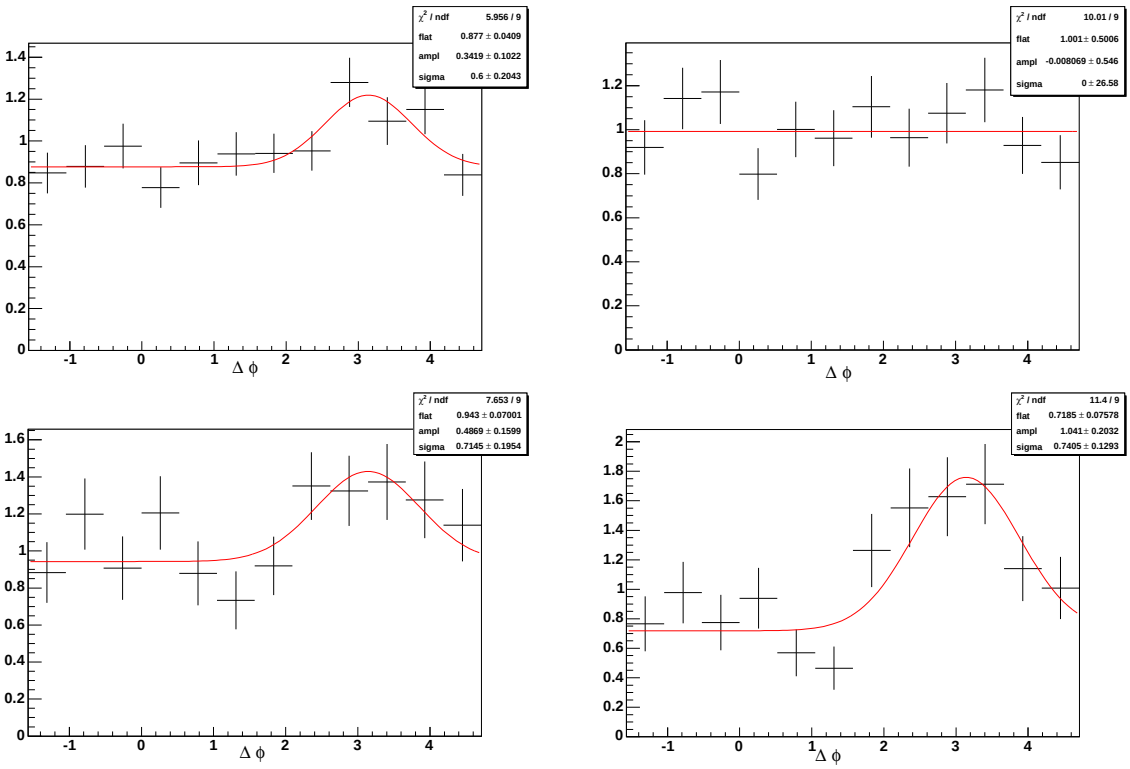

Figure 5.14: $\Delta\phi$ distributions for SC correlations (lift two panels) and NC correlations (right two panels) with $1 < p_T^{trig} < 2$ GeV/c (upper two panels) and $p_T^{trig} > 2$ GeV/c.

suppression on the jet yield at forward rapidity relative to the jet yield at backward rapidity. We can see from Figure 5.14 that in the $p_T^{trig} > 2$ GeV/c bins, a peak at $\Delta\phi = \pi$ radian is clear seen in both the SC and NC correlations, as we expected from regular back-to-back jet correlations. But in the $2 > p_T^{trig} > 1$ GeV/c bin, the peak is only shown up in SC correlation. The disappearing of the $\Delta\phi = \pi$ peak in low p_T^{trig} bin at forward rapidity is consistent with the prediction of mono-jet by CGC because lower p_T^{trig} bin at forward rapidity is more sensitive to low x partons in gold nuclei. However this analysis is still very preliminary, a lot of more careful checks need to be done before we can really draw a conclusion from it.

To summarize, we observe a suppression in hadron yields relative to binary collision scaling at forward rapidities and an enhancement at backward rapidity for central relative to peripheral d+Au reactions at $\sqrt{s_{NN}} = 200$ GeV. The forward ra-

pidity suppression is in qualitative agreement with the expectation of shadowing and saturation effects in the small x region in the gold nucleus. However, other physics effects must also be considered in understanding the full p_T and Q dependence. The source of the backward rapidity enhancement, and the possible contribution of anti-shadowing of large x partons, has yet to be understood.

Bibliography

[1] R.P. Feynman, M Gell-Mann, G. Zweig *Phys. Rev. Lett.* 13, 678(1964)

[2] W.B. Bartel *Phys. Lett.* B28, 148(1968)

[3] Donald. H. Perkins, *Introduction to High Engery Physics* **Addison-Wesley Publishing Company, Inc**

[4] Barnes, V., *et. al., Phys. Rev. Lett.* 12, 204(1964).

[5] Bjorken, J. D., *Phys. Rev.* 163, 1767(1967).

[6] Friedman, J.I, and H,W, Kendall, *Ann. Rev. Nucl. Science* 22, 203(1972).

[7] Collins, J. C., D. E. Soper and G. Sterman, *Nucl. Phys.* B261, 104(1985).

[8] Altarilli, G., G. Parisi, *Nucl. Phys* B126, 298(1977); Gribov, V. N., L. N. Lipatov *Sov. J. Nucl. Phys.* 15 438(1972); 675(1972); Dokshitzer, Y. L., *Sov. Phys. JETP* 46, 641(1977).

[9] Halina A., Allen C. Caldwell, *Rev. Mod. Phys.*, Vol.71, No.5, Oct. 1999.

[10] Kuraev, E.A., L.N. Lipatov, and V.S. Fadin, *Sov. Phys. JETP* 44, 443(1976); 45, 199(1977); Baliskii Y. Y., L.N. Lipatov, *Sov. J. Nucl. Phys.* 28, 822(1978).

[11] Gribov, L. V., E. M. Levin, M. G. Ryskin, *Phys., Rep.* 100, 1(1982).

[12] A.K. Golec-Biernat *et al. PRL.* 86, 596 (2001)

[13] CERN NA2/EMC J.J. Aubert *et. al.* Phys. Lett. B 123(1983)275

[14] G. Piller and W. Weise, "Vector Meson Dominance - Selected Topics", Lecture Notes in Physcis 365(1990) 3. G. Piller *et. al., Phys. Rev.* C42(1990)R1834

[15] Michele Arneodo, *Phys. Rep.* 240, 301(1994)

[16] M. Staszel, J. Rozynek and G. Wilk, *Phys. Rev.* D29, 2638(1984)

[17] F.E. Close, R.G. Roberts and G.C. Ross, *Phys. Lett.* B129 346(1983)

[18] N.N. Nikoleav and V.I. Zakharov *Phys. Lett.* B55, 397(1975)

[19] A.H. Muller and J. Qiu *Nucl. Phys* B268, 427(1986)

[20] E.L. Berge and J. Qiu *Phys. Lett.* B206, 141(1988)

[21] F.E. Close and R.G. Robert *Phys. Lett.* B213, 91(1988)

[22] J. Qiu *Nucl. Phys* B291, 746(1987)

[23] D.M. Alde *et. al.* E772 collaboration, *Phys. Rev. Lett.* 64, 2479(1990)

[24] D. Antreasyan *et. al. Phys. Rev.* D19, 764(1979)

[25] A.Accardi and M.Gyulassy, arXiv:nucl-th/0308029 v2.

[26] Larry McLerran and Raju Venugopalan *Phys. Rev.* D49. 2233(1994). E. Iancu *et. al.* arXiv:hep-ph/0403103 v3.

[27] T. Matsui and H. Satz. *Phys. Lett.* B178, 416(1986)

[28] M. Gyulassy and X.N. Wang *Phys. Rev. Lett.* 68, 1480(1992) M Plumer, M. Gyulassy and X.N. Wang *Nucl. Phys.* A520,511(1995) X.N. Wang *Phys. Rev.* C63, 054902(2001)

[29] Thomas Peitzmann, Markus H. Thoma *Phys.Rept.* 364, 175-246(2002)

[30] S. S. Adler *et al., Phys. Rev.* C69, 034910(2004)

[31] S.R. Klein and R. Vogt *Phys. Rev.* C67, 047901(2003)

[32] D. Kharzeev, E. Levin, L. McLerran *Phys. Lett.* B561, 93(2003)

[33] S.S. Adler *et al., Phys. Rev. Lett.* 91, 072303(2003).

[34] M. Gyulassy, P. Levai and I. Vitev *Phys. Rev. Lett.* 85, 5535(2000)

[35] E. Wang and X.N. Wang *Phys. Rev. Lett.* 87, 142301(2001)

[36] Jamal Jalilian-Marian, Alex Kovner, Larry McLerran and Heribert Weigert *Phys. Rev.* D55, 5414(1997)

[37] *courtesy from Yuri V. Kovchegov's talk for 2004 PHENIX Muon Collaboration meeting in Santa Fe, NM*

[38] Dmitri Kharzeev, Yuri V. Kovchegov and Kirill Tuchin. arXiv:hep-ph/0405045 v1.

[39] R. Vogt arXiv:hep-ph/0405060

[40] M. Harrison, T. Ludlam, and S. Ozaki. Rhic project overview. Nucl. Instrum. Meth., A499:235244, 2003.

[41] K. Adcox et al., NIM A499 469-479 (2003)

[42] M. Allen et al., NIM A499 549-559 (2003)

[43] PHENIX central arm tracking detectors K. Adcox et al., NIM A499 489-507 (2003); PHENIX central arm particle I.D. detectors M. Aizawa et al., NIM A499 508-520 (2003); The PHENIX calorimeter L. Aphecetche et al., NIM A499 521-536 (2003);

[44] S.H. Aronson et al., NIM A499 480-488 (2003)

[45] B. B. Back *et. al., Phys. Rev. Lett.* 87, 102303(2003)

[46] E. Iarocci, Nucl. Instr. and Meth. 217 (1983) 30.

[47] S. Adler et al., NIMA499 593-602 (2003)

[48] H. Akikawa et al., NIM A499 537-548 (2003)

[49] http://pdg.lbl.gov/2004/passagerpp.pdf, Fig.27.1

[50] http://pdg.lbl.gov/2004/hadronicrpp.pdf, Fig.40.10

[51] http://wwwasdoc.web.cern.ch/wwwasdoc/pdfdir/geant.pdf. In our simulation, we use FLUKA for hadronic interaction.

[52] Axel Drees, Tom Hemmick, Barbara Jacak, Jiangyong Jia, Sean Leckey, Sasha Milov, Mike Reuter,Anne Sickles, Ron Soltz PHENIX analysis note 210, http://www.phenix.bnl.gov/phenix/WWW/p/info/an/210

[53] In the present work the Woods-Saxon nuclear density parameters: radius R = 6.38 fm, diffusivity a = 0.54 fm and N-N cross section σ_{NN}^{inel} = 42 mb were used. The deuteron is described by a Hulthén wave function (L. Hulthén and M. Sagawara, Handbuch der Physik **39** (1957)) with $\alpha = 0.228$ fm^{-1} and $\beta = 1.18$ fm^{-1}. Glauber model monte-carlo code: /offline/analysis/glauber_mc

[54] Mike J. Tannenbaum PHENIX analysis note 209, http://www.phenix.bnl.gov/phenix/WWW/p/info/209

[55] A GEANT based PHENIX detector simulation package. http://vpac17.phy.vanderbilt.edu/simulation/PISA/pisa.html

[56] X. N. Wang and M. Gyulassy, *Phys. Rew.* D44,(3501)1991; M. Gyulassy and X. N. Wang, Comput. Phys. Commun. **83**3071994.

[57] S. Belikov. et. al. PHENIX analysis note 184, http://www.phenix.bnl.gov/phenix/WWW/p/info/an/184

[58] S.Bazilevsky et. al. PHENIX analysis note 176 https://www.phenix.bnl.gov/phenix/WWW/p/info/an/176/

Kensuke, Osama and Jiangyong Jia PHENIX analysis note 276 https://www.phenix.bnl.gov/phenix/WWW/p/info/an/276/

[59] I.Arsene et al., PLB595, 209 (2004)

[60] K. J. Eskola, *et.al* arXiv:hep-ph/0302170

[61] V.N. Gribov, *Sov. Phys. JETP* 29 (1969) 483 [Zh. Eksp. Teor. Fiz. 56 (1969) 892].

[62] L. Frankfurt, *et. al* arXiv:hep-ph/0303033

[63] W. Busza and A.S. Goldhaber, *Phys. Lett.* B139, 235 (1984).

[64] I.Arsene et al., Phys. Rev. Lett. 93, 102301 (2004).

[65] PHOBOS Colloboration, arXiv:nucl-ex/0409021

[66] Dmitri Kharzeev *et.al.* arXiv:hep-ph/0403271